L I D A R S T U D I E S

O F

A T M O S P H E R I C A E R O S O L S

By

S. A. Young. B.Sc(Hons)

A Thesis
presented for the degree of
DOCTOR OF PHILOSOPHY
at the
UNIVERSITY OF ADELAIDE
DEPARTMENT OF PHYSICS

JUNE, 1980.

Awarded 5th Dec. 1980.

SUMMARY

This thesis is concerned with the properties of aerosols in the stratosphere and troposphere as determined by optical observations from the ground.

Natural aerosols from volcanic eruptions and man-made aerosols of industrial origin affect the optical transmission properties of the atmosphere and may effect the chemical properties of the ozone layer. Such effects can lead to changes in the global climate.

Interest in the properties of the stratospheric aerosol layer has been heightened in recent years by the affects of the possible introduction of large fleets of supersonic transport (SST) aircraft which were to be operated in the stratosphere.

Observations of the stratospheric aerosol layer, begun in Adelaide in 1969, using a ruby lidar system have been continued and the results examined for both annual variations and long term trends. The increase in the stratospheric aerosol optical thickness has been interpreted in terms of a globally-averaged reduction in solar radiation at the surface.

The variation in the stratospheric aerosol backscatter has been compared to variations in a number of meteorological parameters, including the tropopause height and pressure, the minimum stratospheric temperature, stratospheric winds, and the height of various constant pressure surfaces in the stratosphere.

Scattering from aerosols above 30 km has been detected on several occasions and is of two forms. One is simply the extension of the stratospheric layer into the region above 30 km; the other is in the form of higher layers that are possibly of extraterrestrial origin.

The conversion of the original static system into a steerable lidar for tropospheric observations is described. The need for more profiles to be sampled at a greater rate required the development of an automatic data acquisition system which writes digitised lidar signals and system information on to magnetic computer tape. A fast logarithmic amplifier was developed to accommodate the large dynamic range of the lidar signals and a pulse energy monitor was designed to allow the accurate comparison of consecutive lidar signals. The photomultiplier was calibrated experimentally for variations in linearity. Other experiments showed that the effects of signal induced photomultiplier noise are negligible in the present system.

The tropospheric studies included the determination of a value for the aerosol backscatter-to-extinction ratio and the testing of the validity and accuracy of various methods used in the analysis of the tropospheric data. Some of these methods have been extended to allow their more general use. Several techniques for the determination of the boundary values of extinction coefficients needed in the analysis methods are investigated. All these methods have been tested and used on tropospheric lidar data recorded in Adelaide and Melbourne. The results of a comparative study between lidar and *in situ* measurements of temperature, relative humidity, particle number density and aerosol extinction coefficients are reported.

P R E F A C E

To the best of the author's knowledge this thesis contains no material previously published or written by another person, except where due reference is made in the text. It contains no material which has been submitted or accepted for the award of any other degree or diploma in any university.

Stuart A. Young.

University of Adelaide.

ACKNOWLEDGEMENTS

The work described in this thesis was carried out in the Physics Department of the University of Adelaide under the supervision of Dr W. G. Elford. The author is indebted to Dr Elford for his advice, guidance and continued encouragement during the course of the project.

The author thanks Mr L. Thomas for his technical assistance early in the project and the late Mr M. Manuel who, with Mr Thomas, was responsible for the mechanical design and construction of the azimuth rotation and elevation mirror assemblies.

For the opportunity of participating in a joint lidar/airborne experiment in September 1976 the author is especially grateful to Dr C.M.R. Platt of the C.S.I.R.O. Division of Atmospheric Physics. The author is particularly indebted to his colleague during this experiment, Mr A.C. Dilley for his assistance in the operation of the lidar and in the initial preparation of the lidar, radiosonde and airborne data. Thanks are also due to Mr D. Packham who operated the airborne nephelometer, Pollak counter and temperature sensor.

The author is grateful to Mr D. Booth of the Footscray Institute of Technology for his helpful discussion on the problems of photomultiplier overload and of the digital recording of lidar signals which prompted further work in these areas.

Acknowledgements Continued.....

Thanks are due to Mr J. Cole of Cole Precision Optics and members of the laser group of the Weapons Research Establishment (now Defence Research Centre) for their discussions on the problems of mirror reflective coatings and ruby rod damage.

Finance was provided early in the project by a grant from the Radio Research Board. The author was the holder of a University Research Grant from the University of Adelaide.

C O N T E N T S

CONTENTS Continued.....

CONTENTS Continued.....

CONTENTS Continued.....

CHAPTER 1

A REVIEW OF THE CURRENT KNOWLEDGE OF ATMOSPHERIC AEROSOLS

1.1 Introduction

Interest in atmospheric aerosols has increased in recent years because of the growing concern that they may have significant effects on both local and global climate. For example, Cadle and Grams (1975) have reviewed a number of papers which have developed models to describe the influence of an increase in the aerosol content of the stratosphere on the radiative energy exchange in the earth atmosphere system. Effects of tropospheric aerosols on solar and terrestrial radiation and local climate have been studied also. Paltridge and Platt (1973) measured the change in upward and downward flux caused by a strong aerosol layer of continental origin. Other measurements of the radiative effects of tropospheric aerosol layers have been made by De Luisi *et al* (1976), and Russell *et al* (1979) have measured the change in the earth atmosphere albedo induced by an aerosol layer.

As a result of this concern, there are many groups around the world observing aerosols and their effects by a variety of methods. These include particle collection and light scattering measurements which are performed *in situ* by aircraft, balloons, or rockets, and remote sensing measurements using radiometers, searchlights and lidars (laser radars). Lidar (light detection and ranging) measurements of atmospheric aerosols is the chief topic of this thesis.

Aerosols have many manifestations in the atmosphere. In the troposphere they are responsible, at least in part, for red sunsets, the

whiteness of the horizon sky in the direction of the sun, the solar aureole, city haze, smog and fog. By the processes of scattering and absorption they also limit the maximum visual range through the atmosphere. In the stratosphere they are responsible for the "purple light" at twilight and sometimes visual clouds and striations high in the sky after sunset, especially after large volcanic eruptions. These stratospheric layers are often seen from high altitude aircraft and have been photographed from balloons and spacecraft.

The presence of aerosols in the stratosphere was deduced as early as 1927 by Gruner and Kleinert (1927), and later by Gruner (1942), from observations of twilight effects. Later, more sophisticated twilight sky intensity measurements (Bigg, 1956; Volz and Goody, 1962), and balloon-borne impactor measurements by Junge and his co-workers, (Junge and Manson, 1961; Junge, 1961; Junge *et al* 1961) verified the existence of a stratospheric aerosol layer. Further *in situ* particle counting observations were performed by Mossop (1965), Friend (1966) and Rosen (1964, 1968). Remote sensing of the layer using searchlights was performed by Rosenberg (1960), Elterman (1966), and Elterman *et al* (1969), while the first lidar observations were performed by Fiocco and Grams (1964), Clemesha *et al* (1966), and Grams and Fiocco (1967).

The stratospheric aerosol layer is now known to be a world-wide phenomenon which experiences a marked increase in particle number density with the influx of aerosols and gases from volcanic eruptions. In recent times, dramatic increases in particle concentrations have been measured after the violent eruptions of Gunung Agung (1963), Fernandina (1968) and Volcan de Feugo (1974). The global nature of the layer has been demonstrated by the balloon-borne optical particle counter measurements of

Rosen *et al* (1975) and the sulphate sampling measurements of Lazrus and Gandrud (1974a).

In what follows is reviewed the current knowledge of aerosols in the stratosphere and troposphere, their shapes and sizes, composition and optical scattering properties.

1.2 The Classification of Aerosol Particle Sizes.

The radii of aerosol particles cover several orders of magnitude and the particles exhibit a wide variety of characteristics in lifetime, falling speed, coagulation and so on. Sizes vary from clusters of molecules with radii of 1 nm to the largest aerosols with radii in the range 10 μm to 100 μm. The largest particles in this range are produced by dust storms and sea spray and are removed quickly from the atmosphere by sedimentation. Only rain drops ($r \geqslant 1$ mm), and hail, graupel and snow which can be up to 10 cm in radius, have larger dimensions.

Aerosols are divided into three broad groups according to their sizes. Aitken particles have radii less than 0.1 μm. Those with radii between 0.01 μm and 0.1 μm have fairly stable sizes and reasonable coagulation times. They are usually detected by electron microscope, or alternatively, by an Aitken counter which behaves similarly to a Wilson Cloud Chamber. Smaller particles than these experience large Brownian motions which lead to their rapid coagulation with larger particles and collection on the walls of containing vessels. Aitken particles are also called Condensation Nucleus particles.

Aerosol particles with radii in the range 0.1 μm to 1.0 μm are called "large" particles. These are not affected greatly by either

Brownian motion or by gravitational settling, and are likely to survive longest as individual particles because both diffusive and inertial coagulative processes for this size range are inefficient. They are also unlikely to have been formed directly from the physical grinding together of larger particles, or from condensation from vapour as this process usually tends to produce smaller particles. Because their dimensions are of the order of visible wavelengths, large particles are efficient scatterers of light and are responsible for such optical phenomena as haze.

"Giant" particles are aerosols with radii greater than 1 μm. Their concentration relative to other particles is small. They are large enough to be visible with a light microscope. At the smallest end of this range, falling speeds are of the order of 2×10^{-4} m sec^{-1}, and increase quadratically with radius.

Particles with radii greater than 10 μm are relatively rare and gravitational settling in this range is high. A 10 μm radius particle with a density of 2 gm cm^{-3} has a falling speed under gravity of 2 cm sec^{-1}. They are the approximate size of cloud droplets and can just be seen with the unaided eye.

1.3 The Composition of Aerosols

1.3.1 Tropospheric Aerosols

Aerosols in the troposphere are produced in a variety of ways. The particles generated over land include wind blown dust, organic materials such as fungal spores, and the occasional salt crystal. Natural fires and industry also release particles of soot and ash into the atmosphere, and some particles form from gases released by industry (Ayers *et al* 1979). The aerosols in the giant range, produced over the sea are predominantly sea-spray particles (Woodcock, 1953).

The composition of the tropospheric aerosol in terms of the relative concentrations of continental and maritime components has been studied by Delaney *et al* (1973), who used neutron activation techniques to analyse airborne samples of aerosols collected on filters between ground level and 9.1 km altitude. Sampling was performed at three sites, one mid-continental, one desert and one oceanic.

The aerosols found in the middle and upper troposphere at the three sites were almost uniform, with continental material contributing 90 to 95 percent and marine material 5 to 10 percent. They found the continental profiles to be characterised by a continuous regime which extended from the surface up to 9 km, whereas the oceanic profiles consisted of a marine region below one to two kilometres, and a region above this which resembled the high continental troposphere. Hogan (1976) has suggested that the aerosol above the inversion at oceanic sites could be representative of the world background tropospheric aerosol.

Junge (1953, 1954), using micro-analytical techniques found that the soluble fraction of the large continental aerosols comprised mainly NH_4^+ and $SO_4^=$ ions; the concentration ratio indicated $(NH_4)_2SO_4$ as the likely compound. The giant size particles had considerably less NH_4^+ and indicated that other cations were involved. Particles collected by Ayers *et al* (1979) in ambient tropospheric background air were also ammonium sulphate.

Reagan *et al* (1977) also studied the shape and composition of continental tropospheric aerosols collected in an airborne impactor. An electron micrograph analysis revealed that thirty percent of the particles were sulphuric acid types, five percent were crystal, fifteen percent were

porous and unstable under the electron microscope beam, and the remaining fifty percent were mostly spherical particles which were stable under the electron microscope beam. The particle sphericity was also examined. Fifty out of the 450 particles examined were elliptical with a major-to-minor axis ratio greater than two. The remaining 400 were very nearly spherical.

1.3.2 Stratospheric Aerosols

The earliest measurements of the composition of stratospheric particles were by Junge (1961) and Junge and Manson (1961) using a balloon-borne electron microprobe. The results of these experiments indicated that sulphur was the most common element and because of the hygroscopic nature of the particles Junge *et al* (1961) assumed that the sulphur was most likely in the form of sulphate. From the occurrence in the stratosphere of a maximum in the vertical profile of large particles, they concluded that the aerosols formed *in situ* and proposed a mechanism that involved the diffusion of H_2S and SO_2 from the troposphere and its subsequent photochemical oxidation to sulphate.

Electron diffraction analysis of the crystalline fraction of the stratospheric aerosol by Friend (1966) indicated the presence of ammonium sulphate and persulphate. These observations were supported by Mossop (1963, 1964) who used electron microscope and electron diffraction techniques in his analysis of aerosol samples. In addition, he found ash from the eruption of Mt. Agung, and particles in the form of aggregates and spheres.

Cadle (1972), using neutron activation, atomic absorption and chemical techniques, found low cation to sulphate ratios which implied

that the sulphate was predominantly sulphuric acid. In some places no ammonium ions could be found. Rosen (1971) found that the boiling point of stratospheric aerosols was that of a sulphuric acid solution of 75 percent acid by weight and 25 percent water. Bigg (1975) found both sulphuric acid and ammonium sulphate aerosols collected on his treated microscope slides. The submicron diameter particles were predominantly ammonium sulphate near the troposphere though the ratio of acid to non-acid decreased rapidly with particle diameter, even at higher altitudes.

The uncertainty in the composition of the stratospheric aerosol is further complicated by the observation by Gras (1978) of a change in the nature of the stratospheric aerosol collection at 34° S. During the period 1970 to February 1977, the aerosol collected by jet impaction had been predominantly sulphuric acid. Gras reports that a substantial incursion of ammonia into the stratosphere was sufficient to convert the sulphuric acid almost completely to one of the ammonium salts, either the persulphate or the sulphate.

The physical state of the stratospheric aerosols is not known with complete certainty and it may change with time. Many particles have been found to be solid but to have liquid associated with them on collection and analysis. Others appear to be entirely liquid after collection. Toon and Pollak (1973) compared the equilibrium vapour pressures over sulphuric acid solutions with observations of water and acid vapour pressure in the stratosphere. They concluded that sulphuric acid particles were 75 percent by weight acid solutions in water, and agree with Rosen's (1971) observations. Freezing curves for sulphuric acid solutions indicate that the particles are either solid or supercooled.

An electron microscope analysis of particles collected on impactors by Gras and Laby (1978) revealed that the particles were apparently moist or semi liquid on impact, whereas Bigg's (1975) acid particles were often in the frozen state and irregular aggregates were often observed at an altitude of 20 km.

The knowledge of the chemical composition of aerosols leads to values of the refractive index of the particles. This parameter, and the shape of the particles are important for theoretical light scattering calculations. The majority of scattering calculations have been carried out using Mie theory which assumes that the particles are spherical.

1.4 Aerosol Size Distributions and Concentrations

1.4.1 Continental and Maritime Aerosols in the Troposphere

In the atmosphere aerosol particles vary widely in size. Measurements of the radii of the particles reveal a smooth and continuous variation in size, which often can be described by one of several size distribution laws.

It is convenient to describe the distribution in particle sizes in the following way. If $n(r)dr$ is the number of particles per unit volume with radii in the range r to $r+dr$, then the cumulative distribution which gives the number of particles per unit volume with radii greater than r is

$$N(r) = \int_r^\infty n(r)dr, \qquad 1.1$$

or alternatively,

$$n(r) = \frac{d\,N(r)}{dr} \quad . \qquad 1.2$$

It should be emphasised here that the concept of a particle "radius" is a simplification of the real situation, as not all particles are spherical. Dry salt crystals, ice crystals and snowflakes are obvious examples of non-spherical particles, but the spherical approximation is adequate in most cases.

As mentioned in the previous section, particle radii cover several orders of magnitude, and size distributions are usually plotted on log-log graphs as a function of r. Now

$$\frac{d\,N(r)}{d\,\log r} = \frac{d\,N(r)}{dr} \cdot \frac{dr}{d\,\log r} = 2.3r\,\frac{d\,N(r)}{dr}, \qquad 1.3$$

or

$$\frac{d\,N(r)}{d\,\log r} = 2.3r\,n(r). \qquad 1.4$$

As a result of observations of aerosols in the lower troposphere, Junge (e.g. 1963) found a constant particle volume per log radius interval for particles with radii in the range $0.1\ \mu m \lesssim r \lesssim 10\ \mu m$. This can be expressed as $r^3\,(d\,N(r)/d\,\log r) = C$, or more commonly,

$$\frac{d\,N(r)}{d\,\log r} = C\,r^{-3}. \qquad 1.5$$

A more general form of this distribution is as follows,

$$\frac{d\,N(r)}{d\,\log r} = C\,r^{-\nu}, \qquad 1.6$$

where ν is a constant. Expressions such as 1.6 are usually described as Junge distributions.

Junge (1963) found that the peak in the distribution occurred between $0.01\ \mu m$ and $0.1\ \mu m$, typically about $0.03\ \mu m$, and that the lower limit of the particle sizes was variable, usually as a result of

coagulation of the smaller Aitken particles. Smooth size distribution curves, such as that shown in Figure 1.1(a), are usually the end product of the processes of coagulation of small particles and sedimentation of large particles. The effects of coagulation caused by Brownian motion have been calculated by Junge (1963) and are shown in Figure 1.1(b). Discrete sources of aerosols near the sampling location can cause peaks in the size distribution.

Other measurements of aerosol size distributions have been performed using both direct sampling methods and indirectly by using light scattering and solar radiometry measurements.

Twomey (1976), using nucleopore filters, found a distribution which peaked at 0.01 μm radius and fell off steeply for small sizes. For larger particles, the distribution could be approximated by a Junge distribution with a slope, ν, of 3 for those particles with radii greater than 0.01 μm, and somewhat less than this value in the region 0.01 μm to 0.05 μm. Aerosol impactor measurements by de Luisi *et al* (1976) gave a distribution with a ν of 2.6 but the authors suggested that some small particles were not captured.

Reagan *et al* (1977) made airborne impactor measurements of large particles with a Rich optical particle counter-impactor combination, and compared them with the results derived from solar radiometer observations. For the airborne measurements ν varied from 2.9 to 3.7 whereas the columnar solar radiometer measurements gave values of 3.73 ± 0.11 and 3.43 ± 0.05, if a Junge-type distribution was assumed.

Other optical measurements were made by King *et al* (1978), where inversion of spectral optical depth measurements gave columnar values for

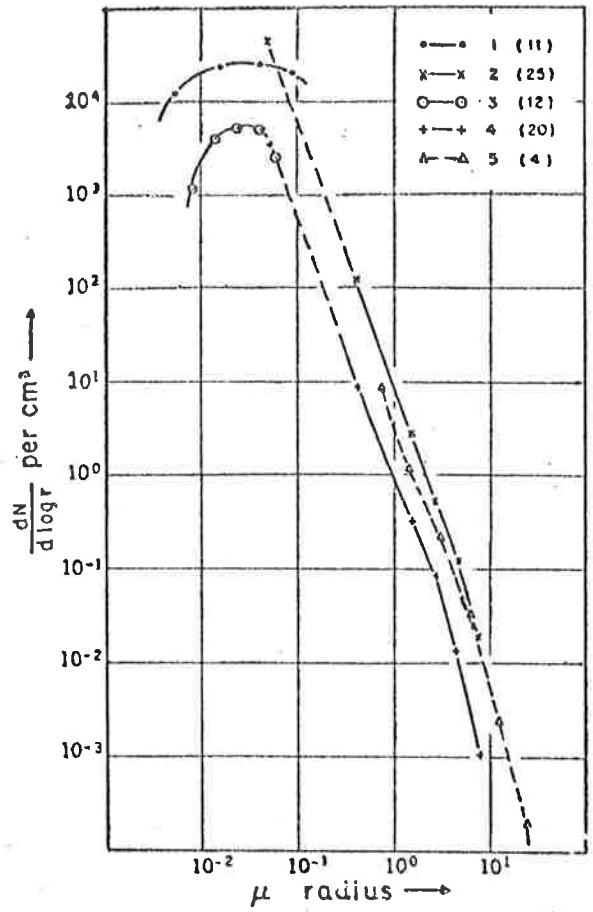

(a)

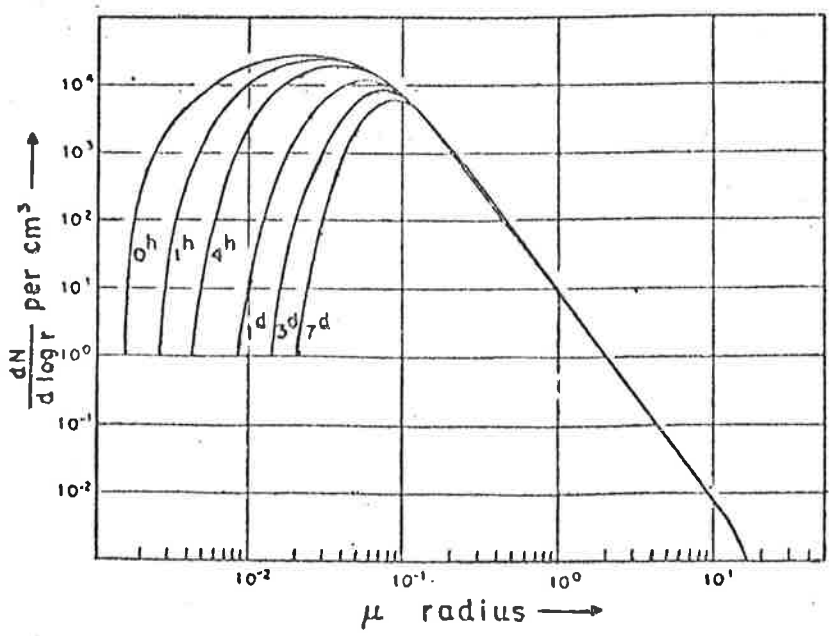

(b)

FIG 1.1 Size distributions of tropospheric aerosols (after Junge, 1963) (a) Measured distributions. (b) Calculated changes due to coagulation.

ν of 3.55, 3.2 and 1.73. The low values of the slope were obtained on a day with low values of aerosol scattering. Waggoner *et al* (1972) using a multi-wavelength nephelometer, found a value of $\nu = 3.7$ for an urban aerosol, whereas Twitty *et al* (1976) deduced values of $\nu = 4$ from their airborne observations of the solar aureole.

Whereas ground based solar radiometer measurements only give integrated or columnar values, several *in situ* measurements of size distributions have been performed. Junge (1963) noted little difference in the relative tropospheric profiles of Aitken and large particles. Similarly, Twitty *et al* (1976) discovered little variation in the aerosol size distributions up to a height of 3 km, and Reagan *et al* (1977) found little change throughout the mixing layer. Figure 1.2 shows size distributions from the last work, plotted for several heights. This observation was supported by the high correlation ($r = 0.92$) obtained between the lidar extinction profiles and the large particle concentration profiles which indicated very little change in the shape of the particle size distribution and refractive index with height.

In contrast to the last observation, there have been some workers that have found a variation in size distribution with height. Bridgman (1979) used an active scattering airborne spectrometer (ASAS) and a classical scattering spectrometer pulse (CSSP) mounted on an aircraft to measure the differences in extinction over urban and rural areas. Some of his results are presented in Figure 1.3 and show differences in aerosol size distributions in the air below an inversion and in the cleaner air above, especially on a moderately polluted day (April 13th, 1976) when there were relatively more small particles below the inversion. He noted also that the difference in size distribution between rural and urban

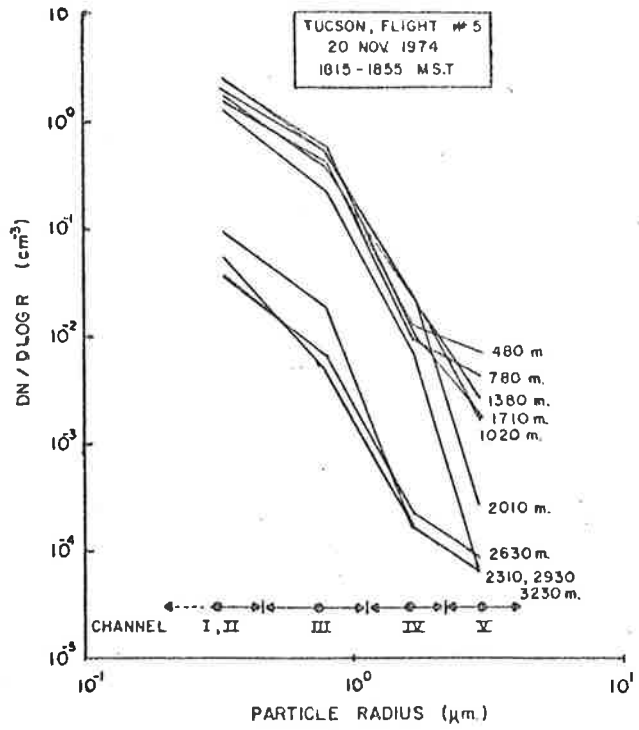

FIG 1.2 Height variation in aerosol size distribution measured by optical particle counter. (after Reagan et al, 1977)

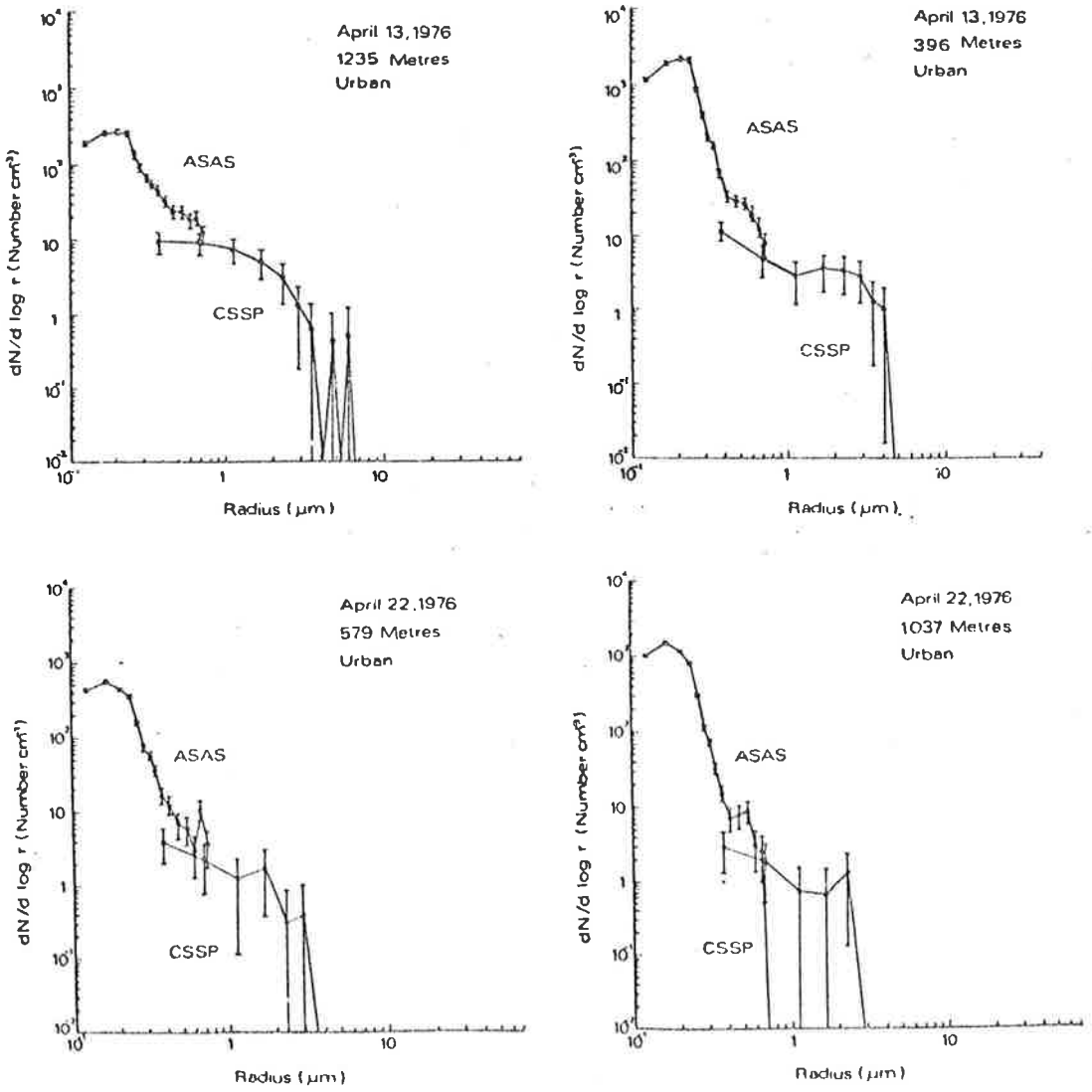

FIG 1.3 Comparison of size distributions at different heights on different days. (after Bridgman, 1979)

sites was less than the day-to-day variation at any one site.

Blifford and Ringer (1969) flew an airborne impactor from 1.5 km to 9.1 km altitude and noted that the size distribution slope ν for the giant particles ($r > 1$ μm) increased with height from a value of 2 low in the atmosphere to 3 at about 9 km, indicating a reduction in the relative numbers of large particles with increasing height. Simultaneously, for large particles, (0.2 μm to 1.0 μm), ν decreased steadily with height together with a compression of the size distribution as a result of the reduction in the fraction of smallest and largest particles by coagulation and sedimentation. These results, therefore are slightly at variance with Junge's (1963) conclusions.

As is shown in Table 1.1, compiled by Landsberg (1938), there is a wide variation in the concentration of Aitken particles. The difference between continental and ocean sites is notable as is the decrease in concentration with altitude. Rosen and Hofmann (1977) measured condensation nuclei concentrations and found a concentration in the troposphere ranging from 200 to 2000 cm^{-3} with a definite maximum just below the tropopause. Their comparison of several measurements by others of condensation nuclei or Aitken particles is shown in Figure 1.4. They pointed out that the good agreement between those tropospheric measurements distributed widely in time shows that the CN concentration remains approximately constant for non-polluted air in the height range from a few kilometres altitude to the tropopause.

The concentration profiles of aerosol particles are often affected significantly by temperature inversions. The trapping of aerosols beneath an inversion has been noted by many workers, including Bridgman (1979) and Reagan *et al* (1977). A typical large particle concentration profile

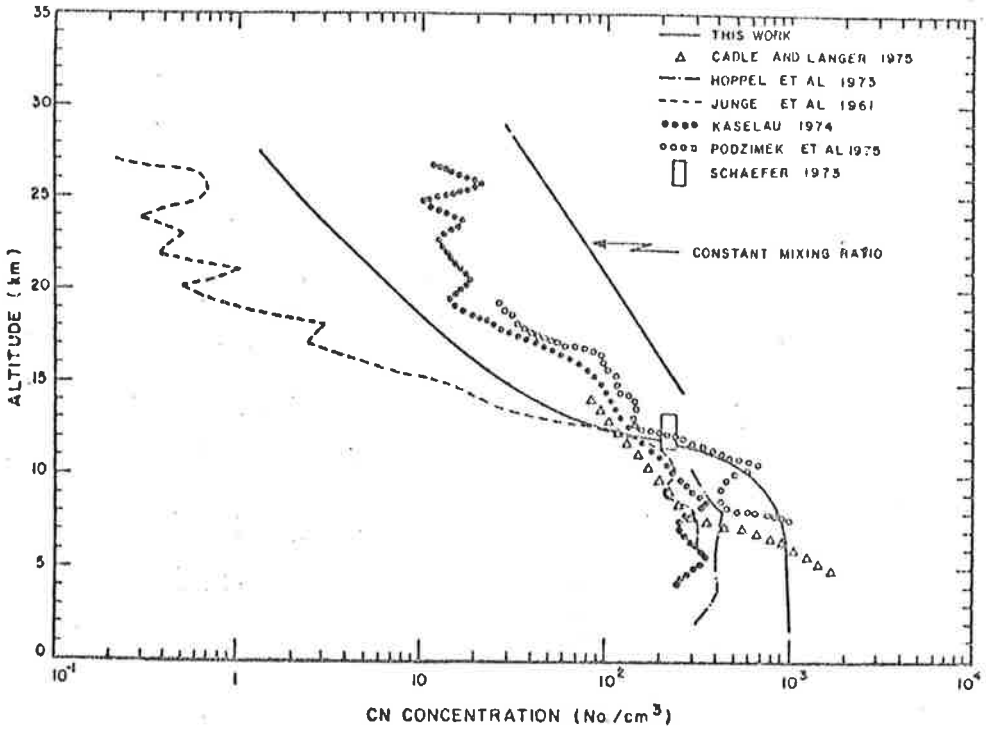

FIG 1.4 A comparison of CN profiles for the upper troposphere and stratosphere. (after Rosen and Hofmann, 1977)

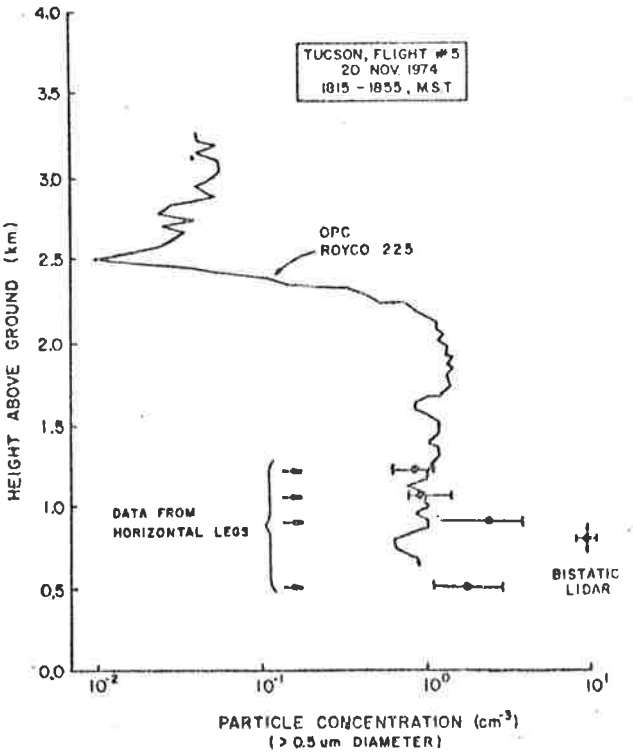

FIG 1.5 Aerosol concentration profile. (after Reagan et al, 1977)

TABLE 1.1

Number of Aitken Particles per cm^3 in Different Localities

(after Landsberg (1938))

Locality	Number of Places	Number of Observations	Average	Average Max	Average Min
City	28	2500	147,000	379,000	49,100
Town	15	4700	34,300	114,000	5,900
Country (inland)	25	3500	9,500	66,500	1,050
Country (seashore)	21	7700	9,500	33,400	1,560
Mountain					
500-1000 m.	13	870	6,000	36,000	1,390
1000-2000 m.	16	1000	2,130	9,830	450
> 2000 m.	25	190	950	5,300	160
Islands	7	480	9,200	43,600	460
Ocean	21	600	940	4,680	840

measured using an airborne optical particle counter obtained from the latter work is presented in Figure 1.5.

Based on measurements by Woodcock (1953), Junge (1963) has proposed the following size distribution for aerosols of maritime origin

$$\frac{dN(r)}{dr} = \frac{K}{r} \exp(-0.66r) , \qquad 1.7$$

where $K = 2.02$. When considered with Table 1.1 there are apparently

relatively few small particles in maritime aerosols. Woodcock noted that giant particles ($r > 1$ μm) are predominantly sea salt and have a well defined and uniform size distribution which is a function of wind strength.

Aerosol size distributions are affected significantly by changes in relative humidity. Hänel (1970) and Fitzgerald (1975) have both developed models that relate the size of atmospheric aerosol particles to the relative humidity and chemical composition. Fitzgerald has derived a formula for the dependence on relative humidity of a chemically homogeneous aerosol distributed according to the Junge Law as

$$\frac{dN(r)}{d \log r} = \frac{c}{\beta} \alpha^{\nu/\beta} r^{-\nu/\beta}, \qquad 1.8$$

where c and ν are constants and α and β are both functions of relative humidity and chemical composition.

Nilsson (1979) calculated the effect of relative humidity on aerosol size distributions and aerosol extinction using Mie theory and an aerosol model that started with dry particles and included a growth factor that was derived according to the relationship between the relative humidity and the equilibrium radius of an aqueous solution droplet. He found that changes in aerosol extinction were caused predominantly by the change in size and not by the change in refractive index.

Hänel (1976) has calculated the change in size distributions with an increase in relative humidity for various aerosol types. Those for maritime, urban and clean mountain air are shown in Figure 1.6.

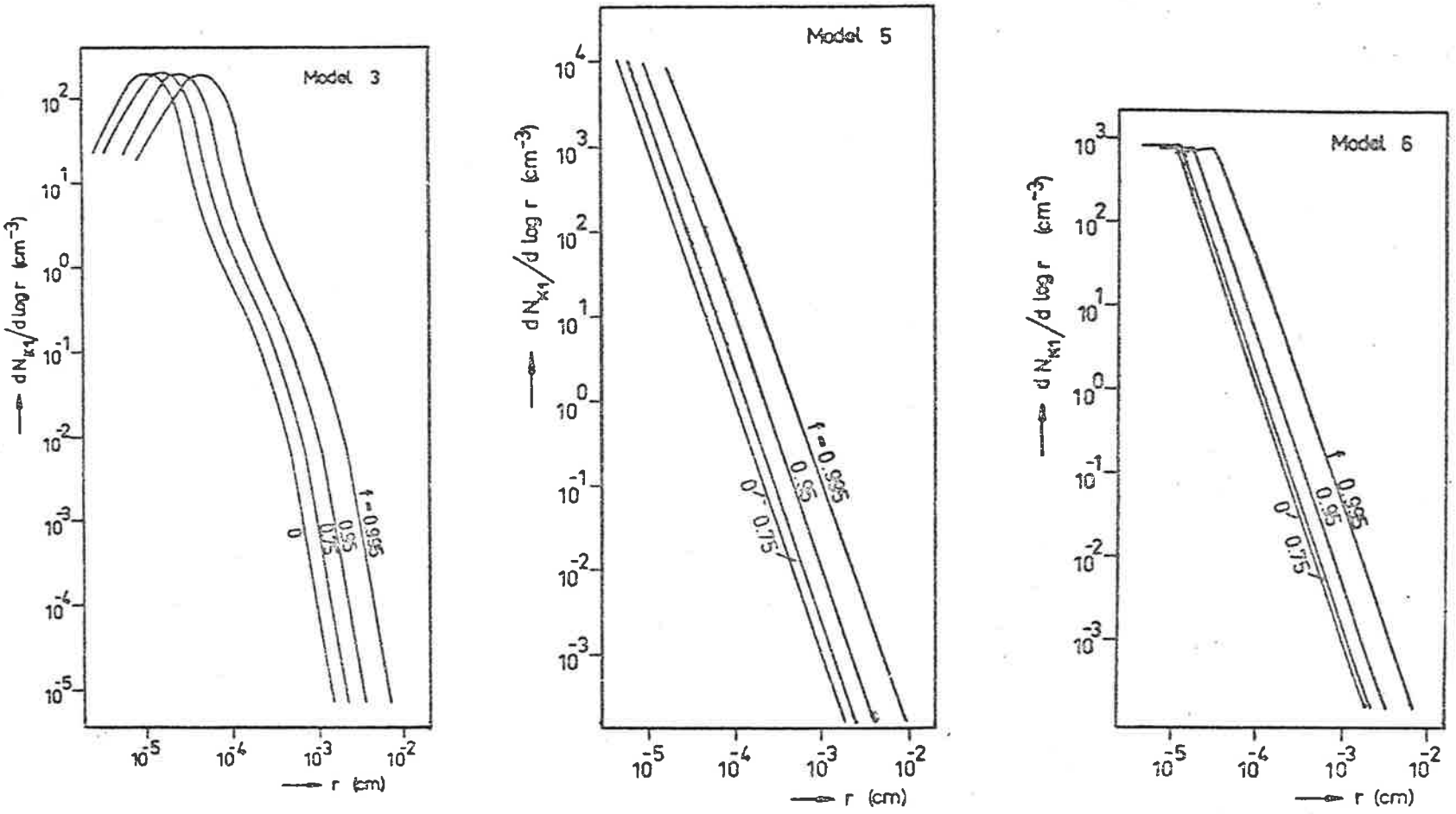

FIG 1.6 Aerosol size distribution $dN_{K1}/d\log r$ vs relative humidity f, where N_{K1} is the particle number cm^{-3} and r the equivalent radius of the particles. The curves for $f = 0.75$ are valid for increasing relative humidity. (after Hänel, 1976)

1.4.2 Stratospheric Aerosols

Stratospheric observations by Junge (1961) of Aitken particles revealed a steady decrease in concentration with height above the tropopause, falling to a value of $10\ cm^{-3}$ at 15 km and $1\ cm^{-3}$ at 20 km; above this height the concentration remained approximately constant.

In the large particle range Junge *et al* (1961), using an impactor, found a maximum concentration of $0.1\ cm^{-3}$ at 20 km; this layer is now often called the "Junge layer". The size distribution could be described by a power law (e.g. Equation 1.6) with exponent $\nu=2$ for particles with radii between 0.1 μm and 1.0 μm, and $\nu=4$ for larger particles.

Vertical profiles of aerosol particle concentrations using an *in situ* optical particle counter have been obtained by Rosen and his colleagues in a world-wide observational program (e.g. Hofmann *et al* 1975; Rosen *et al*, 1975; Pinnick *et al*, 1976). Figure 1.7(a) shows the variation in the summer profiles of aerosol mixing ratio measured at Laramie by these workers.

Various size distribution functions have been used to describe the observations analytically. Not all are in the form of a power law because this only applies over a very limited size range; obviously it cannot be extrapolated indefinitely in the direction of decreasing radii without giving an impossible result. From several years of observations of the stratospheric aerosol over Australia, Bigg (1976) found that the size distribution could best be described by the expression,

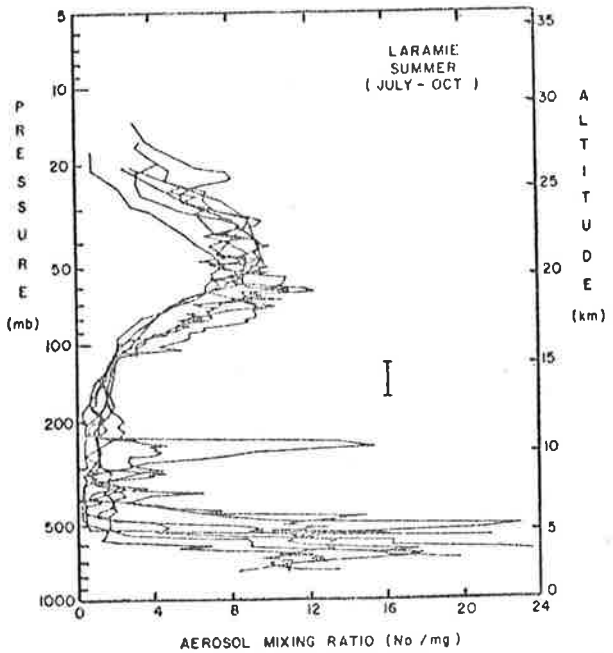

FIG 1.7(a) Mixing ratio profiles over Laramie during the summers of 1972 and 1973. (after Rosen et al,1975)

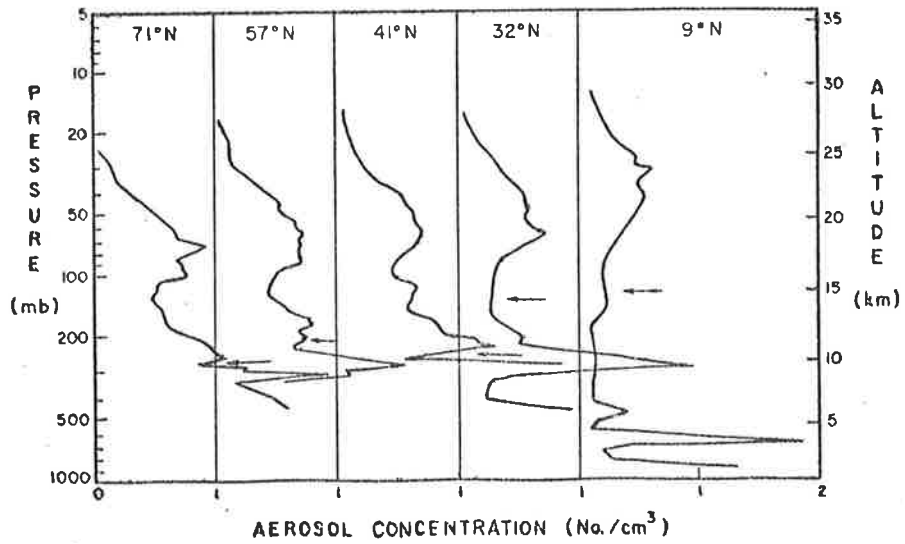

FIG 1.7(b) A comparison of five N.H. soundings made in June 1973. The arrows mark the position of the tropopause. (after Rosen et al,1975)

$$n(r) = a\, r^{\alpha} \exp(- b r^{\gamma}). \qquad 1.9$$

Here $n(r)$ is the number of particles with radius r and α, a, b and γ are constants. Toon and Pollak (1976) summarised recent empirical size distributions determined from impaction measurements and found that for radii between 0.05 μm and 1.0 μm, most would be described adequately by the zero-order logarithmic size distribution

$$\frac{dN(r)}{dr} = A \exp \left[\frac{- \ell n^2 (r/r_m)}{2 \ell n^2 \sigma} \right], \qquad 1.10$$

with $r_m = 0.035$ μm and $\sigma = 2$.

Harris and Rosen (1976) have also reviewed the observed size distributions and their analytic functions used in modelling them. They divided the observational data into two main groups : impactor collection measurements and photoelectric particle counter measurements. They state that collection experiments with volatile aerosols should be treated with caution as they are not reliable and lead to discrepancies. The summary of measured stratospheric aerosol size distributions is presented in Figure 1.8(a) and the analytic representation of the distributions in Figure 1.8(b).

Some attempts have been made to determine the variation in height of stratospheric aerosol size distributions. Pinnick *et al* (1976) measured the variation with height of the ratio of the number of particles with radii greater than 0.3 μm to the number having radii greater than 0.5 μm and found that the ratio decreased from 5 at 12 km to 4 at 23 km. The cause of this decrease was not obvious;

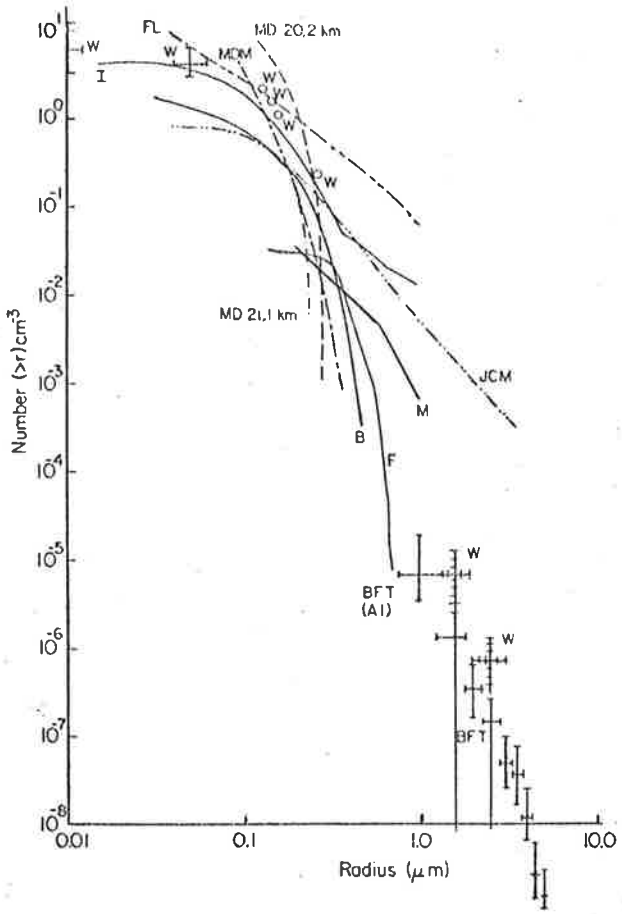

FIG 1.8(a) Measured distributions for statospheric aerosols near 20km. (after Harris and Rosen, 1976)

Code	Reference	Type of Measurement
B	Bigg (1975)	Impactor
BFT	Brownlee et al (1976)	Impactor (large particles)
F	Friend (1966)	Impactor
FL	Ferry and Lem (1974)	Impactor
I	Ivlev (1976)	Impactor (Aug. 1975)
JCM	Junge et al (1961)	Impactor (Aug. 1958)
M	Mossop (1964)	Impactor (Apr. 1964)
MD	Miranda & Dulchinos (1975)	P.E. Particle Counter
MDM	Miranda et al (1973)	"
W	Wyoming (Pinnick et al 1976)	"

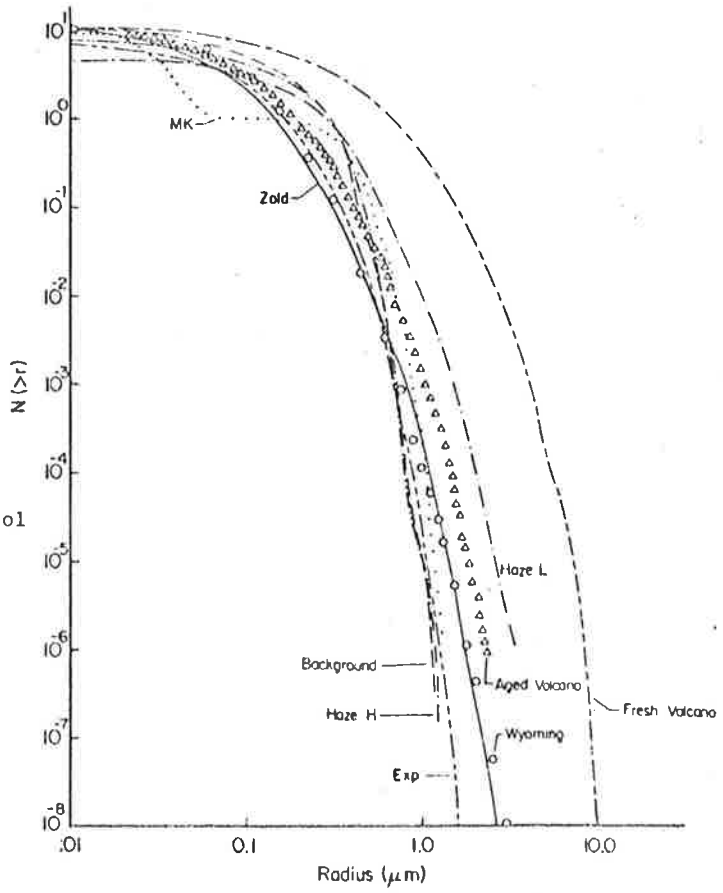

FIG 1.8(b) Summary of analytic functions used in aerosol size distributions. Functions have been normalised to 10 particles/cm^3 at r=0.

Code	Reference	Function type
Haze H	Deirmendjian (1973)	Modified gamma
Haze L	Deirmendjian (1973)	"
MK	Murphy & Kim (1975)	Bimodal lognormal
Fresh volc.	Shettle & Fenn(1975)	Modified gamma
Aged volc.	"	"
Background	"	
Zold	Toon & Pollack (1976)	
Wyoming	Pinnick et al (1976)	Lognormal
Exponential	"	

sedimentation would suggest the opposite. It could have been caused by a variation with altitude of the aerosol production processes, chemical reactions, condensation and coagulation. The data for the Laramie site also showed an abrupt increase in the number of small particles between 23 km and 25 km, whereas the ratio of the number of particles with radii greater than 0.25 μm and 0.28 μm remained constant for all heights studied.

Gras and Michael (1979), using a photoelectric aerosol detection system, found that their observations could be described by a power law, with a height dependent exponent. For the height region 4 km to 10 km and particles with radii in the range 0.16 μm to 1.0 μm the exponent $\nu = 3.3 \pm 0.2$. For heights between 10 km and 16 km they noticed a slight decrease in the exponent for radii less than about 0.3 μm, and that $\nu = 3.1 \pm 0.36$ for the combined data. Between 16 km and 22 km there was a noticeable decrease in the exponent for radii less than 0.3 μm; for larger radii, $\nu = 5.6 \pm 0.66$. A similar behaviour was noticed in the region 22 km to 28 km but the exponent increased to 8.5 ± 2.9. These authors claim that their results agree with other recent measurements but differ from the early impaction measurements which, they suggest, may be in error.

Farlow *et al* (1979) used impaction on fine, carbon-coated palladium wire to study the variation in concentration and size distribution with height and latitude. In general their measured size distributions (Figure 1.9(a)) indicated larger concentrations, particularly of smaller particles ($r \lesssim 0.2$ μm) at higher altitudes in the tropics, and fewer particles at lower altitudes in the polar zone. Their

measurements of total particle concentration, Figure 1.9(b), show that the maximum concentrations of particles occur at high altitudes in the tropics, while a subsidiary maximum occurs at lower levels in the polar regions.

They found that the small particle component was increased significantly in the tropical zones at 18 km, with fewer small particles above this level and virtually none of any size below 15 km because of the removal by large cumulo-nimbus clouds. The large particle component however, varied little between the tropics and the Arctic.

They interpreted their results in terms of a stratospheric aerosol production model in which the particles form *in situ* from gases and grow by additional gas reactions and condensation and coagulative processes. The authors concluded that the tropical zone is a region of aerosol injection and growth with the mature aerosol component being well distributed from higher altitudes in the tropics to lower altitudes in the Arctic.

1.5 Optical Scattering by Air Molecules and Aerosols.

1.5.1 Rayleigh Scattering.

Particles which have dimensions very much less than the wavelength of incident radiation scatter the radiation in a similar fashion to air molecules. This form of scattering is called Rayleigh scattering and is discussed in detail by Van de Hulst (1957). However, when the dimensions are comparable to the wavelength, the scattering is described by the much more complex Mie scattering theory discussed in the next section. The following brief summary of Rayleigh scattering follows Twomey's (1977) treatment.

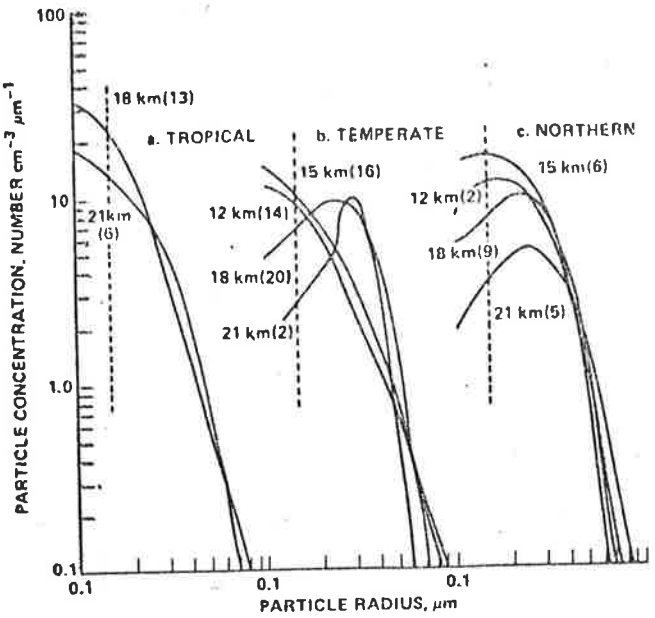

(a) Average particle size distributions versus altitude and latitude, 1976–1977.

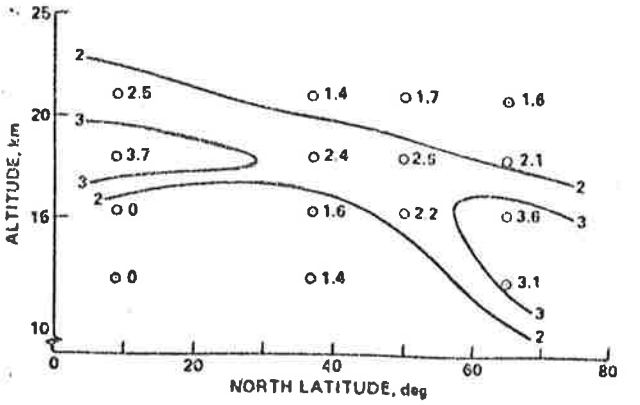

(b) Estimated contours of aerosol concentration, at ambient conditions, particles($r > 0.1$ μm)/cm³.

FIG 1.9 (after Farlow et al, 1979)

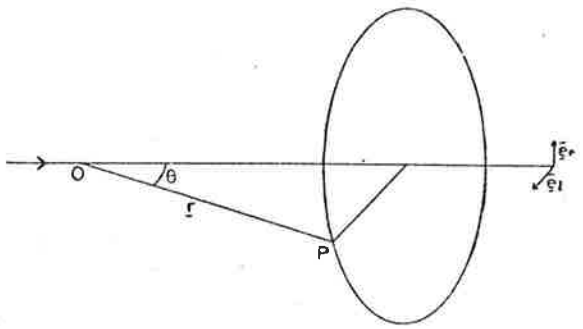

FIG 1.10 Rayleigh scattering geometry. (after Twomey,1976)

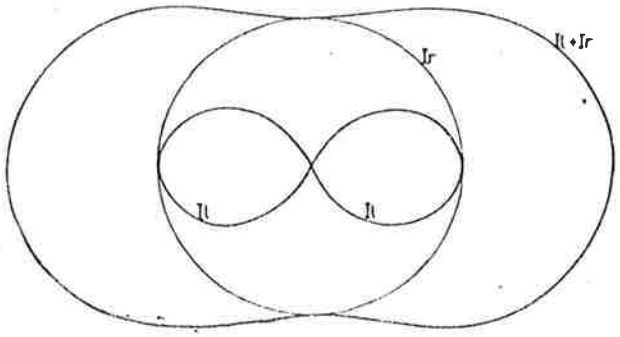

FIG 1.11 Angular distribution of Rayleigh scattering intensities. $I_{\parallel}$ and $I_{\perp}$ relate to separate polarised components, outer curve to total intensity. (after Twomey,1976)

The far field solution for an oscillating dipole of moment $\underset{\sim}{p}\, e^{iwt}$ at a point P in the direction $\underset{\sim}{r}$ is given by electromagnetic theory as

$$\underset{\sim}{E} = \frac{w^2}{c^2 R} \exp [\, i\, w\, (t-R/c)\,]\, \hat{\underset{\sim}{r}} \times (\hat{\underset{\sim}{p}} \times \hat{\underset{\sim}{r}}) , \qquad 1.11(a)$$

$$\underset{\sim}{H} = \frac{w^2}{c^2 R} \exp [\, i\, w\, (t-R/c)\,]\, \hat{\underset{\sim}{r}} \times \hat{\underset{\sim}{p}} . \qquad 1.11(b)$$

Here the symbols c, w and R are the velocity of light, the frequency of oscillation and the distance of P from the dipole situated at a point 0 ; $\hat{\underset{\sim}{r}}$ and $\hat{\underset{\sim}{p}}$ are the unit vectors in the directions $\underset{\sim}{r}$ and $\underset{\sim}{p}$ respectively.

In Rayleigh theory, an incident plane electromagnetic wave with an electric vector $E_0\, e^{iwt}$ will induce a dipole moment in a particle or scattering molecule of polarisability α at 0, which is in the same direction as the electric field vector, has the same phase and is proportional to the magnitude of the vector. Therefore

$$\underset{\sim}{p} = \alpha\, \underset{\sim}{E_0}\, e^{iwt} . \qquad 1.12$$

The scattered wave at P in Figure 1.10, is resolved into two components, one parallel to the plane containing the propagation vector of the incident wave and the vector $\underset{\sim}{r}$ and having unit vector $\hat{\underset{\sim}{e}}_{\ell}$, and one perpendicular to this plane with unit vector $\hat{\underset{\sim}{e}}_r$. For an arbitrary incident vector, $(E_{or}\, \hat{\underset{\sim}{e}}_r + E_{o\ell}\, \hat{\underset{\sim}{e}}_{\ell}) e^{iwt}$, the field component at P generated by the dipole $E_{or}\, \hat{\underset{\sim}{e}}_r$ is obtained using Equation 1.11 as

$$\underset{\sim}{E}_r\, (R) = \frac{w^2}{c^2 R} \exp [\, i\, w\, (t-R/c)\,]\, E_{or}\, \hat{\underset{\sim}{e}}_r . \qquad 1.13$$

Similarly the dipole $E_{o\ell}\ \hat{\underset{\sim}{e}}_{\ell}$ gives the component

$$\underset{\sim}{E}_{\ell}(R) = \frac{w^2}{c^2 R} \exp[i w (t-R/c)]\ E_{o\ell} \cos\theta\ (\hat{\underset{\sim}{e}}_r \times \hat{\underset{\sim}{r}}) . \qquad 1.14$$

The angular distribution of scattered intensities can be derived from the Poynting vectors of the scattered wave and are shown in Figure 1.11. For unpolarised light the intensity is

$$I = \frac{w^4}{c^4 R^2} \alpha^2 (1 + \cos^2\theta) I_0 , \qquad 1.15$$

where the $(1 + \cos^2\theta)$ factor arises from the addition of the contribution of a factor of unity from the r- dipole and of $\cos^2\theta$ from the ℓ- dipole.

For a spherical, isotropic scatterer of radius r and dielectric constant K the polarisability can be written as $[(K-1)/(K+2)]\ r^3$. By introducing the refractive index m through the Lorentz relation, the intensity can be written as

$$I = \frac{w^4}{c^4}\frac{r^6}{R^2}\frac{m^2-1}{m^2+2}(1 + \cos^2\theta)I_o . \qquad 1.16$$

The fraction of the radiation scattered into the unit solid angle Ω in the direction θ can be expressed in terms of a normalised phase function $P(\theta)/4\pi$. For Rayleigh scattering

$$P(\theta)/4\pi = (1 + \cos^2\theta)/\int(1 + \cos^2\theta)d\Omega$$

$$= (3/16\pi)(1 + \cos^2\theta). \qquad 1.17$$

Some important points can be noted from Equation 1.16. The scattered intensity and energy removed from an incident beam by

scattering is proportional to the fourth power of the frequency (i.e. λ^{-4}) and the sixth power of the radius (or the square of the volume for a spherical particle). The absorption however, is proportional to the cube of the radius (ie the volume), so as the radius decreases absorption dominates over scattering. In other words, the single scattering albedo of the particle decreases with decreasing size.

1.5.2 Mie Scattering by Single Particles

For particles which have dimensions comparable to the wavelength of light, as a three-dimensional charge distribution is set up within the particle and the scattering process is much more complex, the scattered radiation can no longer be considered as being emitted by an induced dipole. The solution of the problem of the scattering of radiation from spherical particles of any given radius and refractive index was obtained by Mie (1908). The summary of the results given below is similar to that given by Cadle and Grams (1975).

For homogeneous spherical particles the amplitude of the scattered wave can be resolved into two components, E_r and E_ℓ, which are respectively perpendicular and parallel to the plane containing the incident and scattered waves and the particle. The amplitude components are related to the incident components, E_{or} and $E_{o\ell}$, by the two amplitude functions, $S_1(\theta)$ and $S_2(\theta)$, which are functions of the scattering angle θ between the propagation vectors of the incident and scattered waves. The respective equations are,

$$E_r = S_1(\theta)\, E_{or}\, (e^{-ikR})/ikR, \qquad 1.18$$

and

$$E_{\ell} = S_2(\theta)\, E_{o\ell}\, (e^{-ikR})/ikR, \qquad 1.19$$

where $k = 2\pi/\lambda$, λ being the wavelength of the incident radiation, and R is the distance from the particle.

The scattered intensities, I_r and I_{ℓ}, for the perpendicular and parallel polarisations can be obtained by squaring the moduli in Equations 1.18 and 1.19, giving

$$I_r = |\, S_1(\theta)\,|^2\, I_{or}/k^2R^2 \qquad 1.20$$

$$I_{\ell} = |\, S_2(\theta)\,|^2\, I_{o\ell}/k^2R^2 \,. \qquad 1.21$$

For the special case where the size of the particle is insignificant when compared with the incident wavelength, the particle may be considered as a dipole and the following equations are obtained :

$$I_r = k^4\, \alpha^2\, I_{or}/R^2 \,, \qquad 1.22$$

$$I_{\ell} = k^4\, \alpha^2\, I_{o\ell}/R^2 .\cos^2\theta \,, \qquad 1.23$$

where α is the polarisability of the particle. This is the case of Rayleigh scattering and these equations can be compared with Equation 1.15.

In Mie's solution the amplitude functions $S_1(\theta)$ and $S_2(\theta)$ are described in terms of infinite series as follows:-

$$S_1(\theta) = \sum_{n=1}^{\infty} \frac{2n+1}{n(n+1)} \{\, a_n\, \pi_n(\cos\theta) + b_n\, \tau_n(\cos\theta) \,\} \qquad 1.24$$

$$S_2(\theta) = \sum_{n=1}^{\infty} \frac{2n+1}{n(n+1)} \{\, a_n\, \tau_n(\cos\theta) + b_n\, \pi_n(\cos\theta) \,\} \qquad 1.25$$

where

$$\pi_n(\cos\theta) = dP_n(\cos\theta)/d\cos\theta \qquad 1.26$$

$$\tau_n(\cos\theta) = \cos\theta.\ \pi_n(\cos\theta) - \sin^2\theta\ d\pi_n(\cos\theta)/d\cos\theta\ , \qquad 1.27$$

and $P_n(\cos\theta)$ is a Legendre polynomial of degree n, and the coefficients a_n and b_n are defined by the boundary conditions at the surface of the spheres.

The coefficients a_n and b_n are known as the Mie scattering functions, and they can be written as

$$a_n(m, x) = \frac{\psi_n(x)\ \psi_n'(mx) - m\,\psi_n(mx)\,\psi_n'(x)}{\xi_n(x)\ \psi_n'(mx) - m\,\psi_n(mx)\,\xi_n'(x)} \qquad 1.28$$

and

$$b_n(m, x) = \frac{m\,\psi_n(x)\,\psi_n'(mx) - \psi_n(mx)\,\psi_n'(x)}{m\,\xi_n(x)\,\psi_n'(mx) - \psi_n(mx)\,\xi_n'(x)}\ , \qquad 1.29$$

where ψ_n and ξ_n are the Ricatti-Bessel functions and ψ_n' and $\xi'(n)$ are their derivatives with respect to the arguments, $m = n_{Re} - n_{im}\,i$ is the complex refractive index of the particle of radius r, and x is the Mie size parameter $2\pi r/\lambda$. The imaginary part of the refractive index is an absorption parameter.

These Mie scattering functions can be interpreted in terms of some useful integrated properties of aerosols. These are the extinction, scattering and absorption efficiency factors, the single scattering albedo and the asymmetry factor. These factors are defined in the following way (Twomey, 1977). The energy removed from the

incident beam having energy flux density I_o is $\pi r^2 Q_E I_o$; here Q_E is the extinction efficiency and $\pi r^2 Q_E$ is the extinction cross section of the particle. Similar definitions involving the scattering efficienty Q_S, and the absorption efficiency Q_A, can be written to describe the energy which reappears as scattered energy and the energy lost by absorption. The single scattering albedo $\bar{\omega}_o$, is the fraction of the energy removed from the incident wave that appears as scattered radiation, whereas the asymmetry factor g is the average or statistically expected value of the cosine of the scattering angle. When these are written in terms of Mie scattering functions we have

$$Q_E = \frac{2}{x^2} \sum_{n=1}^{\infty} (2n + 1)\, \mathrm{Re}(a_n + b_n), \qquad 1.30$$

$$Q_S = \frac{2}{x^2} \sum_{n=1}^{\infty} (2n + 1) \{ |a_n|^2 + |b_n|^2 \} \qquad 1.31$$

$$Q_A = Q_E - Q_S , \qquad 1.32$$

$$\bar{\omega}_o = Q_S / Q_E , \qquad 1.33$$

and

$$g = \frac{4}{x^2 Q_S} \sum_{n=1}^{\infty} \{ \frac{n(n+2)}{n+1} \cdot \mathrm{Re}(a_n a_{n+1}^* + b_n b_{n+1}^*) + \frac{2n+1}{n(n+1)} \cdot \mathrm{Re}(a_n b_n^*) \}. \qquad 1.34$$

These quantities are plotted in Figure 1.12 as a function of radius for different values of absorption.

In lidar work, only the light scattered in the backward direction ($\theta=\pi$) is detected, and a backscattering efficiency Q_B has been defined. Figure 1.13, from Collis and Russell (1976), shows the backscattering efficiency plotted as a function of the Mie size

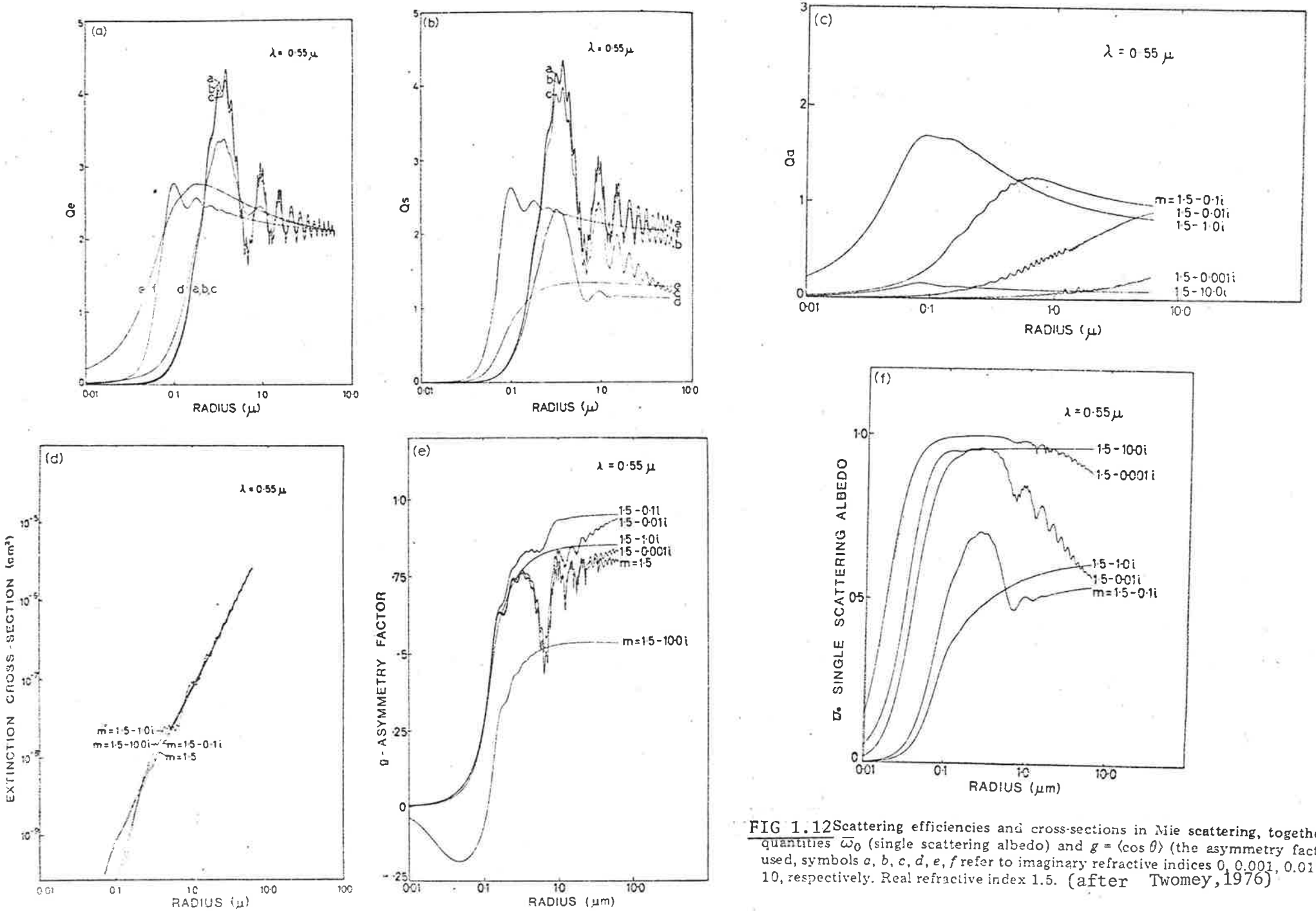

FIG 1.12 Scattering efficiencies and cross-sections in Mie scattering, together with th quantities $\bar{\omega}_0$ (single scattering albedo) and $g = \langle \cos\theta \rangle$ (the asymmetry factor). Wher used, symbols *a*, *b*, *c*, *d*, *e*, *f* refer to imaginary refractive indices 0, 0.001, 0.01, 0.1, 1 an 10, respectively. Real refractive index 1.5. (after Twomey, 1976)

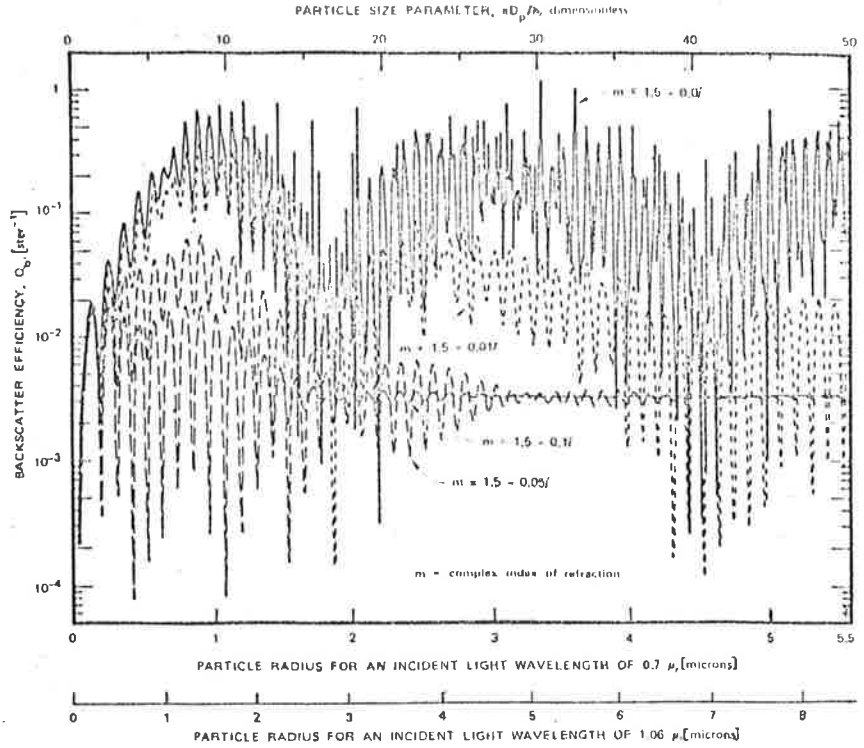

FIG 1.13 Dependence of mie backscattering efficiency on particle size parameter x and complex refractive index m. ($x = \pi D_p/\lambda$, where D_p is particle diameter) (after Russell & Collis, 1976)

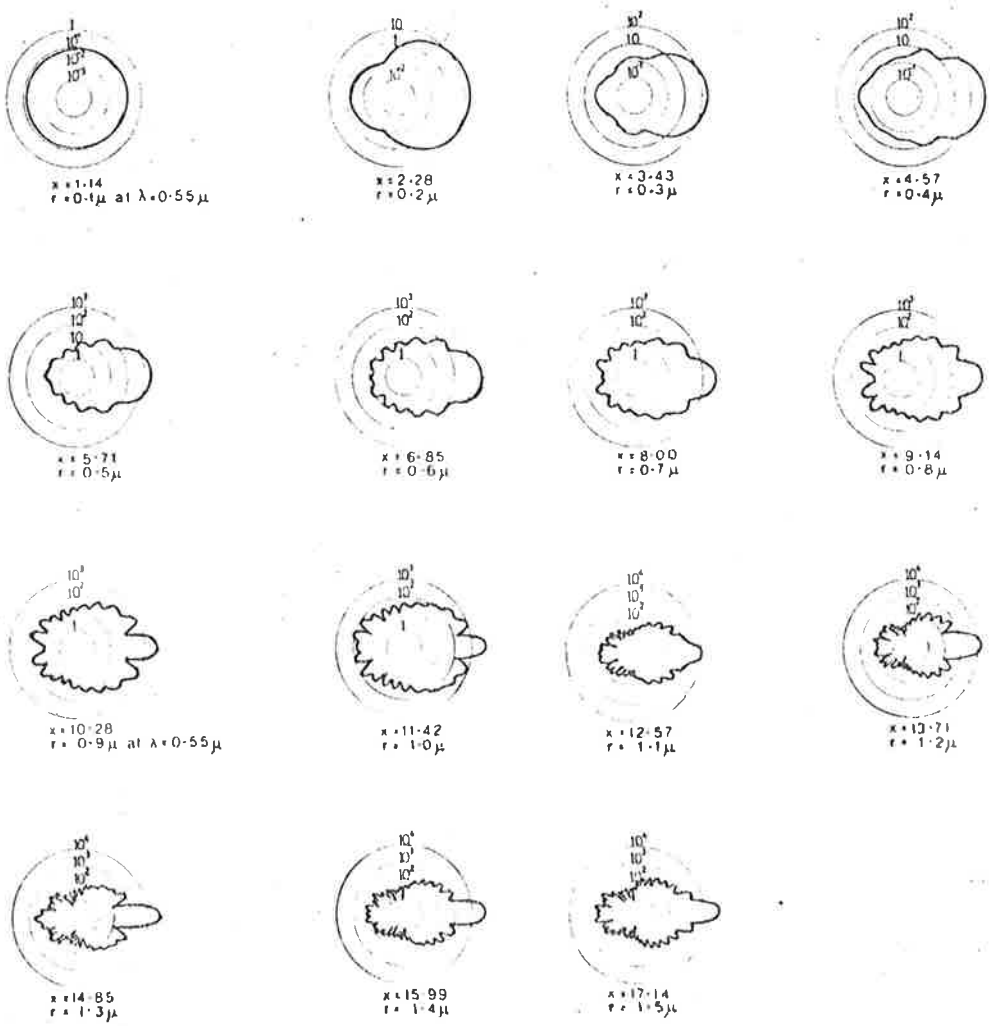

FIG 1.14 Scattering polar diagrams. The size parameter $2\pi r/\lambda$ is indicated on the individual diagrams. (after Twomey, 1976)

parameter x for different values of the complex refractive index.

The most noticeable feature of both Figures 1.12 and 1.13 is the highly oscillatory nature of the quantities plotted. The high frequency component of the oscillations is explained as the result of 'resonances' in the surface waves that travel along the interface between the sphere and the surrounding medium.

Another obvious feature is the different large particle limits for the scattering efficiency in the case of large and small values of the imaginary part of the refractive index or absorption. In the low absorption case half the scattered efficiency arises from the light which is intercepted by the geometrical cross section of the particle and subsequently refracted or reflected, and half from the light diffracted around the circumference of the sphere. Therefore the scattering cross section is twice the geometrical cross section and $Q_s=2$. As the absorption increases a decreasing amount of light is refracted by the particle and the major contribution to scattering arises from the light diffracted around the edge of the particle, and Q_s approaches 1.0 in the large particle limit.

The asymmetry factor plotted in Figure 1.12(e) shows that as the radius of the particle increases from 0.1 to 1.0 μm, in general an increasing amount of radiation is scattered in the forward direction. The development of this forward peak is illustrated clearly in Figure 1.14 for increasing values of the size parameter. It is due in part to the diffraction of light around the outside of the sphere. For the Rayleigh case where $2\pi r \ll \lambda$ or $x \ll 1.0$, the scattering is symmetrical in the forward and backward directions, but as the size parameter increases so does the forward scattering contribution. For

values of size parameter greater than about 0.1 Rayleigh scattering fails to give an accurate description of the scattering (Twomey, 1977). When the size parameter exceeds unity the scattering diagram develops oscillations. The effect of increasing absorption is initially to reduce the amount of scattering into the backward hemisphere; the forward peak is relatively unaffected as it originates mainly from light which has not actually passed through the particle. For very large values of absorption though, we have the case of reflection and the backscattered radiation increases again.

1.5.3 Mie Scattering by Aerosols and its Wavelength Dependence.

Aerosols in the atmosphere are composed of particles that have a smooth size distribution covering a large range of sizes. The main effect of this polydisperse nature of aerosols is the smoothing out of the high frequency oscillations in the scattering and extinction efficiencies defined in the previous section, although the low frequency oscillations remain.

The parameters which describe the size distribution are important in determining the wavelength dependence of the scattering and extinction of radiation incident on the aerosol. Mie theory predicts that the extinction β of the incident radiation is described by the equation

$$\beta \propto \lambda^{-q} , \qquad 1.34$$

where $q = 4$ in the small particle limit and $q = 0$ in the large particle limit. So for atmospheric aerosols q must lie in this range.

If a Junge size distribution is assumed,

$$\text{i.e.} \quad \frac{dN(r)}{d\log r} = C\, r^{-\nu} ,$$

then it can be shown (e.g. Bullrich, 1964) that,

$$\beta \propto \lambda^{-\nu+2} . \qquad 1.35$$

So

$$q = \nu - 2 \qquad 1.36$$

relates the wavelength dependence of the extinction to the slope of the aerosol size distribution on a log-log plot. As mentioned in Section 1.4, Junge (1963) found that $\nu = 3$ described the average continental aerosol best, and this implies that, on average, $\beta \propto \lambda^{-1}$. However, measurements have produced a wide range of values of q. Woodman (1974) has reviewed observations by several workers and decided that $\beta_A \propto \lambda^{-1.3 \pm 0.6}$ where the subscript refers to extinction by aerosols.

The wavelength dependence of extinction has often been analysed by studying the spectral dependence of the extinction of solar radiation, although this method integrates over a column of atmosphere. Direct measurements have been performed using multi-wavelength integrating nephelometers and spectroradiometers. Ahlquist and Charlson (1969) observed aerosols at ground level with a nephelometer and noted that when the aerosol extinction dominated the molecular extinction then $1.2 < q < 2.5$. Their results, which compare the aerosol extinction with the λ^{-4} dependence of the Rayleigh extinction from air and Freon 12, are shown in Figure 1.15. Spectroradiometer measurements in Stockholm of the wavelength dependence of the total scattering from aerosol laden air by Steinvall and Ågren (1975) produced

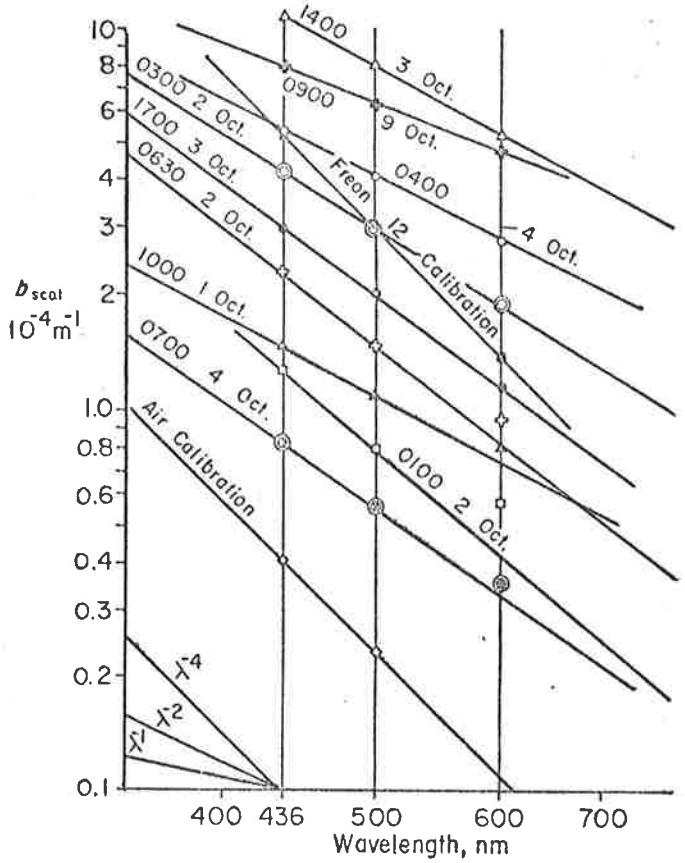

FIG 1.15. Several plots of b_{scat} versus wavelength, λ, both on logarithmic scales. One decade on the abscissa (λ) is four times as long as a decade on the ordinate so that a Rayleigh scatterer (λ^{-4}) has unit slope. Abscissa units are in nm, ordinate in $10^{-4}m^{-1}$. Days and times (PDT) are given, along with Freon-12 and air calibrations for slope reference.

(after Ahlquist & Charlson, 1969)

the result that $0.75 < q < 1.5$. They also noted that high values of q were associated with low values of extinction, implying an increasing contribution by molecular scattering.

As mentioned in Section 1.4.1, it is possible to determine aerosol size distribution from the wavelength dependence of extinction. This can be done in two ways. The first assumes a model size distribution, commonly a Junge power law distribution, with the exponent ν calculated from q using Equation 1.36. The slope of the graph of extinction against wavelength q, can be determined by a best fit using solar spectral attenuation measurements (e.g. Shaw *et al*, 1973; Reagan *et al*, 1977). Russell *et al* (1979) use a modified gamma distribution with a value of q between 0.4 and 1.5 rather than a Junge distribution.

An alternative method is to use linear numerical inversion techniques to derive the size distribution, (Yamamoto and Tanaka, 1969; King *et al*, 1978). The advantage of this method is that it assumes neither an analytic dependence of the extinction on the wavelength nor an analytical expression for the size distribution. King *et al* noticed that large values of aerosol extinction were associated with larger values of q, values of approximately 1.2 being typical, and that the size distributions were of the Junge type. The smallest values of q, around -0.2, were associated with the lowest values of aerosol extinction and with relatively monodisperse aerosols described by log-normal or gamma distributions. Intermediate values of q (around 0.5) and intermediate values of aerosol extinction were associated with aerosol distributions which were a combination of the first two types.

Covert *et al* (1972) have studied the relationship of the chemical composition and relative humidity of aerosols to their light

scattering properties. They list the order of importance of various aerosol parameters to scattering as the aerosol mass concentration, the particle size distribution, the chemical and physical composition (and hence refractive index), the shape, and the relative humidity of the surrounding air. For relative humidities in excess of sixty percent, hygroscopic and deliquescent growth lead to changes in the shape, refractive index, size distribution,and mass concentration. As the change is a second order effect, the change in the physical structure of deliquescent aerosols from crystals to solution droplets would not be expected to influence the light scattering properties of the aerosol as much as the simultaneous change in size.

Similarly, it has been shown (e.g. Horvath and Charlson, 1969, Hänel, 1971; Nilsson *et al*, 1979) that in terms of the light scattering efficiency of aerosols, changes in the real refractive index with relative humidity within typical atmospheric limits (i.e. $1.33 < n < 1.62$ for $100\% > \text{R.H.} > 0\%$) are of secondary importance when compared to changes in particle size.

As the relative humidity approaches saturation, the Mie scattering by the aerosol particles approaches the large particle limit where the scattering tends to become independent of wavelength, as can be seen in the case of fogs. This decreasing wavelength dependence with increasing relative humidity was detected by Steinvall and Ågren (1975) who measured the wavelength dependence of extinction with a transmissometer.

The above discussion has shown that the wavelength dependence of scattering depends on many different factors. While the effect of some factors can be precisely described others are extremely complicated

and usually prevent the accurate prediction or estimation of this dependence. Among the latter is the effect of relative humidity on the size of aerosols where different results are obtained for increasing and decreasing humidity. At best it seems that an inverse dependence of scattering on wavelength is a fair approximation in many cases.

1.5.4 The Aerosol Scattering Phase Function and Backscatter-to-Extinction Ratio.

The aerosol scattering phase function describes the angular distribution of the intensity of radiation scattered by aerosols. According to Deirmendjian (1963), the normalised phase function $\bar{P}$ at any angle θ for a given spherical particle with refractive index m and size parameter x, is defined

$$\bar{P}(m, x, \theta) = \frac{2\left(|S_1(m, x, \theta)|^2 + |S_2(m, x, \theta)|^2 \right)}{x^2 Q_s(m, x)} , \qquad 1.37$$

where the symbols are the same as in Section 1.5.2.

For monostatic lidars only the backscattered radiation is of interest. Using the fact that $S_1(\pi) = S_2(\pi)$ for homogeneous spheres, the following result is obtained for backscatter:

$$\bar{P}(m, x, \pi) = \frac{4|S_1(m, x, \pi)|^2}{x^2 Q_s(m, x)} . \qquad 1.38$$

For an aerosol containing a wide range of particle sizes the resulting phase function must be determined by averaging over the size distribution. As described in Appendix I, the volume backscatter function $B(\pi)$ is related to the volume scatter function β by the aerosol phase function for backscatter $P(\pi)$, by the equation

$$\frac{P(\pi)}{4\pi} = \frac{B(\pi)}{\beta} \quad . \qquad 1.39$$

Now if absorption is considered negligible, which is usually the case in the troposphere where the laser output is tuned away from absorption bands, the scattering coefficient is equal to the extinction coefficient and the normalised phase function for backscatter ($P(\pi)/4\pi$) is numerically equal to the backscatter-to-extinction ratio.

The phase function has been measured for tropospheric aerosols by several workers (e.g. Barteneva, 1960), but the only measurement of this quantity in the stratosphere to date has been by Gibson (1976), who flew a large, balloon-borne, polar nephelometer into the stratosphere to an altitude of 26.5 km and measured the scattering by aerosols at several angles as a function of height.

Numerous calculations of phase functions have been performed using Mie theory and a wide range of size distributions, refractive indices and compositions (e.g. Deirmendjian, 1964; McCormick *et al*, 1968; Harrison *et al*, 1972). As an example, Figure 1.16 shows Deirmendjian's phase functions for haze (b), and cloud (c), for the model size distributions given in (a).

Most calculations of phase functions for model size distributions assume that the particles are spherical. However, non-spherical particles are often found in the atmosphere and these do not conduct the surface waves that produce the resonances seen in Figure 1.13. As a result, significant differences can occur between the actual phase functions and those calculated assuming spherical particles. Chýlek *et al* (1976) have considered the effect of non-spherical particles by excluding the resonances in their Mie calculations and found reasonable

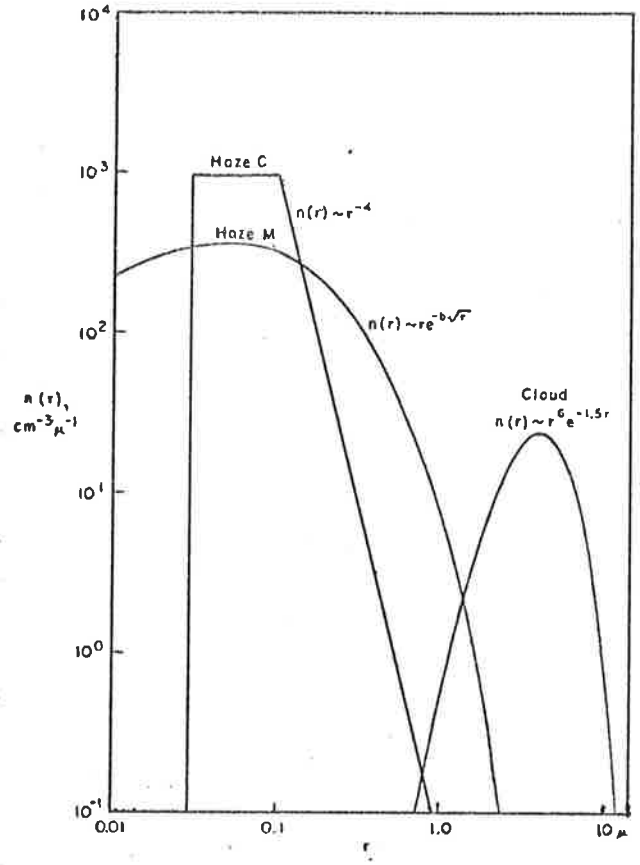

(a)

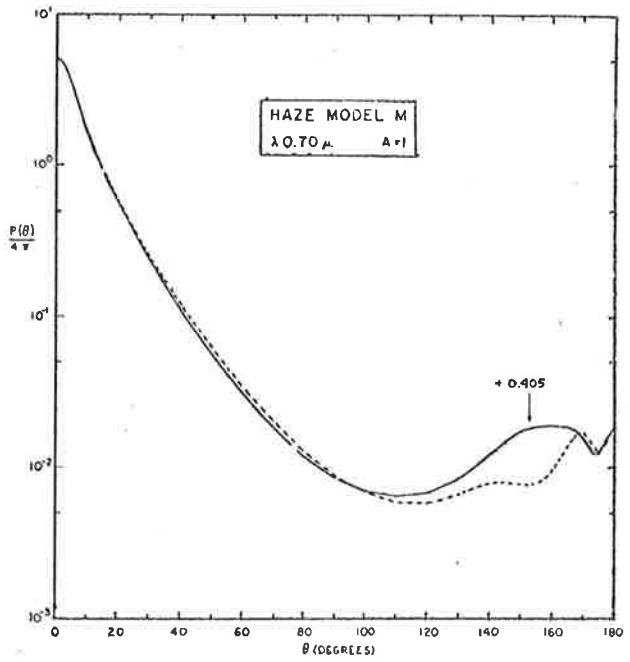

(b)

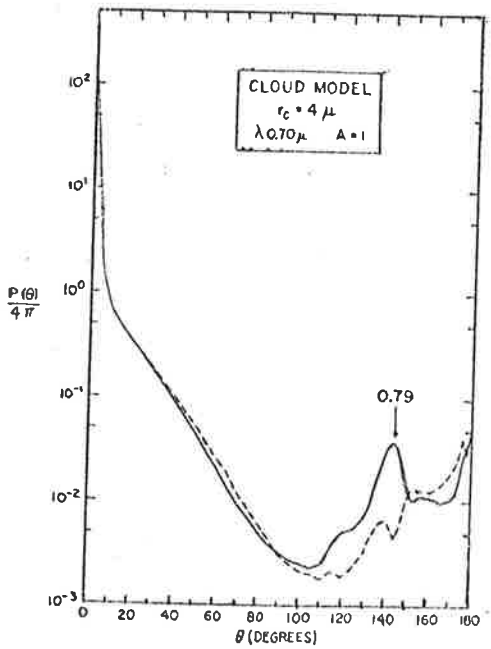

(c)

FIG 1.16 Model size distributions (a), and normalised scattering phase functions for haze(b), and cloud (c).

(after Deirmendjian, 1964)

agreement with experimental measurements of the angular scattering of aerosols, composed of various non-spherical solids.

Rosen (1969) has summarised the values of the phase function and backscatter-to-extinction ratio used in the early stratospheric optical probing experiments. The latter quantity has not been measured in the stratosphere but the phase function has been measured at other angles by Gibson (1976). As a result, model values are still used in the analysis of lidar backscatter signals from the stratosphere. Recent models with an experimental basis have been examined by Pinnick *et al* (1976) and Russell *et al* (1977), and Swissler and Harris (1976), using several models of the stratospheric aerosol, have calculated the spectral dependence of the extinction-to-backscatter ratio.

Most realistic model values of the stratospheric aerosol backscatter-to-extinction ratio lie in the range 0.0132 to 0.0199. The first value is obtained for a model comprising homogeneous, non-absorbing spheres of 75% solution by weight of sulphuric acid, with refractive index 1.42 and distributed in size according to the Deirmendjian (1969) Haze H size distribution. This value has been used by Russell and his coworkers at the Stanford Research Institute. The second value corresponds to an aerosol of spherical, non-absorbing particles with a real refractive index of 1.33 and distributed according to the Deirmendjian (1964,1965) Haze M size distribution shown in Figure 1.16(b). This value was used by many of the earlier stratospheric groups and has continued to be used by the Adelaide lidar group for reasons of consistency in the analysis of stratospheric records extending back to early 1969.

Values of the aerosol backscatter-to-extinction ratio for tropospheric aerosols have been derived using both experimental and

theoretical means. Among the experimental values are those of Waggoner *et al* (1972) who obtained a value of $(0.15 \pm 0.02)/4\pi$ from comparisons of lidar and nephelometer signals from an urban aerosol. Hamilton (1969), using an elevation scanning technique with a calibrated lidar on days of atmospheric horizontal homogeneity, obtained values of $0.33/4\pi$ and $0.5/4\pi$. Fernald *et al* (1972), who calibrated their lidar against clear sky returns and used a solar radiometer and a stratospheric aerosol model to calculate the aerosol optical thickness of the atmosphere above the maximum range of the lidar, measured $P_A(\pi)$ values of 0.87 ± 0.09 and 0.99 ± 0.30.

McCormick *et al* (1968), using Junge power law aerosol model distributions with a wide range of exponents and radius limits, found values of $P_A(\pi)$ lying between 0.386 and 0.602, while Harrison *et al* (1972) used power law aerosols of varying refractive index throughout the particle ("onion aerosols") and obtained an even wider range of values. The most comprehensive study seems to be by Quenzel *et al* (1975) who used 21 haze distribution models with refractive indices ranging from $1.33 - 0i$ to $1.70 - 0i$ and calculated the backscatter-to-extinction ratio for haze to be in the range 0.013 to 0.036 with a mean value of 0.022, which correspond to values of $P_A(\pi)$ of 0.163 to 0.452 with a mean of 0.276.

1.6 A Brief Review of Lidar Observations of Atmospheric Aerosols

The earliest active optical probing studies of the upper atmosphere used searchlight beams and a bistatic geometry. In this arrangement the receiver is situated several kilometres horizontally from the transmitter and the angle between the beams is altered to allow measurements of scattering from a large range of heights.

With the invention of the ruby laser a new transmitter was available which provided the advantages of monochromaticity, low divergence, increased discrimination between scattering from aerosols and air molecules because of its longer wavelength, and the ability to be operated in a pulsed mode as in the case of a normal radar and some of the searchlight experiments (Friedland *et al* 1956). This last feature permits the use of a monostatic configuration in which the transmitter and receiver are mounted adjacently giving the added advantages of simplicity of optical alignment and of a single-site operation. The earliest lidar observations of the atmosphere were made by Fiocco and Grams (1964), and these were soon followed by many others (e.g. Collis and Ligda, 1966; Clemesha *et al*, 1966; Bain and Sandford, 1966; Grams and Fiocco, 1967). These observations followed soon after the volcanic eruption of Mt. Agung in Bali in 1963, and showed enhanced aerosol scattering in the lower stratosphere, the principal region of interest at the time.

Observations of the stratospheric aerosol layer continued in the following period of relatively insignificant volcanic activity, when the scattering from aerosols declined substantially, (Young and Elford, 1979). During this period much attention was paid to the relation between lidar-derived aerosol backscatter values and aerosol particle number densities measured by balloon, (Northam *et al*, 1974) and aircraft, (Russell *et al*, 1976), and the accuracy of the normalisation of lidar backscatter profiles to clear air values (Russell *et al*, 1974b).

The eruption of Volcán de Feugo in 1974 was observed widely by lidar groups (e.g. McCormick and Fuller, 1975; Fegley and Ellis, 1975; Russell and Hake, 1977). The sudden influx of dust permitted the study

of the rate of decay of the aerosol content of the stratosphere and the relationship of its variability to various atmospheric parameters (McCormick *et al*, 1978).

In addition to ground based ruby lidar observations, other measurements have been made of the stratosphere. Fox *et al* (1973), Fernald *et al* (1975) and Fernald and Schuster (1977) made observations of the stratosphere using an airborne dye laser operating at 589 nm during 1971 and 1973, and reported low aerosol concentrations. A more powerful dye laser has been used by Pettifer *et al* (1976) to measure the neutral nitrogen profile in the stratosphere using the vibrational/rotational Raman scattered light, and thereby determining the temperature profile up to 25 km altitude. Still shorter wavelengths were used by Gibson and Thomas (1975) who probed the stratosphere to a height of 19 km with an ultraviolet lidar that operated in the range 297 nm to 308 nm.

While some lidar groups concentrated on the stratosphere others probed higher in the atmosphere to detect cometary dust and other extra-terrestrial material (Clemesha and Nakamara, 1972). The powerful lidar at the University of West Indies has been used to measure atmospheric density variations in the mesophere and thereby detect atmospheric tides (Kent *et al*, 1972) and mean, relative density profiles (Kent and Keenlislide, 1974). Resonance scattering of dye laser radiation has been used to measure variations in the atmospheric sodium layer at an altitude of about 90 km (e.g. Bowman *et al*, 1969; Sandford and Gibson, 1970; Aruga *et al*, 1974).

Other workers turned their attention to the troposphere, where different recording techniques are required because of the much larger

signals. A wide range of features of the lower atmosphere was probed by lidar; the introduction of the steerable lidar permitted the study of atmospheric properties in three dimensions. The measurement of cloud base heights was an obvious and early use for lidar (Collis, 1965).

Vertical profiles of the volume backscatter function and extinction coefficient were measured with a steerable lidar by Hamilton (1969) who was able to make measurements of the backscatter-to-extinction ratio by assuming horizontal homogeneity of the atmosphere. Fernald *et al* (1972), also produced values of this ratio using a steerable lidar and related their backscatter profiles to the temperature structure of the atmosphere.

Barrett and Ben-Dov (1967) applied lidar observations to the measurement of air pollution and produced vertical profiles of the mass concentration of aerosols. Johnson and Uthe (1971) used the relationships between backscatter, extinction and mass concentration to produce contours of mass concentration in their study of the dispersion of smoke plumes from power station chimneys.

By observing the movement of aerosols, the motion of the air in the lower atmosphere has been deduced. Eloranta *et al* (1975) analysed multiple lidar returns at low elevation angles to produce one component of the drift velocity of aerosols and hence of wind speed, and Kunkel *et al* (1977) compared consecutive lidar elevation scans to deduce convective motions in the boundary layer.

Other atmospheric constituents and pollutants have been measured by using Raman scattering (Inaba, 1976) and Differential

Absorption Lidar techniques (Collis and Russell, 1976). Atmospheric temperature and humidity profiles also have been measured by Raman scattering (e.g. Mason, 1975; Cooney and Pina, 1976; Cohen *et al*, 1976; Gill *et al*, 1979; Pourney *et al*, 1979).

The separation of the lidar return signal into two polarised components, one parallel to the transmitted polarisation and one perpendicular, has produced additional information on aerosol and cloud layers (McNeil and Carswell, 1975; Pal and Carswell, 1977). In particular, the depolarisation of lidar returns from clouds has been studied with the aim of determining the presence of water and ice (Sassen, 1976, 1977). Platt (1977) has in fact, used depolarisation ratios to distinguish between layers of water and ice in a mixed phase altostratus cloud. Regions of very high backscatter and low depolarisation have been interpreted by Platt (1978) as being due to horizontally oriented ice crystal plates.

Recently, extensive studies have been reported where lidar backscatter profiles have been compared with atmospheric scattering parameters deduced using other techniques, including solar radiometers, particle counters and nephelometers (De Luisi *et al*, 1976 (a) & (b); Reagan *et al*, 1977; Russell *et al*, 1979). The results of these experiments have been used to provide further information on optical models of atmospheric aerosols and their effects on the radiation balance of the atmosphere.

When this thesis was begun there was a need for information on the natural variability of the stratospheric aerosol layer. Such observations would be useful in the creation of models of the aerosol layer and assist in the prediction of the effect on the layer of the

introduction of a proposed fleet of high altitude supersonic transport aircraft. Accordingly, the aim of the stratospheric observation programme was to determine the short-term natural variability, and the long-term trends in the stratospheric aerosol layer.

Quantitative tropospheric aerosol observations in terms of the extinction of light in the troposphere have often been hindered by difficulties in the determination of suitable boundary values and by the uncertainty in the relationship between backscatter and extinction. The aim of the tropospheric programme was to investigate these areas and to compare the results with other independent measurements.

CHAPTER TWO

EQUIPMENT

2.1 The University of Adelaide Lidar

The basic lidar system used in the present study was designed and built in the Department of Physics, University of Adelaide for the study of the stratospheric aerosol layer. Full details of this system are described by Bartusek (1970) and are summarised by Bartusek *et al* (1970). A brief description follows.

The lidar transmitter is a ruby laser with an output wavelength which is tuned thermally to 694.3 nm by passing refridgerated, distilled water through a double-walled glass water jacket around the ruby rod. The rod has a totally internally reflecting wedge cut at one end and a Brewster face at the other. The laser pulse leaves the optical cavity through a sapphire optical flat of sixteen percent reflectivity which is placed at right angles to the ruby rod. The change in direction is produced by a 90° prism which rotates at 12000 r.p.m. and forms the Q-switch for the cavity.

Optical pumping is performed by a Xenon-filled, FX55 flash tube placed at one focus of an elliptical cavity with the ruby rod at the other. The flash tube is cooled by distilled water pumped from a reservoir at ambient temperature. The output energy of the laser is limited to approximately 0.2 joules per pulse by the Q-switch prism which is destroyed at higher energies. Maximum firing rate is about one pulse per second. A collimator which contains a rotating fluorescence shutter at the focus of the primary lens reduces the output divergence of the laser pulse to less than one milliradian.

The receiver consists of a 0.31 metre diameter, f 6 Newtonian telescope with a variable, field-limiting aperture at the focus. A rotating shutter which is phased with the Q-switch motor is placed immediately behind the aperture to prevent overload of the photomultiplier detector by the strong return from low altitudes during observations of the stratosphere. After passing through the shutter the light is collimated by a field lens before progressing through a 0.85 nm bandwidth interference filter onto the detector surface. This condition of collimation at the detector is desirable as otherwise the image of the light returned from the outgoing pulse would move across the detector surface and possibly be subjected to a variation in detector efficiency. An E.M.I. type 9558B photomultiplier tube having an S-20 photocathode is used as the detector. During stratospheric observations the photomultiplier is cooled by a Peltier battery to approximately - 15° C in order to reduce the dark count rate to about 120 counts per second.

The physical layout of the lidar system is shown in Figure 2.1 and a summary of the system parameters is given in Table 2.1.

TABLE 2.1

Lidar System Parameters

Parameter	Value
Laser wavelength	694.3 nm
Maximum energy per pulse	0.2J
Pulse repetition rate	1 Hz
Pulse length	0.3 μsec
Beam divergence	1 mrad
Receiver mirror area	0.073 m^2
Receiver field of view	2 - 5.4 mrad
Convergence height of transmitter and receiver cones	0.76 - 0.17 km
S-20 detector quantum efficiency	0.03
Filter bandwidth	0.85 nm

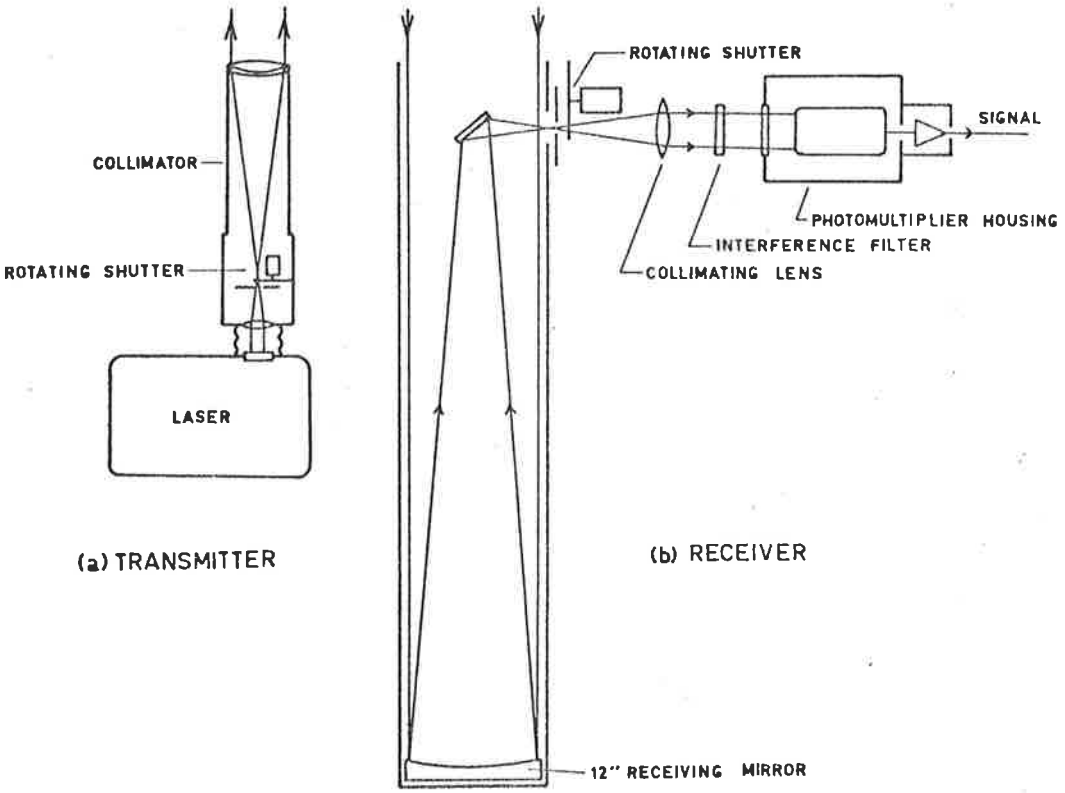

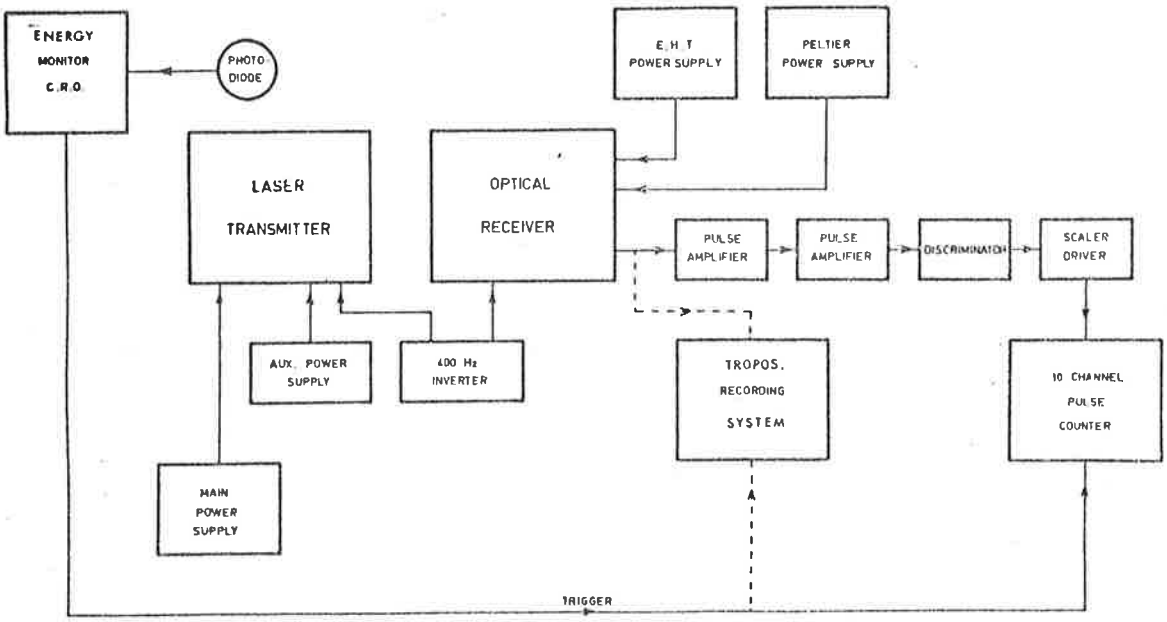

FIG 2.1 The lidar system

2.1.1 Problems Encountered with the Ruby Lidar

During the experimental programme many months were lost because of faults which developed in the early model ruby laser employed in the lidar. Among the more serious faults were the cracking of the ruby cooling jacket, failure of the aluminium to ruby rod seals in the water jacket and the destruction of the aluminium coating on the elliptical mirrors in the laser cavity.

The ruby rod is held in a water jacket by two aluminium ferrules which are heat shrunk onto the rod and also lightly glued with "Araldite". On several occasions the water jacket cracked near the ferrules and allowed water to leak and damage the aluminium coated, elliptical cavity mirrors.

After a new water jacket had been made and fitted to the ruby rod a complete optical re-alignment of the ruby laser was required. This was followed by an alignment of the laser and collimator and then the transmitter and receiver. Because of the many degrees of freedom of movement provided by the ruby rod, Q-switch prism and sapphire flat, re-alignment was a lengthy process involving considerable experimentation in order to reach an optimum in pulse length, shape and energy. For the first two occasions the laser and all electronic and cooling equipment were removed from the caravan to a laboratory for re-alignment in mechanically stable conditions. However, with practice the alignment procedures were improved and streamlined, and subsequent re-alignments were performed in the laser caravan.

It was thought originally that differential contraction between the aluminium ferrules and the glass jacket during cooling caused the cracking. Further investigation showed that the excess stresses on the glass jackets were more likely the result of the swelling of the "Araldite"

due to absorption of water. In an attempt to cover both possibilities the "Araldite" was replaced with white "Silastic RTV 732", a silicone rubber, sealing and adhesive compound. No further cracking was experienced.

The stripping of the aluminium reflecting surface from the cavity mirrors was the most difficult problem to overcome. New batches of mirrors began deteriorating after only tens to hundreds of laser shots whereas, originally, the mirrors had lasted tens of thousands. As the stratospheric observation experiments usually involved three to four thousand shots a night this situation was clearly unsatisfactory.

Many different ways of producing a reliable aluminium coating were tried. Experiments which were too lengthy to detail here, were also performed with the aim of electropolishing a pair of solid aluminium mirrors which had been machined and polished from a solid cylinder of aluminium. The inconsistent quality of results and the hazardous nature of the technique led to the termination of this approach.

Eventually some mirrors were completed to the specifications supplied by the manufacturer of the laser who had long since ceased production of the mirrors. These were machined from a solid aluminium cylinder, polished, electroplated with a very hard nickel surface, re-polished, coated with evaporated aluminium and baked at a high temperature. They were then placed in the laser cavity and the flash tube fired. It was with no small amount of disappointment and frustration that the author found that although the reflective coating was successful, no lasing was achieved even at the maximum available flash tube energy.

It was found that during the several months of experimenting with alternative mirrors, one of the aluminium ferrules which held the ruby rod had leaked and deposits of some solid material had formed on the

wedge cut, thereby destroying its reflective qualities. Rectification of this problem required the breaking open of the water jacket. A new aluminium ferrule, "anodised" to prevent further corrosion, was fitted, sealed with "Silastic" and enclosed in a new water jacket. After yet another complete optical re-alignment the laser performed satisfactorily.

A significant deterioration in laser output occurred when a new batch of flash tube jackets began to darken after only a few hundred flash tube firings. Baking in an oven returned the jackets to their original transparency but darkening re-occurred on re-exposure to flash tube radiation. Similar problems have been encountered by Gibson (1972) More success was obtained by using jackets made of transparent "Vitreosil", a pure vitreous silica, rather than synthetic vitreous silica, the former being distinguishable by its much lighter colour when viewed along the length of the tube.

Approximately eighteen months were spent on the repairs and consequent re-alignments of the laser cavity and the development of more reliable components. During this time methods for producing excellent, durable cavity mirrors and ruby water jackets were developed, and the problem of energy loss caused by darkening flash tube jackets was solved. The solution of these problems produced a far more reliable laser.

2.1.2 Modifications to the Lidar Transmitter and Receiver

The lidar was originally built for stratospheric observations and later used for the vertical sounding of the troposphere, (Gambling and Bartusek, 1972). Modifications to the system were required, therefore, if observations were to be made at various angles of elevation and azimuth.

The sheer bulk of the f6 Newtonian receiver and the attached laser transmitter and collimator excluded possible systems which required steerability of the whole combination. A compromise was reached by varying the elevation angle of propagation of the lidar pulses by reflecting the transmitted and received beams from mirrors. The azimuth angle was varied by rotating the whole system on a large roller bearing taken from a scrapped Bofors anti-aircraft gun turret. The bearing was very satisfactory and provided a very stable and smooth rotation through a full 360 degrees. Cables for supplying the electrical signals to the laser head and receiver, and the water hoses for cooling the ruby rod, flash tube and Peltier battery were re-routed along the floor and up through the axis of the rotating bearing. Twisting of these cables provided the main limitation to the rotation of the system.

The size of the caravan that houses the lidar imposed limitations on the size of the mirrors, and hence the range of elevation angles which could be studied. Separate mirrors were chosen for both the receiver and the transmitter as a single mirror would have been very large and would probably have distorted under its own weight. The mirror for the transmitter was 40.5 cm by 27.6 cm and that for the receiver was 81 cm by 38.5 cm. These dimensions permitted scans in elevation up to an angle of approximately 65 degrees. Both mirrors were coated on the front (lower) surface with evaporated aluminium and a protective coating of magnesium fluoride. To provide maximum reflection of the transmitted signal over a wide range of elevation angles the plane of the mirrors was aligned parallel to the plane of polarisation of the laser output pulse.

The use of small, separate mirrors permitted a simple mounting consisting of a rectangular frame which had a double, central mainspar of

PLATE 2.1 The mounting for the transmitter and receiver mirrors.

steel bars, 1.2 cm wide by 5.0 cm deep. The mirrors were supported by their edges on 1 cm "L" section aluminium strips which were bolted into adjustment slots in the mainspars and in the outer edges of the frame. Both the ends and the edges of the frame were made from lighter steel bars, 3 cm deep by 0.6 cm wide.

Both mirrors were initially aligned in the laboratory using an autocollimation technique and were further checked while supported in a horizontal position on the lidar by using a spirit level with a sensitivity of ten seconds of arc. Once the mirrors were aligned they were locked in position by bolts on the backs of the mirrors.

A lead counter balance facilitated the pivotting of the mirrors which could be locked at any elevation angle by tightening a nut on the pivot bearing. For vertical firings the mirrors were swung out of the way to the vertical position to allow the transmitted and received beams to pass unhindered. Plate 2.1 illustrates the mirrors in their mounting and Plate 2.2 shows the general arrangement of equipment in the caravan with the lidar system on its rotating base at the rear.

During an experiment the author could set the mirror elevation and azimuth angles by referring to the corresponding scales and also ensure that the field of view was clear of buildings or aircraft by sighting through a small telescope which, with a right-angle prism and the transmitter mirror, formed a periscope.

Uneveness in the reflection coefficient of the evaporated coating on the mirrors over their complete lengths caused a variation in the measured signal with elevation angle. As this parameter was difficult to measure precisely the variable reflection coefficient was simply included

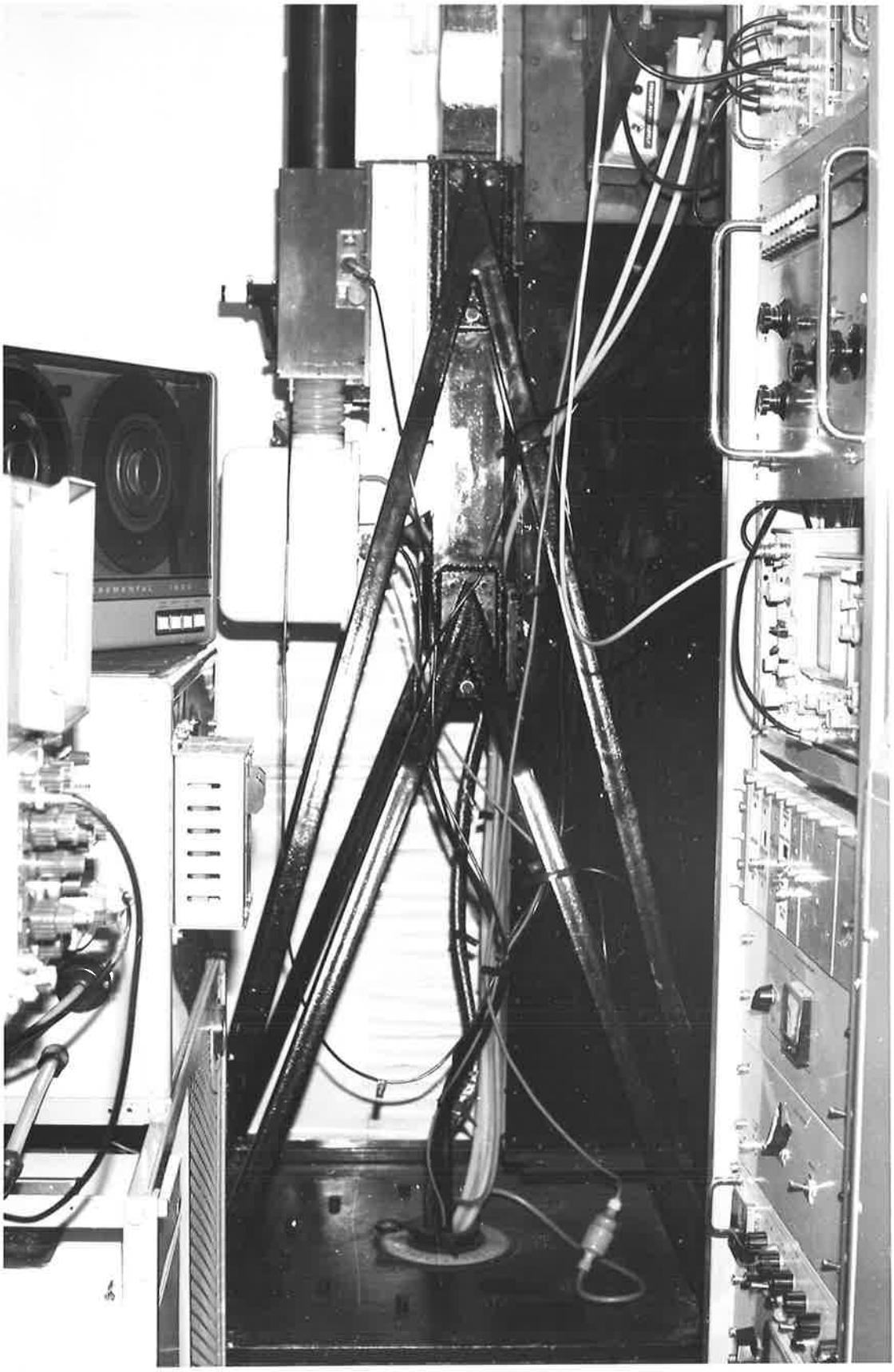

PLATE 2.2. The lidar system inside the caravan.

in the system constant during the analysis of the signal.

2.2 Investigations into Photomultiplier Tube Irregularities

2.2.1 Measurements of Signal Induced Noise

Measurements by Pettifer and Healey (1974) of the enhancement in dark current due to signals on a Mullard 56TUVP photomultiplier were applied by Pettifer (1975) to the case of lidar measurements. Because the dark current enhancement (signal induced noise) can last for several hundreds of microseconds after the removal of the signal the effect could be important in the measurement of lidar returns where the signal decreases rapidly with time.

The signal induced noise in a time-gated photon counting system such as used for stratospheric lidar measurements can be considered to add in accordance with a linear superposition principle described by Pettifer and causes an increase in the ratio of the signal induced noise to signal in successive channels. In the lidar system described by Pettifer, the calculated ratio of induced noise to signal reached a maximum of eleven percent. Pettifer also described the effect this would have in measurements by other lidars, in particular the one used in the present study. Measurements were made, therefore, of the signal induced noise in the EMI 9558B photomultiplier tube used in the lidar of the University of Adelaide, employing a similar technique to the one used by the other workers.

The experiment and the results are detailed by Young (1976). As can be seen in Figure 2.2, the signal induced noise measured in the present system was found to be slightly over two orders of magnitude lower than that measured by the other workers. The figure shows the ratio

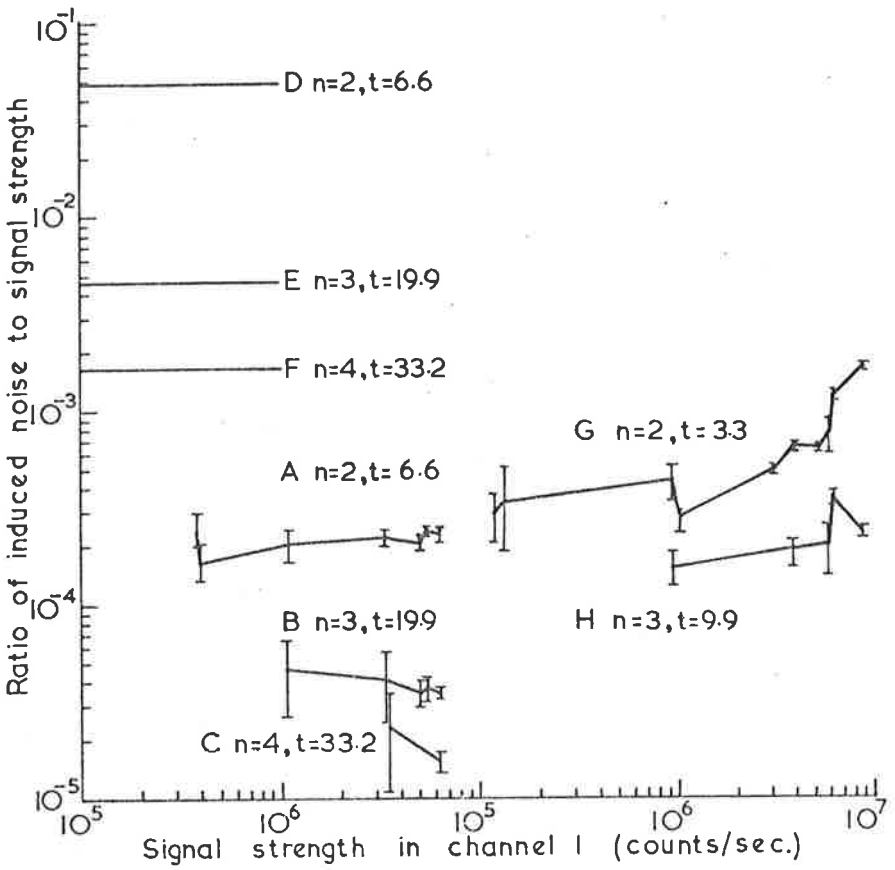

FIG 2.2 The ratio of induced noise to the measured signal as a function of the signal in channel 1. The symbols A to H are explained in the text.

of induced noise to the measured signal plotted against the signal recorded in channel 1. The curves labelled A to C are compared with those labelled D to F, the latter being taken from Figure 1 of Pettifer (1975), where a 13.3 μsec pulse was used with channels 2 km wide. Curves G and H are the present results obtained by using a 6.6 μsec pulse and channels 1 km wide. It was concluded that signal induced noise would not be a problem in the present lidar system.

2.2.2 Measurements of Non-Linearity

The logarithmic amplifier to be described in Section 2.4.2 needed a minimum input current of about 30 μA to produce an output signal with an adequate bandwidth. Because the lidar signal decreases rapidly with the square of the range, the expected maximum measured signal from shorter ranges was between 1 mA and 5 mA. Such anode currents often cause non-linear effects in photomultiplier tubes.

According to an EMI brochure on photomultiplier tubes (1967), the effects of large pulsed signals can be cancelled without the need for large chain currents by connecting decoupling capacitors between the final dynode stages and earth. Despite the addition of these capacitors the output signal was still non-linear at high currents. A calibration curve was obtained, therefore, by the following method.

The photomultiplier tube was illuminated by a temporally shaped light pulse from a Light Emitting Diode (LED) which produces a rapidly decreasing exponential signal of approximately 20 μsec duration. Neutral density filters were used to change the maximum signal level, and at the same time to maintain the tube output signal in the optimum range of the recorder, so that the LED simulated lidar signal covered a range from less than 1 μA to approximately 5 mA. By assuming that the

weakest signals recorded were undistorted, the correction coefficient, C(I) for a given recorded signal level could be obtained by finding the ratio of the assumed undistorted reference signal current I_r to the recorded current I and normalising the result to unity for small signals by dividing by the ratio of the transmission coefficients of the filters used during recording, i.e.

$$C(I) = (I_r/T_r)/(I/T) \qquad 2.1$$

Here the correction coefficient is defined as the ratio of the "true" signal level to the recorded signal level.

The transmission coefficients of the various filters were measured with a spectrophotometer but the uncertainty in the optical bandwidth of the LED output and the variation in the transmission of the filters over this bandwidth produced inconsistent values and indirect methods were necessary. The wide range of signal recorded using a given filter meant that below some signal level each recorded signal was undistorted. A comparison of the signal strength recorded in these regions using the different filters provided the required values of transmission and the correction coefficient could then be calculated.

A power law function was fitted to the measured values of correction coefficient minus one, using the recorded current as the independent variable. The data and the fitted function are shown in Figure 2.3. The points at the bottom of the graph do not appear to agree with the fitted function as well as the other values but the correction function is very close to unity here and discrepancies are virtually insignificant. The fitted correction function, $F_c(I)$ may be expressed in terms of the recorded current I (in milliamps) as

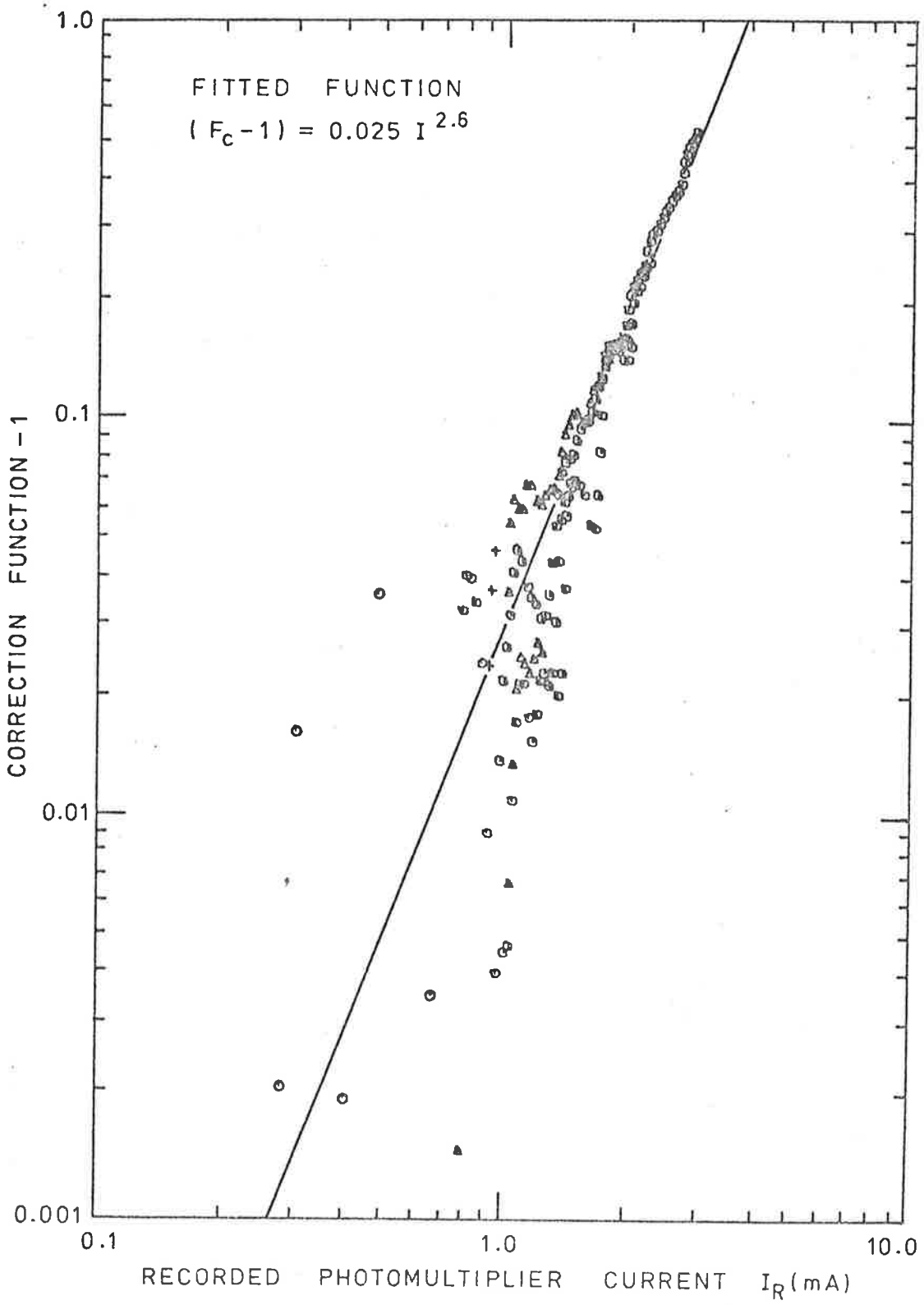

FIG 2.3 Values of correction function-1 (i.e. F_c-1) plotted against the recorded signal.

$$F_c(I) = C(I)-1 = AI^B \qquad 2.2$$

where $A = (0.025 \pm 0.002)$, $B = (2.6 \pm 0.1)$. The correlation coefficient was 0.85. The uncertainties in A and B lead to an increasing relative uncertainty in the corrected value of the current. This uncertainty increases from 0.0004 percent at currents of 0.1 mA to 0.17 percent at 1.0 mA and 9.5 percent at 10 mA . In practice most recorded currents were less than about 5 mA .

2.3 The Stratospheric Data Recording System

The recording system used for stratospheric observations is described by Bartusek *et al* (1970) and will only be summarised here.

The photoelectron signal across a 50 ohm load is increased by an amplifier with a gain of 100 and a risetime of 3 nsec. A discriminator with a threshold set to 100 mV is used to eliminate noise spikes caused by relays and motors and the signal is then passed through a prescaling device to produce pulses of a standard size ready for storage in a ten channel counter.

Recording is done in four sequences; namely, 8 km to 18 km, 12 km to 22 km, 20 km to 30 km and 20 km to 60 km by varying the starting time of the first channel and by changing the channel width from 1 km to 4 km. The wide dynamic range of the signal is accommodated by limiting the signal in the first two sequences with neutral density filters.

2.4 The Tropospheric Data Logging System

2.4.1 Introduction

The accuracy and the extent to which the troposphere could be probed with the original lidar was increased by recording the back-

scattered signal on magnetic tape for subsequent analysis on the University's computer. This technique made it possible for more profiles to be recorded in a shorter time span than the original method of manually digitising photographs of the signal recorded on a storage oscilloscope. Because the duration of lidar return signal was only a few tens of microseconds, it was not possible to directly record onto computer tape and an intermediate step was required.

Signals were stored temporarily in the memory of a Biomation 610B digital transient recorder for subsequent interrogation at a much slower rate. The transient recorder stores signals with six binary bit accuracy in 256 words and provides a cycled, smoothed, analogue output signal for inspection on an oscilloscope. In this way the signal could be viewed before actually writing onto computer tape, a facility which was particularly useful during the setting up of an experiment on a particular day. Once the recorded signals were adjudged satisfactory the recorder was switched to a locally modified "PLOT" mode in which the signal was automatically written onto magnetic tape immediately after recording.

The bandwidth of the transient recorder was quoted as 2.5MHz for input signals in the 5V to 50V range. When fast risetime test pulses were stored using a 0.1 μsec sample interval and the 10V input range, the time for recorded signal to rise from 10 percent to 90 percent of the full signal was less than 0.1 μsec. This indicated that the bandwidth was at least 3.5MHz and would limit the range resolution to about forty-five metres. As this range resolution was similar to that imposed by the 0.3 μsec pulse length of the laser it was considered adequate.

For sample intervals of 0.2 μsec and 0.5 μsec the sampling theorem limited the resolution to 60 and 150 metres respectively. The most commonly used sample intervals were 0.1 μsec and 0.2 μsec.

The rapid decrease of the lidar atmospheric return with range and the limited number of digitisation levels of the six-bit recorder often cause poor amplitude resolution over a considerable portion of the recorded signal. A solution to this problem is provided by either the use of a logarithmic amplifier or a gain-switching amplifier. In the present work the logarithmic amplifier worked more satisfactorily and was chosen in preference to the other device.

The output energy of the laser varied by up to fifteen percent from pulse to pulse. Thus it was necessary to monitor this variation if an accurate analysis of the lidar signals were to be made. Because the thermopile previously used for calibration had a very slow response and no digital output, a photodiode energy monitor was designed and built. This provided both a digital output and a front panel display of the laser energy.

A digital recording unit was built so that the lidar profile stored in the transient recorder could be transferred, word by word, to the tape recorder at the maximum writing speed of 300 words per second. The unit also provided the required inter-record pulses to the tape recorder, a Kennedy Incremental Model 1600, which recorded on standard, seven track, half inch computer tape. In addition to the laser profile up to fifteen words of housekeeping information could be written onto tape. These included the laser profile number, the laser output energy, both of which were displayed on the front panel of the unit, and the beam elevation and azimuth angles. The beam direction information was set on

the front panel using rotary thumb switches. The time for recording the lidar signal, writing the 256 data words, sixteen housekeeping words and an inter-record gap was less than two seconds.

A simplified block diagram of the tropospheric data recording system is shown in Figure 2.4. The digital recording unit and housekeeping electronic circuitry is discussed in Appendix II.

2.4.2 The Logarithmic Amplifier

As commercial units proved to be unsatisfactory a simple logarithmic amplifier was built using the logarithmic dependence of voltage on the current in a semiconductor diode. Several diodes were tested for accuracy in this logarithmic relationship and an AN2003 silicon diode proved to be the best. Deviations from the true logarithmic relationship were a fraction of one percent of the output voltage for input currents in the range 10 μA to 10 mA , increasing to four percent at 2 μA.

Initially a simple, manually-controlled bias circuit similar to that used by Allan and Evans (1972) was used, but it was found that when the lidar was pointed at a brighter region of the sky or a cloud, the background current increased and the operating point on the diode characteristics changed. This caused the offset of the output signal to increase from zero and also compressed the signal. Both of these effects were unsatisfactory as they led to a decrease in the optimum signal size for digitisation by the transient recorder. An automatic electronic biassing circuit was incorporated into the logarithmic amplifier to overcome this problem. A brief description follows.

In Figure 2.5(a) the integrated circuit labelled IC-1 senses the very low frequency drifts of the diode bias level and drives current

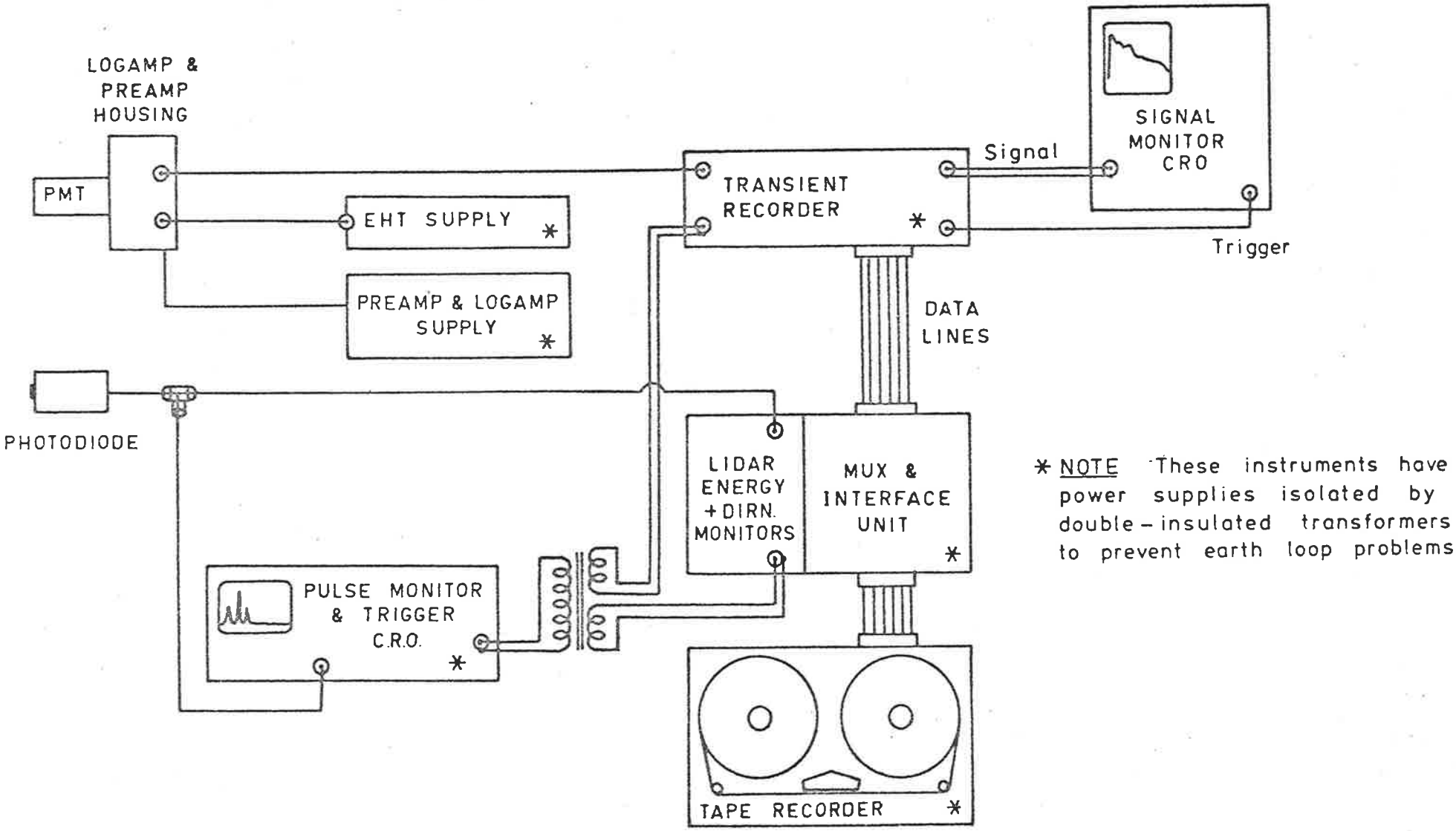

FIG 2.4 The tropospheric data recording system.

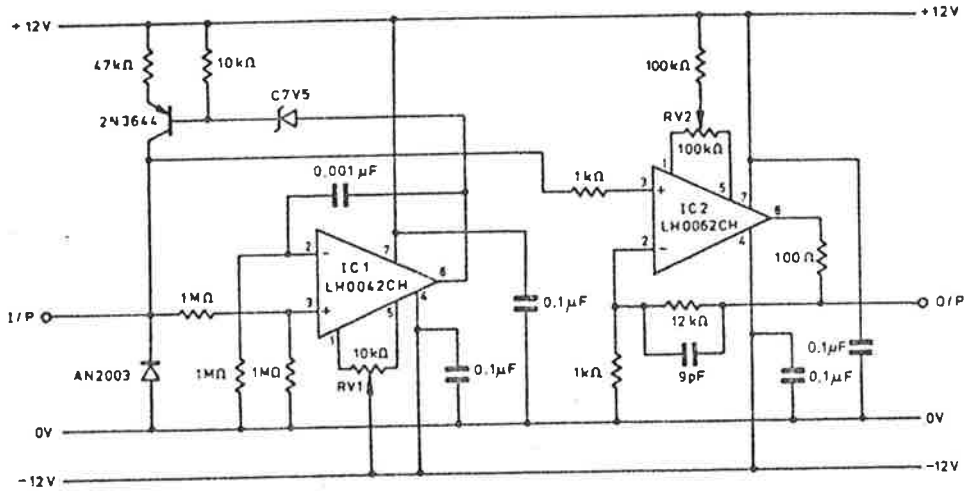

FIG 2.5(a) The logarithmic amplifier.

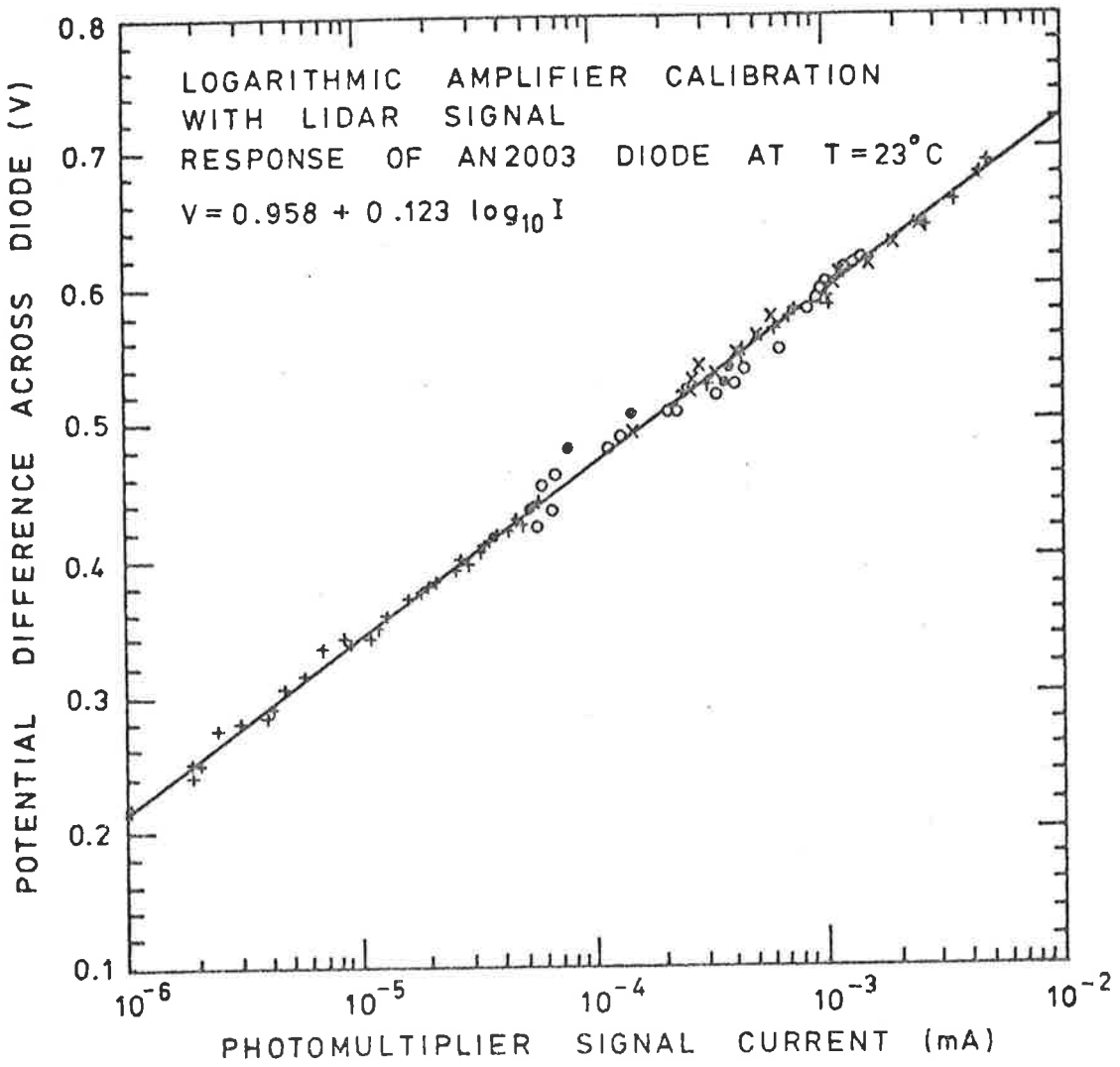

FIG 2.5(b) Calibration curve for the logarithmic amplifier.

into the diode from the collector of a transistor amplifier in the direction required to bring the bias current back to the level set by the variable resistor RV1. The second integrated circuit, IC-2, provides sufficient gain to produce a maximum output voltage of ten volts with a risetime of approximately 55 nsec. Both integrated circuits have field effect transistor inputs which provide an input impedance of 10^{12} ohms. The complete amplifier is mounted on a printed circuit board located near the photomultiplier anode.

The bandwidth was checked using signals from a light emitting diode and was found to change from approximately 2.5MHz at input currents of 30 μA to a maximum of 6MHz (limited by IC-2) above 500 μA . Over a large range of diode currents the bandwidth is inversely proportional to the dynamic impedance of the diode which decreases with increasing input current.

A calibration curve, shown in Figure 2.5(b), was obtained by comparing lidar return signals recorded using the logarithmic amplifier and a rudimentary gain-switching amplifier. As the diode characteristics are dependent on temperature the logarithmic amplifier was recalibrated periodically during each set of observations by comparing the logarithmic signal with the signal across a one kilohm resistor. Temperature changes were reduced by the air conditioning in the lidar caravan.

2.4.3 The Energy Monitor

As the laser pulse travels through the transmitter collimator some of the energy which is reflected from the plane, bottom surface of the output lens is sampled by an E.G. and G. brand SGD-100 silicon diffused photodiode. The integrated output of the photodiode is assumed to be proportional to the total output energy of the lidar. As is shown

in Figure 2.6, the signal is coupled by a 0.1 µf capacitor to a fast preamplifier, IC-1, which charges a 100 pf integrating capacitor through a 10 kilohm resistor and an AAZ13 diode which has a 3 Megohm reverse resistance to reduce leakage. A fast, high input impedance amplifier, IC-2, provides sufficient gain to drive a fast, positive-peak detector. The peak detector, comprising IC-3 and IC-4 was required because the integrating capacitor was incapable of holding its charge during the 50 µsec required for digital conversion by the analogue-to-digital converter (ADC), IC-8. The output of the peak detector was amplified to an optimum value for digital conversion by IC-5.

When the laser is fired the photodiode output is also used to trigger an oscilloscope used for monitoring the laser output pulse and for triggering all the recording electronics including the energy monitor. The dual monostable, IC-7, provides a delayed 50 µsec reset and sample pulse to the ADC, and the other dual monostable, IC-6, provides a discharge pulse, delayed by 200 µsec, to the 1000 pf polyester storage capacitor in the peak detector via a switch comprising T1 and FET-1.

The ADC is a Datel Systems Inc. "Econoverter" with a 20kHz conversion rate and six binary bit accuracy. The digital output is written onto tape via the interface unit and is also converted by IC-9 and IC-10 and displayed on LED displays IC-11 and IC-12 as an octal number, octal being preferred for reasons of simplicity and economy of space.

Calibration was achieved by firing laser shots through a beam splitter with the transmitted energy being sampled by the photodiode

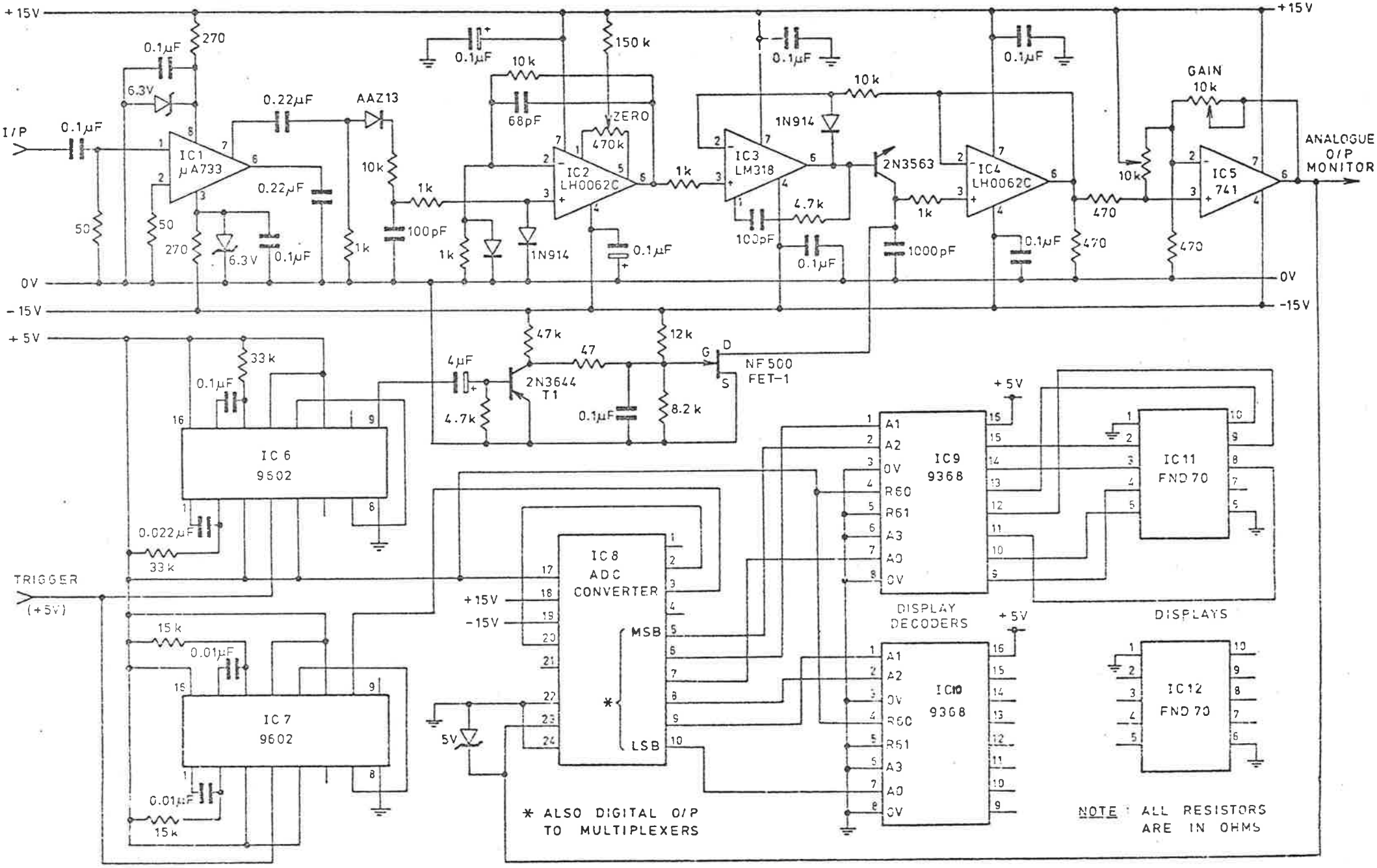

FIG 2.6 The energy monitor circuit.

and energy monitor and the reflected component by a thermopile. The output of the energy monitor was adjusted so that it was numerically equal to the thermopile output in microvolts.

CHAPTER 3

A STUDY OF THE STRATOSPHERIC AEROSOL LAYER OVER ADELAIDE

3.1 Method of Data Analysis

For an atmosphere consisting of aerosol particles and air molecules the number of photons scattered back from a height interval between h and $h + \Delta h$ and detected by the receiving equipment of a vertically pointing lidar is given by equation A1.11 derived in Appendix I as

$$C(h) = KT^2(o, h)[B_M(\pi,h) + B_A(\pi,h)]/h^2 \qquad 3.1$$

where $C(h)$ is the number of photons counted. K is a system constant which includes the effects of the lidar geometry, the efficiency of the optics and electronics, the laser output power, and the height interval Δh. $B_M(\pi,h)$ and $B_A(\pi,h)$ are the volume backscattering functions for air molecules and aerosols at the height h, and $T(o,h)$ is the transmittance of the atmosphere, at the lidar wavelength, between the lidar and height h.

The transmittance of the atmosphere $T(h_1, h_2)$, between heights h_1 and h_2 is a measure of the fractional attenuation of a vertically directed beam and is given by

$$\begin{aligned} T(h_1, h_2) &= T_M(h_1, h_2).\ T_A(h_1, h_2).\ T_O(h_1, h_2) \\ &= \exp\left[- \int_{h_1}^{h_2} \{ \beta_M(h) + \beta_A(h) + \beta_O(h) \}dh \right] \\ &= \exp[- \tau_M(h_1, h_2) - \tau_A(h_1, h_2) - \tau_O(h_1, h_2) \qquad 3.2 \end{aligned}$$

where β_M and β_A are the molecular and aerosol volume scattering coefficients, β_O is the ozone absorption coefficient, and τ_M, τ_A and τ_O are the respective optical thicknesses. For lidar studies it is necessary to introduce the volume scattering function $B(\theta, h)$ which is a measure of the radiation scattered per unit solid angle in the direction θ at the height h in the atmosphere. The total radiation scattered out of the beam is

$$\beta(h) = \int_{4\pi} B(\theta, h)\, d\omega$$

and the fraction of the scattered radiation directed in the backwards direction is given by $(P(\pi)/4\pi) = B(\pi,h)/\beta(h)$, where $P(\pi)$ is the value of the phase function for the case of backscatter. The transmittance due to aerosols $T_A(h_1, h_2)$ between heights h_1 and h_2 can be related to the integrated backscatter function by

$$-\ln [\, T_A(h_1, h_2)] = \tau_A(h_1, h_2) = \int_{h_1}^{h_2} \beta_A(h)\, dh$$

$$= (4\pi/P_A(\pi)) \int_{h_1}^{h_2} B_A(\pi, h)\, dh \,. \qquad 3.3$$

Equation 3.1 can be re-arranged to give

$$B_A(\pi, h) = C(h)h^2 / \{KT_M^2(o, h) \cdot T_O^2(o, h)\, T_A^2(o, h)\} - B_M(\pi,h). \quad 3.4$$

Equations 3.3 and 3.4 can then be solved for B_A and T_A by employing an iterative technique developed by Elterman (1966). At the height or heights in the range 9 km to 30 km where the total scattering is a minimum, the aerosol is assumed initially to be zero and the measured scattering profile is normalised to the calculated molecular scattering profile at these heights. This procedure is justified by the detection

of regions of very low aerosol content by direct sampling techniques. This point is discussed further in Section 3.2. Values of B_A and T_A are then determined for successive height increments by iteration of equations 3.3 and 3.4 at each level. The constant $P_A(\pi)/4\pi$ was taken as $0.25/4\pi = 0.0199$ and the ozone transmittance was calculated from the tables of Elterman (1968). The molecular parameters B_M and T_M are calculated from the molecular density profile, $N_M(h)$, using

$$B_M(\pi, h) = (P_M(\pi)/4\pi)\beta_M(h) = (P_M(\pi)/4\pi)\sigma_M N_M(h). \quad 3.5$$

The value of $P_M(\pi)$ is 1.5 for the backscatter of plane polarised light from air molecules and $\sigma_M = 1.76 \times 10^{-31} m^2$ is the scattering cross section of an average air molecule. The atmospheric density profile is measured by radiosonde balloons launched from Adelaide Airport, 7 km west of the lidar site, on the night of the lidar measurements or on the following morning.

Another useful quantity in describing aerosol scattering is the scattering ratio, R(h), which is the ratio of the measured total scattering at a certain height to that which would be measured from an atmosphere consisting of air molecules only. It is defined as

$$R(h) = 1 + B_A(\pi,h)/B_M(\pi,h) = C(h)h^2 / \{KB_M(\pi, h). T^2(o, h)\}. \quad 3.6$$

Normalisation of the measured scattering profile to the molecular profile is performed initially in the relatively clear region near 10 km where $B_A(\pi, h)$ is assumed to be zero and the scattering ratio unity. However, the presence of aerosols in this region will cause the calculated aerosol profile to be underestimated over its whole range and scattering ratios less than unity and negative values of $B_A(\pi, h)$ may

be produced. Conversely, statistical errors in the measured photon count rate and errors in the measured density profile can produce scattering ratios which are too small and if one of these values happens to be at the normalisation height then the whole profile of calculated aerosol values will be overestimated.

To minimise the effect of these difficulties the following procedure is adopted. Firstly, the minimum scattering ratio, R_{min}, in the height range 9 km to 30 km is found and then a weighted mean is calculated of this value and all those ratios that do not differ significantly from it. These ratios are those values of $R(h)$ which satisfy the equation

$$R(h) - \Delta R(h) \leqslant R_{min} + \Delta R_{min} \qquad 3.7$$

where ΔR and ΔR_{min} are the standard deviations in R and R_{min} respectively. The system constant in equation 3.6 is then adjusted so this weighted mean minimum scattering ratio, given by

$$R'_{min} = \frac{\sum_i R(h_i)/(\Delta R(h_i))^2}{\sum_i (1/\Delta R(h_i))^2}$$

is unity. The weighted mean (Bevington 1969) was chosen in preference to the usual arithmetic mean because the standard deviation due to statistical fluctuations in the measured photon count rate increases rapidly with height and this could cause the mean value to be biassed incorrectly by a low value of doubtful statistical reliability. Profiles of $R(h)$ and $B_A(\pi,h)$ are then re-computed using equation 3.6 and the new value of K.

3.1.1 Analysis of Errors

From equation 3.6 the relative uncertainty in the scattering ratio at a certain height can be expressed as

$$\left(\frac{\Delta R}{R}\right)^2 = \left(\frac{\Delta C}{C}\right)^2 + \left(\frac{\Delta B_M}{B_M}\right)^2 + \left(\frac{\Delta T^2}{T^2}\right)^2 + \left(\frac{\Delta K}{K}\right)^2 . \qquad 3.8$$

where ΔX signifies the standard deviation in the quantity X. Although a value for ΔK could be obtained during the calculation of the weighted mean scattering ratio this is not done as it cannot give a reliable estimate of the amount by which aerosol at the normalisation height causes an error in the system constant. There may be no aerosol-free region in the height range being studied! Also, any error in K will produce a systematic shift of all values in the profile and will not alter the relative value of any point relative to the others. Errors due to normalisation are discussed in the next section and are here taken to be zero.

The cross correlation term between the uncertainties in B_M and T^2 has been neglected because it is insignificant compared with the contribution from the other errors. From equation 3.5

$$\Delta B_M / B_M = \Delta N_M / N_M .$$

where the probable relative radiosonde density error is taken as one percent (Lenhard 1973).

The error in the transmittance can be separated into its aerosol, ozone and molecular components in the following fashion.

$$\left(\frac{\Delta T^2}{T^2}\right)^2 = \left(\frac{\Delta T_A^2}{T_A^2}\right)^2 + \left(\frac{\Delta T_O^2}{T_O^2}\right)^2 + \left(\frac{\Delta T_M}{T_M}\right)^2 .$$

Because the molecular and ozone optical thicknesses are so small compared with the aerosol optical thickness at the laser wavelength, relatively large errors in the measured molecular density profile or the assumed ozone extinction model (Elterman 1968) are required to produce significant relative errors in the corresponding transmittances. Russell *et al* (1973)

have shown that changes of 50 percent or more in the molecular atmosphere density profile and 160 percent or more in the assumed ozone distribution would be required to change the two-way molecular or ozone transmittances by as much as one percent. Accordingly, these errors are neglected in the present analysis.

As discussed in the previous section, values of aerosol extinction are evaluated during the analysis of the data for a given height and then used in the analysis of the next height interval. The aerosol optical thickness used in the calculation of the transmittance is the product of the integrated backscatter function and the reciprocal of the aerosol phase function for backscatter (Equation 3.3). Values for the latter quantity depend on the aerosol model assumed, its particle size distribution, refractive index, composition, particle shape and so on. As could be expected there is a wide range of possible values. Values for this function are derived from models by McCormick *et al* (1968), Deirmendjian (1969) and others, and discussed critically by Russell *et al* (1974) in the light of comparative balloon and aircraft experiments. Russell *et al* decided to use a value $(P_A/4\pi) = 0.0132$, which is applicable if the stratospheric particles are non-absorbing, homogeneous spheres of 75 percent concentrated sulphuric acid with real refractive index 1.42 and distributed in size according to the Deirmendjian Haze H distribution model.

The value of $(P_A/4\pi) = 0.0199$ given by Deirmendjian (1965) is used in the present analysis. Calculations show that a choice of .0132 instead of .0199 creates a difference of less than two percent in the integrated backscatter function and less than one percent in the two-way aerosol transmittance for the average of the 1969 data when the aerosol layer was at its strongest. For the 1973 data when the aerosol

values were low the difference in the two-way aerosol transmittance is less than one half of one percent. So variations in $P_A(\pi)$, although they affect the value of aerosol optical thickness derived from the integrated backscatter coefficient directly, do not cause significant errors in the two-way aerosol transmittance. Such errors are less than one percent over the height range considered here.

The remaining source of uncertainty in R(h) is the error in the photoelectron count rate. The errors are from optical, electrical and statistical considerations. Background sky radiation, multiple scattering of the laser beam, and fluorescence of the ruby rod are all possible optical sources of spurious photoelectron counts, whereas the photomultiplier tube dark count rate is the predominant source of electrical noise.

Tests have shown that multiple scattering is insignificant. It is minimised by the separation of the lidar transmitter and receiver and by the narrow field of view of the receiver, while a rotating fluorescence shutter is used to eliminate ruby fluorescence. A narrow bandwidth interference filter centred on the ruby wavelength limits the sky background radiation and the photomultiplier dark count is reduced by cooling. The remaining background count rate is measured separately during the experiment and is subtracted from the raw count rate during the analysis.

The remaining errors are all dependent on the rate of arrival of the photons at the photomultiplier. As discussed in Chapter 2 some photomultipliers experience significant signal induced noise following a strong signal pulse. Such noise has been found to be insignificant in the photomultiplier used in the present equipment and the use of an adjustable receiver shutter for blocking the strong light returned from

lower altitudes is added protection.

The finite resolving time t of the receiving electronics can cause a reduction in the observed count rate n at high true count rates N owing to the simultaneous arrival of two or more photons during the dead time.

The true count rate is given by the equation

$$N = \frac{n}{1 - nt} \quad . \qquad 3.9$$

Very high count rates, though, require the resolving time to be known very accurately so the signal count rate for the lower altitudes is limited by neutral density filters.

The random and low photoelectron counts recorded per laser shot necessitate the averaging of signal counts over several laser firings if results are to be statistically significant. After a number of such laser firings the total number of photoelectrons counted C, will be the sum of C_s actual signal photoelectrons and C_N noise pulses. As mentioned previously the average expected noise count rate $\overline{C}_N$ can be measured separately and subtracted. Morton (1968) has shown that the relative error e in the measured signal count rate is given by

$$e = \frac{\Delta C_s}{C_s} = \frac{C^{\frac{1}{2}}}{(C - \overline{C}_N)} \quad . \qquad 3.10$$

where ΔC_s is the standard deviation in C_s. Typically, e varies from one to two percent at 9 km to five to six percent at 30 km.

Equation 3.8 now reduces to

$$\left(\frac{\Delta R}{R}\right)^2 = \left(\frac{\Delta C}{C}\right)^2 + \left(\frac{\Delta B_M}{B_M}\right)^2 ,$$

$$\text{or} \quad \left(\frac{\Delta R}{R}\right)^2 = \frac{C}{(C - \bar{C}_N)^2} + (0.01)^2 . \qquad 3.11$$

The combination of equation 3.6 and 3.11 allows the uncertainty in the aerosol volume backscattering function to be written as

$$\Delta B_A = B_M \cdot \Delta R$$

$$\text{or} \quad \frac{\Delta B_A}{B_A} = \frac{\Delta R}{R}$$

3.1.2 Discussion and Assessment of Normalisation Errors

Earlier in this chapter it was shown how the analysis of lidar data involves the assumption of the existence of an aerosol-free region somewhere in the range of the lidar profile. This "clean-air" or "molecular layer" normalisation technique is made necessary by the difficulty and unreliability of calibrating lidars absolutely. Not only is the system constant K in equation 3.1 difficult to measure, if only for the reason that many lidars cannot measure the energy of the actual lidar pulse used for producing a scattering profile, but the atmospheric transmittance from ground level to the minimum lidar height can, and does, vary appreciably from night to night. This quantity, which is usually absorbed into the system constant, can even vary during the three or so hours required to measure a lidar profile on a single night.

There have been two main height regions in the atmosphere where lidar profiles have been normalised; these are around 10 km and above about 30 km. Both are usually regions of low relative lidar scattering and have been shown to be regions of low aerosol content by balloon and aircraft direct sampling techniques (Rosen (1968, 1971), Lazrus and

Gandrud (1974), Northam *et al* (1974)). The Adelaide lidar group chose the lower region for two reasons. Firstly, the relative error in the lidar signal is only about one percent at 10 km whereas at 30 km it increases to five or six percent for a reasonable number of laser firings, and secondly, the radiosonde balloon flights do not reach 30 km on every ascent. This would require the normalisation of the lidar profile to a model atmosphere and thereby introduce more possible errors.

Errors will arise, however, when there is no clean region in the range of the lidar profile. Normalisation will then occur at a height containing aerosols and the whole profile of derived aerosol values will be underestimated. Without comparison with other profiles taken at a similar time, but containing a clear layer, there is no way the error can be estimated from the lidar data alone.

Russell *et al* (1974b, 1976) have made a detailed estimation of the occurrence and magnitude of likely calibration errors by converting Rosen's 22 month series of dust concentration profiles (in number per cm^3) to profiles of mixing ratio (in number per mg). In this form they are directly comparable to lidar profiles of scattering ratio if one assumes the conversion factor is constant with height. This factor, the ratio of aerosol backscattering to aerosol number has been shown to be independent of height by lidar/balloon comparative experiments (Northam *et al* (1974)). By using the balloon data, Russell *et al* were able to show that most errors in the lidar-derived scattering ratios for the non-volcanic period studied should be less than ten percent of the peak value of R-1, with slightly higher values in early Spring.

The analysis also showed that most minimum ratios occurred between the altitudes of 5 km and 10 km with only a few above the peak,

near 30 km, mainly in Spring. This means that unless the lidar observations extended below 10 km, or even 5 km, the minimum value of mixing ratio would not have fallen in the range of the profile and aerosol values would have been underestimated.

By raising the lower extent of the lidar observations progressively the value of the minimum ratio in the range increases and the derived aerosol scattering profile is underestimated increasingly. A lower limit of 10 km would have produced errors which were mostly less than about ten percent of $R_{max}-1$, and only occasionally as large as about twenty percent in Spring. If the lidar had been normalised at or above 15 km then errors sometimes exceeding thirty percent would have been introduced.

Although these results only apply to the location investigated (Laramie, Wyoming, 42° N), Rosen *et al* (1975) concluded from their world-wide monitoring program that there was no major difference between the Northern and Southern Hemispheric stratospheric aerosol layers. Indeed, a cross section of the aerosol mixing ratio in the Southern Hemisphere showed similar low values at or around the tropopause, in particular around ten kilometres at 35° S, the latitude of the present observations. In addition, as most of the stratospheric lidar observations reported in this thesis were made during the non-volcanic period considered by Rosen, similar arguments should apply to normalisation errors in the present data. Accordingly, as the minimum height in the lidar profile is 9 km, errors in derived values of scattering ratios are probably less than or of the order of ten percent of $R_{max}- 1$, with slightly higher values possibly occurring in Springtime.

CHAPTER FOUR

RESULTS OF STRATOSPHERIC LIDAR MEASUREMENTS

4.1 General Comments

Observations of the stratospheric aerosol layer began in Adelaide in March 1969, and results of these observations up until May 1970 have appeared in the literature (Bartusek *et al*, 1970; Gambling *et al*, 1971). The observations in the present study extended over the period April 1972 to April 1976. An attempt was made to make regular stratospheric observations from October 1972 onwards but breakdowns frustrated this attempt and stopped observations during December 1973. No further results were obtained until June 12, 1975, and after this date further maintenance and problems with the system led to the termination of stratospheric measurements in April 1976. Table 4.1 lists the total number of observations for each month and shows the distribution of the data with respect to the 1969 to 1971 period and the 1972 to 1976 period.

The two observational periods were significantly different in that the early period, particularly 1969 to 1970, was influenced by increased scattering by dust from the Fernandina volcanic eruption in 1968 whereas the later period was noticeably less perturbed. The earlier results are included in this work as they allow useful comparisons with the data for the quieter, later period and when combined with the later data help illustrate the rate of transition from disturbed to undisturbed conditions.

Monthly mean profiles of the aerosol backscatter function are plotted for the 1972 to 1976 period in Figures 4.1(a) and 4.1(b) with the profile for July 1969, the period of maximum scattering included for

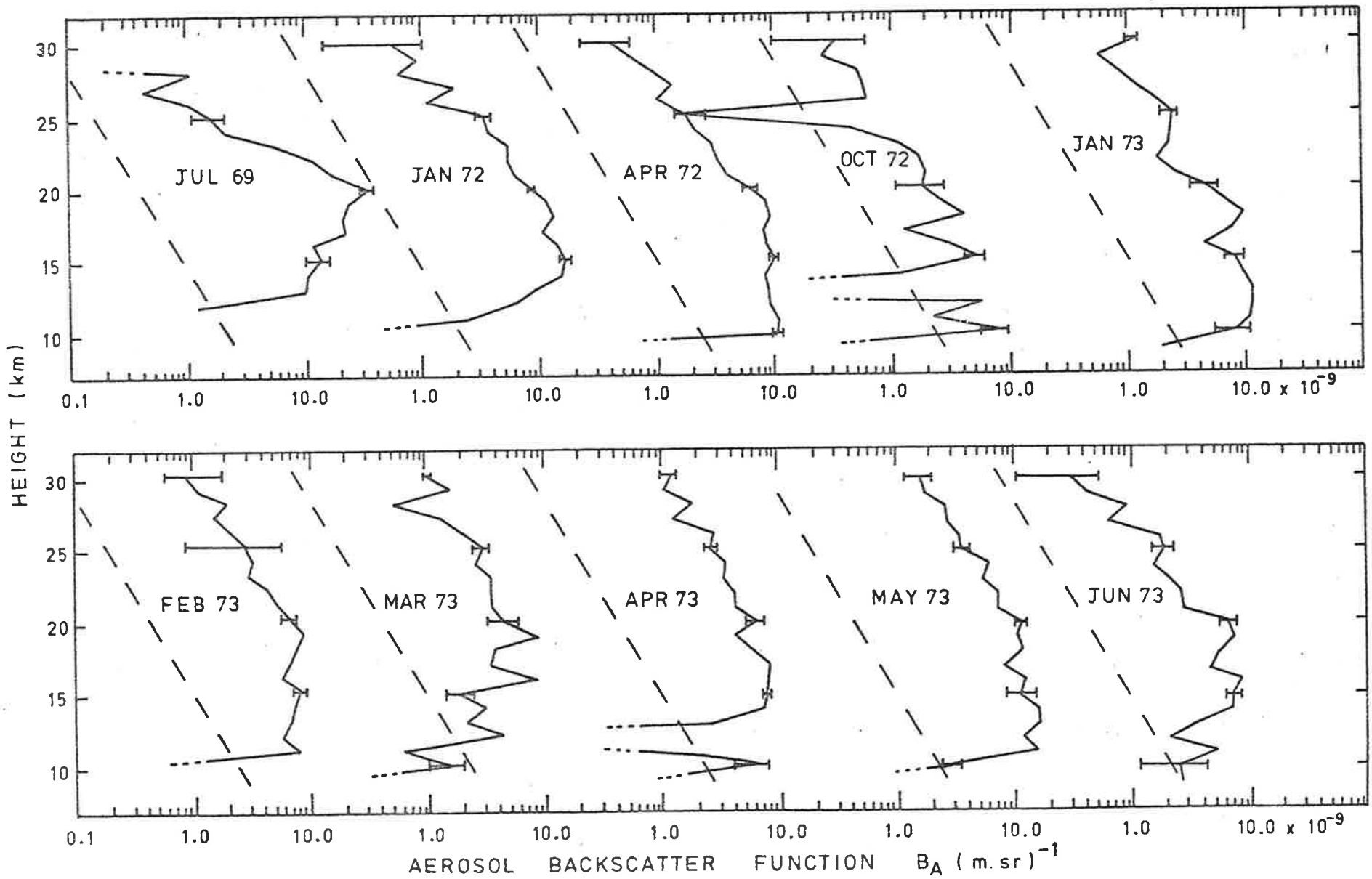

FIG 4.1(a) Monthly mean profiles of Aerosol Backscatter Function. Dashed line represents 1% of Molecular Backscatter Function.

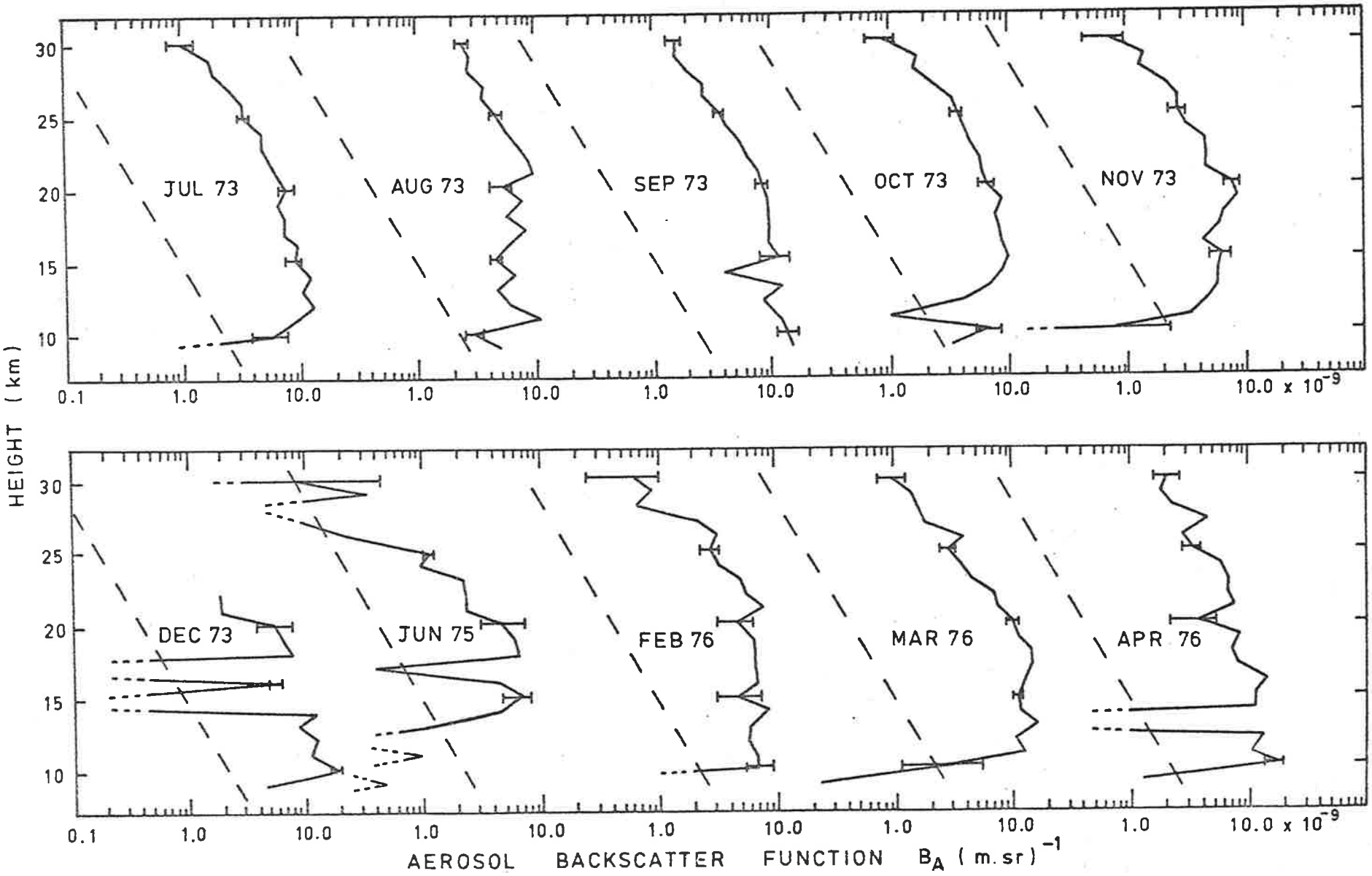

FIG 4.1(b) Monthly mean profiles of Aerosol Backscatter Function.

comparison. These profiles are compared with the scattering expected from clear air which is indicated by a dashed line representing one per cent of the molecular backscatter function (0.01 x $B_M(h)$). The error bars, plotted every 5 km represent one standard deviation in the mean value plotted and are calculated as explained in Chapter 3. Because the actual number of laser firings and the laser energy often varied considerably from night to night and resulted in greatly different uncertainties in the calculated profiles of backscatter function, the mean profiles for any one month are produced by calculating a weighted average of the nightly values for a particular height.

TABLE 4.1 Distribution of Lidar Observations

Month	Number of Observations		
	1969-1971	1972-1976	Total
January	7	3	10
February	6	3	9
March	7	4	11
April	14	6	20
May	14	1	15
June	12	3	15
July	5	2	7
August	8	4	12
September	3	3	6
October	1	5	6
November	5	3	8
December	4	1	5

It should be emphasised here that as lidar observations of the stratosphere can only be made on cloudless nights, the mean of the results obtained during any month may not represent truly the average value for the whole month. This is because cloudiness is related to the

prevalent synoptic situation and there is some evidence that the amount of dust in the stratosphere is also affected. The monthly mean profiles and the seasonal variations derived from them later in this chapter should be considered with these facts in mind.

A comparison of the monthly mean profiles plotted reveals some interesting changes that have occurred during the period of observation. The general shape of the profile has changed from 1969, when there was a strong peak near 19 km with a rapid increase in scattering above and below this height. The later profiles indicate reduced scattering at the layer peak which has moved to lower altitudes, accompanied by a scattering increase above about 20 km. In several cases the mixing ratio above 20 km is almost constant with height. This increase in scattering above the layer peak is most noticeable as enhanced scattering at 30 km first observed during February 1970, (Gambling *et al*, 1971). The single profile for December 1973 was terminated at 22 km by the development of faults in the laser cavity.

Figure 4.2 shows the change in the mean profile of the aerosol backscatter function for the years 1969 to 1976. Again error bars represent one standard deviation in the mean value. The relative size of the error bars is a reflection of the number of profiles used in calculating the yearly means. In the case of the 1975 profile only one observation was made and the error bars are typical of a single profile.

The general decline in the strength of the scattering mentioned earlier is shown clearly here. Although each profile used in the calculation was normalised to a height where the aerosol contribution was assumed to be zero, the average profiles often show no region of zero aerosol scattering. This is to be expected.

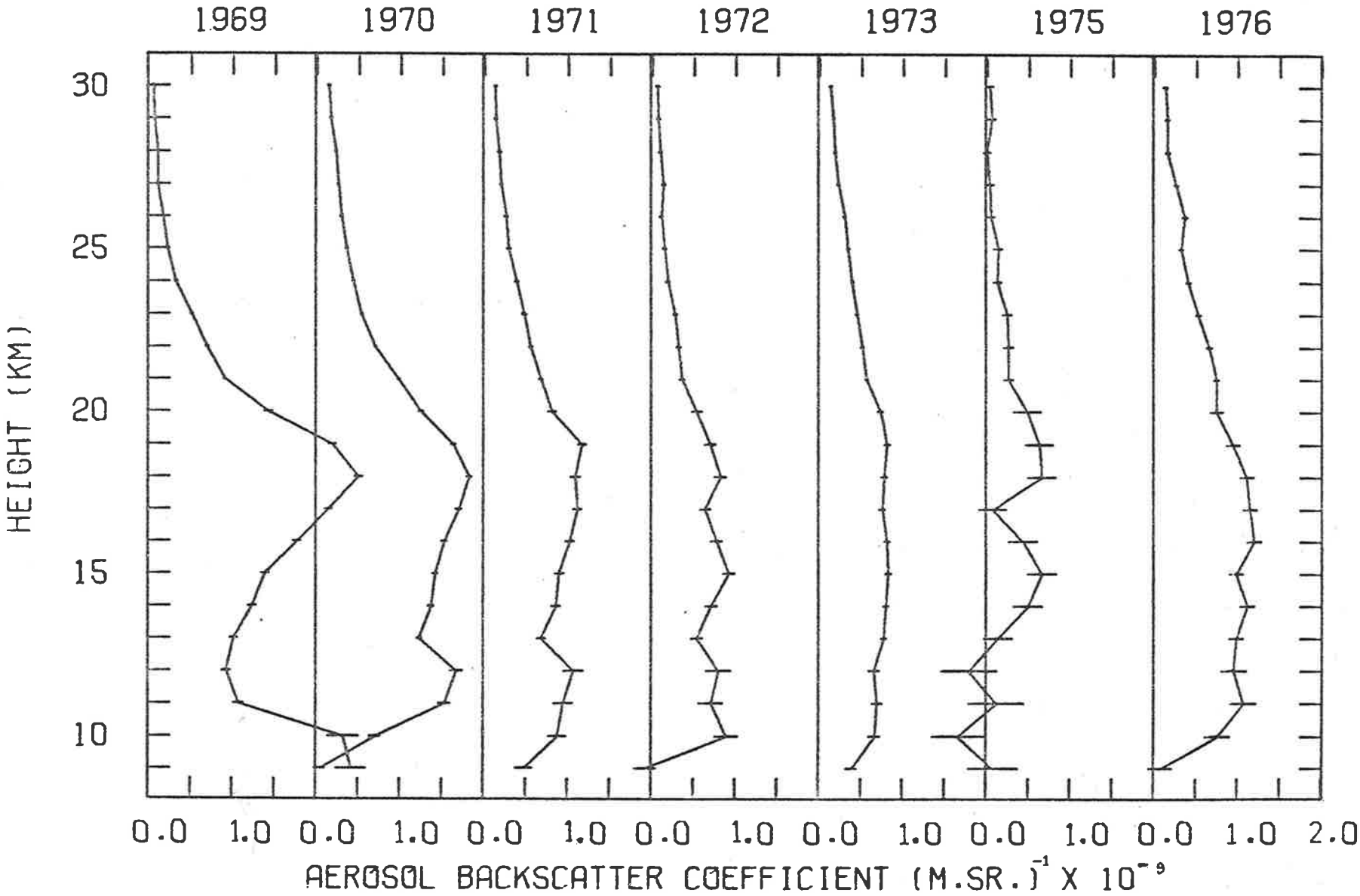

FIG 4.2 Yearly mean profiles of Aerosol Backscatter Function.

During 1970 and 1971 a second scattering maximum occurred at a height of 12 km and a minimum at 13 km. These may possibly be associated with the effect of multiple tropopauses over Adelaide. Tropopause heights at Adelaide can be as low as about 8 km when the polar tropopause is present, and as high as 16 km or more when the tropical tropopause is present. It has been noticed that a scattering minimum is usually associated with a tropopause at a nearby height, so that multiple tropopauses can be expected to influence the shape of the aerosol backscatter profile. This multi-layered appearance is not uncommon, as can be seen in the monthly mean data for 1972 to 1976 in Figure 4.1, but the variations in height of the layers often smooths the features out when the mean profiles are calculated.

To illustrate how the aerosol backscatter function has behaved with height and time a 2-D diagram of the monthly mean values of the aerosol backscatter function is presented in Figure 4.3. The data are presented as a ten-level intensity plot of values of $10 \log_{10}(\overline{B}_A(h)/B_A(\text{ref}))$. Here $B_A(\text{ref})$ is $4.0 \times 10^{-10}\,(\text{m.sr})^{-1}$ so the maximum level, as indicated by the scale at the right of the figure, is 20 dB greater than this, that is $4.0 \times 10^{-8}\,(\text{m.sr})^{-1}$. The time scale has been altered after December 1973 so the next month plotted is June 1975 followed by February to April 1976.

The distinctive features of Figure 4.3 are the maximum in scattering in the region 18 km to 20 km during the mid to later part of 1969, and the general decline in scattering at the height of the layer peak. During 1969 and 1970 there is the occasional occurrence of strong scattering in the region 9 km to 15 km, and after 1971 this is often the height of the maximum value of the aerosol backscatter function.

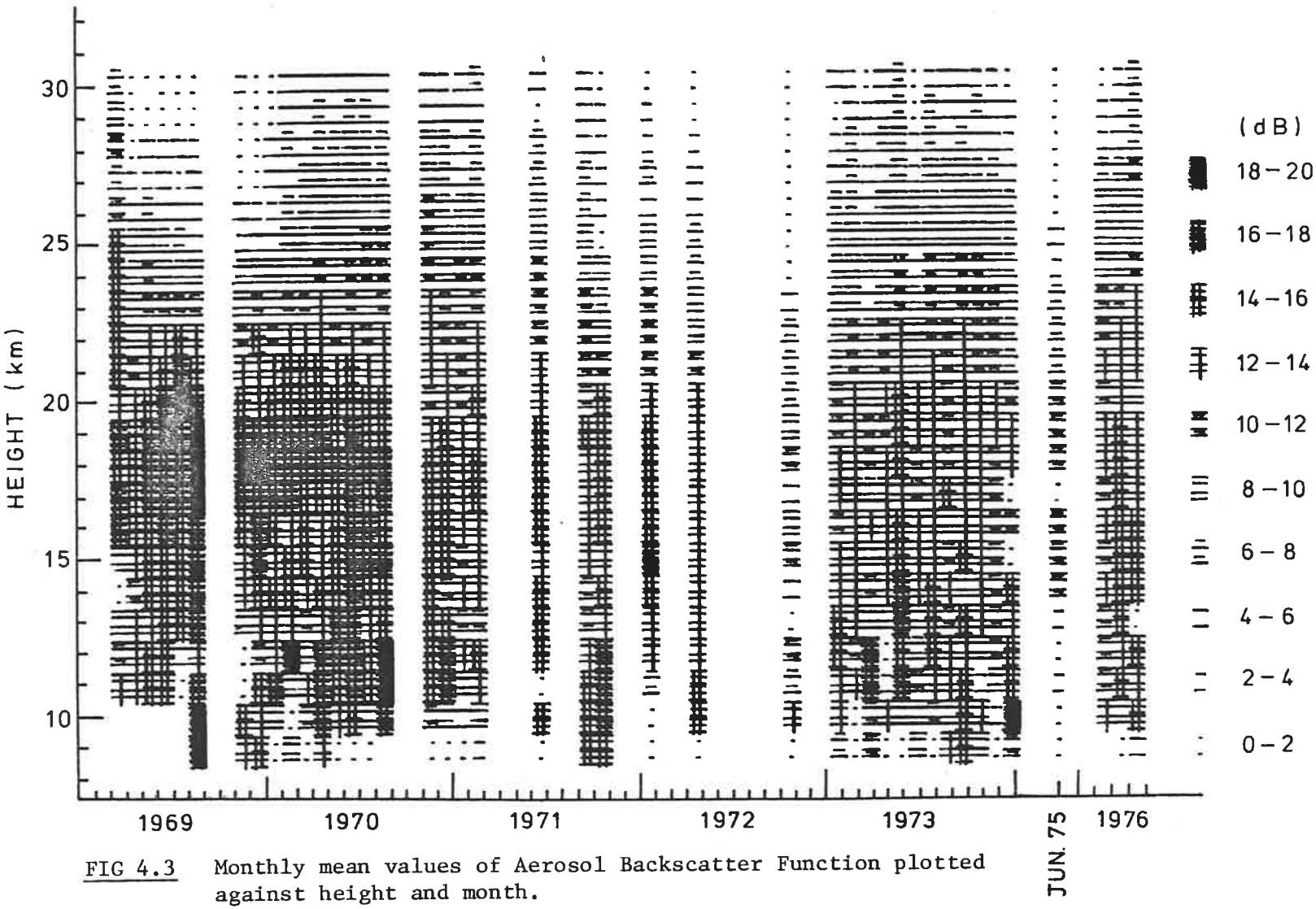

FIG 4.3 Monthly mean values of Aerosol Backscatter Function plotted against height and month.

An annual variation in scattering above 25 km can be seen by studying, for example, the height of the 6dB level which seems to be greater in winter and less in summer. The upward progression of the maxima below about 16 km, especially in the 1969 to 1970 period, does not necessarily imply that the material or a layer has been moved upwards as it could be that the height of the source of the aerosols is changing during this time.

4.2 Discussion and Comparison with other work

The Adelaide work has already been compared with the results of other observations of stratospheric dust during the period 1969 to 1973 by Russell *et al*, 1977. Their comparison is shown in Figure 4.4. The decline in scattering ratio observed at Adelaide compares favourably with the other results.

The maximum scattering ratio recorded at 20 km at Adelaide in July 1969 coincides with the maximum Southern Hemisphere sulphate concentration measured at 19.2 km by Castleman *et al*, (1974). According to these workers the maximum in particle concentration is reached some time after the penetration of volcanic gases into the stratosphere. The maximum in scattering and sulphate concentration occurred 13 months after the eruption of the Fernandina volcano (0.5°S, 92°W) in June 1968. This delay, according to Castleman *et al*, is due in part to the time required for the volcanic gases to convert to particles.

To emphasise any seasonal variations in the Adelaide lidar data, the mean annual variation was calculated for four heights, namely, 15 km, 20 km, 25 km and 30 km and is presented in Figure 4.5(a). Because the aerosol layer was in a perturbed state during 1969 and 1970 the data have been separated into two groups and the average yearly variations replotted.

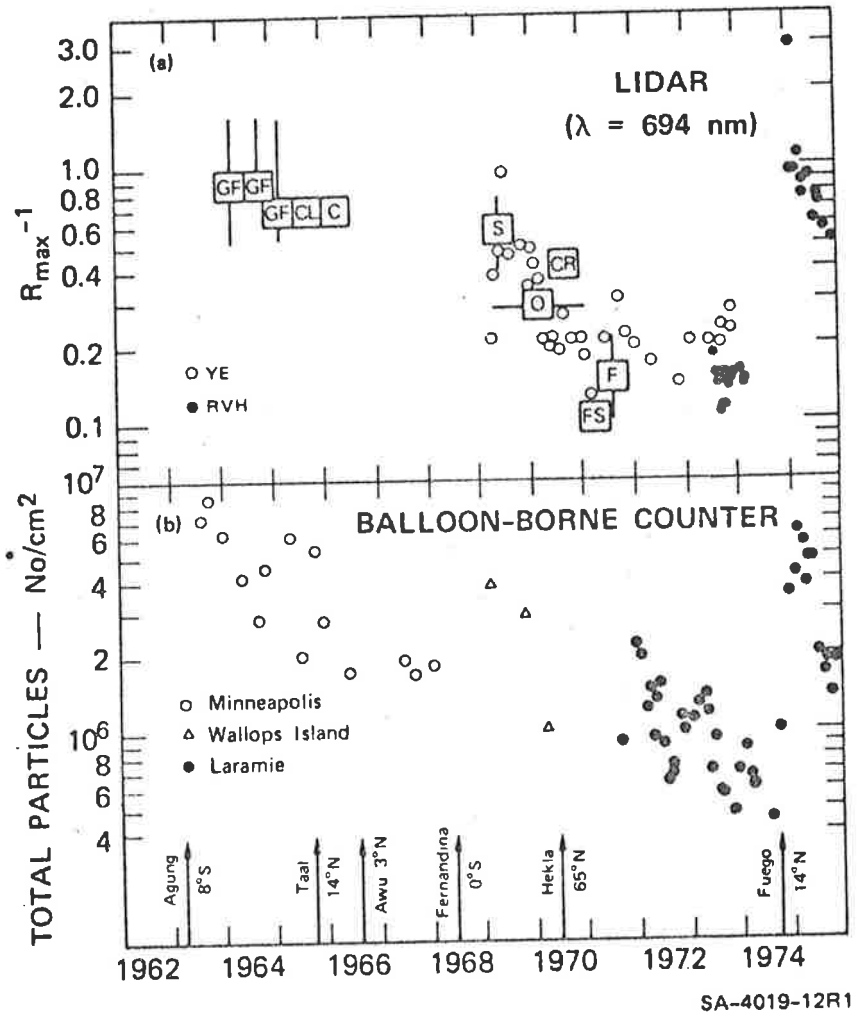

FIGURE 4.4 COMPARISON OF LIDAR AND BALLOON-BORNE PARTICLE COUNTER MEASUREMENTS OF THE STRATOSPHERIC AEROSOL, 1963-1975

a. Maximum ratio of particulate to gaseous backscattering measured by a number of stratospheric lidar groups. Boxes indicate mean of many observations; bars indicate range in time and magnitude. GF: Grams and Fiocco (1967), Massachusetts; CL: Collis and Ligda (1966), California; C: Clemesha et al. (1966), Jamaica; S: Schuster (1970), Colorado; CR: Clemesha and Rodrigues (1971), Brazil; O: Ottway (1972), Jamaica; FS: Frush and Schuster (unpublished), Colorado; F: Fox et al. (1973), Hawaii and Bermuda; YE: Young and Elford (1975), Australia; RVH: Present work and Russell et al. (1974, 1975b), California.
b. Number of particles (radius $\gtrsim$ 0.15 μm) above tropopause as measured by photoelectric particle counter (Hofmann et al.; 1972-74; 1973 , 1974, 1975, 1976). Arrows give times of volcanic erruptions with appreciable stratospheric penetration.

Figure 4.5(b) represents the conditions during 1969 and 1970 and Figure 4.5(c) the period after 1970. Work on the lidar prevented observations during September and October in both 1969 and 1970.

These results may be compared with those obtained by Bigg (1976) who studied the variation in particle concentration using an impactor carried by balloons launched from Mildura during the period 1969 to 1975. Over the height interval 10 km to 16 km the concentration of particles having diameters greater than 0.14 μm shows a definite minimum in April and reaches a maximum in August. This annual variation can be seen clearly in the 1969 to 1970 lidar data for 15 km altitude, but does not occur in the later data.

There are two possible reasons for the apparent lack of an annual variation in the data for the later years. Firstly the number of observations in any month is generally less than in the first two years, as can be seen in the relative sizes of the error bars in Figures 4.5(b) and 4.5(c), and the observations are more likely to be affected by day to day variation in scattering. Secondly, the values of the aerosol backscatter function are much lower than for the early period and any error in normalisation will have a relatively greater effect.

The variations at the greater heights seem less organised and this agrees generally with Bigg's observations for the particle size in question. However, the low values in December and January which emphasise the variation above the main layer seen in Figure 4.3 are not apparent in the particle counter data.

The vertical distribution of dust observed at different locations is also interesting. Figure 4.6 compares the average profile of scattering ratio for 1973 at Adelaide (35° S, 138° E) with a similar profile

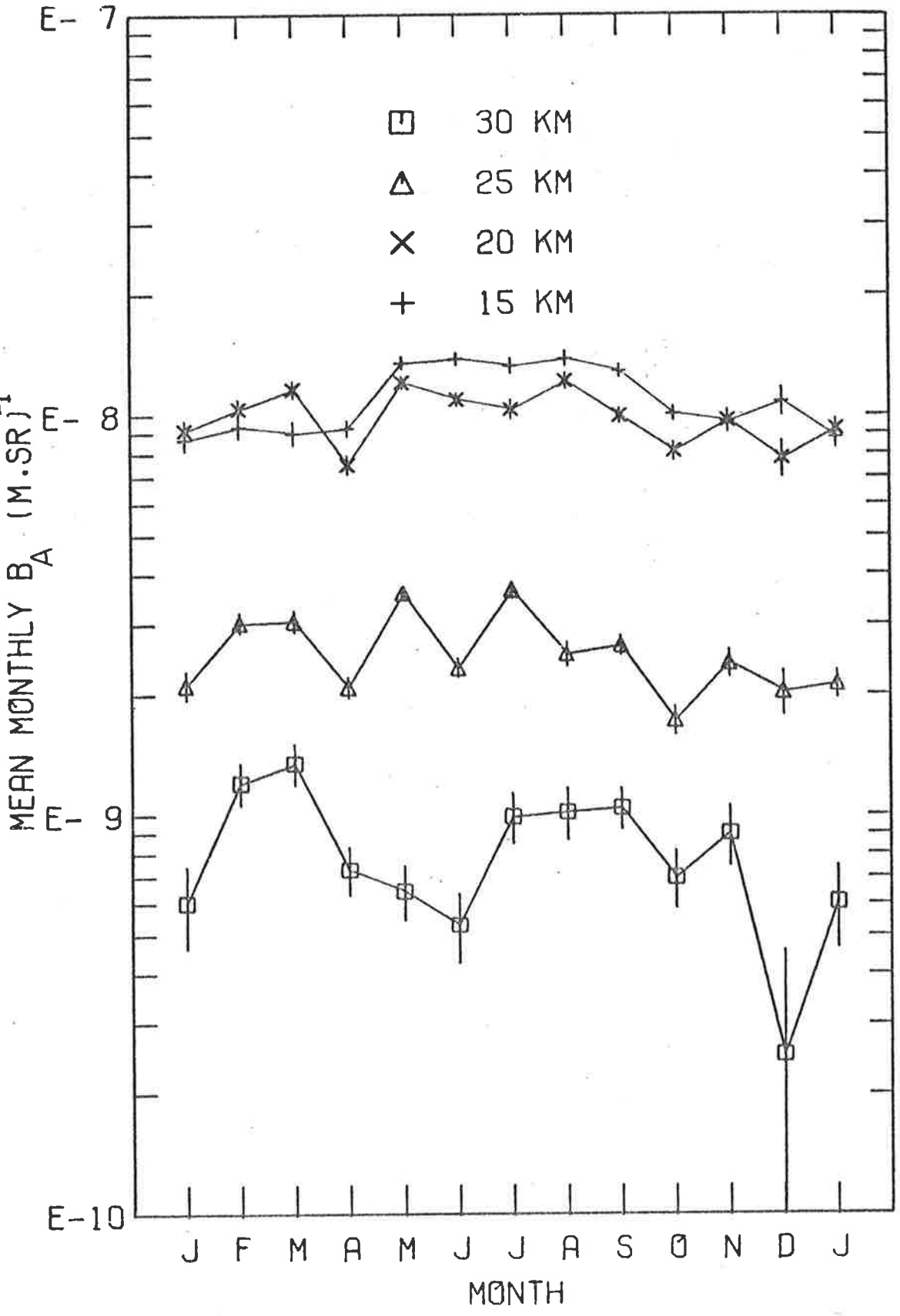

FIG 4.5(a) Mean monthly values of B_A for 1969 to 1976.

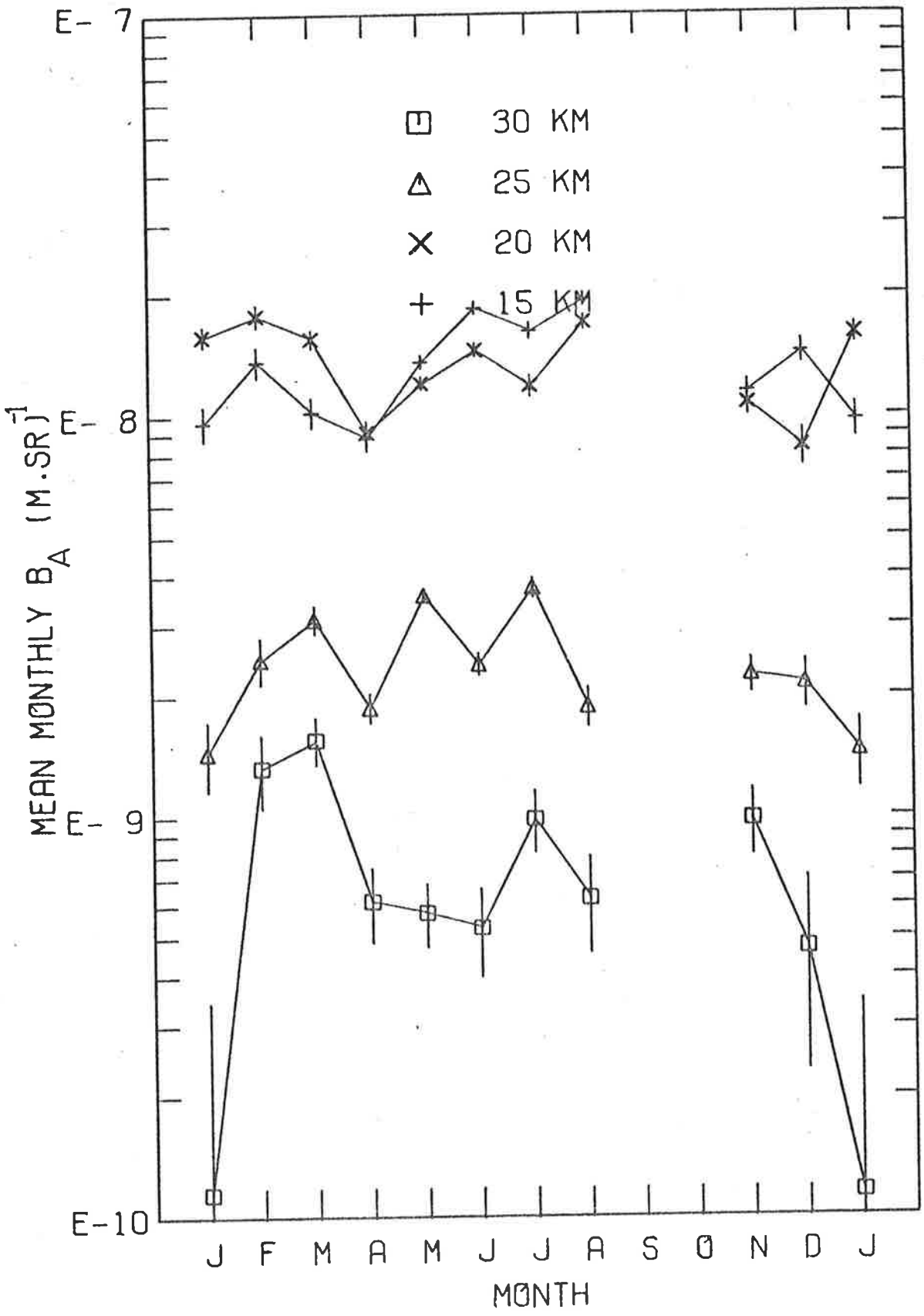

FIG 4.5(b) Mean monthly values of B_A for 1969 and 1970.

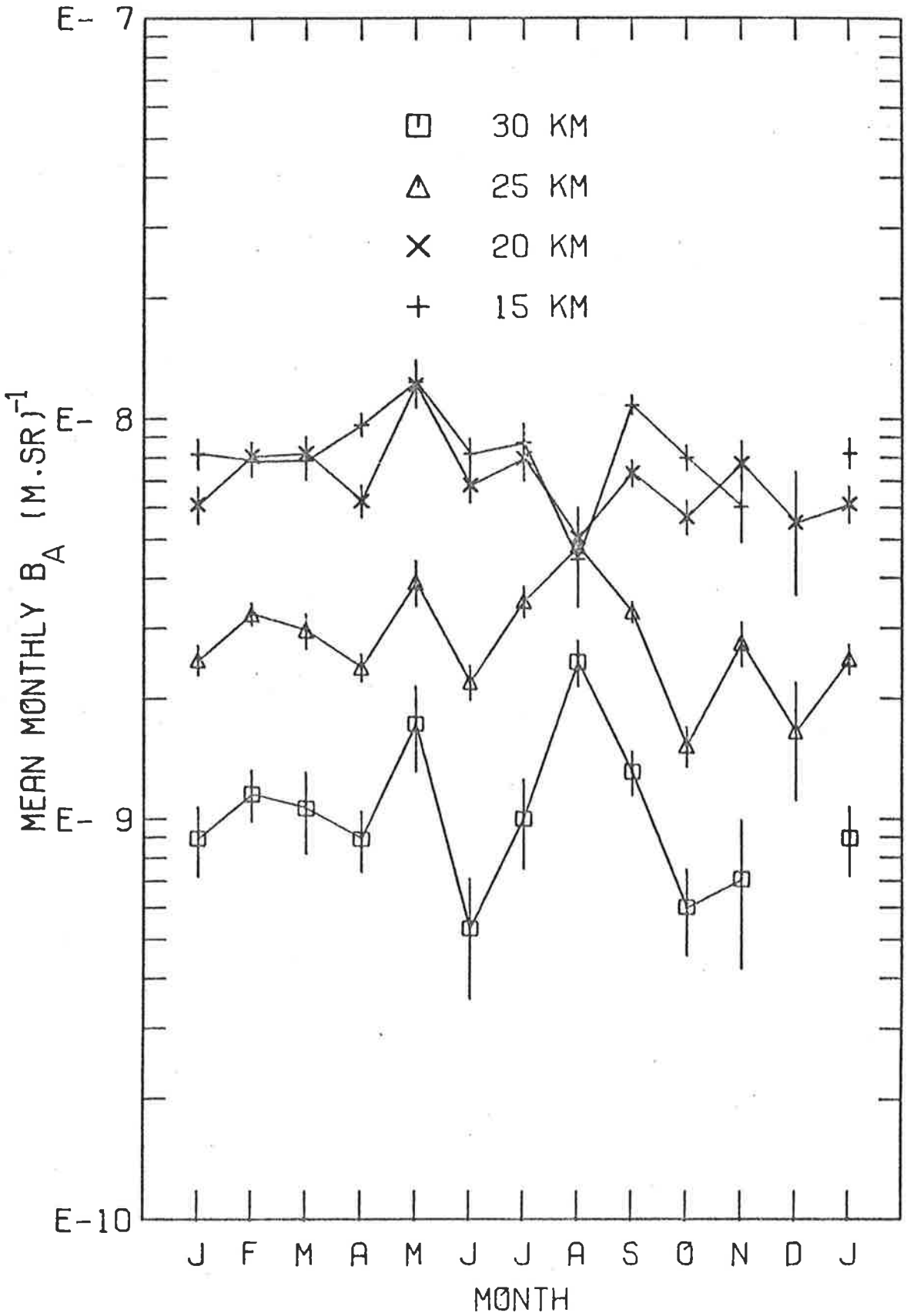

FIG 4.5(c) Mean monthly values of B_A for 1971 to 1976.

averaged over the period mid-1973 to early 1974 at Menlo Park (37.5° N) in California, (Russell *et al*, 1976). The profiles are similar in both shape and magnitude and both show the presence of significant aerosol scattering at 30 km. These profiles of scattering ratio may be converted directly to turbidity profiles. The turbidity is defined as

$$t(h) = \beta_A(h)/\beta_M(h) = [B_A(\pi,h)/P_A(\pi)]/[B_M(\pi,h)/P_M(\pi)]$$

$$= [R(h) - 1]\, P_M(\pi)/P_A(\pi) \qquad (4.1)$$

where the symbols have the same meanings as in Chapter 3.

To compare with the 550 nm searchlight measurements of turbidity by Elterman *et al*, (1973, 1976) the aerosol scattering was assumed to be proportional to λ^{-1} (Pinnick *et al*, 1976). Equation 4.1 shows that the value of turbidity is inversely proportional to the assumed value of $P_A(\pi)$. As discussed in Chapter 3, Russell *et al* use a different value for this quantity to that used in the present study. Accordingly a separate scale is used for converting their scattering ratio profile to one of turbidity.

The searchlight turbidity profiles of 1970 and 1973 to 1974 are described as representing normal stratospheric conditions with little influence of volcanic material. Differences in latitude could explain some of the difference in magnitude and height of the lidar and searchlight profiles.

In Figure 4.7 the average lidar profile of aerosol backscatter function for early 1976 is compared with the average of several profiles of particle concentration made during 1975 to mid-1976, 340 km north-east of Adelaide at Mildura (34.2° S, 142.1° E). Gras and Laby (1978) obtained the profile using an *in situ* optical particle counter similar to that described by Hofmann *et al*, (1975). Considering that the two profiles were

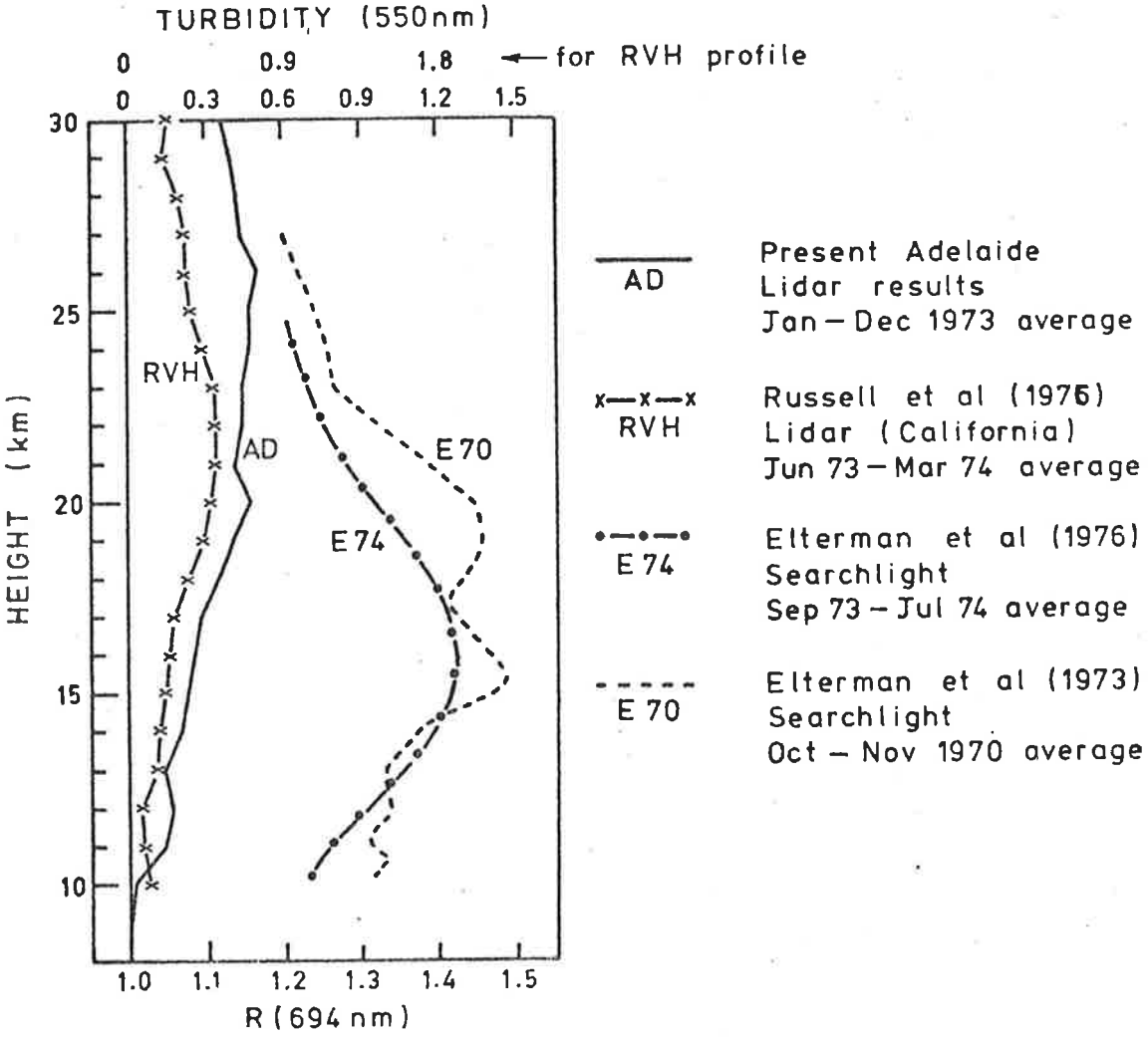

FIG 4.6 Comparison of Turbidity and Scattering Ratios.

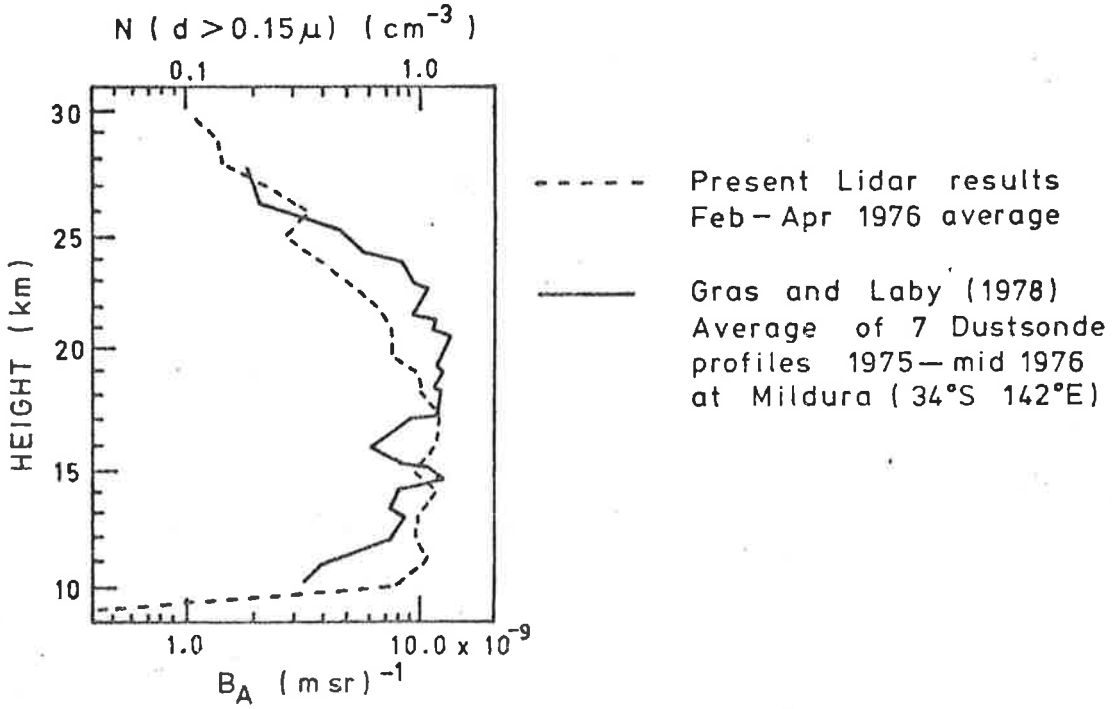

FIG 4.7 Comparison of lidar and balloon-borne optical particle counter profiles.

measured at different times and locations and that the lidar has a broader height resolution, reasonable agreement exists.

Using the results of a simultaneous, comparative lidar-dustsonde experiment in 1972, Northam *et al*, (1974) calculated an effective aerosol scattering cross-section as the ratio of the aerosol backscattering function to the particle number density. When the two 1976 profiles are matched, as in Figure 4.7, the value of this cross section is $10^{-14}\ m^2\ sr^{-1}$ for particles with diameters greater than 0.15 μm. This value is considerably higher than the 1972 value for similarly sized particles. This is possibly because of the difference in latitude and time. Alternatively, intervening volcanic eruptions between 1972 and 1976 may have led to a real change in the effective scattering cross-section by causing changes to the particle size distribution, shape, or refractive index.

4.3 Comparison with Meteorological Measurements

Because the amount of dust at any given latitude is affected to a large extent by transport processes, a possible correlation may exist between the aerosol backscatter function measured by lidar and the direction and strength of the winds at the heights concerned. For this reason the monthly mean aerosol backscatter functions for 15 km and 20 km are plotted on the same time axis as the monthly mean zonal and meridional winds at 100 mb and 50 mb. These data are plotted in Figure 4.8(a) for the period 1969 to 1971 and in Figure 4.8(b) for 1973. It must be emphasised here that the lidar data are averages of only a few clear nights in the month whereas the wind data are the averages of every night radiosonde flight from Adelaide airport during the month (Australian Bureau of Meteorology (a) and (b), 1969-1976).

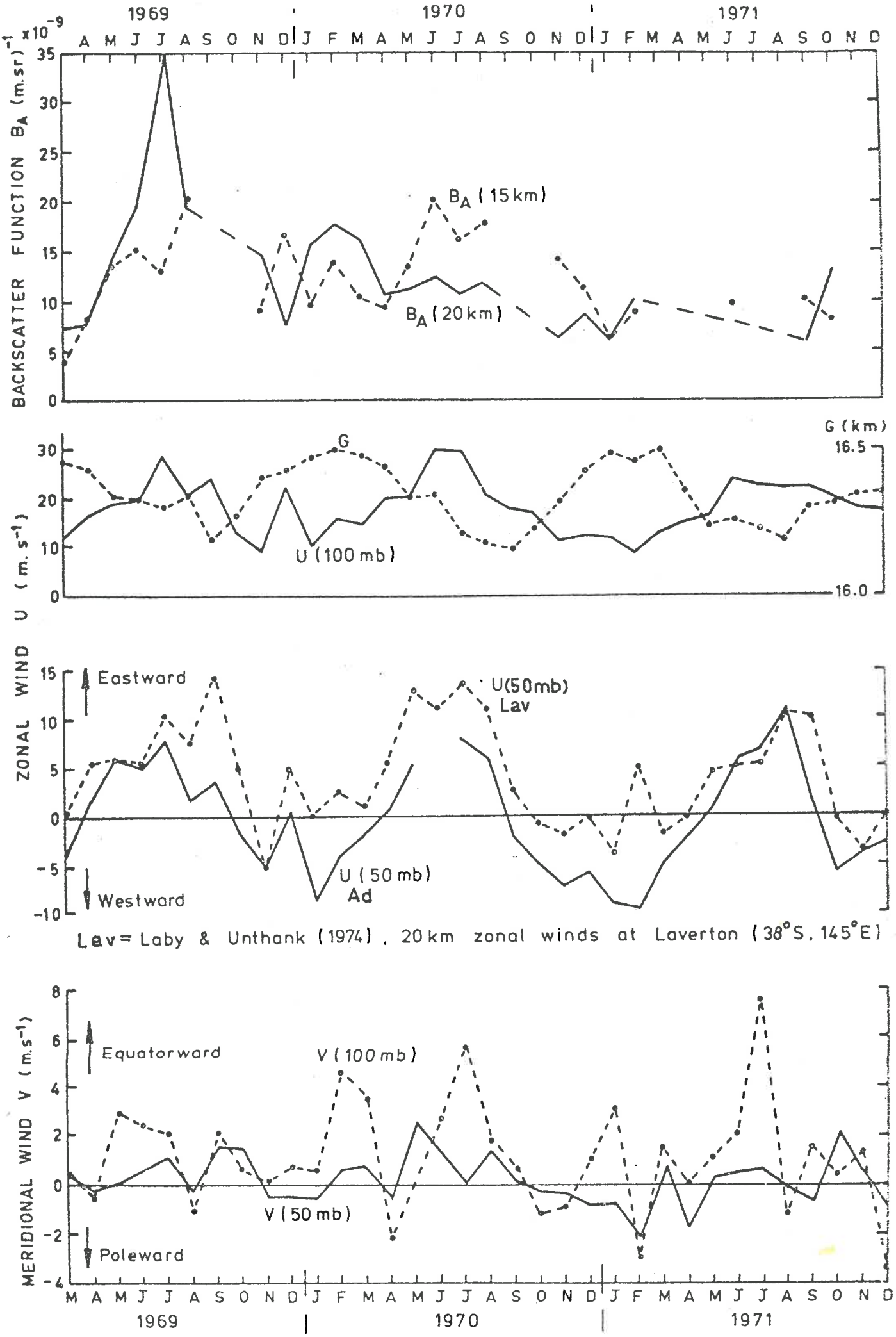

FIG 4.8(a) A comparison of monthly mean values of B_A and meteorological parameters during 1969-1971.

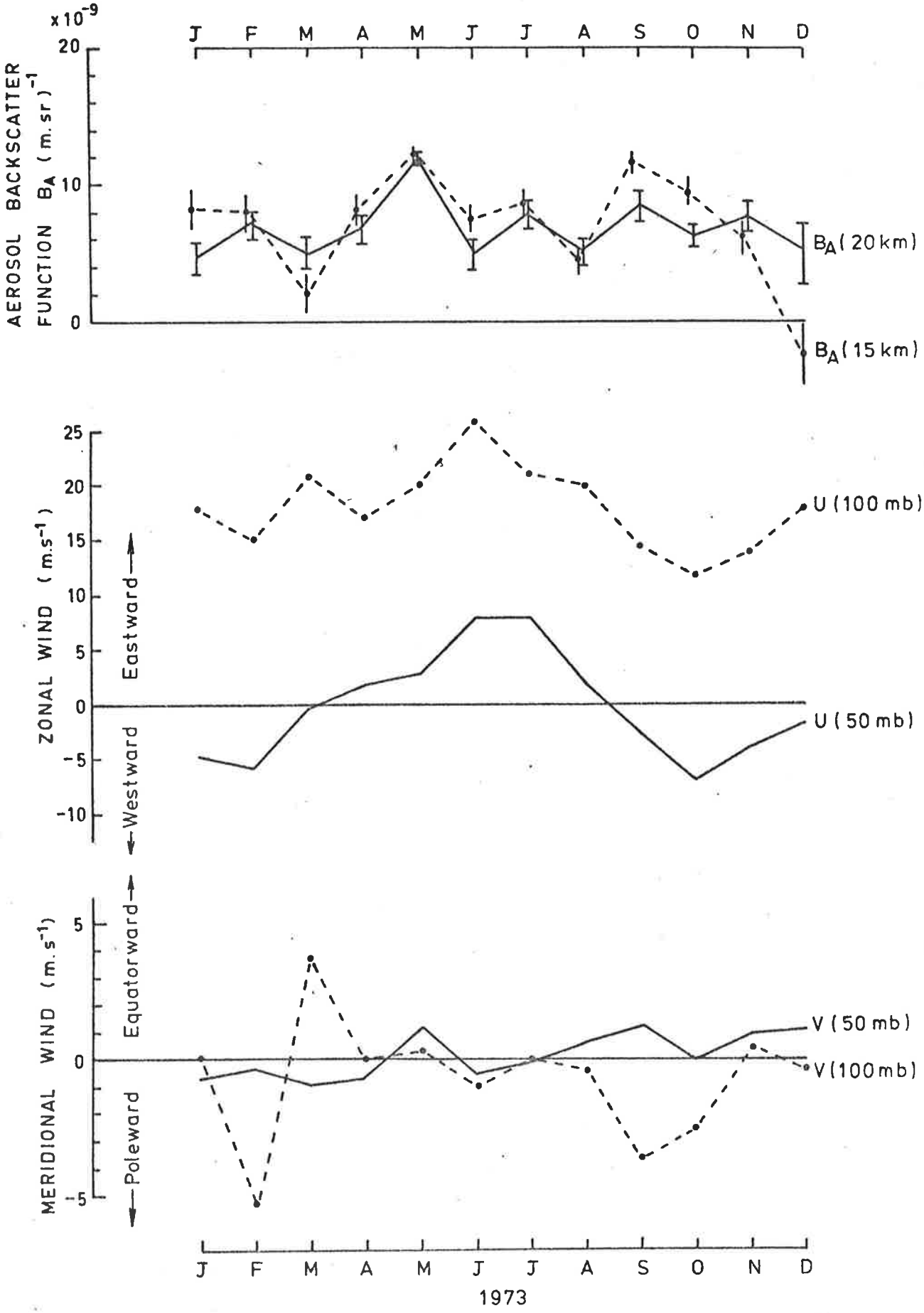

FIG 4.8(b) A comparison of monthly mean values of B_A and meteorological parameters during 1973.

A study of the figures reveals that during the period 1969 to 1971 when aerosol scattering was high, strong eastward winds at 100 mb are associated with larger values of the aerosol backscatter function at 15 km, and vice versa. Such a correlation is not evident in the zonal wind data of 1973 (Figure 4.8(b)). The meridional winds show no correlation with aerosol scattering in either period, although in 1973 (Figure 4.8(b)) there is some evidence that strong equatorward winds are associated with low aerosol values. During the earlier period, when the 50 mb winds blow polewards and westwards simultaneously (e.g. late 1969 and 1970), the aerosol values at 20 km usually tend to be low or decreasing.

The wind is not the only parameter that affects stratospheric aerosol concentrations. For example, during 1969 to 1971 (Figure 4.8(a)) the aerosol values at 15 km seem to be strongly anti-correlated with the average 100 mb geopotential height G , calculated from only those measurements taken on the nights of the lidar observations. Low 100 mb heights during late winter and early spring are associated with higher aerosol scattering values and vice versa.

Other factors which possibly may affect the aerosol layer are the height and pressure of the tropopause and the minimum stratospheric temperature. These are now investigated further. In Figure 4.9 are plotted the variation in nightly values of the aerosol backscatter coefficient integrated over the height range 10 km to 30 km (hereafter referred to as B1), and 10 km to 15 km (B2), the geopotential height of the 250 mb surface, the height and pressure of the lowest tropopause, and the minimum stratospheric temperature during March 1969 to February 1971. Note that the graph of minimum temperature is inverted so that variations are in the same sense as those in the geopotential and tropopause heights. If the general increase in scattering during early to mid-1969 is taken

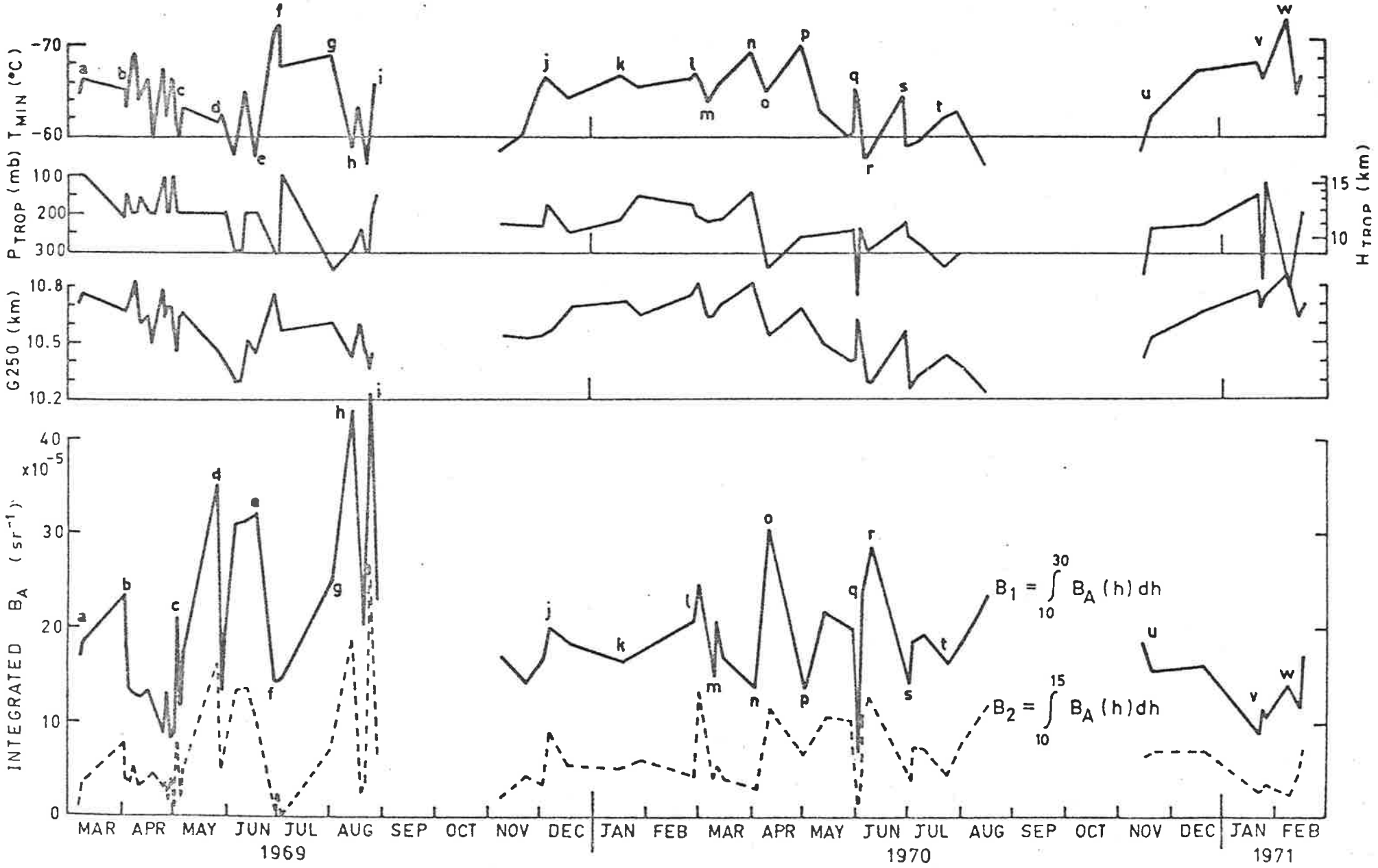

FIG 4.9 A comparison of nightly lidar results and meteorological measurements

into consideration, there is a suggestion of a positive correlation of B1 with both the minimum temperature and the tropopause pressure, and a negative correlation with the 250 mb geopotential height, especially if large scale changes are considered (e.g. the periods e to h, n to p q to s etc,). Note that because of the way the graphs are plotted, decreasing values of the top three graphs will appear correlated with increasing values in the lower (lidar) graphs. In 1969 the meteorological parameters are only plotted to the nearest 50 mb.

A large drop in minimum temperature in late June to early July 1969 (e to f) occurs simultaneously with a drop in B1 and B2 and a general increase in the geopotential height, whereas the subsequent rise in temperature (f to g) and an increase in the tropopause pressure coincides with an increase in B1 and B2. The changes in the four quantities seem to be simultaneous. This can often be seen where observations are made on consecutive nights, for example, the large and sharp drop in B1 and B2 values in late May 1970 (q) coincides with a sharp increase in tropopause pressure and a decrease in minimum temperature. This is an interesting case as although the agreement between variations in minimum temperature, geopotential height and B1 is as expected, the tropopause pressure behaves in the opposite sense with an increase in the pressure (decrease in the height) of the tropopause being associated with an increase in B1. A more likely result is shown in late August 1969 (h to i) and January 1971 (v).

The correlations between B1 and the tropopause pressure and minimum temperature are shown in more detail in Figures 4.10(a) to (f). A linear, least squares fit was applied to the data and the results are listed in Table 4.2, which contains the linear correlation coefficient R and the probability P(R,n) of obtaining the same value of R using n random data points. Good correlations are obtained for the years 1969

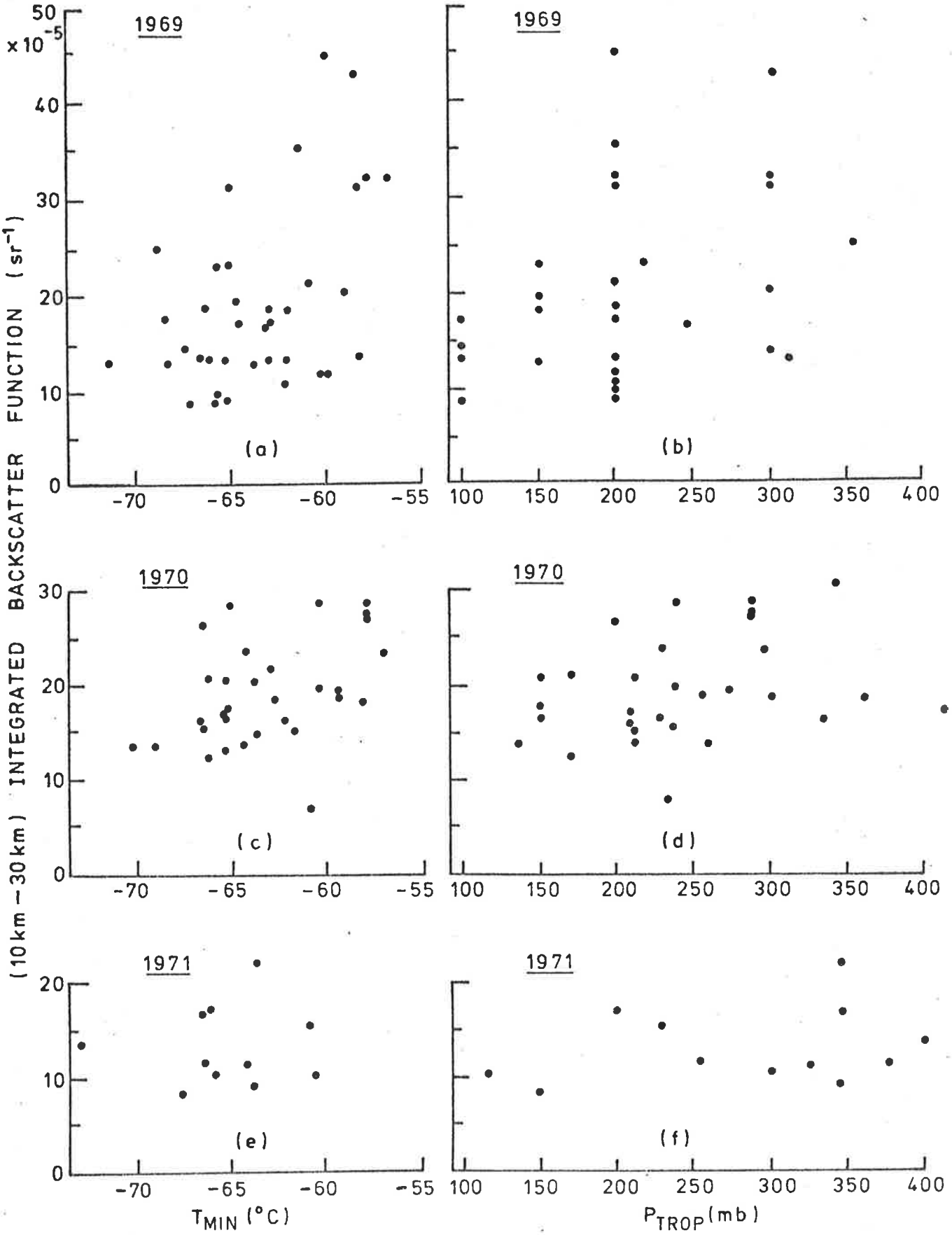

FIG 4.10 Correlations of Integrated Backscatter with T_{MIN} and P_{TROP}.

and 1970, especially for the minimum temperature where the results are significant at the 0.3 per cent and 2 per cent levels respectively. Data for 1972 which include only six data points are not plotted. The results for 1973 are shown in the lower part of Figure 4.11. Poor correlations are obtained between B1 and both the minimum temperature and tropopause pressure. As seen in Table 4.2 poor correlations are obtained in general in the later years where the actual value of B1 is much less and possible normalisation errors are relatively more significant.

These correlations should be compared with the observations by Hofmann *et al*, (1975) which show a correlation between tropopause height and total stratospheric aerosol. They proposed that low tropopauses provide a greater stratospheric volume for aerosol formation and transport. McCormick *et al*, (1978) also noticed a similar correlation in their lidar-derived integrated aerosol backscattering and the tropopause pressure.

TABLE 4.2(a) Least Squares Fit of B1 to T_{MIN}

Period	n	R	P(n,R)
1969	44	.426	.003
1970	31	.404	.02
1971	11	.020	-
1972	6	-.685	.15
1973-6	32	-.091	-
1969-76	124	.180	.07

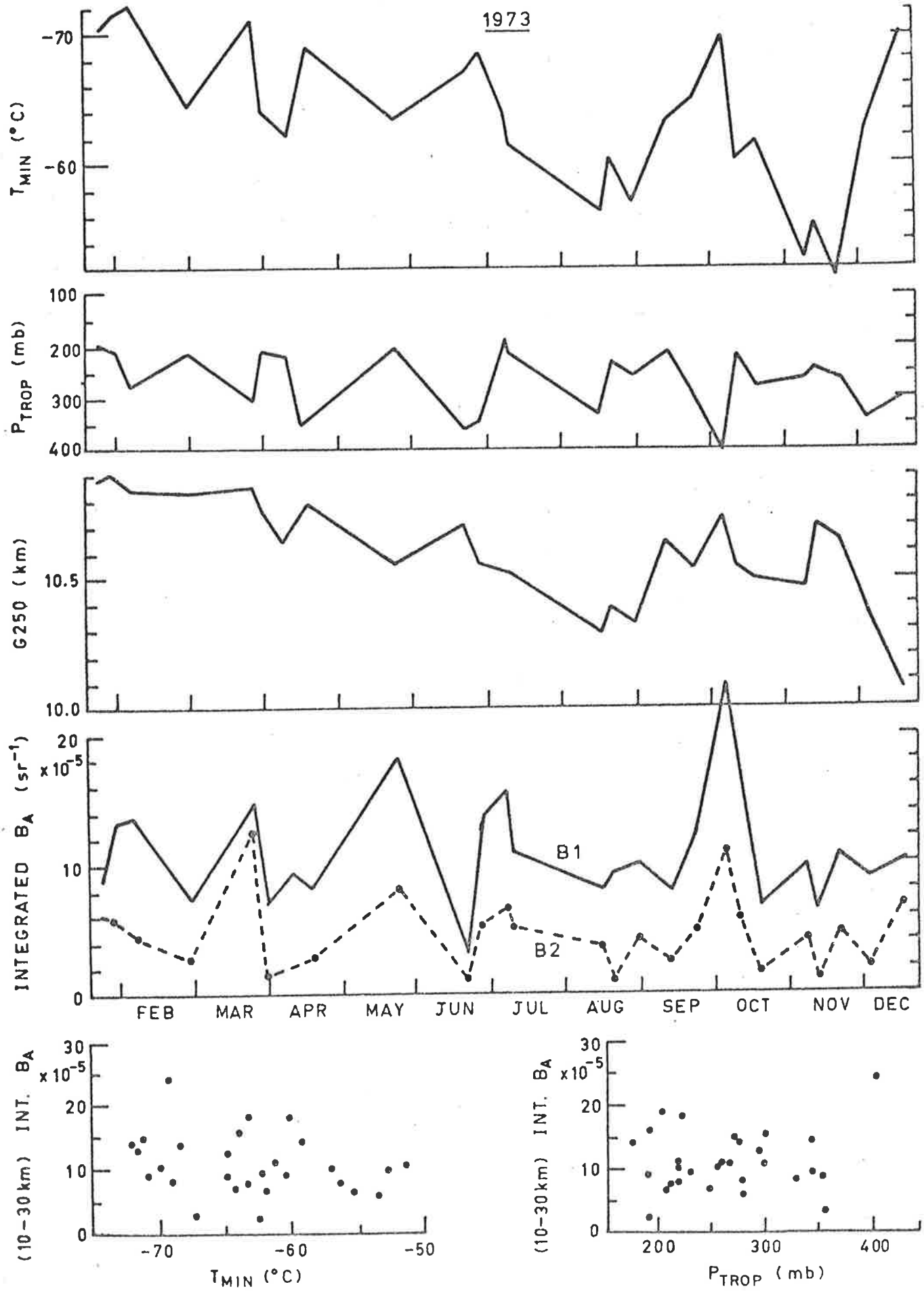

FIG 4.11 Comparison of lidar and meteorological data for 1973.

TABLE 4.2(b) Least Squares Fit of B1 to P_{TROP}

Period	n	R	P(n,R)
1969	44	.297	.06
1970	31	.220	.05
1971	11	.278	-
1972	6	.064	-
1973-6	32	.159	-
1969-76	124	.047	-

A positive correlation between the minimum stratospheric temperature and the integrated aerosol backscatter was also noticed by McCormick *et al*, (1978) in the lidar measurements following the eruption of Volcán de Feugo. They found that the minimum stratospheric temperature was at its highest when the integrated aerosol backscatter was at a local maximum, but emphasised that the higher temperatures were not necessarily due to the heating effects of volcanic aerosols but could be due to the advection of warmer, aerosol laden air. This latter possibility is also more likely than the possibility of warmer air temperatures increasing the rate of formation of aerosols, as this is a slow process.

The relationship between the geopotential height of the 250 mb pressure surface and the integrated aerosol backscatter function (B2) for the same night is shown in Figure 4.12, while Figure 4.13 shows a comparison of the geopotential height with the weighted mean aerosol backscatter function, where the averaging is taken over the height range 10 km to 16 km. Although poor correlations are seen in later years when the aerosol concentrations were low, there is good correlation in 1969 and 1970 between low 250 mb geopotentials and high values of both B2 and mean

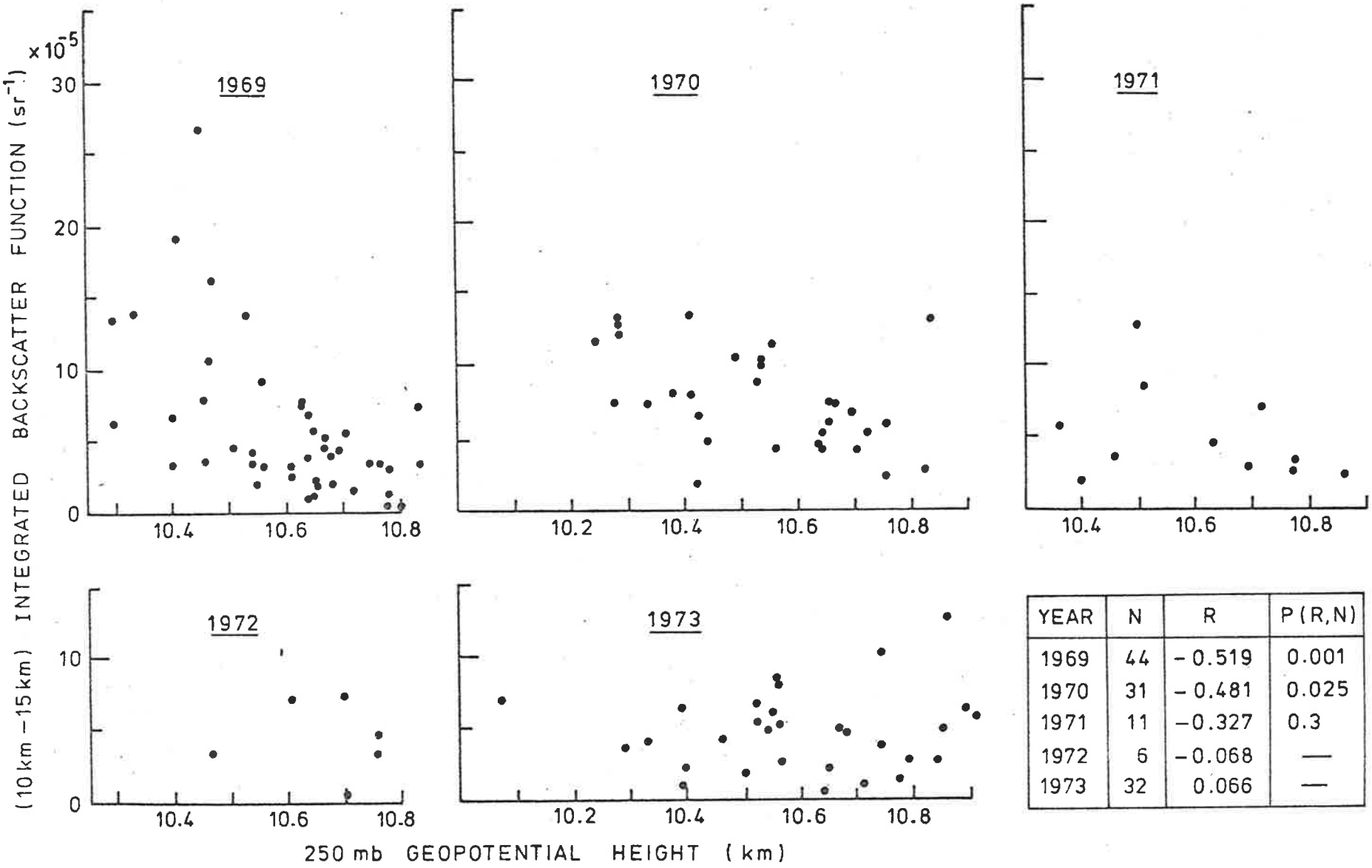

YEAR	N	R	P(R,N)
1969	44	-0.519	0.001
1970	31	-0.481	0.025
1971	11	-0.327	0.3
1972	6	-0.068	—
1973	32	0.066	—

FIG 4.12 Correlation of Integrated Backscatter Function with Geopotential Height.

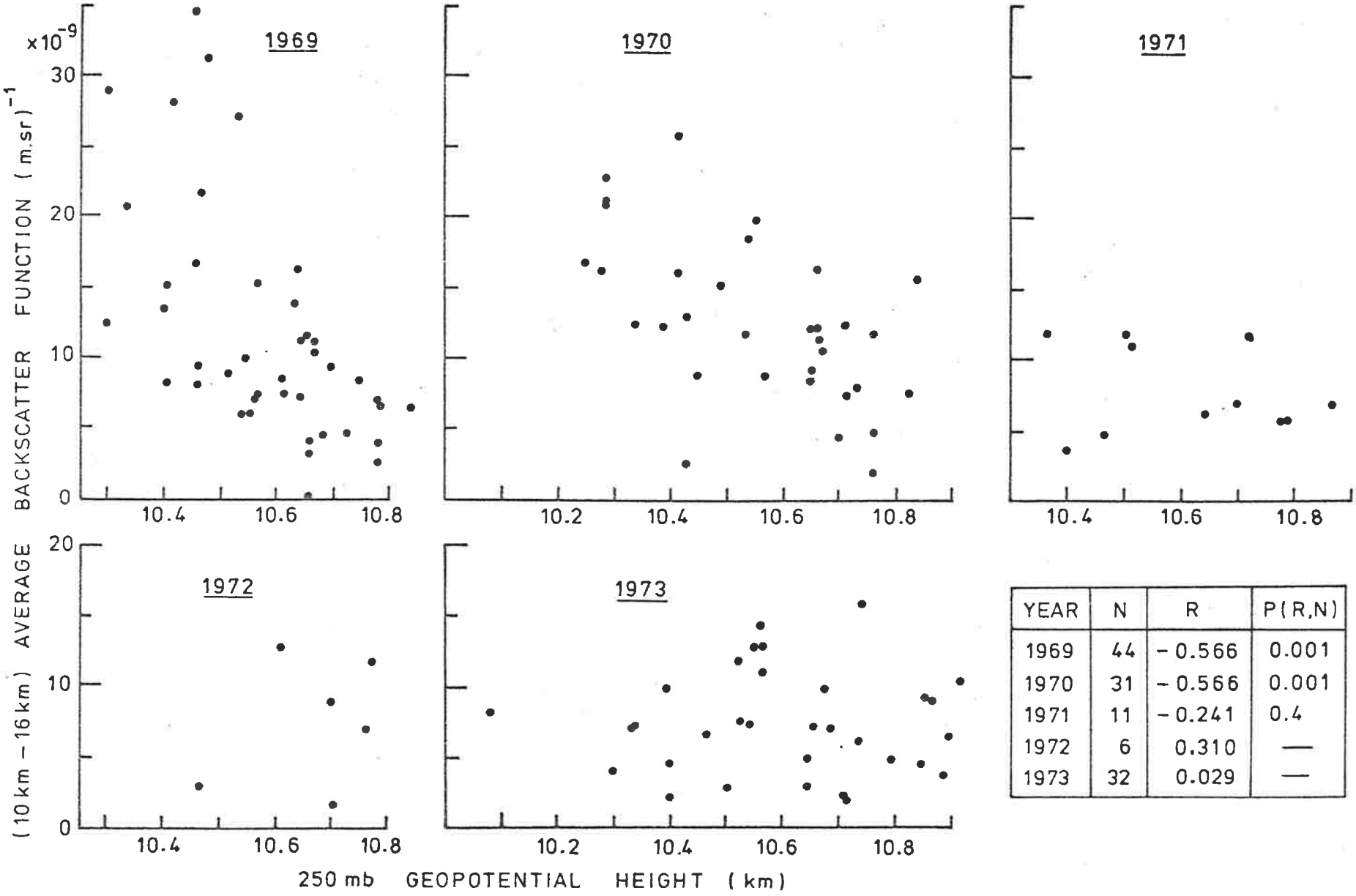

YEAR	N	R	P(R,N)
1969	44	– 0.566	0.001
1970	31	– 0.566	0.001
1971	11	– 0.241	0.4
1972	6	0.310	—
1973	32	0.029	—

FIG 4.13 Correlation of Average Backscatter Function with Geopotential Height.

backscatter function. The converse is also true. A similar result (not plotted) is obtained when the 1969 100 mb geopotentials are compared with the aerosol backscatter function integrated over the 15 km to 20 km height range but the correlations are not quite as good.

The evidence for a good correlation between the height of the constant pressure surfaces and the variation in the aerosol backscatter in the region between 10 km and 20 km presented in this section, tends to support the observation by Gambling *et al*, (1971) that higher aerosol scattering values are associated with upper level troughs and low values with upper level ridges. According to these authors this correlation suggests a downward transfer of material from above, together with a horizontal poleward movement by eddy processes , the troughs and ridges representing the eddies of the general circulation flow pattern.

As described in Chapter 3, increased amounts of aerosol in the height region used for the normalisation of the lidar scattering profile can cause an underestimate in the derived aerosol scattering values. For this reason care must be taken during normalisation of profiles on those nights when a trough in the 250 mb surface occurs over the lidar site. If normalisation in this height region is necessary, then the resulting scattering values should be treated with caution.

4.4 The Stratosphere above 30 km

The discussion of the stratospheric aerosol layer so far has been limited to the height region between 9 km and 30 km. The reason is that the bulk of the layer, in terms of mass, particle number density, or any of the light scattering properties, is concentrated in this region.

There have been occasions however, when scattering has been measured from aerosols above this region. These measurements tend to be of two kinds. The first refers to scattering from an extension above 30 km, of the main lower layer, and the second refers to material at greater heights which seems to be isolated from the main layer and may be of a different origin, possibly extra-terrestrial.

Early scattering profiles obtained by most lidar groups (e.g. Bain and Sandford, 1966; Kent *et al*, 1967) showed a return to purely molecular scattering near 10 km and above 30 km. The Adelaide scattering profiles for April 1969 to January 1970 (Gambling *et al*, 1971) showed a similar behaviour. However, as can be seen in the same paper, the scattering ratio profiles from February 1970 to May 1970 did not return to unity at 30 km. A similar behaviour was often noted by Russell *et al*, (1976) for the 1973 to 1974 period in California.

Gambling *et al* normalised their scattering ratio profiles for the region above 30 km to unity at this height, and found that in the monthly mean profiles the ratios were usually within one standard deviation of unity. However, their profiles for April, May, June and November 1969 show a monotonic decrease in scattering ratio up to at least 40 km, indicating the possible existence of aerosols in this region. Schuster (1970) also reported aerosol scattering in the 30 km to 40 km region and Clemesha and Simonich (1978) observed excess scattering from the "tail" of the main layer up to as high as 34 km.

Observations of dust layers above the main layer have been reported by several workers. Clemesha and Simonich reported excess scattering in the region 40 km to 50 km in October 1971, September to October 1972 and October 1973. Rössler (1968, 1972) measured diffuse

sky brightness from rockets launched over the Sahara in April 1963 and August 1970, and detected dust layers in the height regions near 20 km, 50 km and 80 km. He observed that these were regions in which the rate of change of temperature was constant with altitude. Cunnold *et al*, (1973), using horizon observations from an X-15-1 aircraft observed excess scattering from near 50 km, and Giovane and Schuerman (1976), using Skylab solar occultation observations during November 1973, observed a layer at 48 km.

As the 1962 U.S. Standard Atmosphere is used in the calculation of Adelaide aerosol scattering data above 30 km, any seasonal variation in atmospheric density would be expected to produce an apparent variation in scattering ratios at these heights. To reduce the effect of any such variations, the monthly mean scattering ratios were re-calculated using an average yearly variation in density calculated from falling sphere density measurements made at Woomera (31° S, 137° E), South Australia, (Pearson 1973(a) and (b)). When the standard deviations in scattering ratio and density are considered there are some months for which the mean scattering ratios are significantly greater than unity. These are plotted in Figure 4.14. Those months in which observations were made of the 30 km to 60 km region are indicated by horizontal bars on the time axis. Normalisation of the scattering profiles for the region above 30 km is achieved by matching the profiles of total scattering in this region with those from the lower regions which are normalised by the method described in Chapter 3. Because of the large variation in the aerosol backscatter function in the range 20 km to 60 km, values of scattering ratio are preferred and were used in the figure.

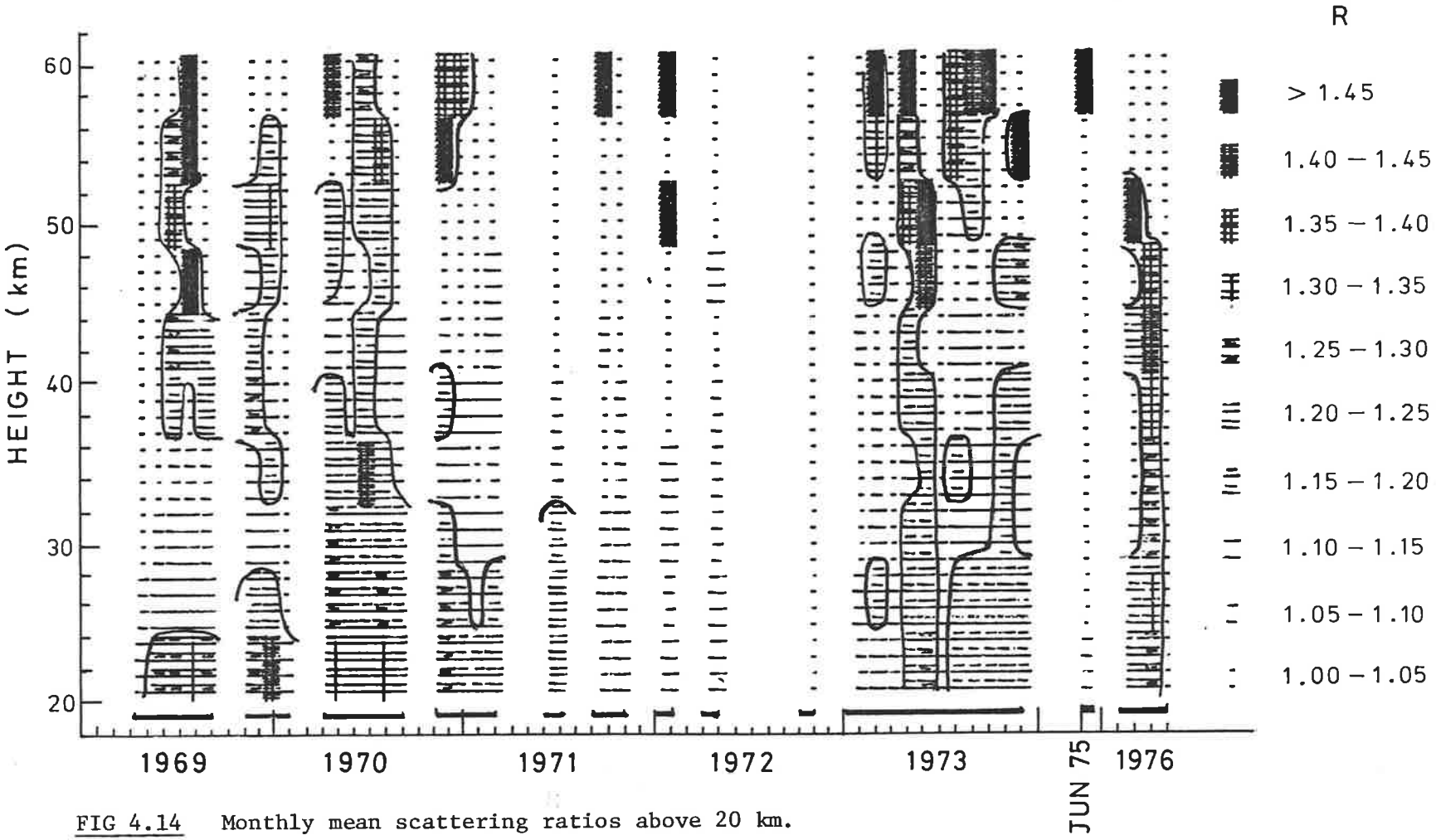

FIG 4.14 Monthly mean scattering ratios above 20 km.

Scattering ratios as high as ten per cent above the value expected for a clear air return are sometimes observed above the main stratospheric layer to a height of up to 40 km. There is a relatively clear region above about 31 km to 36 km with an increase in scattering above this height, especially in the region between 46 km and 60 km, the latter being the maximum height studied with the lidar. These observations of the existence of excess scattering above the main stratospheric layer are in general agreement with those of the other workers mentioned earlier.

According to Clemesha and Simonich (1978), the source of this material is possibly extra-terrestrial, a possibility also proposed by Rosinski (1972) and Rosinski *et al*, (1975), who noted an extra large influx of magnetic spherules at the time of Clemesha and Simonich's lidar observations of an increase in scattering. It is unlikely that volcanic eruptions inject dust into these relatively high altitudes.

It should be noted in conclusion that high scattering ratios observed at high altitudes do not imply the existence of large amounts of dust because the scattering is expressed as a ratio of the aerosol to the molecular scattering, and the latter is very low at these heights. If the material is extra-terrestrial, the scattering ratio of a cloud or layer of this dust would be expected to decrease as the layer descended into the denser regions of the atmosphere, provided the layer did not change in thickness and the particles retained their optical properties during the descent.

4.5 Stratospheric Dust Observations and their Implication for The Global Radiation Flux

Variations in the aerosol content of the stratosphere will lead to variations in the solar flux reaching the earth by scattering of

radiation upwards from the aerosol layer and by absorption within the layer. In this section the variations in the lidar derived stratospheric aerosol optical thicknesses are translated into solar flux variations at the surface.

Monthly mean values of the vertically integrated backscatter function are illustrated in Figure 4.15 for the period 1969 to 1976. As discussed in Chapter 3, these measurements may be expressed as optical thicknesses, the precise value depending on the value of the aerosol phase function chosen. The optical thicknesses are indicated by the scales at the right of the figure. Scale A uses a value of $P_A(\pi)/4\pi = 0.0199\ Sr^{-1}$ and Scale B uses $0.013\ Sr^{-1}$.

To relate this aerosol optical thickness at the lidar wavelength of 694 nm to the equivalent optical thickness for a beam of solar radiation, the relative extinction for the two spectral distributions was calculated by employing a stratospheric aerosol size distribution given by Bigg (1976), and extinction efficiency factors averaged over the solar range of wavelengths obtained from the work of Cadle and Grams (1975). The aerosol distribution was the average of 35 balloon-borne impactor measurements during the period 1969 to 1974.

The extinction per metre or volume scattering coefficient, of a monochromatic beam of light of wavelength λ, by a layer of monodisperse aerosols having N spherical particles per cubic metre with radius r metres, refractive index m and a Mie extinction efficiency factor $Q_{EXT}(m, \lambda, r)$, is

$$\beta_\lambda = N\pi r^2 Q_{EXT}(m, \lambda, r). \qquad 4.2$$

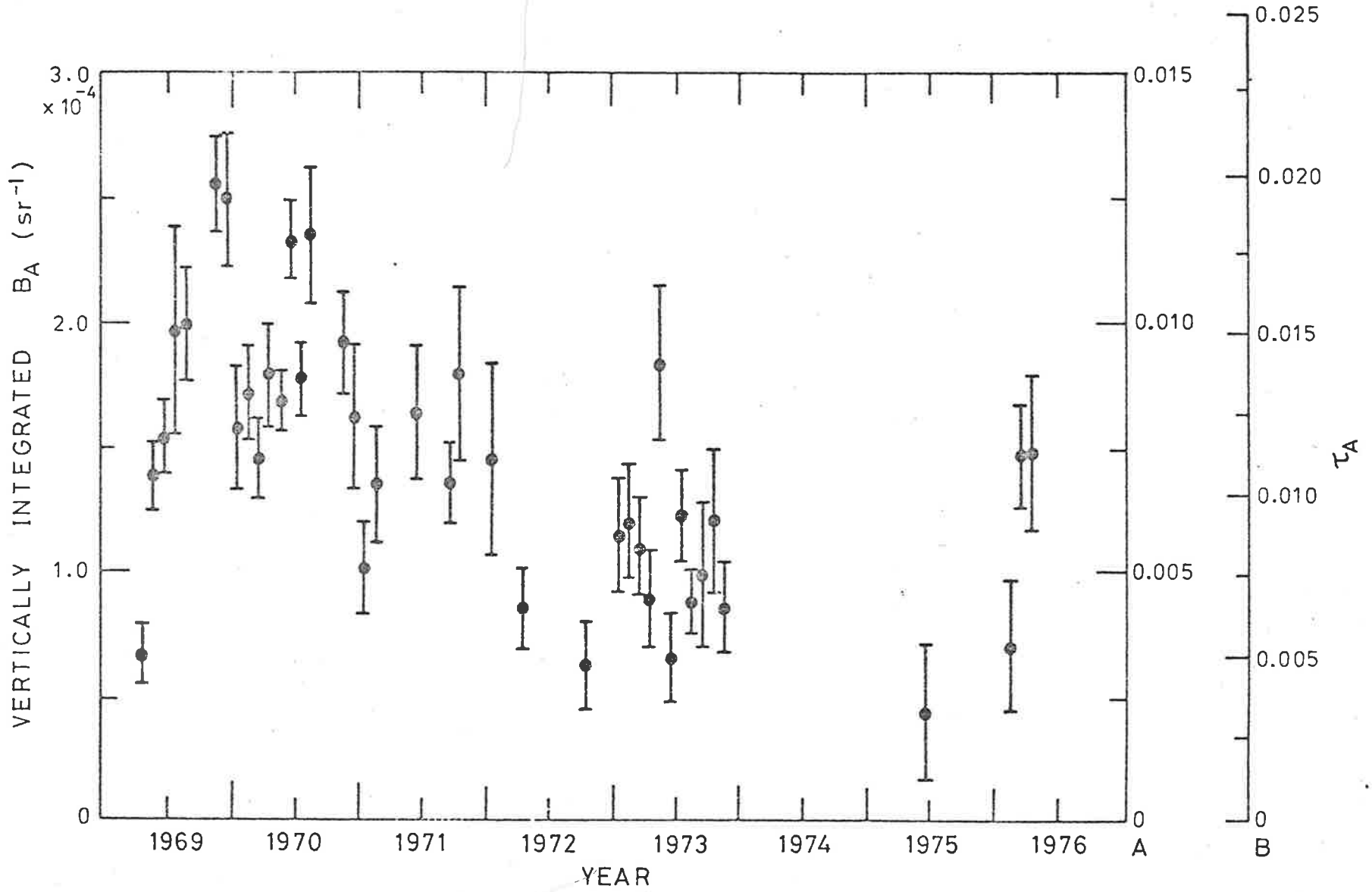

FIG 4.15 Monthly mean values of vertically integrated backscatter coefficient (10 km - 30 km), and corresponding values of aerosol optical thickness assuming values of $P_A(\pi)/4\pi = 0.0199$ (R.H. Scale A), and 0.013 (R.H. Scale B).

If the depth of the layer is Δh metres then the optical thickness $\tau = \beta_\lambda \Delta h$. Now as the transmittance $T = e^{-\tau} \approx 1 - \tau$ for small h, the fractional loss of energy due to the combined effects of scattering and absorption from a beam passing vertically through the layer is τ.

The extinction efficiency factor averaged over solar wavelengths is

$$\overline{Q}_{EXT}(m, r) = \frac{\int_{0.3\mu}^{\infty} Q_{EXT}(m, \lambda, r).\ B(\lambda,T)d\lambda}{\int_{0.3\mu}^{\infty} B(\lambda,T)d\lambda} \qquad 4.3$$

and $$\tau = N\pi r^2\ \overline{Q}_{EXT}(m, r). \qquad 4.4$$

Cadle and Grams (1975) assumed the solar spectrum can be described by a Planck distribution function $B(\lambda, T)$ for a blackbody at a temperature T of 6000K, and neglected all wavelengths shorter than $0.3\mu m$ to approximate the effect of ozone absorption. Their calculations of percentage energy loss, $P_{EXT} = 100\tau$, used a layer of one kilometre thickness, and N spherical particles of radius $r(\mu m)$ per cubic centimetre, with a specific gravity of 2 and a mass concentration of one microgram per cubic metre. By using these values and writing

$N(cm^{-3}) = (3/4\pi)(M/r^3 d)$, the percentage loss of energy in a one kilometre layer is

$$P_{EXT}(km^{-1}) = 0.075\ M\ \overline{Q}_{EXT}(m, r)/rd\ . \qquad 4.5$$

which can be solved for the solar averaged extinction efficiency factor.

$$\text{i.e.} \quad \overline{Q}_{EXT}(m, r) = 26.7\ P_{EXT}(km^{-1}).\ r\ . \qquad 4.6$$

Values for $\overline{Q}_{EXT}$ for particles with radii in the optically important range of $0.01\ \mu m$ to $10.0\ \mu m$ were obtained from Figure 11 of Cadle and

Grams (1975) for a real refractive index of 1.4, which compares with the value of 1.42 used in the model of Russell *et al*, (1976), and an imaginary index of 0.001, which is the smallest value used by these authors. Values of $Q_{EXT}(m, \lambda, r)$ for the lidar wavelength were obtained from their Figure 10 and adjusted to the appropriate refractive index. The effect of the stratospheric particle size distribution was included as follows. For a polydispose aerosol layer having n(r)dr particles per cubic metre in the size range r to r+dr, the optical thickness τ_λ for a monochromatic beam of wavelength λ is given by

$$\tau_\lambda = \int_{r_1}^{r_2} \pi r^2 Q_{EXT}(m, \lambda, r)\, n(r)dr \quad . \qquad 4.7$$

and for a solar beam

$$\tau_{SOLAR} = \int_{r_1}^{r_2} \pi r^2 \bar{Q}_{EXT}(m, r)\, n(r)dr . \qquad 4.8$$

For a given aerosol size distribution the ratio of the optical thickness of a vertically incident solar beam to the corresponding optical thickness of a monochromatic light beam is

$$\frac{\tau_{SOLAR}}{\tau_\lambda} = \frac{\int_{r_1}^{r_2} \pi r^2 \bar{Q}_{EXT}(m, r)\, n(r)dr}{\int_{r_1}^{r_2} \pi r^2 Q_{EXT}(m, \lambda, r)\, n(r)dr} . \qquad 4.9$$

Bigg's (1976) aerosol size distribution corresponds most closely in time and location to the present measurements of the stratospheric aerosol layer over Adelaide, and therefore was used in this analysis. Numerical integration of the ratio in Equation 4.9 yielded a value of 0.87, thus

$$\tau_{SOLAR} = 0.87\tau_{LIDAR} . \qquad 4.10$$

To relate the optical thickness measurements at Adelaide to the globally averaged reduction in solar flux at ground level, allowance must be made for the different solar zenith angles at different latitudes on the globe and, consequently, for the different path lengths the radiation traverses. The correct solar optical thickness can be obtained by multiplying by $\sec\theta$ where θ is the solar zenith angle. The total illuminated area of a sphere is exactly twice that of a flat disc at normal incidence. Thus an equivalent spherical geometry situation is obtained by choosing plane parallel earth model with a zenith angle of 60 degrees. The resulting globally averaged percentage extinction loss P_{GAV} is twice that for the case of vertical incidence.

Cadle and Grams have calculated values of $P_{GAV}(r)$ for a similar layer of monodisperse aerosols to the one used for the calculation of $P_{EXT}(r)$ discussed earlier, but with a total thickness of 10 km rather than 1 km. This loss comprises absorption and scattering away from the earth into the upper hemisphere, that is, the hemisphere containing the incident solar beam. Similar reasoning to that used for the calculation of $\overline{Q}_{EXT}(r, m)$ gives

$$\overline{Q}_{GAV}(r, m) = (4d/3M).\ P_{GAV}(\text{per 10 km}).r\ . \qquad 4.11$$

For the polydisperse aerosol distribution defined earlier, the total mass M, per unit volume is

$$M = (4/3)\pi d \int_{r_1}^{r_2} r^3\ n(r)dr\ . \qquad 4.12$$

and the percentage energy loss per unit mass is

$$\frac{[P_{GAV}]}{M}\ 10\ km = \frac{0.75}{d}\ \frac{(4/3)\pi d \int_{r_1}^{r_2} (r^3/r)\ \overline{Q}_{GAV}(r, m)\ n(r)dr}{(4/3)\pi d \int r^3\ n(r)dr} \cdot \qquad 4.13$$

Substitution for $\overline{Q}_{GAV}(r, m)$ from Equation (4.11) gives

$$\frac{[P_{GAV}]}{M}\ 10\ km = \frac{0.75}{d}\ \frac{\int_{r_1}^{r_2} [\frac{4}{3}\frac{d}{M}]\ P_{GAV}(10\ km).\ r.\ \frac{r^3}{r}\ n(r)dr}{\int_{r_1}^{r_2} r^3\ n(r)dr} \cdot$$

$$\text{So}\quad [P_{GAV}]_{10km} = \frac{\int_{r_1}^{r_2} P_{GAV}(10\ km).\ r^3\ n(r)dr}{\int_{r_1}^{r_2} r^3 n(r)dr} \cdot \qquad 4.14$$

$$\text{Similarly}\quad [P_{EXT}]_{10\ km} = 10.\ \frac{\int_{r_1}^{r_2} P_{EXT}(1\ km).\ r^3\ n(r)dr}{\int_{r_1}^{r_2} r^3\ n(r)dr} \cdot \qquad 4.15$$

where $[P_{EXT}]$ has now been calculated for a 10 km layer. Both ratios were integrated numerically with the result that the ratio

$$[P_{GAV}]/[P_{EXT}] = 0.20/0.56 = 0.36. \qquad 4.16$$

The actual size distribution chosen does not effect greatly the ratio in Equation 4.16. A distribution which decreased much more rapidly at higher particle sizes gave a value which differed from the above ratio by less than four per cent. Note that the ratio is independent of layer thickness.

If the decrease in stratospheric aerosol optical thickness averaged over the globe was of a similar magnitude to that observed at Adelaide then the resultant globally averaged reduction in solar flux loss at ground level can be computed in the following way. Firstly, if values of 0.016 and 0.004 are taken as representing maximum and minimum values of optical thickness measured at the lidar wavelengths during the period 1969 to 1976, then the corresponding values for solar

wavelengths are given by Equation 4.10 as 0.014 and 0.0035. The total globally averaged percentage loss in solar radiation can be obtained from the equation.

$$[P_{GAV}] = 0.36(\tau_{SOLAR} \times 100) = 36\tau_{SOLAR} . \qquad 4.17$$

Therefore the values of τ_{SOLAR} just calculated imply that the globally averaged percentage loss in solar radiation at ground level varied from 0.52 per cent to 0.13 per cent during the period 1969 to 1976.

CHAPTER FIVE

METHODS OF ANALYSIS OF TROPOSPHERIC LIDAR DATA AND THE DETERMINATION OF BOUNDARY VALUES

5.1 Introduction

The purpose of this chapter is to examine various analysis techniques which are used to determine values of atmospheric extinction from backscattered lidar signals. Only those techniques which are suitable for the analysis of elastically-scattered (same frequency) radiation detected by monostatic lidars are discussed. Raman scattering (Cooney, 1975; Herrmann *et al*,1974) and differential absorption methods are not discussed here.

One of the fundamental problems in the analysis of backscattered lidar signals is that lidars are extremely difficult to calibrate absolutely. Attempts have been made to measure the signal returned from targets of known reflectivities (Hall and Ageno, 1970) but the technical problems are severe. Because the target must be placed beyond the range of overlap of the transmitter beam and the receiver field of view, a large target is required to ensure that it reflects the whole area of the illuminated pulse. As the signal from a solid target of high reflectivity is many times greater than the atmospheric return, dense optical filters are necessary to reduce the signal to useful levels and heavy demands are placed on the linearity, over a large dynamic range, of the filters and the recording system. The atmospheric attenuation between the target and the lidar is not negligible and its effect must also be included.

Waggoner *et al* (1972) have devised a method using an integrating nephelometer to calibrate their system. As a bonus this method produces a value of the backscatter-to extinction ratio for aerosols; this ratio is

equal to the value of the aerosol phase function in the backscatter direction. Absorption is negligible for the ruby laser wavelength and the extinction coefficient is assumed equal to the volume scattering coefficient. Problems with this method were discovered during the present work and will be discussed later.

As discussed in Chapter 1, the lack of a unique relationship between the volume backscatter function $B(\pi)$ and the volume scattering coefficient or extinction coefficient β, reflects the variability and uncertainty in aerosol phase functions. A difficulty arises because atmospheric extinction is not negligible in the troposphere and model values are rarely valid for the particular case studied, so the extinction must be derived from the backscatter function by using some theoretically derived or experimentally determined relationship.

The difficulties just mentioned make various assumptions necessary during the analysis of lidar data in the case of some techniques. Several techniques overcome the calibration problem by assuming a boundary value of extinction; the most common situation is the one where the aerosol scattering contribution is zero at some point. Even here the relationship between $B(\pi)$ and β still needs to be assumed so that the atmospheric extinction can be calculated from the backscatter. Other methods capable of determining both the system constant K, and the $B(\pi)/\beta$ relationship require the assumption that the atmosphere is horizontally homogeneous.

Various techniques, their assumptions and limitations will now be discussed in detail. Methods for obtaining boundary values of extinction and their use in a computer program which produces a two dimensional map of atmospheric extinction from a series of lidar firings at different elevation angles will be examined also.

5.2 The Clear-Air Calibration Technique

This technique, also referred to as the "molecular layer" method is the one most commonly used in the analysis of stratospheric signals. As it has been described in detail in this context in Chapter 3, it will not be re-analysed here. The method can be extended easily to accept non-zero boundary values of aerosol extinction.

The basic assumption in the method is that there is some height at which the aerosol scattering contribution is either zero, or negligible, or is previously known. For profiles that extend to the tropopause, use may be made of the fact that low amounts of aerosol are usually found in this region. As mentioned in Section 3.1.2, a relatively clean region near 10 km is often used in the analysis of stratospheric profiles. Measurements have shown, (e.g. Rosen and Hofmann, 1977; Gibson, 1976) that optical scattering from particles generally decreases with altitude up to the tropopause region. Although very low values of aerosol scattering are often detected in the lower troposphere and can be used for the normalisation of scattering profiles, it has been found that the choice of greater heights in the troposphere for normalisation is less likely to introduce errors caused by the presence of aerosols. As mentioned earlier, the extinction must be included and the value can be derived from the backscatter function if a suitable relationship between the two is assumed. Usually this relationship is assumed to be independent of height. Atmospheric measurements of scattering from several angles using a balloon-borne nephelometer (Gibson, 1976) have shown that this latter assumption is not always true although the phase function may be constant over large regions of the atmosphere.

5.3 The Elevation Scan Method

Several methods which compare scattering of lidar pulses directed at different elevation angles have been used to deduce profiles of atmospheric transmittance and extinction. (Sandford *et al*, 1967; Hamilton, 1969; Ottway *et al*, 1971). If the lidar is calibrated then both the backscatter function and extinction coefficient, and hence the ratio of these quantities can be derived also. The methods of Hamilton and Sandford *et al* are similar in that they compare lidar returns from several elevation angles whereas that used by Ottway *et al* only compares signals measured at two angles. Equation A1.9 in Appendix 1 gives the lidar equation for a vertical propagation as

$$V(h) = K(B_M(\pi,h) + B_A(\pi,h))T^2 (o, h)/h^2 \qquad 5.1$$

which may be re-arranged and simplified as

$$Vh^2 = KB_T T^2 \qquad 5.2$$

where B_T is the total backscatter function. For a lidar directed at an elevation angle θ, the signal, V_θ returned from a height h and range $R = h \operatorname{cosec} \theta$ is given by

$$V_\theta R^2 = K B_T T^{2\operatorname{cosec} \theta} \qquad 5.3$$

Taking the ratio of equations 5.3 and 5.2 gives

$$\frac{V_\theta}{V} \operatorname{cosec}^2 \theta = T^2 (\operatorname{cosec} \theta - 1) \qquad 5.4$$

which may be solved for T. By using returns at 30° and 90° elevation, Ottway *et al* (1971) found

$$T = 2(V_{30}/V)^{\frac{1}{2}} . \qquad 5.5$$

The methods of Sandford *et al* (1967) and Hamilton (1969) proceed differently. By taking natural logarithms in equation 5.3 we obtain

$$\ell n\ (V_\theta R^2) \;=\; \ell n\ (KB_T) + 2\ \text{cosec}\ \theta\ \ell n(T). \qquad 5.6$$

A graph of $\ell n(VR^2)$ plotted against cosec θ for a certain height and several elevation angles has a slope of $2\ell n(T)$ and the intercept on the Y-axis is KB_T. As $T = e^{-\tau}$ then

$$\ell n(T) \;=\; -\tau \;=\; -\int_o^h \beta(r)dr \;=\; -\Delta h\ \Sigma\beta\ . \qquad 5.7$$

Therefore, by measuring the slopes in equation 5.6 for several heights and solving for β in equation 5.7, a profile of volume scattering coefficient or extinction is derived. By assuming a value for K, Hamilton was able to derive a profile of B_T also, and on two days found the ratio β_T/B_T varied between approximately 2 and 3.

The main assumptions for the validity of this method are firstly, the atmosphere is horizontally homogeneous up to the maximum height studied, secondly, the transmitted pulse is sufficiently short that the atmosphere does not vary much about h , and thirdly, the atmospheric transmittance does not vary much over the range of wavelengths emitted by the laser.

The second two conditions can be met satisfactorily by most lidars but it is the first condition, one over which the experimenter has no control, which causes problems. Any lack of horizontal homogeneity will become obvious if firings are made at several angles but not necessarily if only two angles are studied. For this reason the method used by Sandford *et al* or Hamilton is to be preferred to that of Ottway *et al* for observations in the troposphere. The latter method was designed for the stratosphere where multi-angle observations are impractical because of the excessive number of laser firings required to give reliable statistics.

Other advantages of these methods are that they do not require boundary values nor do they assume any form of relationship between B_A and β_A. The Sandford/Hamilton method can be used to study this relationship and its variability with height, if any exists. Provided the conditions for the applicability of the method hold, it is superior to most other methods for the determination of the relationship between B_A and β_A as the same wavelength and bandwidth are used for the measurement of both quantities.

5.4 The Depolarisation Ratio Method

The main problem in the analysis of lidar data is the separation of the molecular and the aerosol components in the measured atmospheric return signal. An interesting method, which uses the components of the signal which are parallel and perpendicularly polarised with respect to the transmitted pulse, has been used by Cohen and Graber (1975) and Cohen and Kleiman (1978). The following notation is consistent with that used elsewhere in this thesis rather than that used by these authors.

The lidar equation for scattering from height h_i can be written in the form

$$I_j(h_i) = V_j(h_i)h_i^2 = K_j(B_{Mj}(h_i) + B_{Aj}(h_i))\, T_j^2(o, h_i),$$

where $j = 1$ and $j = 2$ refer to the parallel and perpendicular components respectively, and $I(h)$ is the range corrected signal received at height h. The equation can be simplified by letting the dependence on height h_i be denoted by the subscript i giving

$$I_{i,j} = V_{i,j}\, h_i^2 = K_j\, (B_{Mi,j} + B_{Ai,j})T_{i,j}^2 . \qquad 5.8$$

In particular, the total cross polarised return from air molecules and aerosol particles at h_i is

$$I_{i,2} = K_2 T_{i,2}^2 \, (B_{Mi,2} + B_{Ai,2}) \, , \qquad 5.9$$

and the total parallel component is

$$I_{i,1} = K_1 T_{i,1}^2 \, (B_{Mi,1} + B_{Ai,1}). \qquad 5.10$$

The ratio of the cross polarised to the parallel polarised returns is called the depolarisation ratio, and for clear air Cohen *et al* (1969) have measured its value as $\gamma = 0.015 \pm 0.001$. So

$$B_{Mi,2} = \gamma \, B_{Mi,1} \, . \qquad 5.11$$

Now if we assume that the aerosol size distribution is constant within the layer and only the number density varies with height, then the aerosol backscatter function at the next height h_{i+1} is related to that at h_i by the ratio of the number densities, $C_{i+1} = (N_{i+1}/N_i)$, so

$$B_{Ai+1,j} = C_{i+1} \, B_{Ai,j} \, . \qquad 5.12$$

As the lidar system constant should be the same for both polarisations and as the transmission of a light beam through the atmosphere is independent of its polarisation, $K_1 = K_2 = K$ and $T_{i,2} = T_{i,1} = T_i$. Equations 5.9 and 5.10 can now be combined using 5.11 and 5.12 to give

$$I_{i,2} - \gamma I_{i,1} = KT_i^2 (B_{Mi,2} + B_{Ai,2}) - \gamma KT_i^2 (B_{Mi,1} + B_{Ai,1})$$

$$= KT_i^2 (B_{Ai,2} - \gamma B_{Ai,1}). \qquad 5.13$$

A similar equation can be written for height h_{i+1} and, when used with equation 5.13, can be re-arranged to give

$$C_{i+1} = \frac{1}{T^2 (h_i, \, h_{i+1})} \quad \frac{(I_{i+1,2} - \gamma I_{i+1,1})}{(I_{i,2} - \gamma I_{i,1})} \, . \qquad 5.14$$

For the stratosphere and for tropospheric layers with low values of optical thickness, Cohen *et al* assume $T^2(h_i, h_{i+1}) = 1.0$. However, in most cases in the troposphere this is not so, especially when successive products are formed to relate the aerosol number density N_i at any height h_i to that at a reference height h_1 through the equation

$$N_i = \frac{N_1}{T^2(h_1, h_i)} \prod_{n=2}^{i} C_n \,. \qquad 5.15$$

If there is an aerosol-free interval within the region being probed it will be indicated by its low depolarisation ratio ($\gamma = 0.015$). Another advantage of the method is that by eliminating the molecular contribution in equation 5.13, knowledge of the atmospheric density profile is made unnecessary except in the calculation of T^2 where an exponential approximation is adequate.

In the present work this method has been used to calculate profiles of aerosol number density N_i and extinction β_i by using a boundary value of each at h_1 in the following way:-

Step 1. Initially assume $T^2(h_i, h_{i+1}) = 1.0$, and evaluate C_{i+1} using 5.14 and β_1 and N_1.

Step 2. Using C_{i+1} evaluate N_{i+1} using 5.15.

Step 3. Assuming $\beta_i \propto N_i$ evaluate $\beta_{i+1} = C_{i+1}\,\beta_i$ and $T^2(h_i, h_{i+1})$.

Step 4. Recalculate C_{i+1} using 5.14 and compare with previous value.

Step 5. Return to Step 2 and iterate until convergence is achieved to produce profiles of N_i and β_i .

The assumption made in the depolarisation method for determining extinction profiles is contained in Step 3 i.e. that the aerosol scattering properties are proportional to the number density for the whole

region being studied. If there is no aerosol-free region then boundary values of number density or extinction must be used also.

5.5 Methods involving the Solution of Differential Equations

The final class of methods to be discussed here derive solutions of backscatter or extinction from the lidar equation expressed in a differential form. Among these solutions are those of Barrett and Ben-Dov (1967), Viezee *et al* (1969), Fernald *et al* (1972) and Collis and Uthe (1972).

The method of Viezee *et al* is interesting because, as an intermediate step, use is made of the function

$$S(R) = 10 \log_{10} \left(\frac{P(R) R^2}{P(R_o) R_o^2} \right) = 10 \log_{10} \left(\frac{B_T(R) T^2 (R)}{B_T(R_o) T^2 (R_o)} \right), \quad 5.16$$

where the notation is that used in Appendix I. When the atmospheric attenuation is small, for example over short ranges, T^2 is approximately unity and the S function becomes an expression for the logarithm of the ratio of the backscatter function at some range R to the reference value at R_o. This form of presentation is equivalent to that for the stratospheric backscatter function in Figure 4.3.

By taking the derivative of the S function in equation 5.16 with respect to range and then solving the resultant differential equation Viezee *et al* obtain the following solution,

$$\beta(R) = \exp [C_1 S(R)] / \{ C_I - C_2 \int_o^R \exp [C_1 S(\ell)] d\ell \}, \quad 5.17$$

where C_I is an integration constant, $C_1 = 1/4.34\ k_2$ and $C_2 = 2/k_2$. Here k_2 arises from the use of the relationship

$$B \propto \beta^{k_2}, \quad 5.18$$

obtained from the work of Curcio and Knestrick (1958). Johnson and Uthe (1971) take the analysis one step further as do Barrett and Ben-Dov (1967), and express the result in terms of aerosol mass concentration.

Fernald *et al* (1972) improve on the method of Barrett and Ben-Dov by considering two cases. In one case the scattering is predominantly due to a single class of scatterers, and in the other the scattering is due to both air molecules and aerosols. During their analysis the atmospheric optical thickness from ground level to the maximum height studied is calculated by subtracting values of the optical thickness for a model stratosphere from values of the total atmospheric optical thickness obtained using a solar radiometer. Following Barrett and Ben-Dov they normalise their profiles to the atmospheric returns from an aerosol-free region. The system constant is derived and this allows the ratio of extinction-to-backscatter to be determined. In this method the differential equation and its solution result from the differentiation of an expression for the atmospheric transmittance with respect to range and a solution of a somewhat similar form to equation 5.17 is obtained.

The major difference in the methods of Viezee *et al* and Fernald *et al* is that in the former analysis the relationship between backscatter and extinction has to be assumed, while in the latter analysis the relationship may be determined provided the stratospheric and total optical thicknesses are known. Both methods require the use of boundary values, the former as a reference for the extinction profiles, and the latter, which assumes zero aerosol scattering at some height, to calibrate the lidar and determine the system constant.

As lidar profiles over larger ranges were contemplated in the present work it was considered necessary that the effects of attenuation be included. It was anticipated also that in at least some part of the profile both aerosols and air molecules should be considered separately. Accordingly, the following method of analysis was derived. The necessary

requirements are a knowledge of the backscatter-to-extinction ratio, a boundary value of extinction or backscatter, the ground level value of molecular extinction, and the molecular extinction or density scale height of the atmosphere. These last two parameters are obtained easily if the density profile is known.

At any given height the total backscatter function, using the notation of Appendix I, is given by

$$B_T(h) = B_A(h) + B_M(h) \quad . \qquad 5.19$$

By expanding $B_A(h)$ in terms of the total and molecular extinction coefficients we obtain

$$B_T(h) = \frac{1}{4\pi} P_A \beta_T(h) - \frac{P_A}{4\pi} \beta_M(h) + B_M(h)$$

$$= \frac{1}{4\pi} P_A \beta_T(h) + (1 - \frac{P_A}{P_M}) B_M(h). \qquad 5.20$$

Re-arranging gives

$$\beta_T(h) = \frac{4\pi B_T(h)}{P_A} + 4\pi \left(\frac{P_A - P_M}{P_A . P_M} \right) B_M(h). \qquad 5.21$$

Now an approximate value of $B_M(h)$ can be obtained using $B_M(h) = B_M(o)\ e^{-h/H}$ where H is the density scale height for the lowest six kilometres of the atmosphere. This has been a useful and fairly accurate approximation in the present analysis where maximum altitudes have usually been three and sometimes six kilometres. Deviations from values derived from radiosonde measurements have usually been less than two per-cent over the lower height range but increase to five per-cent or more at six kilometres. The approximation is useful in that the computer programs for the analysis of the data are simplified greatly and it is also useful for the analysis of data on days when there is no local radiosonde data readily available or available for the right time, use being made of local

ground level temperature and pressure measurements.

For a lidar directed at an elevation angle θ, $h = R \sin\theta$ and equation 5.21 becomes

$$\beta_T(h) = 4\pi\, B_T(h)/P_A + 4\pi(1/P_M - 1/P_A)\, B_M(0)\, \exp\{-R\sin\theta/H\}. \qquad 5.22$$

Differentiating equation 5.16 and simplifying by dropping the notation that indicates height dependence gives

$$\frac{dS}{dR} = 4.34\,\frac{1}{B_T}\,\frac{dB_T}{dR} - 8.68\beta_T .$$

This equation can be rewritten by substituting the expression for β_T in equation 5.22, then simplified by making the substitution $y = 1/B_T$ and $c = -R \sin\theta/H$. The result is

$$\frac{dy}{dR} + \left(\frac{1}{4.34}\,\frac{dS}{dR} + 8\pi\left(\frac{1}{P_R} - \frac{1}{P_A}\right).\, B_M(o)e^{cR}\right).y = \frac{-8\pi}{P_A} . \qquad 5.23$$

By re-writing in the following form,

$$\frac{dy}{dR} + x(R).y = b,$$

the equation can be solved by multiplying both sides by an integrating factor $e^{X(R)}$, where $dX(R)/dR = x(R)$.

Thus,

$$e^{X(R)}.\frac{dy}{dR} + e^{X(R)}.\,x(R).y = b\, e^{X(R)},$$

where the L.H.S. is now an exact derivative,

i.e. $$\frac{d}{dR}\left[\, e^{X(R)}.\, y\,\right] = b\, e^{X(R)}.$$

Now integrating both sides with respect to R gives

$$y\, e^{X(R)} = b \int e^{X(R)} dR + C_I,$$

and on replacing y with $1/B_T$ and solving for B_T gives

$$B_T(R) = \frac{e^{X(R)}}{C_I + b \int_R e^{X(R)} dR} \quad .$$

The integral must be solved numerically. If it is to be dependent on R then the upper limit must be R . The lower limit can be set as R_o, the range of overlap of the transmitter and receiver cones. X(R) can be evaluated from $X(R) = \int x(R) dR$.

i.e. $$X(R) = 0.2303\, S(R) - \frac{8\pi}{\sin\theta} \left(\frac{1}{P_M} - \frac{1}{P_A} \right) . B_M(o) . H . \exp(-R\sin\theta/H),$$

5.24

and $$B_T(R) = \frac{e^{X(R)}}{\{ C_I - \frac{8\pi}{P_A} \int_{R_o}^{R} e^{X(r)} dr \}} \quad . \qquad 5.25$$

If boundary values $B_T^*(R)$ can be obtained, the integration constant C_I can be evaluated as

$$C_I = \frac{e^{X(R)}}{B_T^*(R)} + \frac{8\pi}{P_A} \int_{R_o}^{R} e^{X(r)} dr. \qquad 5.26$$

It would be particularly useful if the boundary value were determined at R_o, for then

$$C_I = e^{X(R_o)} / B_T^*(R_o). \qquad 5.27$$

This method has the combined advantages over others of this kind, of considering both aerosol and molecular scattering, and of relative simplicity enabled by the introduction of a reasonable approximation which expresses the molecular contribution in an analytical form. Differences in the solutions between this method and those where aerosol scattering and molecular scattering are not considered separately are most marked when the analysis is performed over a large height range. In this case the molecular contribution decreases steadily with height, and, as it is unlikely that the aerosol contribution has a similar behaviour, the ratio of total backscatter to total extinction assumed in the latter type of analysis must change and significant errors will occur.

The major assumption and source of uncertainty is, again, the dependence of B_A on β_A, that is the aerosol phase function $P_A(\pi)$. The values for $B_M(o)$ and H do not affect the result markedly, especially if values are obtained by fitting an exponential function to the measured radiosonde data. Largest errors arise when incorrect boundary values are used, especially if they are too large. Then the integration constant C_I is too small and, because the result for a particular height is used in the analysis of the next height, the solution diverges rapidly.

5.6 Obtaining Boundary Values for Solutions of the Lidar Equation

There are several ways of obtaining boundary values for use in the analysis of lidar data, but many are limited in their applications to special atmospheric conditions, for example, constant backscatter or extinction over some height range, or horizontal homogeneity of the atmosphere. Others have the disadvantage of producing only average values from measurements at another wavelength. The methods discussed here are those used in Chapter 6 where the results of tropospheric lidar

measurements are analysed.

The two methods of analysis discussed in Section 5.3 can sometimes be used to produce boundary values even though atmospheric conditions preclude their use throughout the whole region under study. These methods require that the atmosphere be horizontally homogeneous, and although this does not seem to occur often throughout a whole region of the atmosphere, it is sometimes true for small parts of the region. A general impression of the likelihood of such conditions existing can be obtained by plotting a two-dimensional picture of the range-corrected power received from different elevation angles. The acceptable region if one exists, can then be chosen and boundary values found by analysing returns from paths at two or more elevation angles passing through the region.

A modification to the method of Ottway *et al*, which compares returns from two elevation angles, permits the use of the method in circumstances where horizontal homogeneity does not exist at heights between the lidar and the region studied. This method was found necessary when results of the present lidar system were analysed, because the transmitted and received beams are directed by a pair of front-surfaced mirrors whose reflectivity is not uniform because of the difficulty in coating mirrors of their size. This causes a change in reflecting efficiency with elevation angle in addition to that expected from an aluminium mirror, so that the lidar system constant is a function of elevation angle. In addition, atmospheric inhomogeneities below the region studied can result in one beam experiencing greater attenuation than the other. This case can be made similar to that of differing reflectivities by including in the system constant the effect of the transmittance between the lidar and the lower boundary of the region of interest.

Equation 5.3 gives the lidar signal $V_\theta(h)$ from an elevation angle θ and height h as

$$V_\theta(h)\, R^2 = K\, B_T(h)\, T^c(o, h),$$

where $R = h\,\mathrm{cosec}\theta$ and $c = 2\,\mathrm{cosec}\theta$. This may be rewritten in a form which includes the changes just mentioned, and gives the signal from height h at an angle θ, as

$$V_{\theta_1}(h_1)R_1^2 = V_1(h_1)h_1^2\ \mathrm{cosec}^2\theta_1 = [\ K_1T^{c_1}(o,h_1)\ ]B_T(h_1),$$

$$= k_1B_T(h_1), \qquad 5.28$$

and from a height h_2 ($> h_1$) as

$$V_1(h_2)h_2^2\ \mathrm{cosec}\theta_1 = k_1B_T(h_2).\ T^{c_1}(h_1, h_2)\ .$$

Similar equations can be written for a larger elevation angle θ_2 and combined with those for θ_1 in the following way to solve for $T(h_1, h_2)$.

$$\frac{V_1(h_2)h_2^2\ \mathrm{cosec}^2\theta_1.\ V_2(h_1)h_1^2\ \mathrm{cosec}^2\theta_2}{V_1(h_1)h_1^2\ \mathrm{cosec}^2\theta_1.\ V_2(h_2)h_2^2\ \mathrm{cosec}^2\theta_2} = \frac{V_1(h_2).\ V_2(h_1)}{V_1(h_1).\ V_2(h_2)}$$

$$= \frac{k_1B_T(h_2).\ T^{c_1}(h_1, h_2)}{k_1B_T(h_1)} \cdot \frac{k_2B_T(h_1)}{k_2B_T(h_2)\ T^{c_2}(h_1, h_2)}$$

$$= T^{c_1-c_2}(h_1, h_2). \qquad 5.29$$

Therefore,

$$T(h_1, h_2) = \left[\ \frac{V_1(h_2).V_2(h_1)}{V_1(h_1).V_2(h_2)}\ \right]^Y \qquad 5.30$$

where $Y = 1/(c_1-c_2) = 1/(2\mathrm{cosec}\theta_1 - 2\mathrm{cosec}\theta_2)$.

As the solution for $T(h_1, h_2)$ is of the form

$$T = X^Y = e^{Y\ell nX}$$

the relative error in T is given by

$$\Delta T/T = (Y(\Delta X/X)^2 + (\Delta Y \ell n X)^2)^{\frac{1}{2}}, \qquad 5.31$$

where $$\left(\frac{\Delta X}{X}\right)^2 = \left(\frac{\Delta V_1(h_2)}{V_1(h_2)}\right)^2 + \left(\frac{\Delta V_1(h_1)}{V_1(h_1)}\right)^2 + \left(\frac{\Delta V_2(h_2)}{V_2(h_2)}\right)^2$$

$$+ \left(\frac{\Delta V_2(h_1)}{V_2(h_1)}\right)^2, \qquad 5.32$$

and $$\Delta Y = \left[\frac{\cos\theta_1 \sin^2\theta_2 - \sin^2\theta_1 \cos\theta_2}{2(\sin\theta_2 - \sin\theta_1)^2}\right] . \Delta\theta . \qquad 5.33$$

Now if the average value of the extinction coefficient in the range h_1 to h_2 is $\bar{\beta}$, then

$$\ell n\, T(h_1, h_2) = \ell n[\exp\{-\int_{h_1}^{h_2} \beta(r)dr\}] = (h_1 - h_2).\bar{\beta},$$

and the required boundary value of extinction is, therefore,

$$\bar{\beta} = [\ell n\, T(h_1, h_2)] / (h_1 - h_2), \qquad 5.34$$

with a relative error

$$\frac{\Delta\bar{\beta}}{\bar{\beta}} = \left(\frac{\Delta T}{T}\right) . \frac{1}{(h_1 - h_2)\,\bar{\beta}} . \qquad 5.35$$

Error calculations have been performed using various values of extinction coefficient, height interval, angular separation of the lidar shots and for typical values of the relative error in the recorded signal voltage. The best results occur for values of $\bar{\beta}$ greater than about $10^{-4}\,m^{-1}$, height intervals greater than 200 metres and as wide an angular beam separation as the homogeneous region will allow. Table 5.1 lists some typical results for the relative errors in T and $\bar{\beta}$ using the present lidar system.

TABLE 5.1

Relative Errors in T (upper triangular array) and β (lower triangular array) Determined by the Two Beam Method for the Adelaide Lidar System.

(a) $\beta = 1.0 \times 10^{-4}\ m^{-1}$, $\Delta h = 1.0$ km , $\Delta x/x = 0.3$

θ_2 \ θ_1	3°	5°	10°	20°	30°	40°	45°	50°	60°	90°
3°		.057	.045	.039	.038	.037	.037	.037	.036	.036
5°	.567		.040	.031	.028	.027	.027	.027	.026	.026
10°	.447	.399		.055	.042	.038	.037	.036	.035	.034
20°	.394	.306	.550		.163	.110	.100	.093	.085	.078
30°	.378	.283	.421	1.63		.338	.256	.216	.178	.150
40°	.370	.273	.379	1.10	3.38		1.06	.599	.374	.270
45°	.367	.269	.367	.997	2.56	10.6		1.38	.578	.362
50°	.365	.267	.359	.930	2.16	5.99	13.8		.995	.491
60°	.362	.264	.348	.851	1.78	3.74	5.78	9.95		.970
90°	.360	.261	.337	.783	1.50	2.70	3.62	4.91	9.70	

(b) $\beta = 5.0 \times 10^{-5}$, $\Delta h = 1.0$ km , $\Delta x/x = 0.3$

θ_2 \ θ_1	3	5	10	20	30	40	45	50	60	90
3		.033	.024	.021	.020	.020	.020	.020	.020	.019
5	.662		.030	.022	.020	.019	.019	.018	.018	.018
10	.488	.605		.053	.040	.036	.035	.034	.033	.032
20	.426	.431	1.07		.162	.110	.099	.093	.085	.078
30	.407	.394	.809	3.25		.338	.256	.216	.177	.150
40	.398	.378	.725	2.19	6.75		1.06	.599	.374	.270
45	.395	.373	.702	1.99	5.12	21.2		1.38	.578	.362
50	.393	.370	.685	1.86	4.32	12.0	27.6		.995	.491
60	.390	.365	.663	1.70	3.55	7.48	11.6	19.9		.970
90	.388	.360	.642	1.56	3.00	5.40	7.24	9.82	19.4	

TABLE 5.1 Continued..... (Upper triangular array)

(c) $\beta = 5 \times 10^{-5}\ m^{-1}$, $\Delta h = 0.5$ km , $\Delta x/x = 0.3$

$\theta_1 \backslash \theta_2$	3	5	10	20	30	40	45	50	60	90
3		.024	.016	.013	.013	.012	.012	.012	.012	.012
5	.949		.027	.019	.017	.016	.016	.016	.016	.015
10	.624	1.09		.053	.040	.036	.035	.034	.033	.032
20	.533	.745	2.12		.162	.110	.099	.093	.085	.078
30	.508	.675	1.60	6.50		.338	.256	.216	.177	.150
40	.496	.646	1.43	4.39	13.5		1.06	.599	.374	.270
45	.493	.637	1.39	3.98	10.2	42.4		1.38	5.78	.362
50	.490	.631	1.35	3.71	8.64	24.0	55.1		.995	.491
60	.486	.622	1.31	3.39	7.10	14.7	23.1	39.8		.970
90	.482	.613	1.27	3.12	6.00	10.8	14.5	19.6	38.8	

(d) $\beta = 1.0 \times 10^{-4}\ m^{-1}$, $\Delta h = 1.0$ km , $\Delta x/x = 0.16$

$\theta_1 \backslash \theta_2$	3	5	10	20	30	40	45	50	60	90
3		.054	.044	.039	.037	.036	.036	.036	.036	.035
5	.542		.033	.027	.025	.024	.024	.024	.023	.023
10	.437	.331		.032	.025	.023	.022	.022	.021	.021
20	.387	.267	.320		.087	.059	.054	.050	.046	.042
30	.370	.249	.252	.870		.180	.137	.115	.095	.080
40	.362	.241	.229	.590	1.80		.565	.320	.200	.144
45	.360	.238	.223	.535	1.37	5.65		.735	.308	.193
50	.358	.236	.218	.500	1.15	3.20	7.35		.531	.262
60	.356	.233	.212	.458	.948	2.00	3.08	5.31		.517
90	.353	.231	.206	.422	.802	1.44	1.93	2.62	5.17	

A simple method for the determination of boundary values of extinction is applicable when the extinction coefficient β is constant with height in some height region h_1 to h_2. Then for some height h in the region,

$$V(h)R^2 = \{ KT^2(o, h) \}. B_T(h). \exp[2(h_1-h_2)\beta], \qquad 5.36$$

and

$$\ell n[V(h).R^2] = [\ell n\{ KT^2(o, h) \} + 2h_1 \beta] - 2h \beta. \qquad 5.37$$

The extinction coefficient can then be obtained from the slope of a graph of $\ell n[VR^2]$ against h or by applying a linear, least-squares fit to the data in the region h_1 to h_2.

Whether or not the above method is applicable on a particular day can be tested by performing the above analysis on a number of profiles at different elevation angles within the region of interest. If a definite trend in the results is found with increasing elevation angle, it is likely that the extinction coefficient is changing with height, and the method should not be used in this region.

To conclude this section, two optical methods independent of the lidar are discussed. These are the use of integrating nephelometer extinction measurements and of measurements of atmospheric visibility or visual meteorological range. Although nephelometer measurements have been used successfully to calibrate a lidar (Waggoner *et al*, 1972) there are several difficulties with the method. First, the operating wavelength of the nephelometer is likely to be different from the laser wavelength and, more importantly, the optical band width much broader, especially if a ruby laser is used. In addition high, but commonly observable, relative humidities cause unreliable results. (Waggoner *et al*, 1972). To produce reliable boundary values for use with the lidar, a large range of extinction values should be sampled, the relative humidity should be low

and fairly constant, and the aerosol backscatter-to-extinction ratio must remain constant during the experiment.

As a last resort, an estimate of the average extinction coefficient $\bar{\beta}$ in the lowest regions of the atmosphere can be obtained by measurements of the atmospheric visibility or meteorological visual range, R_V. The two quantities are related by the Kochmeider visibility theory (Middleton, 1963) using the equation

$$R_V = 3.912/\bar{\beta} . \qquad 5.38$$

The visual range is defined as that distance at which the contrast of a black object against the sky background drops to 0.02.

Equation 5.38 is related to the total extinction coefficient averaged over solar visual wavelengths. An estimate of the aerosol extinction coefficient at a particular wavelength, λ, can be obtained, if extinction is assumed to be due entirely to scattering by aerosol particles and air molecules, by the following relation,

$$\beta_A(\lambda) = (3.912/R_V - \beta_M(0.55))\ (\lambda/0.55)^{-1}, \qquad 5.39$$

where the wavelength is expressed in micrometers and the visual range in kilometres. The equation assumes an inverse relationship between aerosol scattering and wavelength (Pinnick *et al*, 1976). A semi-empirical expression has been used by Kruse *et al*, (1962),

$$\text{i.e.} \quad \beta_A(\lambda) = (3.912/R_V)\ (\lambda/0.55)^{-q}, \qquad 5.40$$

where $q = 0.585\ R_V^{1/3}$ for $v \leqslant 6$ km,

and $q = 1.3$ for "average seeing conditions".

Both expressions give similar results for the conditions prevalent in the present analysis but the former treats the aerosol and molecular

components separately, and is possibly more generally applicable. The latter equation (5.40) and various models and their limitations when used for estimates of atmospheric transmission are discussed by Woodman (1974).

Boundary values of extinction obtained in these ways should be treated with caution as they are usually derived from meteorological visual ranges which are averaged in several directions and over a variable height range. The value of extinction derived is the average value along a path between the observer and the object studied. The other main source of possible error is the assumed wavelength dependence of aerosol scattering. The two main advantages are that the measurement is reasonably easy to perform and that varying relative humidities do not affect the result significantly.

5.7 The Presentation of Lidar Results in Two Dimensions

Diagrams of atmospheric extinction in two dimensions have many advantages over single profiles. The degree of homogeneity or layering and the distribution of material in space can be studied, isolated areas or "blobs" of enhanced scattering can be distinguished from layers, and diagrams of successive elevation scans show any movement of material.

The difficulties that arise in the normalisation or calibration of single lidar profiles are multiplied when elevation scans include many profiles. Unless care is taken different normalisation errors for each profile in the scans can result in a confused, uninterpretable picture. Various techniques employed to minimise these discrepancies in the production of the rectangular arrays of extinction values presented in Chapter 6 will now be discussed.

A computer program which can produce profiles and two-dimensional diagrams of the distribution of extinction coefficient from lidar scattering measurements at several angles of elevation has been written so that data in a variety of formats can be analysed. The different formats reflect the fact that the basic data comes from three possible sources: Adelaide lidar system, where profiles recorded on Polaroid film were digitized manually and punched onto computer cards, the data recorded with the new tropospheric recording system, and the results obtained during a joint experiment in Aspendale with the CSIRO Division of Atmospheric Physics. In this last data set, in addition to the lidar scattering profiles, radiosonde measurements of temperature, pressure and humidity and airborne measurements of temperature, pressure and nephelometer extinction profiles were used. The angular separation of consecutive profiles during elevation scans was five degrees for the Aspendale data and ten degrees for the Adelaide data.

The lidar scattering profiles are arranged in two parts. The first part contains system information including lidar shot number, the number of points in the profile, the laser energy and the elevation and azimuth angles and digitizer settings. The second part contains the values of the lidar signal which have been corrected for detector non-linearities, for the decrease with the square of the range, and for variations in lidar energy.

Various options have been written into the program. These include data output format, the selection of a particular radiosonde or aircraft data set, and the desired backscatter-to-extinction ratio. For each profile to be analysed the program reads a card selecting the desired profile number, its format type, the last profile number in the set, the calibration height and boundary value, the minimum range and the maximum

height to be used.

To initiate the analysis the system constant is calculated from the first profile at the lowest elevation angle, using a boundary value and the lidar return signal at the calibration height HCAL. Ideally HCAL should be as low as possible so that the transmittance to this height, which will vary with elevation angle, is negligible. The program then calculates the values of extinction, aerosol and molecular backscatter, transmittance, turbidity, and relative error in extinction for the rest of the profile.

To check whether a suitable boundary value has been chosen the calculated profiles of extinction and backscatter are then tested as follows. Too low a boundary value of extinction can cause the calculated values of aerosol extinction and backscatter to be negative in regions where such values would normally be small and positive. Some negative values are due to noise in the signal, but if there are too many negative values the boundary value is increased slightly and the analysis repeated.

The method of analysis used in the program is the modified clear-air calibration method, discussed in Section 5.2, which accepts independently derived boundary values of extinction in addition to the values of zero aerosol extinction at HCAL usually used in this method. The clear-air calibration method was chosen because radiosonde and aircraft data were available on many of the days and provided the opportunity of using virtually contemporary, high resolution data. Other methods of analysis, for example, the method discussed in the latter part of Section 5.5, could have been used. For those heights where both aircraft and radiosonde density profiles were available, the former were preferred because they were simultaneous with the lidar observations, more numerous, and measured

closer to the lidar site.

The analysis proceeds as follows. The values of extinction calculated are assigned to positions in an array containing one hundred positions in the horizontal direction and fifty locations in the vertical direction. Where more than one profile value is assigned to a particular location the values are averaged.

For the second and successive profiles in the elevation scan the calibration can be performed in either of two ways. In the first method, the calibration height is chosen as the height corresponding to the minimum or overlap range of the immediate profile, and the value of extinction from the previous profile for this height is used as the boundary value. This boundary value and the value of the system constant from the last profile are then used in the analysis of the signals from the other heights in the profile. Alternatively, if it is considered that more consistency between scattering values measured at different elevation angles exists in another height region, the value of HCAL can be changed during the program. The values of extinction and transmittance for this height from the previous profile are then used to initiate the analysis using the new HCAL.

If an indicator is set in the data cards, the program then performs a series of consistency checks on each extinction profile. These checks help overcome further variations in the calibration of the calculated profiles caused by noise fluctuations in the original signal. In the first test the optical thickness between two specified heights is calculated and compared with the value obtained from the previous profile (i.e. an adjacent region in space). If the ratio of the current optical thickness to the previous value, DOR, differs from unity by more than ten percent then the boundary value is adjusted and the extinction profile is re-calculated. After adjustment, consecutive values of optical thickness usually vary by less

than two to five percent because of the interpolation formula used.

A further check tests whether there has been a progressive upward increase in the value of the boundary value. This is done by testing a progressive product, PRODOR, of consecutive optical thickness ratios which if it is greater than 1.10, leads to the re-adjustment of the boundary value of extinction.

When the profile of extinction passes all of these tests satisfactorily, the values are assigned to positions in the array. The program then fills in the spaces between the profiles by performing a two-dimensional linear interpolation or extrapolation on the data, depending on where the space is in the array.

The output format of the data is determined by the programmer who can select various options. These include a tabular printout of values of total extinction and backscatter, and aerosol and molecular backscatter, and a plot of profiles of total extinction and molecular extinction for the profiles studied. The contents of the array are presented as a two-dimensional intensity modulated display in which overprinting on the computer's line printer is used to generate ten different levels of intensity. In addition the contents of the array can be plotted as a contour diagram or an intensity modulated display similar to that used with the line printer but this time using the CALCOMP plotter output of the University's computer, a CYBER 173. A simplified flow chart of the program is shown below.

(1) First Profile

(a) Calculate system constant K from boundary value using $\beta_A=0$ or $\beta=\beta^*$.

(b) Calculate profiles of B_R, B_A, B_T, β_T, T, $\Delta\beta_T/\beta_T$.

(c) Check number of negative B_A values. If NEGS >0.1 x

NTOT increase β(HCAL).

(d) Assign values of β_T to positions in 100 x 50 array. Average values if more than one value per position.

(2) Second and Successive profiles on Scan

(i) Either

(a) Calculate HMIN and use value of β(HMIN) and K from previous K.

OR

(b) Use β(HCAL) and T2(HCAL) calculated from previous profile where HCAL is read from input.

(c) Calculate profiles as in 1(b).

(ii) Perform Consistency Checks

(a) If requested check optical thickness between 2 specified heights with value from previous profile, i.e. If $\tau > 1.1 \times \tau_{PREV}$ or $\tau < 0.9 \times \tau_{PREV}$ adjust β(HCAL) and recalculate profile.

(b) Check that there has been no progressive increase in β(HCAL).

i.e. If PRODOR = PRODOR x DOR > 1.1 decrease β(HCAL) and re-calculate profile.

(iii) Assign values of β_T to positions in ARRAY as in 1(d).

(iv) Interpolate or extrapolate in 2-D to fill in space between this and previous profile.

(v) Print out data and 2-D diagram on line printer.

(vi) Plot diagram on drum plotter.

Here $\Delta\beta_T/\beta_T$ is the relative error in the extinction coefficient, NEGS is the number of negative values of extinction in the profile containing

a total of NTOT points, τ_{PREV} is the value of optical thickness for the previous profile and T2(HCAL) is the square of the optical transmittance of a beam directed vertically from the lidar to the calibration height HCAL.

CHAPTER SIX

RESULTS OF LIDAR OBSERVATIONS OF THE TROPOSPHERE

6.1 Introduction

This chapter presents the results of lidar observations of the troposphere performed at Adelaide (S.A.) and Aspendale (Vic.). The methods of analysis described in Chapter 5 are used to calculate profiles of extinction. Diagrams of its distribution in two dimensions allow the study of changes in the location and intensity of scattering irregularities in the atmosphere.

Although the fundamental result of lidar measurements is the backscatter function, the extinction coefficient is more useful as it determines the decrease in intensity of a light beam passing through the atmosphere and is related to the atmosphere visibility and visual range. For this reason, measurements of backscatter function are converted to extinction values by the use of the backscatter-to-extinction ratio. A value for this quantity is derived in Section 6.2.

Included in this Chapter are some initial results of observations made at Adelaide using the data recording system designed and built by the author and described in Chapter 2 and Appendix II.

In September 1976, a joint study was performed with the Division of Atmospheric Physics (CSIRO), to investigate the relationship between lidar and *in situ* measurements of aerosols. The results of these observations are studied more closely than the Adelaide data as more co-operative measurements were available.

6.2 The Measurement of the Aerosol Backscatter-to-Extinction Ratio

To relate lidar observations of aerosol backscatter function to the more useful extinction coefficient, a conversion factor is required. This quantity is usually referred to as the backscatter-to-extinction ratio and is numerically equal to $P_A(\pi)/4\pi$, the value of the normalised aerosol phase function for the case of backscatter. Several methods were tried in an attempt to determine a representative value for this quantity.

An experimental program conducted at Aspendale, Victoria, during September 1976 provided the opportunity for the derivation of the ratio. In addition to the CSIRO's fully steerable ruby laser, a small aircraft was equipped with an integrating nephelometer, a Pollak counter, and pressure and temperature sensors so that vertical profiles of extinction, particle number density, and temperature could be measured. Radiosonde ascents were made from Laverton, 36 km to the North West, across Port Phillip Bay, at 0900 and 2100 EST, and from Aspendale, 4 km east of the lidar site at around noon. Standard meteorological measurements made on site at the CSIRO's Division of Atmospheric Physics were available also. The data used in the determination of the ratio were obtained on the afternoon of the 15th and the morning and afternoon of the 16th of September, the days studied in most detail later in this chapter.

The first method tried was the direct comparison of extinction profiles measured by airborne nephelometer with profiles of backscatter function derived by lidar, using the extinction profiles to correct for the attenuation of the lidar beam as it passed through the atmosphere. Difficulties were experienced with this method for several reasons; on most days the nephelometer gave extinction values which were too low to account for the attenuation of the lidar beam and did not agree with the other values of extinction derived from visibility estimates and lidar elevation scans.

Apart from possible spatial differences in the sampling volume, which would be expected to average out over several observations, significantly low values of extinction were measured in layers of high humidity. Waggoner *et al*, (1972) state that the nephelometer warms the air that it samples, thereby causing a decrease in the size of the aerosols as they lose absorbed water, and as a result, a decrease in extinction. In addition, the lidar and nephelometer wavelengths were different, 694.3 nm and 641 nm respectively, and the nephelometer's optical bandwidth was much wider. As there is some uncertainty in the exact wavelength dependence of aerosol extinction, some error could have occurred in the conversion from one wavelength to the other.

Another approach was the elevation scan method described in Section 5.3. This method produces profiles of the product of the backscatter function and the system constant, in addition to the profiles of extinction. Unfortunately no day studied had sufficient horizontal homogeneity to permit the use of this method over a large enough range of heights or extinction values. However, the method was useful in determining boundary values on some days and remains the most promising method because the same device, and hence wavelength and bandwidth, is being used to determine both extinction and backscattering profiles.

Ultimately the extinction profiles were obtained from profiles of aerosol number density measured by an airborne Pollak counter. Initially this method was treated with caution as the Pollak counter also detects many small (Aitken) particles which are not detected efficiently by the lidar. However, provided the aerosol size distribution and phase function do not vary significantly over the height range studied, the extinction profile will be proportional to the particle number profile; the constant

of proportionality can be determined from a boundary value of extinction. Several workers (e.g. Twitty *et al*, 1976; Reagan *et al*, 1977) have found the aerosol size distribution to be constant over significant height ranges and Reagan *et al*, have in fact found excellent correlation between lidar extinction and large particle ($d > 0.5$ μm) concentration profiles.

One further refinement to this last method is the consideration of the effect of the change in relative humidity with height on the extinction profile derived from particle number densities. Werner (1972), in studying the effect of relative humidity on lidar measurements of atmospheric aerosols, compares his lidar results with the empirical formula of Kasten (1968), which gives the ratio of extinction coefficients at two different relative humidities, f_1 and f_2, as

$$\beta(f_1)/\beta(f_2) = ((1 - f_2)/(1 - f_1))^{2\varepsilon} . \qquad 6.1$$

Hänel (1971) found values of $\varepsilon = 0.26$ for maritime aerosols and $\varepsilon = 0.17$ for continental aerosols.

In the present study relative humidity profiles were obtained from radiosonde flights made from Laverton and Aspendale. If the radiosonde flights and lidar soundings were well separated in time, linear interpolation was used to give a more representative profile. For two of the sets of data studied, the afternoon airstream was flowing from over Port Phillip Bay and a maritime aerosol was assumed; for the other the morning wind was NNW at 0.5 $msec^{-1}$ and a continental aerosol was assumed. As a check on the assumed dependence on relative humidity, the formula of Barnhardt and Streete (1970) was used for the maritime aerosols and similar results were obtained.

Boundary values of extinction were derived by two methods, both discussed in Section 5.6. The method where several lidar returns from different elevation angles are compared was used when the atmosphere was sufficiently homogeneous in the horizontal direction, otherwise the derivation of extinction boundary values from concurrent, on site, measurements of visibility was used.

The derivation of a boundary value using the elevation scan method is illustrated in Figure 6.1. In (a) the range-corrected lidar signals measured at five degree elevation increments between fifteen degrees and ninety degrees are plotted. A strongly scattering layer below 480 m and a weaker region of enhanced scattering below 1500 m are common to all profiles. The main differences are attributable to the overlap height, which increases with elevation angle, and the attenuation of the lidar signal in the lower layer which decreases with elevation angle.

Section 5.3 shows that the atmospheric transmittance between the ground and a particular height can be derived from the slope of a graph of $\ell n(PR^2)$ against cosec θ for that height. In (b) the data in (a) are replotted in this manner. The lack of linearity in the graphs and the lack of a monotonic increase in slope, particularly above 400 m , is caused by inhomogeneities in the atmosphere. To reduce this effect, two elevation scans were averaged and the slopes ($B = 2\ \ell n\ T$) of the resultant graphs are plotted in (c). The average extinction between 200 m and 400 m calculated using Equation 5.7 is $1.6 \times 10^{-4}\ m^{-1}$.

The profiles of extinction derived from the Pollak counter data for the three experimental sessions used are plotted in Figure 6.2. The molecular extinction profiles derived from radiosonde measurements and the total extinction profiles are also shown. It should be emphasised that the

FILE 30 760916 0953-0959

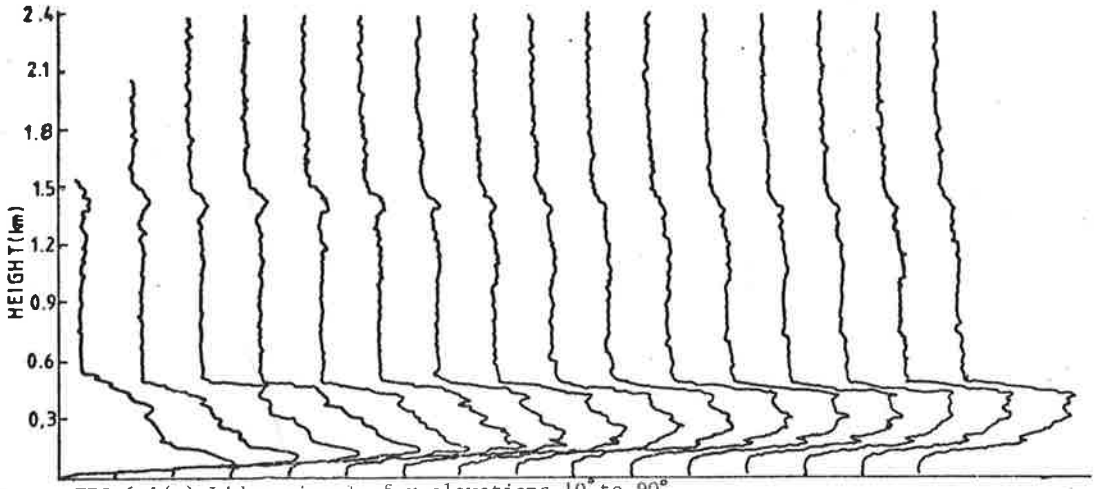

FIG 6.1(a) Lidar signals for elevations 10° to 90°.

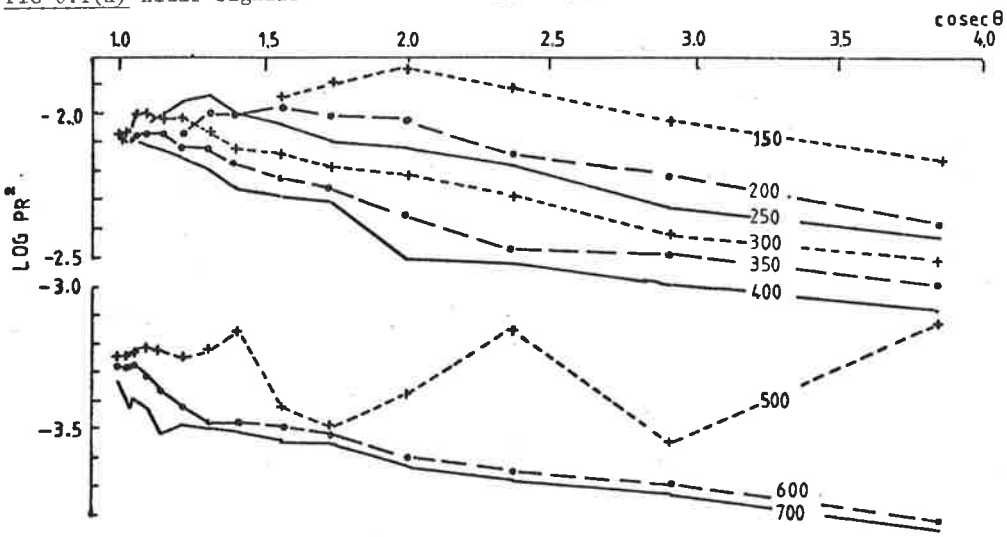

FIG 6.1(b) Calculation of $B(h) = 2\log_{10}(T(0,h))$

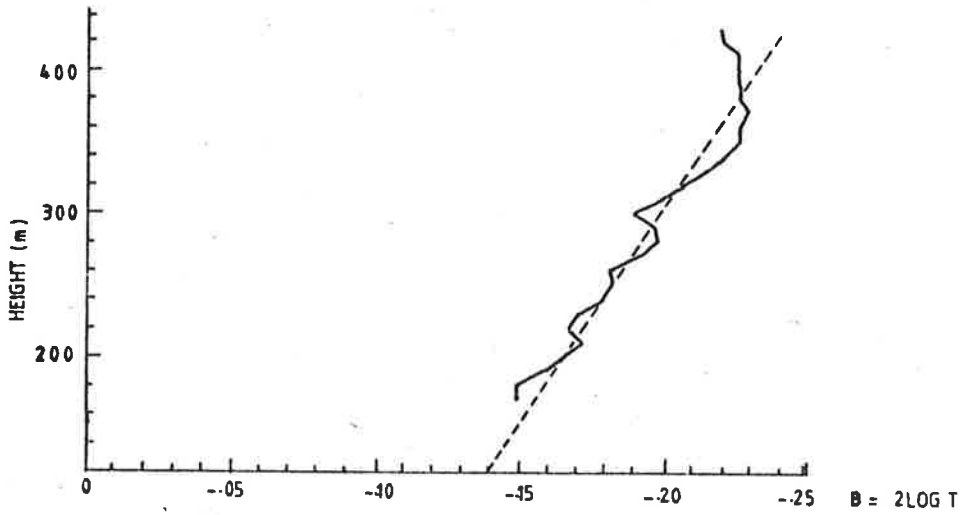

FIG 6.1(c) Calculation of an average boundary value of extinction.

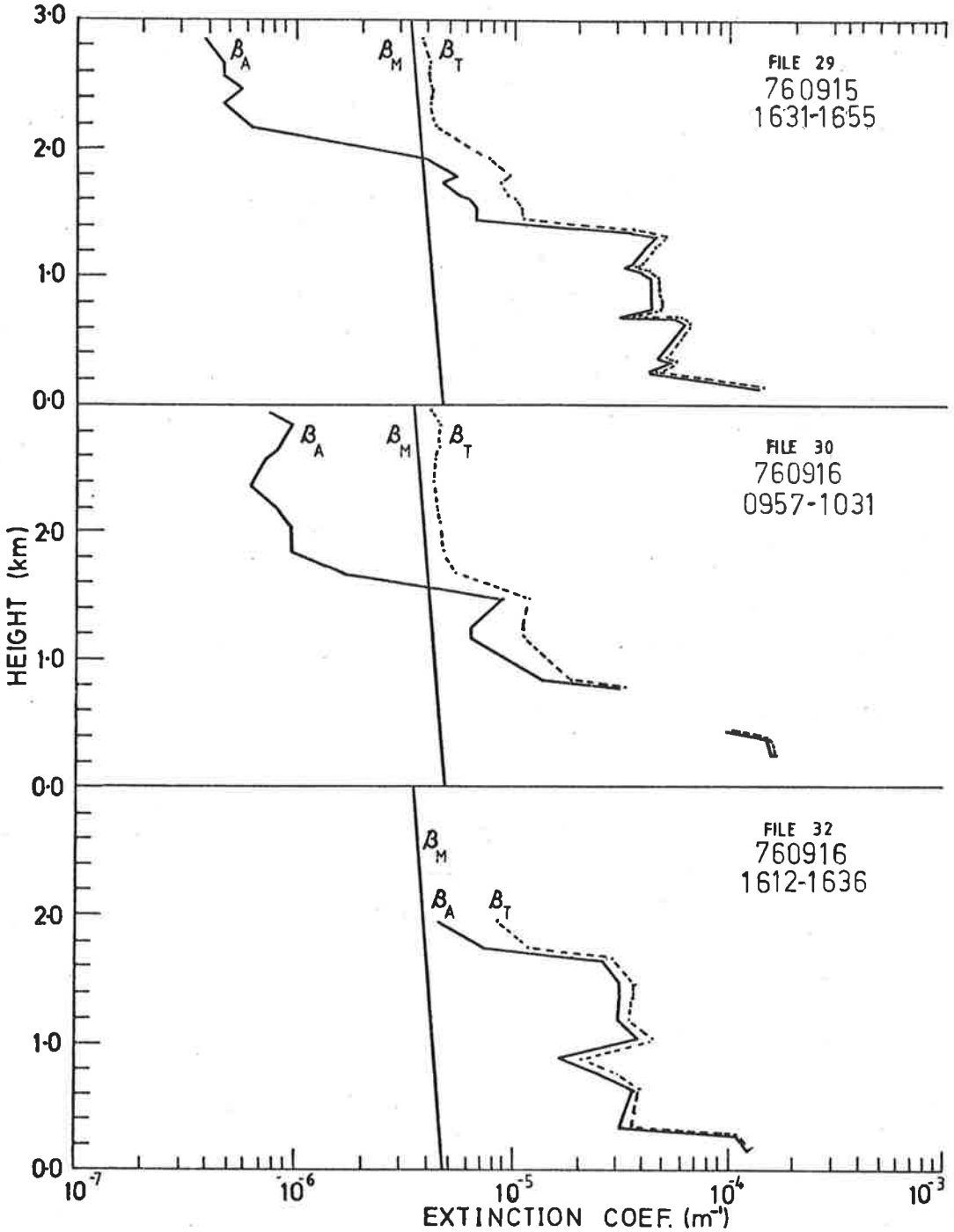

FIG 6.2 Extinction profiles calculated from composite Pollak counter profiles.

graphs are derived from a composite of two or more Pollak counter profiles.

Lidar measurements of PR^2 at several elevation angles, as shown in Figure 6.1(a), were divided by values of transmittance derived from the extinction profiles in Figure 6.2 to produce an average profile of KB_T for each session. These profiles were then used with the extinction profiles to derive a value for both the lidar system constant and the backscatter-to-extinction ratio. The symbols used here and in the following discussion are consistent with their use elsewhere in this thesis.

In their comparison of ground level nephelometer extinction values with the backscatter from a horizontal lidar beam, Waggoner *et al*, (1972) plotted KB_T *vs* β_T and were able to solve for K and $P_A(\pi)$. In the present case the height studied varies and β_M is not constant, so the following procedure is adopted.

As $$B_T = B_A + B_M \ , \qquad 6.2$$

then $$KB_T = K(P_A(\pi)/4\pi).\beta_A + KB_M \ , \qquad 6.3$$

and therefore $$KB_T/B_M = K(P_A(\pi)/4\pi).\beta_A/B_M + K \ . \qquad 6.4$$

A graph of KB_T/B_M plotted against β_A/B_M has slope $K\,P_A(\pi)/4\pi$ and intercept K, both of which may be obtained graphically or by linear regression. A graph using the present data appears in Figure 6.3. A linear, least squares fit to these data yielded the following values :

$$K = (4.1 \pm 0.4) \times 10^4 \ ,$$
$$P_A = 0.32 \pm 0.02 \ , \qquad 6.5$$

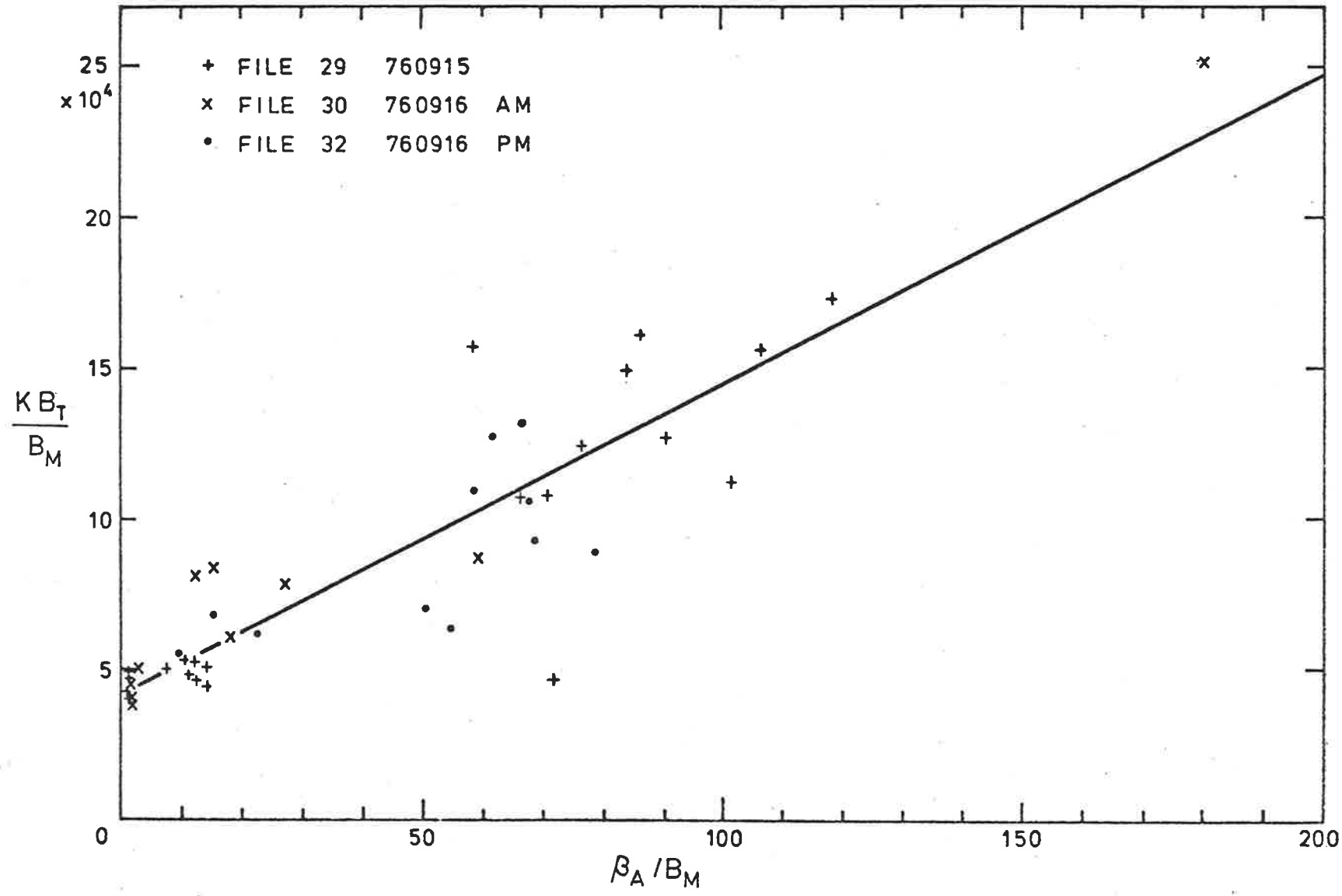

FIG 6.3 Calculation of the Backscatter-to Extinction Ratio.

with a correlation coefficient of 0.91 for the fifty points used.

Four data points were excluded from the analysis because they seemed unrepresentative. They were the lowest two points in File 30 and File 32. It is considered that errors in the relative humidities used to adjust the extinction coefficients at these heights led to incorrect values. In the first case it is possible that the relative humidity of the air measured at Laverton, across Port Phillip Bay, could have been modified in the lowest regions by the sea air. In the second case no relative humidity profile was measured concurrently with the lidar sounding and an interpolated profile using the 1200 EST, Aspendale radiosonde and the 2100 EST, Laverton radiosonde was used. Again, errors could have occurred if there had been modification by the sea air.

It has been assumed in this analysis that absorption is negligible at the wavelengths used and that the attenuation of the lidar beam is due entirely to scattering. Visual observations of the quality of the air on the days in question supported this assumption. The limitation in visibility was caused by a slightly "milky" appearance of the air, with no brown patches of industrial pollution apparent to the naked eye. It would seem then that the attenuation was due predominantly to scattering.

While the value of $P_A(\pi)$ may change in time and location, the value derived here is considered the most applicable to the Aspendale data analysed in this chapter. In the absence of any similarly derived value for the Adelaide data the same value is used for that also.

6.3 Values of Extinction Derived from Lidar Backscatter Measurements

For the reasons discussed earlier in this chapter, lidar results

are presented as extinction coefficients rather than values of backscatter function. Over small height ranges and low values of extinction, profiles of extinction for different values of the backscatter-to-extinction ratio can be obtained by simple proportion.

An example showing the variation in vertical profiles of atmospheric extinction over Adelaide during the period 0445 to 1030 CST appears in Figure 6.4. The left hand side of the figure gives the relevant meteorological data measured by the Adelaide radiosonde balloon launched at 2300 Z (0830 CST). The day was fine with a maximum temperature of 17°C and a large, weak high pressure system to the east brought light northerly winds from over the land.

Each profile represents the average of ten lidar returns. These profiles show the limitation of using the six-bit recording system without the logarithmic amplifier. The relatively small recorded signal scattered from the clearer air above the mixing layer is reduced further by the range squared decrease in the signal, and consequently, digitisation uncertainties cause large fluctuations in the upper part of the derived extinction profiles.

The oscillation apparent in some profiles is a result of the deconvolution of the recorded data to remove the effect of the limited bandwidth of the recording system when it is used in this mode of operation. The decrease in intensity at the lower end of the profiles is attributable to the gradual reduction in overlap of the transmitter and receiver cones, and the missing portions of the profiles represent regions where the calculated extinction is negative.

Apart from the profile at 1020, each profile shows the presence of a lower layer which decreases in scattering intensity to a relatively

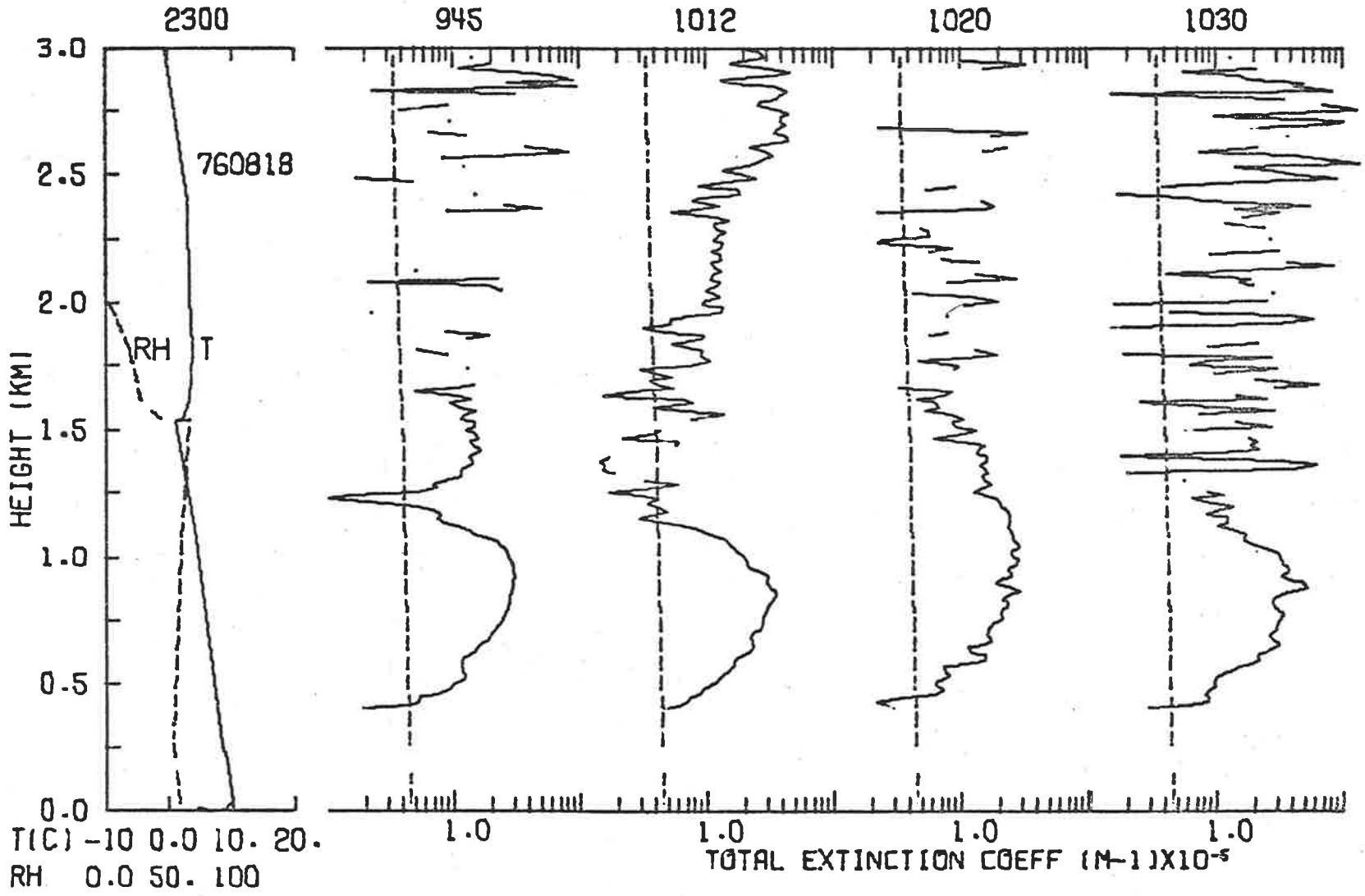

FIG 6.4 The LHS graph shows the temperature profile (——) and relative humidity profile (---) measured by radiosonde. The RHS graphs show extinction profiles derived by lidar (——) compared with the molecular extinction profile (---).

clear region near 1250 m . The vertical extent of this clearer region varies between profiles but the confidence in the extinction values in this region is low.

The data presented in Figure 6.5 were recorded using a logarithmic amplifier which permitted the measurement of signals over a greater range. The profiles were recorded at the various elevation angles shown and are plotted as a function of height, not range.

The radiosonde profiles were measured at 1100 Z (2030 CST), some 8½ hours after the lidar observations; this possibly explains why the top of the moist layer measured by the radiosonde is slightly higher than that measured by lidar. On this day a high pressure system was centred just south of Adelaide and brought light, easterly winds over the continent to Adelaide.

The profiles were calibrated with a boundary value of $1.6 \times 10^{-4} m^{-1}$ obtained from the comparison of lidar returns from 3° and 5° elevation between the heights of 50 m and 180 m. The two beam method described in Section 5.6 was used with Equation 5.34.

These data have been used to produce a diagram (Figure 6.6) of the spatial distribution of the scattering inhomogeneities using the computer program described in Section 5.7. Strength of scattering is indicated by the darkness of the plotted region using a logarithmic scale. The values plotted are $10 \log_{10} (\beta/\beta_{MIN})$, and the key at the bottom indicates ten, evenly spaced, logarithmic intervals between $\beta_{MIN} = 2.0 \times 10^{-5} m^{-1}$ and $\beta_{MAX} = 1.0 \times 10^{-4} m^{-1}$. Figure 6.6 shows a well defined layer below about 1000 m which includes a scattering minimum at about 500 m , and weaker scattering above 1000 m. Scattering is not

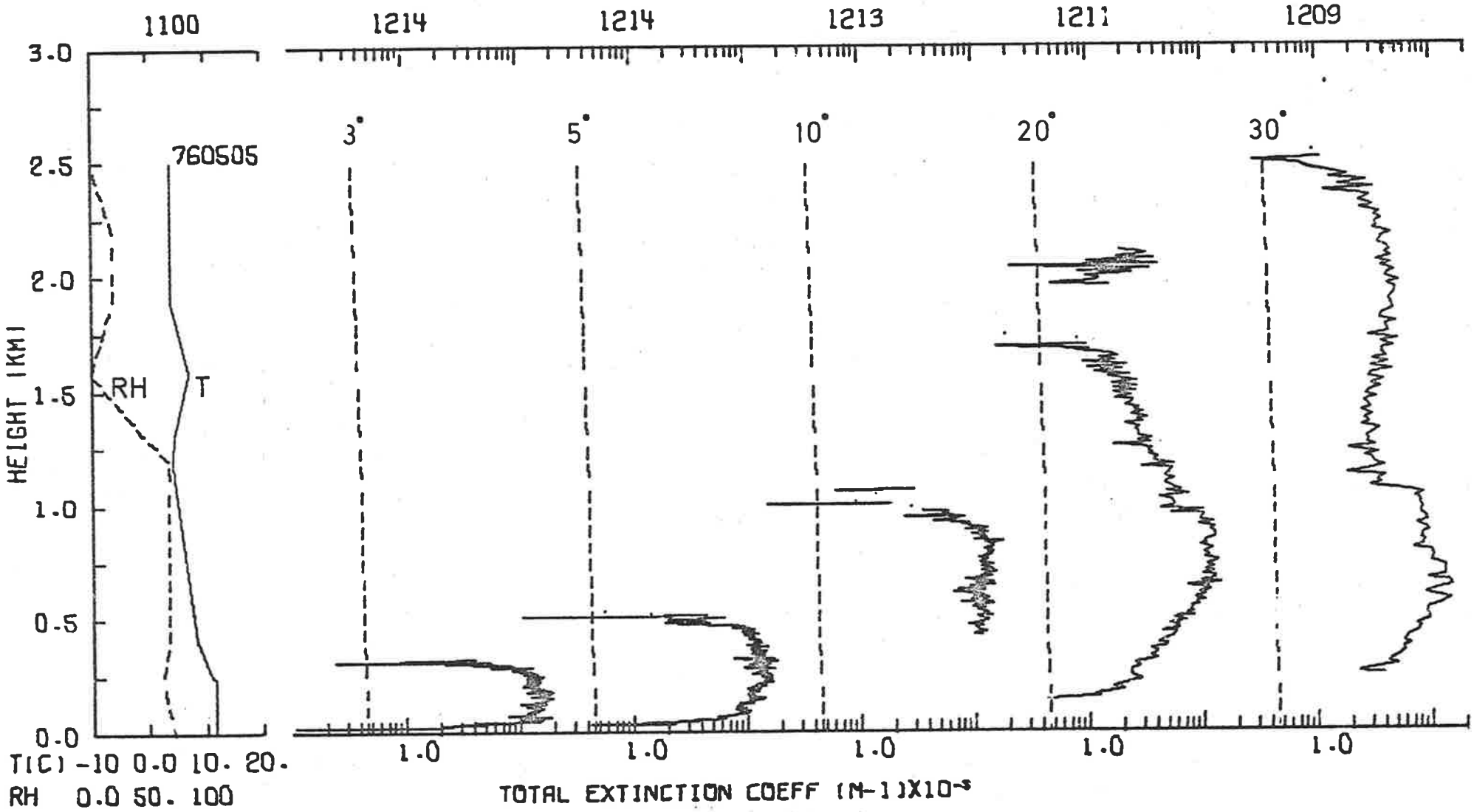

FIG 6.5 Caption as in Fig 6.4 .

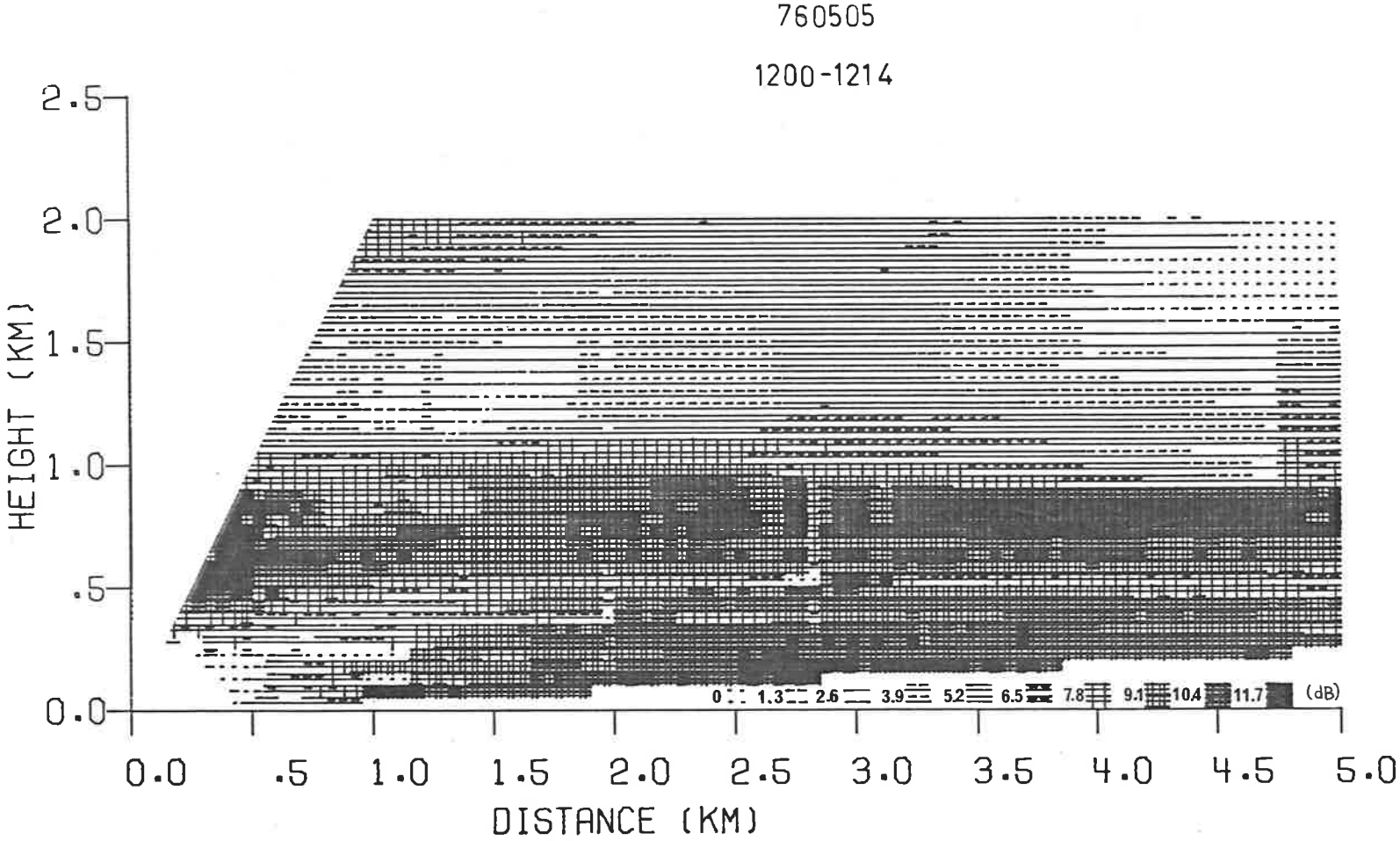

FIG 6.6 Lidar-derived values of total extinction coefficient. Key shows 10 levels of $10 \log_{10}(\beta_{MAX}/\beta_{MIN})$

$\beta_{MAX} = 2.0 \times 10^{-4} m^{-1}$, $\beta_{MIN} = 1.0 \times 10^{-5} m^{-1}$

homogeneous, either in the unstable boundary layer or in the region above.

In September 1976 an experimental program was performed in Aspendale, using the SRI-CSIRO Mk X lidar, (Allen and Platt, 1977). The essential features of the equipment and treatment of the data are as follows.

The CSIRO lidar system has a 1.5J ruby laser transmitter and a 35.5 cm diameter receiver. A fast, mini-computer controlled, Biomation transient recorder with a capacity of 2024 8-bit words samples the data at intervals as short as 10 ns. The storage of several hundred profiles, each with 2024 words, on the memory disks of the computer used for analysis created problems of space. To alleviate these problems each profile was subjected to an initial treatment before being studied in more detail. Here, regardless of the original elevation angles or sample intervals, points corresponding to measurements at each ten metres in height were calculated by averaging all points in the original profile within five metres above or below a particular height. Thus, new profiles were created with points evenly spaced in height; the number of points in each varied with the elevation angle.

The results are presented in Figure 6.7 in a form similar to Figures 6.4 and 6.5. In addition, in the left hand diagram, the temperature profile measured by aircraft at about the time of the lidar elevation scan is indicated by discrete points. The profile of extinction measured by nephelometer on the same flight, and adjusted to the lidar wavelength assuming a λ^{-1} dependence for aerosol extinction, is plotted with the lidar extinction profiles as the main part of the diagram. Error bars ($\pm$ 1 s.d.) are plotted every 250 m in height. These include the

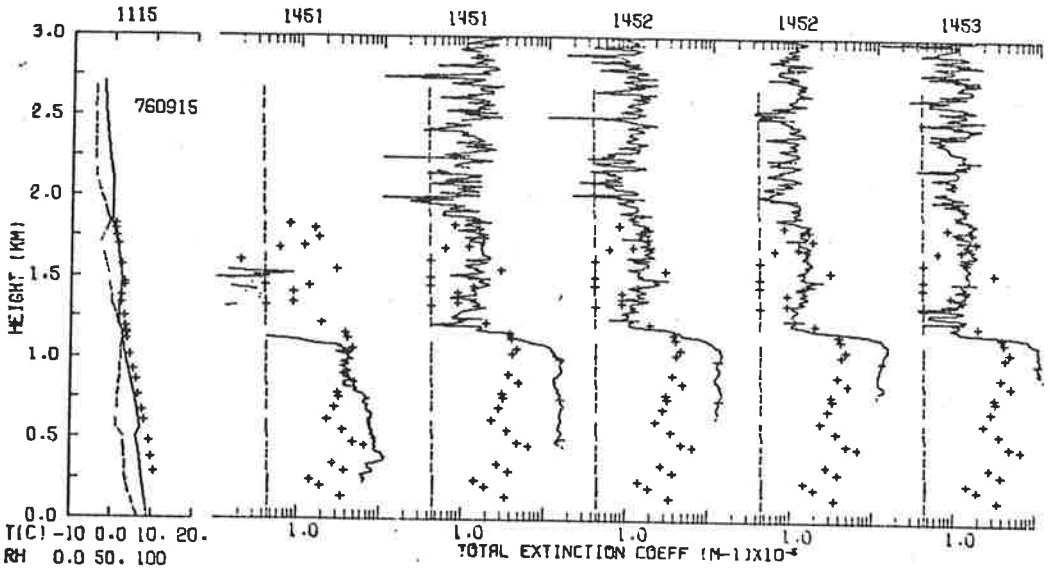

FIG 6.7(a) The LHS graph shows temperature profiles measured by radiosonde (——) and aircraft (+++) and the radiosonde relative humidity profile (---). The RHS graphs show extinction profiles, derived by lidar (——) at 15°, 30°, 45°, 60°, 90°, and nephclometer (+++), compared with the molecular extinction profile, (___).

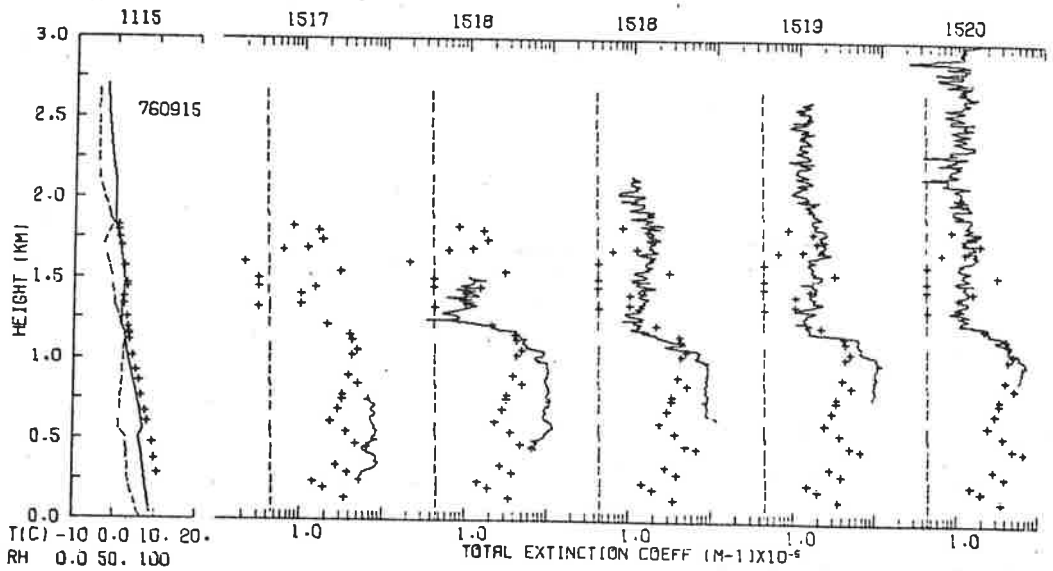

FIG 6.7(b) The LHS graph shows temperature profiles measured by radiosonde (——) and aircraft (+++) and the radiosonde relative humidity profile (---). The RHS graphs show extinction profiles, derived by lidar (——) at 15°, 30°, 45°, 60°, 90°, and nephclometer (+++), compared with the molecular extinction profile, (___).

effects of uncertainties in the measured signal, the backscatter-to-extinction ratio, the molecular density and transmittance profiles, and the aerosol transmittance profile; they do not include the effect of errors in normalisation. They are almost indistinguishable on the lower diagrams.

The results presented in Figure 6.7 were obtained from observations on the afternoon of September 15th. The day was characterised by early morning fog, with 1/8 of low strato-cumulus cloud around midday and 1/8 of low cumulus at 1500 EST, after which time the sky in the region over the lidar site cleared completely. Winds which were northerly at 3 m sec^{-1} in the morning gave way to SSW winds at 5 m sec^{-1} by the afternoon. Visibility increased from 2 km in the morning to 12 km around midday and then to 24 km at 1500 EST.

The two elevation scans presented in Figure 6.7, as can be seen by the shot-times above each profile, were taken approximately twenty minutes apart. Each scan contains sixteen profiles covering the range 15° to 90° in 5° steps. The laser was fired once every ten seconds so the scan was completed in two and a half minutes. The airborne nephelometer and temperature data were measured between 1441 to 1449 and a dry adiabatic lapse rate (DALR) was recorded up to approximately 1200 m, the height corresponding to the top of the mixing layer as measured by the lidar and the nephelometer.

The calibration of profiles for this day with boundary values of extinction was complicated by two factors. The first was the lack of horizontal homogeneity in scattering which precluded the calculation of extinction values by the elevation scan technique. The second was the use of a small receiver acceptance angle which caused a large overlap range and, when combined with a minimum elevation angle of fifteen degrees set by the

presence of buildings and other obstructions, set the minimum observable height at approximately 230 m. This was considered too great a height for the direct comparison and calibration with boundary values obtained from visibility measurements, so a value corresponding to the minimum lidar height was obtained from the aerosol number density profile described earlier.

The strength of the signal returned from the minimum elevation angle changed from scan to scan with the passage of air with a different aerosol content. The lidar signal strength at the minimum range was assumed to be directly proportional to the aerosol backscatter, and the boundary value for each elevation scan was scaled accordingly, using the scan measured at the time of the visibility observation as a reference. The presence of a strongly scattering region at a range less than the overlap range would, of course, cause an apparent reduction in the signal of the minimum useful range and invalidate the previous assumption, but none was obvious in an examination of the data.

The boundary value chosen in Figure 6.7(a) was $6.4 \times 10^{-5} m^{-1}$ at a height of 233 m. The elevation scan was at an azimuth of 70°, the approximate direction of the measurement of the nephelometer profiles in spiral ascents and descents by the aircraft. With the lack of homogeneity in the distribution of aerosols, exact agreement would not be expected between the profiles measured by nephelometer and by lidar at a given elevation angle, although successive lidar profiles do intersect the aircraft's spiral path at different heights. In general the nephelometer profiles indicate lower extinction values than those measured by lidar. Note that in the clearer air above the mixing layer, the nephelometer values are less accurate and fluctuations due to signal noise are apparent.

The elevation scan in Figure 6.7(b) was to the north of the lidar site and despite differences in time and direction of the two scans, the broad features of the lidar profiles are similar although they differ in the finer detail. The sampling interval in the second scan is half that of the former so the maximum range is half.

The general features seen in both scans are the 1200 m depth of the mixing layer and the appearance of a broad layer of weaker extinction extending from above the main layer to approximately 2000m . The error bars at 250 m height intervals increase markedly at heights above the main layer where they are dominated by the noise fluctuations in the weaker signal which are comparable in size.

The full information available in the sixteen profiles in an elevation scan has been used to produce diagrams of the spatial distribution of aerosols; examples of these appear in Figure 6.8. The range in extinction between a minimum value of $2.0 \times 10^{-6} m^{-1}$ and a maximum of $2.0 \times 10^{-4} m^{-1}$ is divided into equal logarithmic intervals, each of 2 dB. Values which correspond to the lowest level shown in the left of the key at the bottom of the figure correspond to values in the range 0 to 2 dB above the minimum level, or extinction values of between $2.0 \times 10^{-6} m^{-1}$ and $3.17 \times 10^{-6} m^{-1}$. Note that data within 900 m range of the lidar are inside the region of incomplete overlap of the lidar beams and may not indicate the correct extinction values there; those values plotted are obtained from the extrapolation of neighbouring data.

The upper scan occurred between 1503 and 1505 EST in an approximately easterly direction and the lower, twelve minutes later, to the north. Both the main mixing layer below 1200 m and the weaker layer above are shown in (a) and (b). A layer of stronger scattering between about 500 m and 750 m also exists and can be compared with the 15°

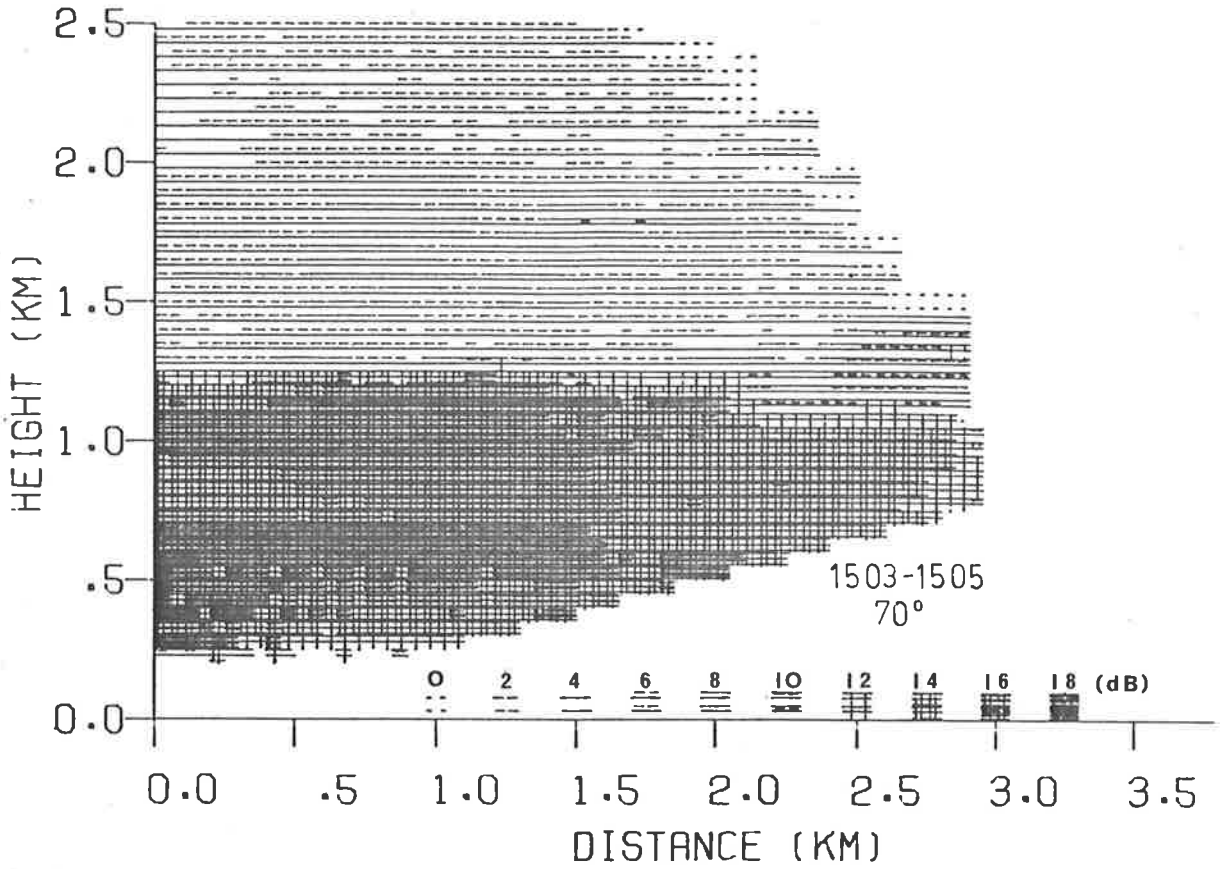

FIG 6.8(a) Lidar-derived values of total extinction coefficient. Key shows 10 levels of $10 \log_{10}(\beta_{MAX}/\beta_{MIN})$

$\beta_{MAX} = 2.0 \times 10^{-4} m^{-1}$, $\beta_{MIN} = 2 \times 10^{-6} m^{-1}$

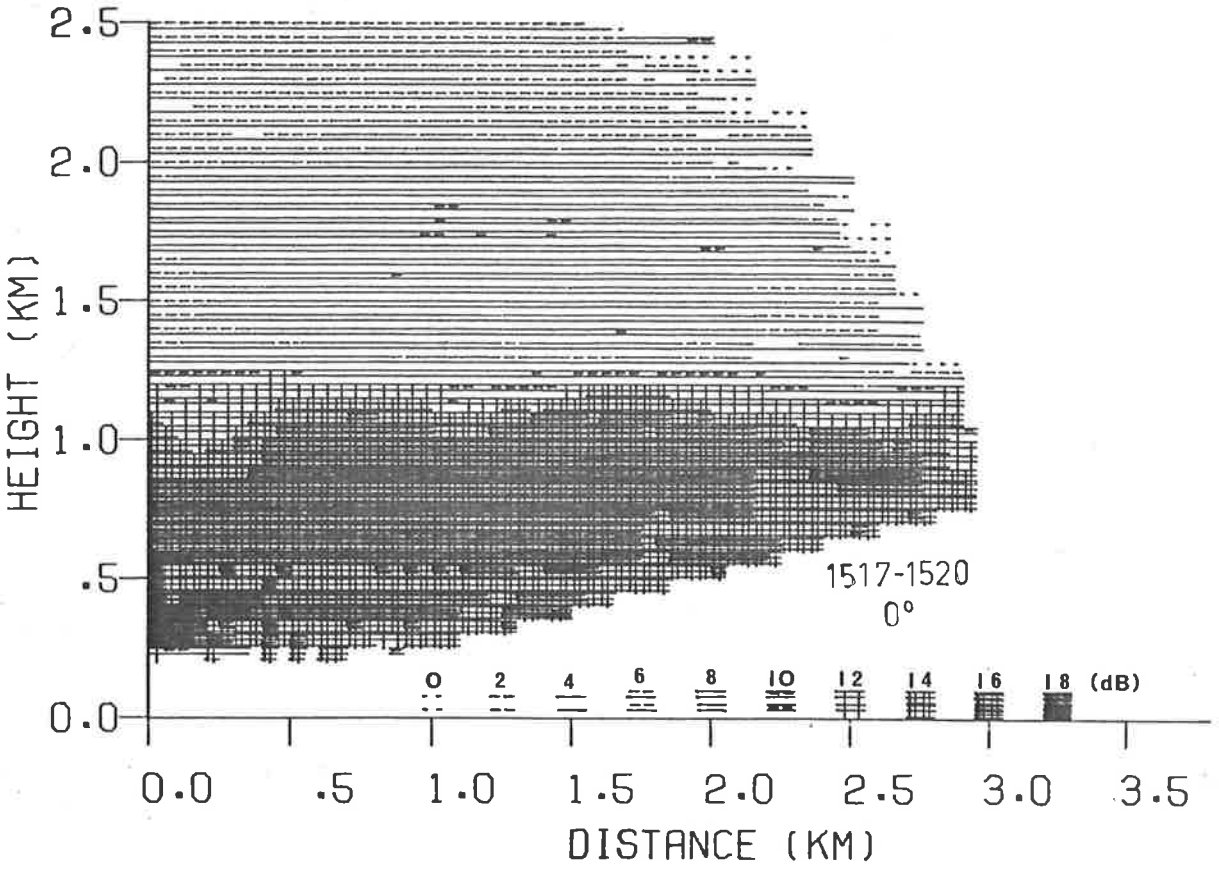

FIG 6.8(b) Lidar-derived values of total extinction coefficient. Key shows 10 levels of $10 \log_{10}(\beta_{MAX}/\beta_{MIN})$

$\beta_{MAX} = 2.0 \times 10^{-4} m^{-1}$, $\beta_{MIN} = 2 \times 10^{-6} m^{-1}$

elevation profile in Figure 6.7(a). The distinct lack of horizontal homogeneity shows in both scans above and below the main layer indicate that methods which require this condition for the calculation of extinction values are invalid here.

As discussed in Section 5.7, consecutive profiles can be adjusted to achieve consistency in the optical thickness between two specified heights. In Figure 6.8 the heights are 1800 m and 3000 m, thus defining a region above the distinct layers where the distribution of aerosols is more random, so that the value of the optical thickness is more likely to average out to the same value for successive profiles.

Note that in Figure 6.8(b) there are many places above the main layer where the plotted extinction is higher by one contour level than in (a). Two factors contribute : one is the uncertainty in normalisation, an effect which has been minimised but obviously still can exist to some degree; the other is the noise in the signal which is comparable to the lower contour levels at heights above the main layer where the signal becomes weaker.

After a break of about half an hour, lidar observations were resumed to coincide with another airborne sampling sequence. The most noticeable features in the new set of observations, presented in Figure 6.9, are the appearance of another strongly scattering layer at about 1400 m, and the decrease in the extinction below this layer when compared with earlier values. Apparently convection has carried aerosols up to a greater height with the increase in the depth of the mixing layer, or alternatively, advection has introduced the new layer. The former is considered more likely in view of the decrease in scattering below the new layer.

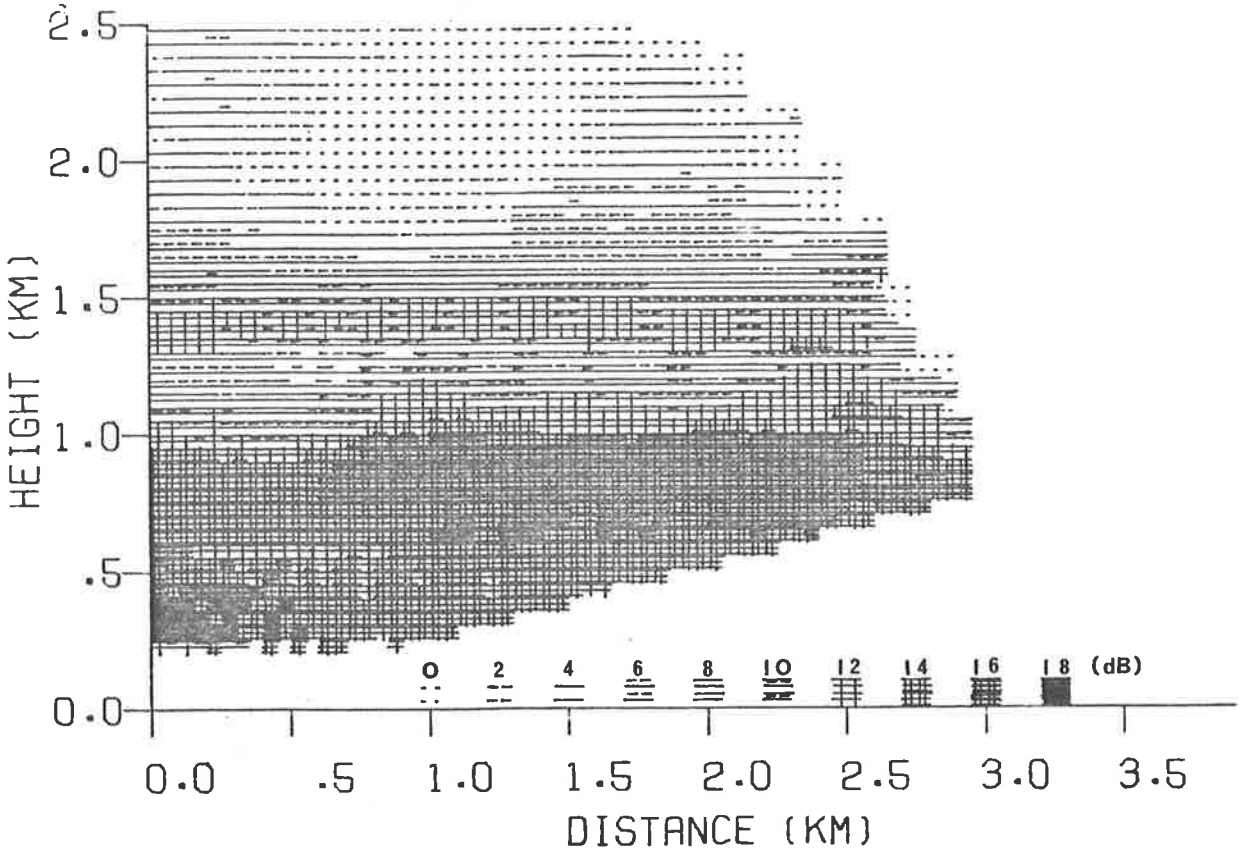

FIG 6.9(a) Lidar-derived values of total extinction coefficient. Key shows 10 levels of $10 \log_{10}(\beta_{MAX}/\beta_{MIN})$

$\beta_{MAX} = 2.0 \times 10^{-4} m^{-1}$, $\beta_{MIN} = 2 \times 10^{-6} m^{-1}$

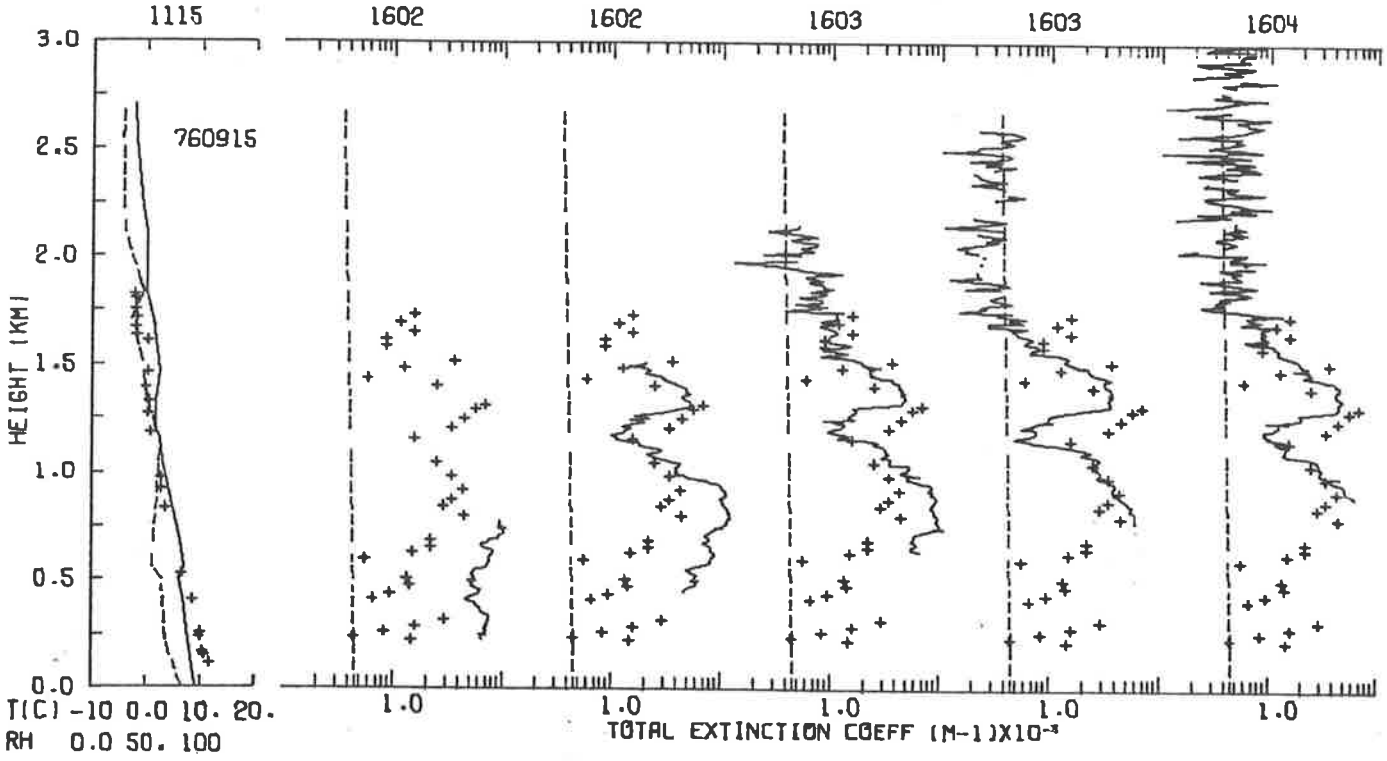

FIG 6.9(b) The LHS graph shows temperature profiles measured by radiosonde (——) and aircraft (+++) and the radiosonde relative humidity profile (---). The RHS graphs show extinction profiles, derived by lidar (——) at 15°, 30°, 45°, 60°, 90°, and nephclometer (+++), compared with the molecular extinction profile, (___).

The nephelometer extinction profile also shows the new layer but in this case the values for the upper layer are inexplicably greater than those for the lower, a fact not shown in the lidar profiles although they do show a weakening of the lower layer. The nephelometer profile is one measured between 1645 and 1655 EST on a descent from 1800 m. The previous ascent and descent which were contemporary with the lidar scan shown and also extended to 3000 m altitude were not used. During the aircraft's tightly banked spiral ascent and descent, direct sunlight and sunlight scattered from the atmosphere to the west in the late afternoon had leaked into the nephelometer and caused a strong, periodic increase and decrease with height to be recorded in the extinction profiles. The profiles were therefore unusable, and the later profiles are shown here.

Two other elevation scans of the later scattering situation appear in Figure 6.10. The upper is a scan at 70° azimuth at 1558-1600 EST and the lower to the north at 1609-1613 EST. The boundary values for extinction at a height of 233 m for the 15° elevation profile are $6.5 \times 10^{-5} m^{-1}$ and $7.7 \times 10^{-5} m^{-1}$ respectively. Because a study of the raw data showed a degree of consistency in the features of the upper layer, optical thickness comparisons during the analysis of the data from both scans were made in the region from 1350 m to 1500 m which includes the layer. A strongly scattering layer within the main layer is detectable in Figures 6.9 and 6.10.

Figure 6.11 extends the data in Figure 6.10(a) up to 12 km, the limit of the local radiosonde launched at 1115 EST. The signal returned from these greater heights is weak and there is a considerable uncertainty in the extinction values as is evidenced by the magnitude of the error bars which are often large and lost in the signal noise, the dominant contributor

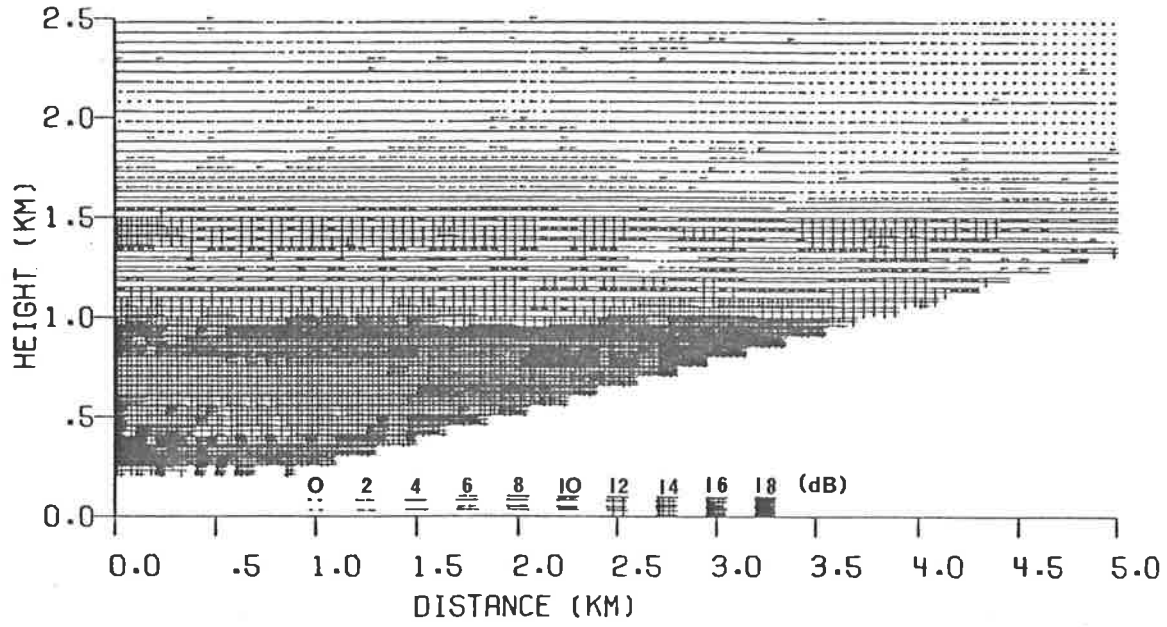

FIG 6.10(a) Lidar-derived values of total extinction coefficient. Key shows 10 levels of $10 \log_{10}(\beta_{MAX}/\beta_{MIN})$

$\beta_{MAX} = 2.0 \times 10^{-4} m^{-1}$, $\beta_{MIN} = 2 \times 10^{-6} m^{-1}$

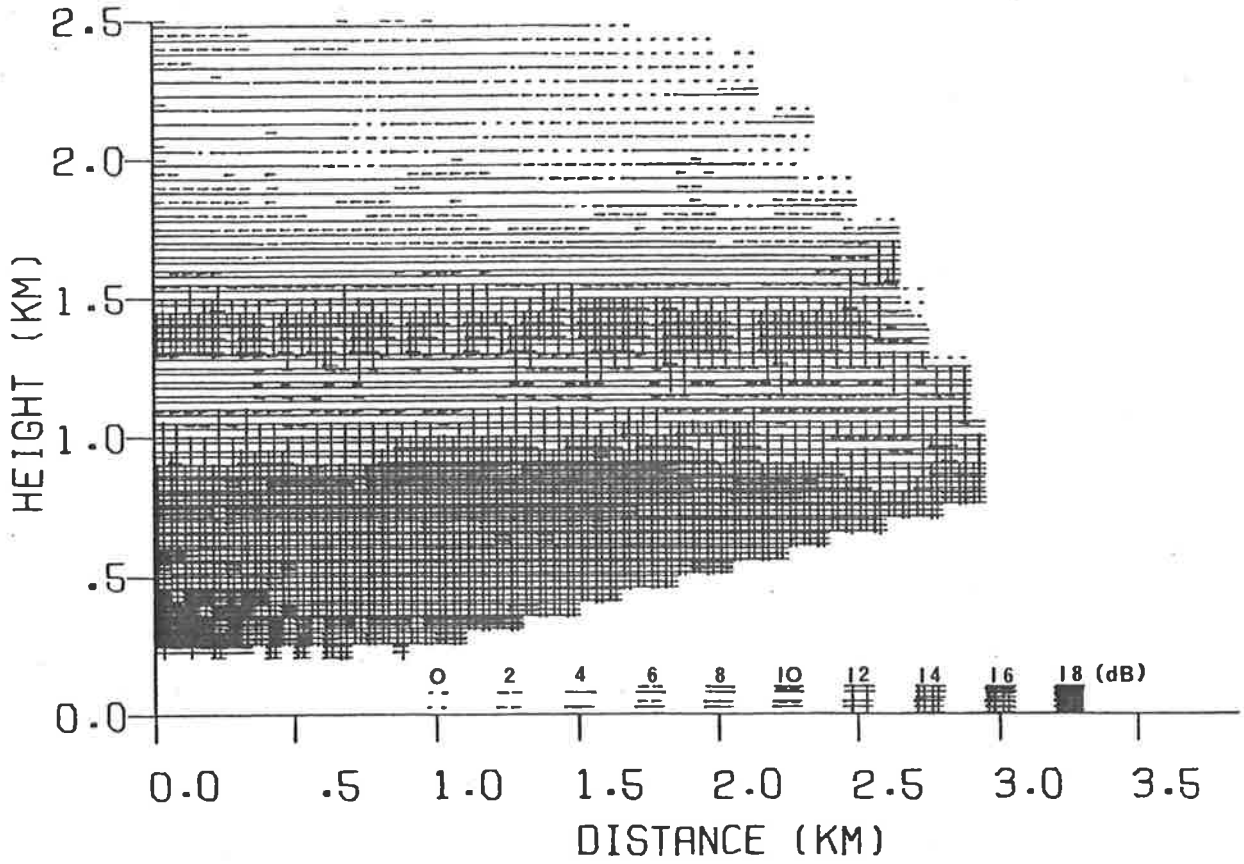

FIG 6.10(b) Lidar-derived values of total extinction coefficient. Key shows 10 levels of $10 \log_{10}(\beta_{MAX}/\beta_{MIN})$

$\beta_{MAX} = 2.0 \times 10^{-4} m^{-1}$, $\beta_{MIN} = 2 \times 10^{-6} m^{-1}$

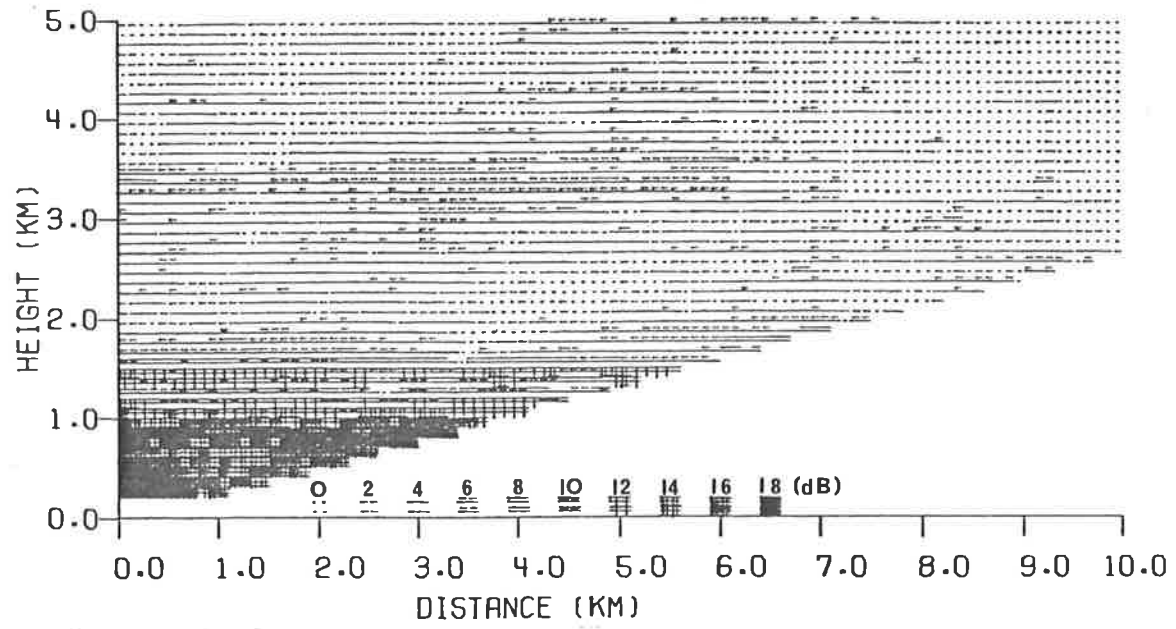

FIG 6.11(a) Lidar-derived values of total extinction coefficient. Key shows 10 levels of $10 \log_{10}(\beta_{MAX}/\beta_{MIN})$

$\beta_{MAX} = 2.0 \times 10^{-4}\,m^{-1}$, $\beta_{MIN} = 2 \times 10^{-6}\,m^{-1}$

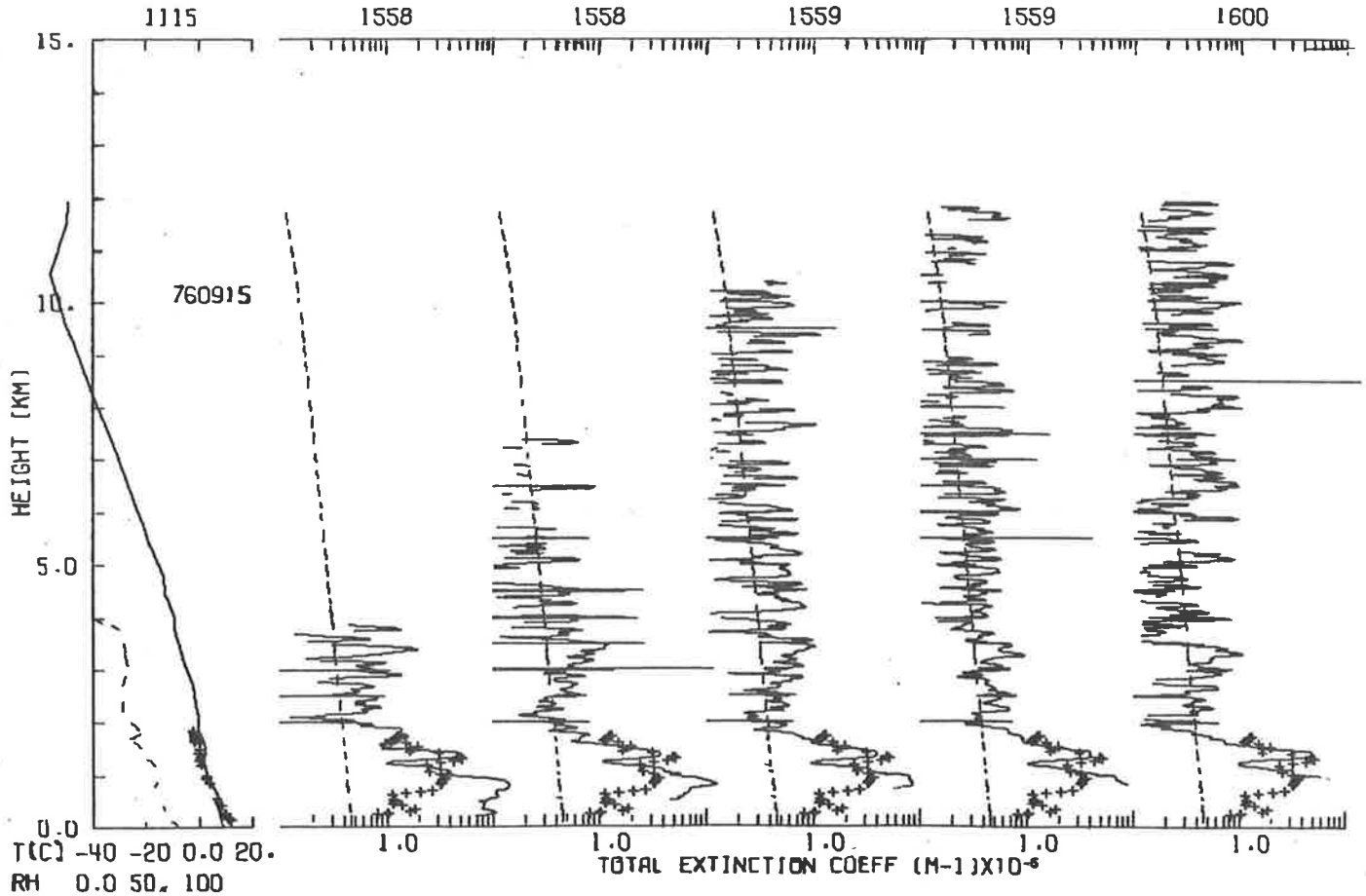

FIG 6.11(b) The LHS graph shows temperature profiles measured by radiosonde (——) and aircraft (+++) and the radiosonde relative humidity profile (---). The RHS graphs show extinction profiles, derived by lidar (——) at 15°, 30°, 45°, 60°, 90°, and nephclometer (+++), compared with the molecular extinction profile, (___).

to errors at these heights.

The problem of signal noise and the resultant fluctuation in the calculated extinction profiles can be overcome to some extent by smoothing. Because the array of values presented in Figure 6.11(a) contains 50 points in the vertical direction and 100 points in the horizontal direction and corresponds to an area of 5 km in height by 10 km in distance, each element represents a block of atmosphere of dimensions 100 m by 100 m. As the profile values are calculated every ten metres, the final value of the array element may be the average of ten values of extinction taken from the profiles, depending on the angle of elevation. As a result, a significant amount of smoothing occurs which is supplemented by the interpolation in two dimensions used to calculate the values of the elements between the profiles.

A study of Figure 6.11(a) reveals that the averaging discussed has been successful. An elevated layer between about 2.5 km and 4 km is shown clearly in the upper diagram whereas in the lower it is virtually hidden by noise. The layer corresponds approximately in height to the slight increase in the relative humidity detected in the region by the morning radiosonde. Most of the extinction values in the upper regions of (b) are not significantly different from the molecular values, although there is some evidence of scattering irregularities near 6 km.

The following day was clear in the morning with NNW winds at 0.5 $msec^{-1}$ and a visibility of 16 km. By midday the visibility had decreased slightly to 15 km as winds swung SSW at 3 $msec^{-1}$, and 2/8 of cumulus cloud formed at 2.5 km with 1/8 of alto-cumulus at 5.5 km. By 1500 EST the wind had swung to southerly at 3.5 $msec^{-1}$ and was

accompanied by an increase in visibility to 30 km. The cumulus decreased to 1/8 while the alto-cumulus increased to 3/8. The maximum temperature for the day was 14.8°C.

In the presentation of the extinction profiles for this day, the maximum and minimum values in the contour diagram are set at $2.0 \times 10^{-4} m^{-1}$ and $1.0 \times 10^{-5} m^{-1}$ respectively because the calculated extinction values cover a smaller range of values than on the previous day. This change has the advantage of providing more contour levels within the range of values and outweighs the disadvantage of the resultant non-integral contour levels which are now 1.3 dB. Data within 500 m of the lidar are within the region of incomplete convergence on this day and have been excluded.

On this afternoon the lidar detected two well defined aerosol layers below a cloud layer at 2.5 km. Another cloud layer was detected at 5.5 km. The nephelometer also revealed two aerosol layers with a minimum in extinction at a height of about 800 m, and a return to low values above the second maximum, at about 2 km. The whole region below about 2.7 km, just above the base of the lowest clouds, was one with a relative humidity in excess of fifty percent.

Boundary values for extinction were found in two ways to check on their reliability. The first was derived, as in the previous data, from the aerosol number density measurements which were calibrated with a value of extinction derived from visibility measurements and corrected for relative humidity variations with an interpolated relative humidity profile. The value used to calibrate the Pollak profile was $1.25 \times 10^{-4} m^{-1}$ at 150 m.

The raw lidar profiles do show a considerable amount of horizontal homogeneity and constancy in the region 250 m to 500 m and a value of extinction of $(4.5 \pm .3) \times 10^{-5}$ was obtained using the elevation scan

method. This value has been used for the boundary value for the elevation scans. A few minor differences appear between the lidar extinction profiles and that derived from the composite number density profile; a layer below about 250 m appears stronger on the latter which also shows a variation in extinction in the low region where the lidar profile is approximately constant.

In Figure 6.12 an elevation scan to the north of the lidar site is presented. The lidar profiles agree well with the trend of the concurrent nephelometer profile, including the return to approximately molecular values above about 2 km, but as before the nephelometer values are slightly low.

The extinction results above the cloud layers should be treated with caution as the backscatter-to-extinction ratio for clouds differs from that for aerosols. Also, the signal from the cloud layer has overloaded the receiver in the cases shown.

A second scan, made six minutes later at an azimuth of 70° appears in Figure 6.13. The sampling interval here was doubled to give a greater range. The data in this diagram have been smoothed with a gaussian weighting function whose width (2σ) was three points for the nephelometer profile and five points for the lidar profiles. The effect is to show more clearly the magnitude of the error bars, which indicate the uncertainty in the unsmoothed data.

Again, the values of extinction both in and above the cloud layers should be treated with caution. The 60° elevation profile, the fourth from the left, is terminated above the cloud layer as the calculated

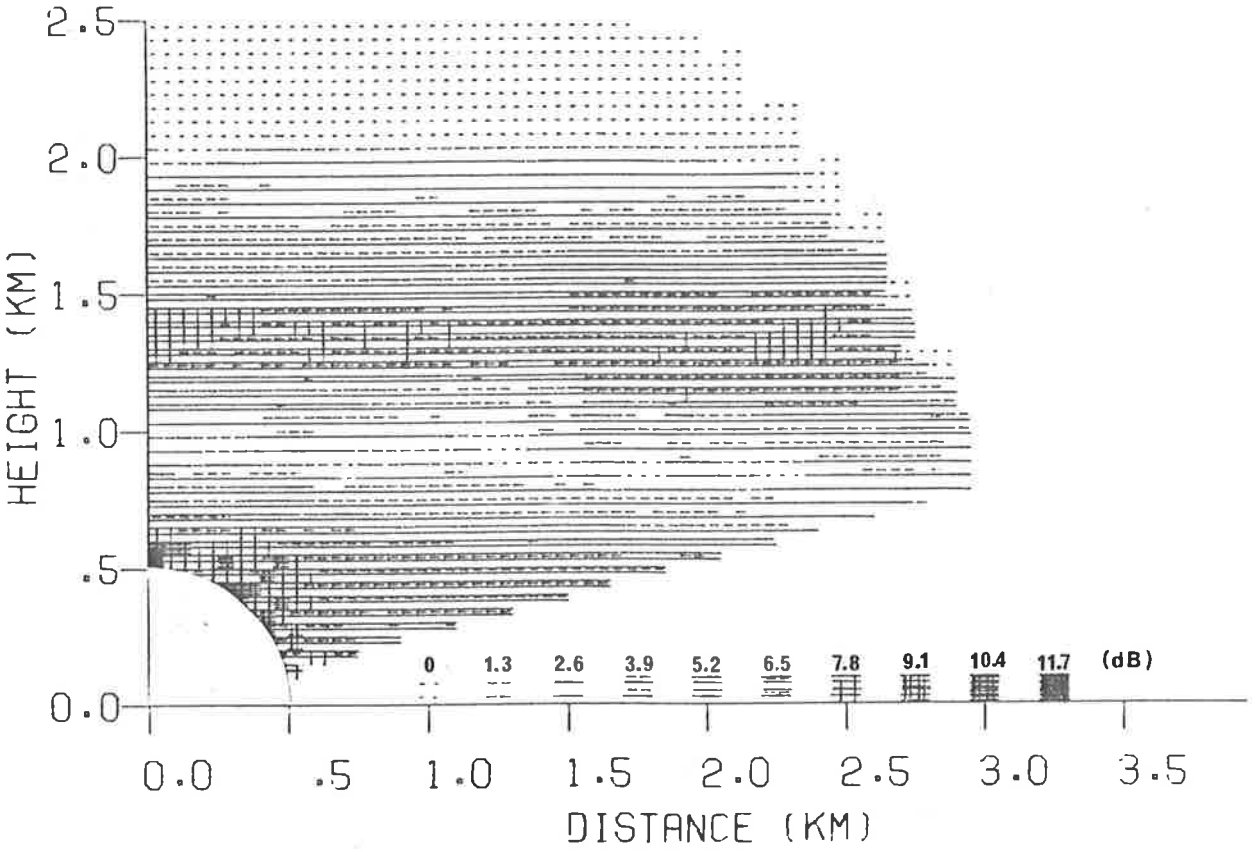

FIG 6.12(a) Lidar-derived values of total extinction coefficient. Key shows 10 levels of $10 \log_{10}(\beta_{MAX}/\beta_{MIN})$

$\beta_{MAX} = 2.0 \times 10^{-4}\,m^{-1}$, $\beta_{MIN} = 1.0 \times 10^{-5}\,m^{-1}$

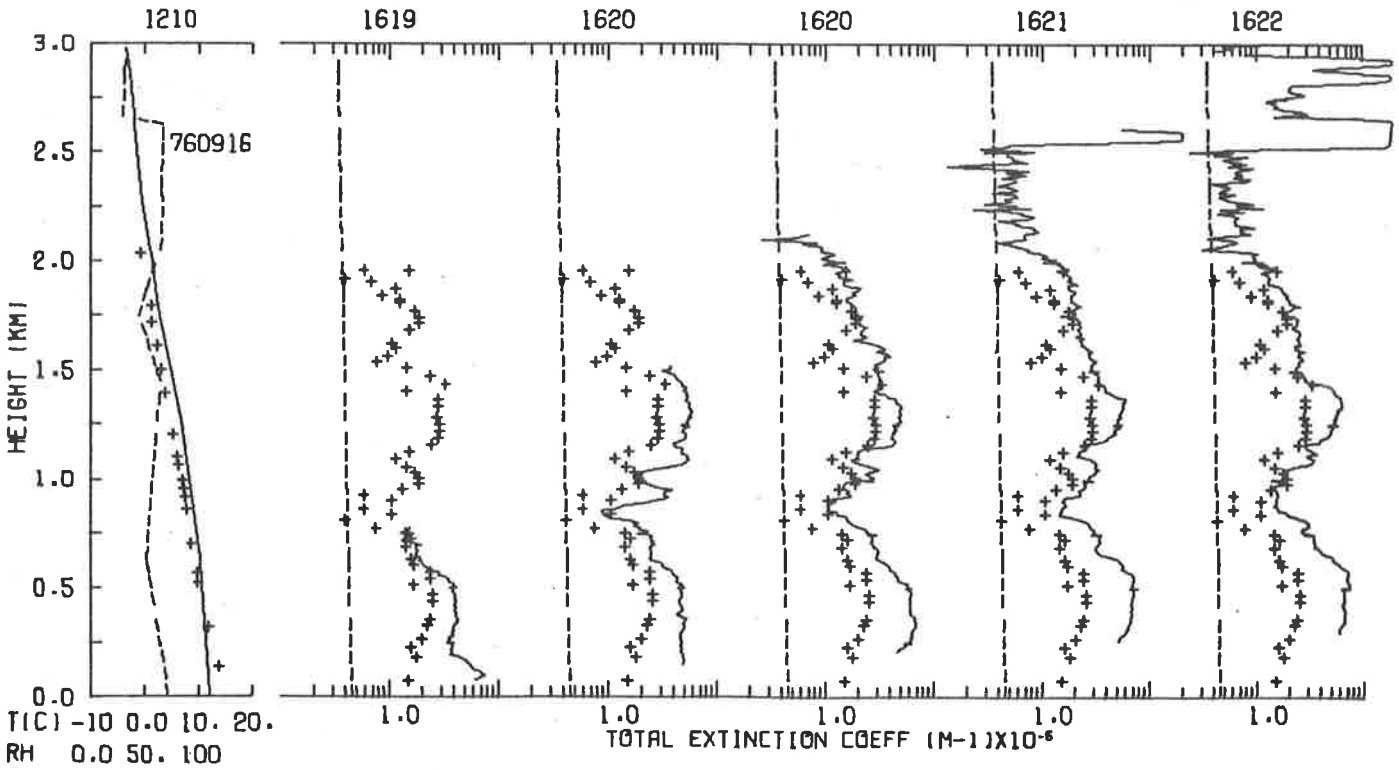

FIG 6.12(b) The LHS graph shows temperature profiles measured by radiosonde (——) and aircraft (+++) and the radiosonde relative humidity profile (---). The RHS graphs show extinction profiles, derived by lidar (——) at 15°, 30°, 45°, 60°, 90°, and nephclometer (+++), compared with the molecular extinction profile, (___).

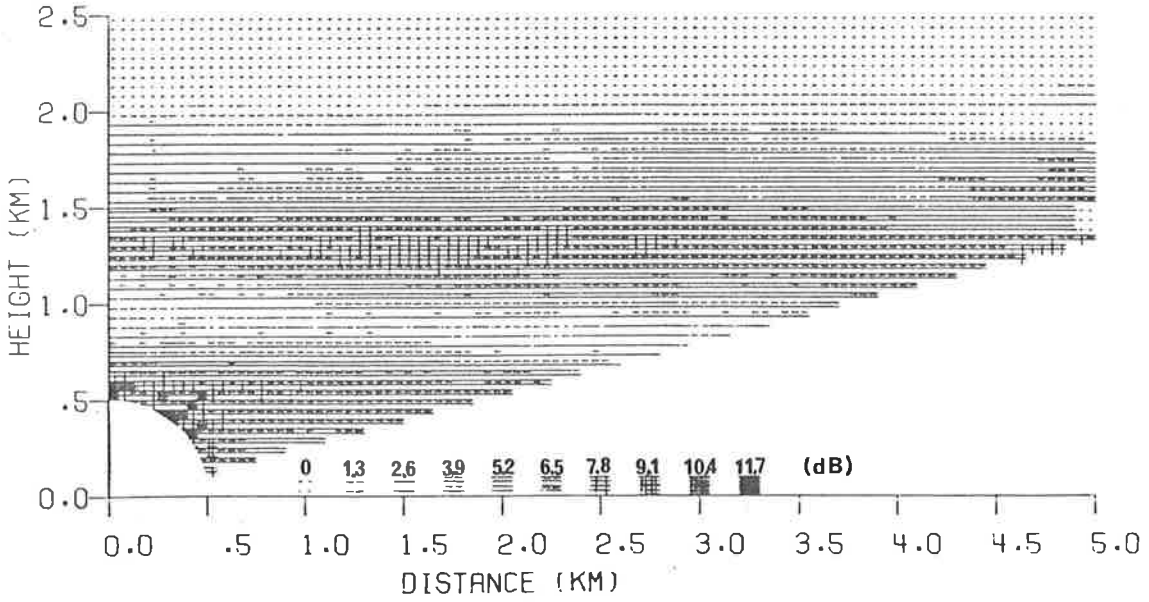

FIG 6.13(a) Lidar-derived values of total extinction coefficient. Key shows 10 levels of $10 \log_{10}(\beta_{MAX}/\beta_{MIN})$

$\beta_{MAX} = 2.0 \times 10^{-4}\,m^{-1}$, $\beta_{MIN} = 1.0 \times 10^{-5}\,m^{-1}$

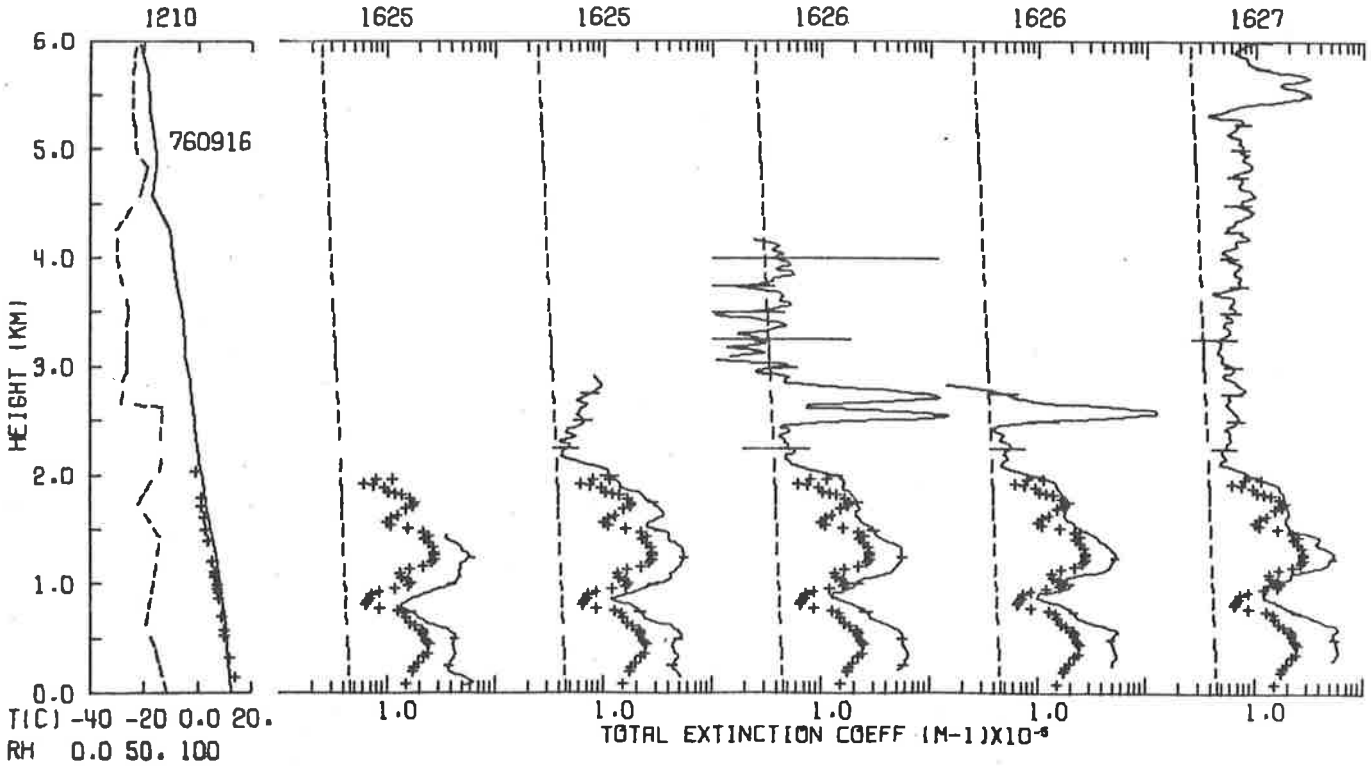

FIG 6.13(b) The LHS graph shows temperature profiles measured by radiosonde (——) and aircraft (+++) and the radiosonde relative humidity profile (---). The RHS graphs show extinction profiles, derived by lidar (——) at 15°, 30°, 45°, 60°, 90°, and nephclometer (+++), compared with the molecular extinction profile, (___).

extinction values became too small.

As seen in the profiles of meteorological data at the left of Figure 6.13(b), the relative humidity drops sharply in the region above the clouds. Much lower values of extinction would be expected in this region because there is less water vapour available to condense on the particles, thereby swelling them and making them more efficient scatterers of light. This is shown in the 90° elevation profile at the far right in which there is a sharp decrease in extinction at about 2300 m and values approaching the molecular extinction values above this height.

A gradual increase in extinction then occurs with height until another cloud layer is detected at about 5.4 km. This increase in extinction could be related to the increase in relative humidity above 4.3 km although the change in extinction is less abrupt. The lack of an exact correspondence between lidar extinction and relative humidity profiles could be due to the lapse of over four hours between the radiosonde flight and the laser firings.

The final elevation scan was performed five minutes later at an azimuth of 70° and the extinction values are shown in Figure 6.14. The nephelometer profile was measured during the aircraft's descent between 1624-1636 EST. The optical thickness comparison in this and the previous scan was performed in the relatively clear region between 2100 m and 2450 m.

A comparison of the extinction profiles in Figure 6.14 and 6.12 shows that although there is a difference of some thirteen minutes in time and seventy degrees in azimuth angle there is a considerable agreement between the scans. There is, however, some variability in the lower parts of the two nephelometer profiles. The lower part of the final profile was measured as the aircraft was flying back to the airfield and may have

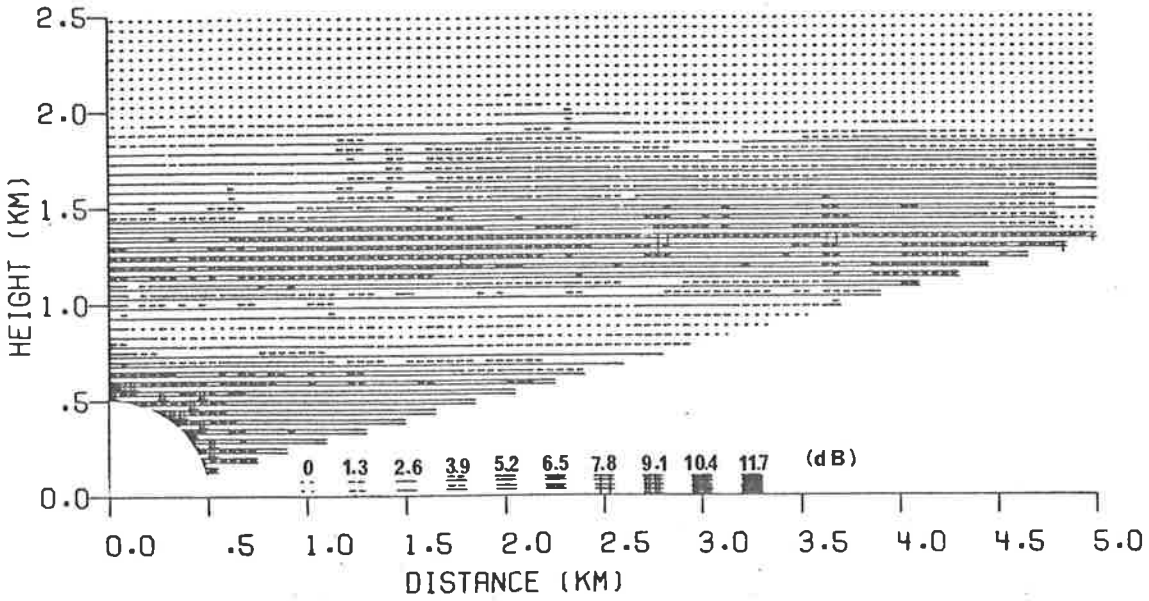

FIG 6.14(a) Lidar-derived values of total extinction coefficient. Key shows 10 levels of $10 \log_{10}(\beta_{MAX}/\beta_{MIN})$

$\beta_{MAX} = 2.0 \times 10^{-4}\,m^{-1}$, $\beta_{MIN} = 1.0 \times 10^{-5}\,m^{-1}$

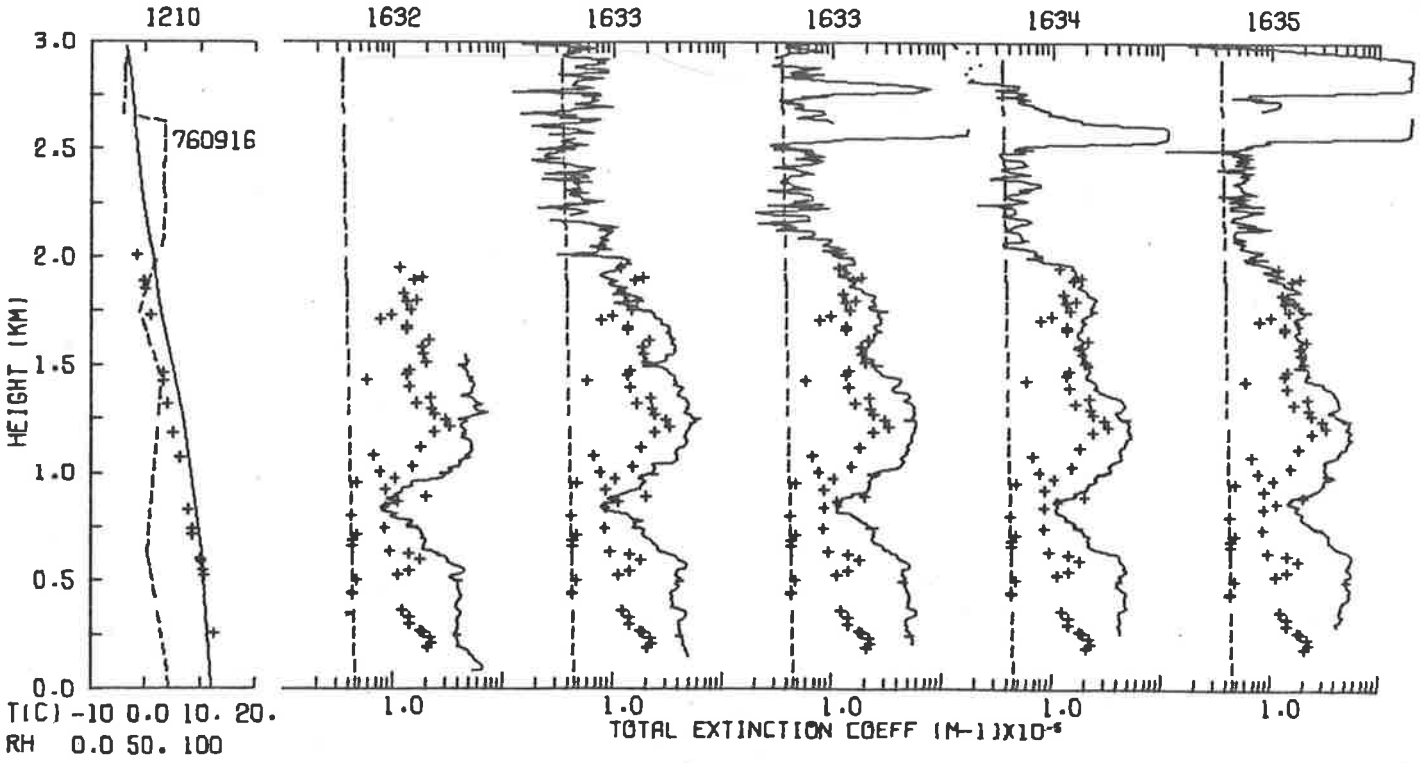

FIG 6.14(b) The LHS graph shows temperature profiles measured by radiosonde (——) and aircraft (+++) and the radiosonde relative humidity profile (---). The RHS graphs show extinction profiles, derived by lidar (——) at 15°, 30°, 45°, 60°, 90°, and nephclometer (+++), compared with the molecular extinction profile, (___).

passed through air of different aerosol content to that in the area probed by the lidar.

The changes in the spatial distribution of extinction can be seen clearly in the upper diagrams in Figures 6.12 to 6.14. This form of presentation has several advantages over the presentation of mere profiles as, although the scattering at various heights may be compared for different profiles, the horizontal distance from the lidar of a particular point on the profiles is not obvious. This also permits the study of any movement of material through the region studied by the lidar.

In Section 5.5 alternative methods of deriving extinction profiles were discussed. Figure 6.15 presents an example of the application of these methods to the vertically pointing profiles in each of the five elevation scans performed on the afternoon of the 16th September, three of which appear in Figures 6.12 to 6.14. The results obtained using Equation 5.17 are indicated by the discrete point plot whereas the continuous line profile represents the results of using Equations 5.22 and 5.24. The continuous diagonal line is the analytic approximation to the molecular extinction profile.

The solution using Equation 5.17 assumes that extinction and backscatter are related by the Equation $d(\ell n\ B_T)/d(\ell n\ \beta_T) = k_2$ where k_2 is assumed here to be unity. This value was chosen because in the evaluation of the aerosol backscatter-to-extinction ratio discussed earlier, a linear dependence seemed to exist. Provided the aerosol extinction is significantly greater than the molecular, or vice versa, this linear approximation should hold for B_T and β_T.

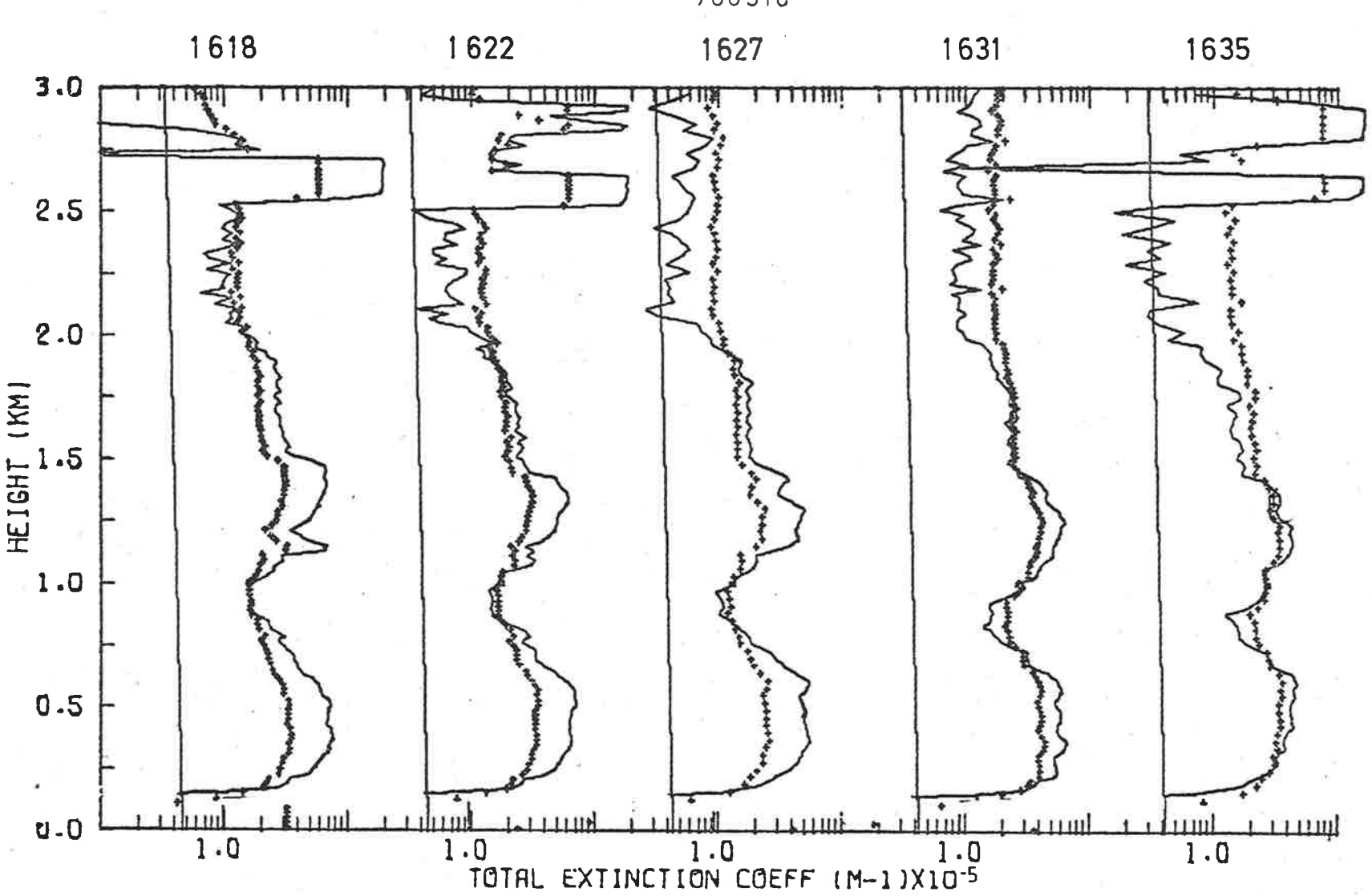

FIG 6.15 Extinction profiles calculated using Equations 5.17 (+++) and 5.25 (——).

The solution using Equation 5.25 developed by the author considers the aerosol and molecular contributions to scattering separately. The aerosol backscatter and extinction are assumed to be related by the Equation $B_A = k_1\beta_A$ where $k_1 = 0.32/4\pi$. The molecular extinction component is approximated by the Equation $\beta_M(h) = \beta_M(0)\ e^{-h/H}$. In Figure 6.15 the scale height H, is 9.17 km, a value obtained previously from the local midday radiosonde data. The approximation simplifies and speeds up the analysis program as it eliminates the necessity of looking up radiosonde values of pressure, temperature and height from arrays and interpolating to find the value of molecular extinction at the particular height required in the analysis of the lidar profile. In the example shown the program's central memory requirement has been reduced further by the use of only 256 or fewer data points out of the maximum of 2024 available. The advantages of reduced central memory, field length, and central processor time on a large, heavily used, multi-user computer are obvious : they may also allow the use of the program on a dedicated minicomputer planned for the future.

A comparison of the results obtained using the latter analysis with those obtained using the method described in Section 5.2 and used throughout this chapter revealed that identical results are obtained when the same boundary values are used. The simpler analysis, represented in Figure 6.15 by discrete points, differs considerably from the results just mentioned, being too low in regions of high aerosol extinction and too high in regions of low aerosol extinction. Each profile has been normalised at a height of 1.0 km and both the solutions shown meet at this height.

The reason for the difference is that in the derivation of the first method it is assumed that $\beta_T \propto B_T$ rather than the relationship

given by Equation 5.21,

$$\text{i.e.} \qquad \beta_T(h) = \frac{4\pi}{P_A(\pi)} \cdot B_T(h) + 4\pi \left(\frac{P_A - P_M}{P_A P_M} \right) . B_M(h) .$$

For those conditions when the air is very clean and molecular scattering predominates, or when there is a predominance of aerosols, the simpler method can be expected to produce reliable results because there is a constant ratio between backscatter and extinction. In regions though, where significant changes occur in the proportion of aerosols and molecules, the more complex method is necessary.

6.4 Extinction Coefficients derived from Lidar Depolarisation Measurements

The depolarised component of lidar atmospheric returns has been used to calculate profiles of relative particle number density (Cohen and Graber, 1975; Cohen and Kleiman, 1978). This method has been extended here to provide profiles of atmospheric extinction in the troposphere; the procedure is described in Section 5.4.

As emphasised by the authors just cited, the original method, which only calculates number ratios, has the advantage of not requiring the knowledge of the molecular density or extinction profile. In the present analysis, however, the tropospheric extinction due to aerosols and air molecules up to the height studied must be considered, and although the aerosol contribution is calculated during the analysis, the molecular contribution must be found otherwise. It was found that sufficient accuracy could be obtained over the height range studied by assuming that the molecular extinction profile could be described by an equation of the form $\beta_M(h) = \beta_M(0)\ e^{-h/H}$, where the symbols have the same meaning as elsewhere in this thesis.

Figure 6.16 is an example of some data used for the calculation of extinction profiles. Depolarisation ratios were calculated for signal returns at five degree elevation intervals; the examples presented in the upper diagram are at fifteen degree elevation intervals. The profiles shown were calculated from cross-polarised returns measured in an elevation scan, and the average of two parallel-polarised scans one preceding and one following the cross-polarised scan. These latter elevation scans have been presented already in Figure 6.9 and 6.10.

Ideally the two components of the lidar return from a given elevation angle could be divided to produce a profile of depolarisation ratios. This profile could then be searched for a region with a ratio of 0.015, since such a region would be one where the sky was entirely molecular and would therefore be a region suitable for the normalisation of lidar returns in the conventional molecular-normalisation method. Unfortunately, the cross-polarised lidar signals from the relatively clear air above 1800 m are relatively weak, and become lost in the background sky noise which is increasing with the square of the range because of the range compensation unit employed on the receiver.

To overcome the difficulty in separating the cross-polarised signal from noise, it was assumed that the signal returned from above 1800 m was all noise and it was subjected to an analysis which fitted a function of the form $y = a + bR^2$ where R is the range, b is a scaling factor and a is an offset. This function was then used to remove the noise contribution from the rest of the signal below 1800 m. By assigning the clear air value of .015, to the depolarisation ratios above 1800 m, the previously undetermined background component and signal offset in the cross-polarised returns was also calculated and removed from the signal. The

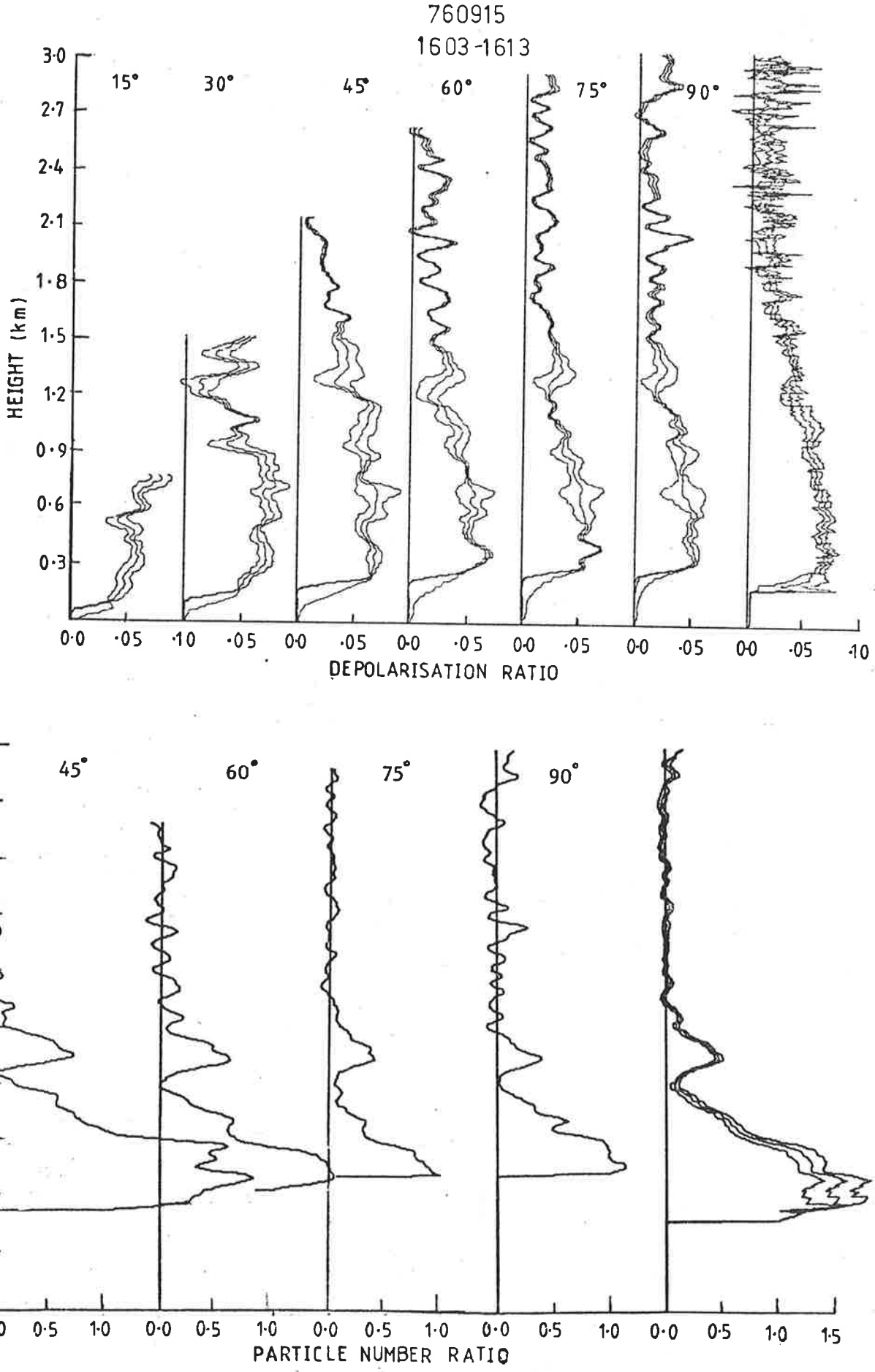

FIG 6.16 Depolarisation and Number ratio profiles for various elevations and the average for elevations greater than 40°.

profile of depolarisation ratios was then calculated by dividing the treated cross-polarised signal by the average of the two parallel-polarised signals.

The depolarisation ratios calculated in this way are shown in Figure 6.16(a). The uncertainty in the value of the ratio at any height is indicated by a profile on either side differing by one standard deviation above and below the centre profile values respectively. These uncertainties arise from the variations in the two parallel-polarised returns which were averaged to form the denominator in the ratio.

Each profile has been subjected to a five-point smoothing, corresponding to fifty metres in height, to remove some of the noise from the ratios and improve their presentation. The average profile shown at the far right is calculated from the unsmoothed profiles and is itself unsmoothed. It is calculated from only those profiles that extend above 1800 m, that is those profiles with elevations greater than forty degress.

The profiles presented in the example show a general decrease in the depolarisation ratio with height. The layer of increased scattering shown in Figures 6.9 and 6.10 is not as noticeable in these profiles. Also, the lack of any consistent, significant structure in the ratio profiles in the region above about 1800 m lends support to the assumption of the existence of a clear region, or at least a region of low and constant aerosol number density.

The aerosol number ratio profiles shown in Figure 6.16(b) show a much more rapid decrease with height because of the successive products from which they are formed. The layer at about 1400 m has become more prominent in the number ratios than in the depolarisation ratios. The

smoothing of these profiles is the same for those in (a), the negative number ratios are just a result of noise fluctuations in the signal and, as can be seen in the average profile, all are less than the uncertainty in the average.

Whereas the depolarisation ratios are shown extending down to the lowest heights from which signals are received, the aerosol number ratio profiles are truncated at the overlap range because, as can be seen from Equation 5.14, the actual magnitudes of signals at different heights is used and not just the relative magnitude of the two polarisation components at the same height.

In Figure 6.17, the average profiles of depolarisation ratio calculated from several scans are shown. The most striking feature in this figure is the decrease in the ratio with time, dropping from a maximum of 0.15 to values of about 0.07. The decrease in the sharpness of the boundary of the mixing layer as another upper layer is formed is also noticeable, as are the high ratios near the top of the layer in the early profiles. This feature is not apparent in the parallel-polarised returns nor in the corresponding extinction profiles shown in Figure 6.7(a). The explanation of these observations may possibly lie in the deepening of the mixing layer and the resultant spreading of the aerosol through this greater depth. The corresponding number density ratios, not shown here, also show a decrease with time, thus supporting this argument. The correlation of high depolarisation ratios and high aerosol concentrations has also been noticed by McNeil and Carswell (1975).

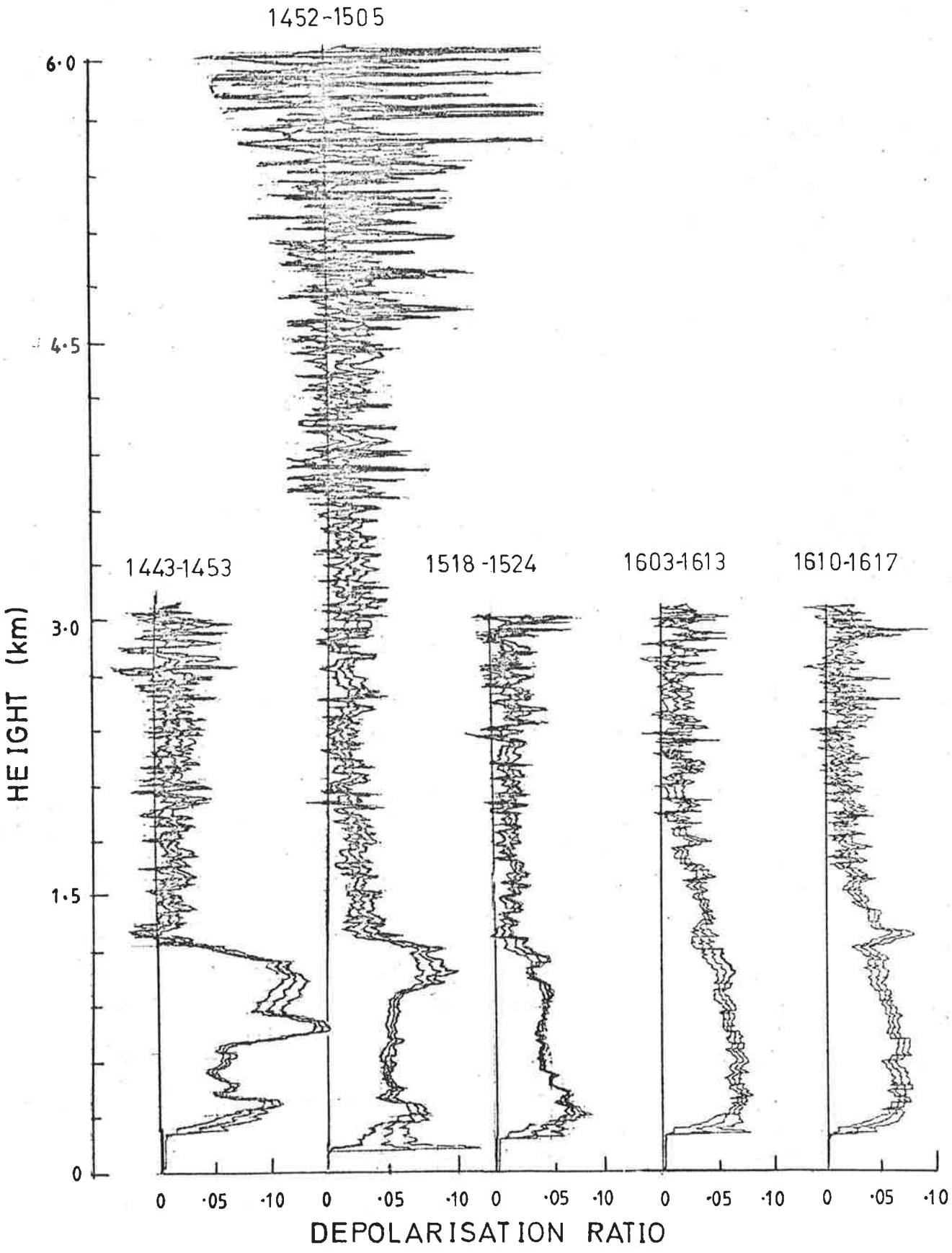

FIG 6.17 Average Depolarisation Ratios for elevations greater than 40°.

The averaging of several profiles in the scan has brought out many details more clearly. An example in one of the earlier scans is shown in the second profile in Figure 6.17. Apart from the sharp drop in depolarisation ratio at 1200 m , corresponding to the top of the mixing layer at the time, a decrease in the region 1800 m to 2100 m is also noticeable and corresponds to an isothermal layer measured by the radiosonde and to a decrease by a factor of two in the particle number measured by the Pollak counter. Also, a slight increase in the ratio between the heights 2700 m and 3800 m corresponds to a slight increase in the relative humidity.

An extinction profile calculated from the data presented in Figure 6.16 is shown in Figure 6.18. The error bars represent one standard deviation in the mean value. Also shown for comparison are the extinction profiles derived from the conventional analysis described in the previous section and the extinction profile deduced from a composite of several Pollak counter flights during the afternoon. Although the composite profile does not present a picture of the actual situation at any particular time, it does provide many more data points and allows a useful comparison with the other data.

The agreement between the three profiles is good, especially in the case of the conventional analysis and the depolarisation analysis profiles, despite the fact that the latter were virtually normalised to molecular extinction values above 1800 m. The good agreement at the other heights is due to the low values of aerosol extinction obtained by the

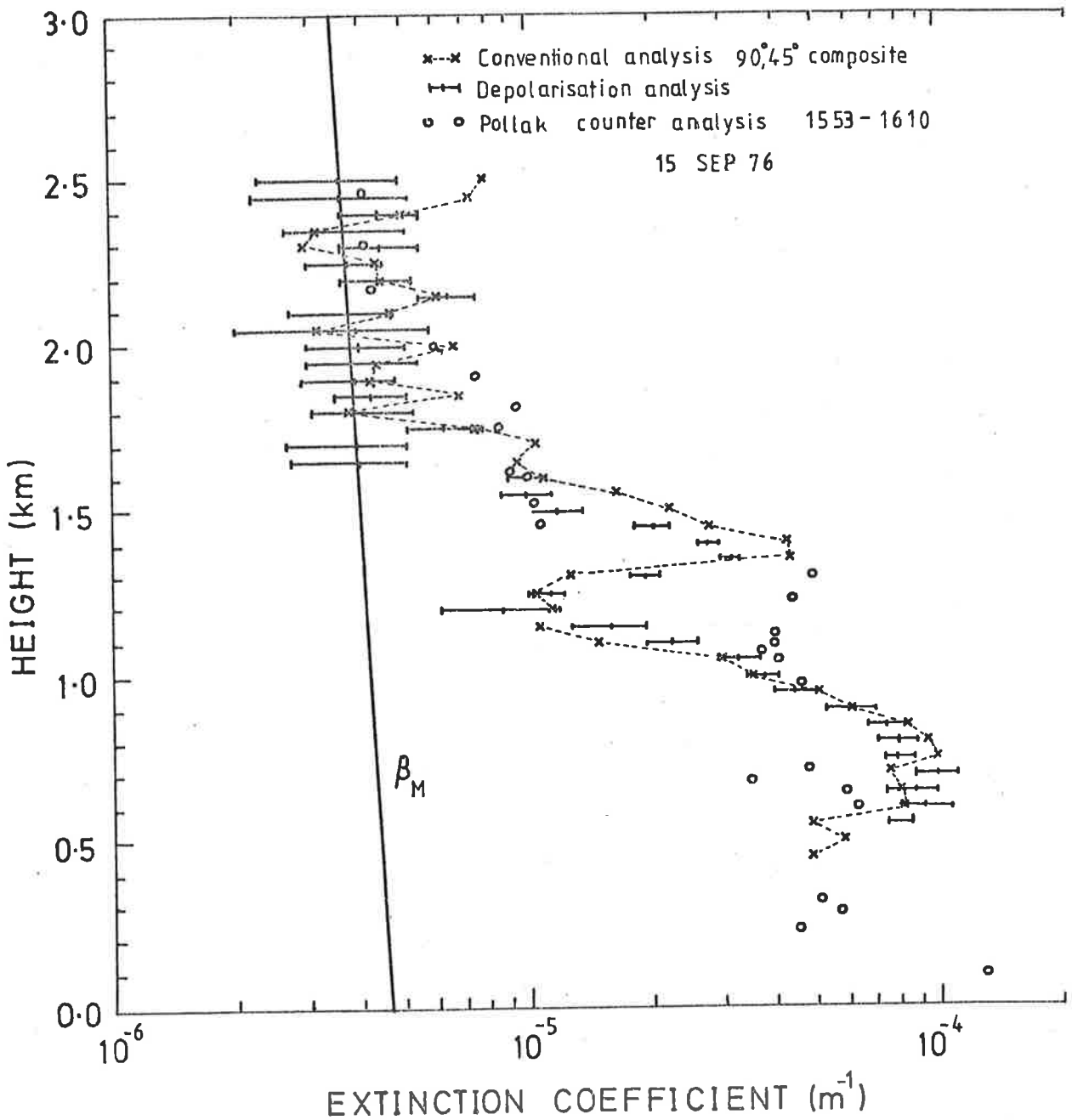

FIG 6.18 A comparison of Extinction profiles derived by the Depolarisation Ratio Method and the Molecular Normalisation Method compared with a composite profile derived from 4 Pollak counter profiles.

conventional analysis above 1800 m. In fact, the differences in the two profiles above this height is rarely greater than the uncertainty in the depolarisation-derived profiles. The lack of agreement at some heights between the profile derived from the Pollak counter data and the two lidar profiles can be attributed to differences in observation times.

6.5 Discussion

The aerosol backscatter-to-extinction ratio derived in Section 6.2 $(0.32 \pm 0.02)/4\pi$, lies in the general range of values determined by other workers using both theoretical and experimental means, and reviewed in Chapter 1. This value is considered typical of the atmospheric conditions prevalent during the experimental program carried out in Aspendale and, as similar conditions existed in Adelaide, this value has been used in the analysis of these results also.

The experimentally derived ratio has been used with the modified molecular normalisation method to produce profiles of extinction which are consistent with other profiles derived from the same and other elevation scans. These profiles also agree favourably with profiles of extinction derived from airborne Pollak counter particle number measurements when similar boundary values were used and the effects of relative humidity were considered. The implication here is that, on those days studied, the aerosol size distribution did not vary much over the range of heights investigated. This in turn justified the use of a single value of the ratio for all heights in the subsequent analysis of lidar profiles.

Although good consistency was achieved between lidar and airborne nephelometer extinction profiles in the determination of the heights of the mixing layer and the position of upper layers, generally poor agreement

was obtained between the actual magnitudes of extinction in both cases. Possible reasons are the different operating wavelengths and bandwidths of the two devices, and spatial differences in the sampling volumes although the latter should have averaged out. It is also possible that the nephelometer slightly warmed the air it was sampling and evaporated some of the moisture from the aerosol particles, thereby reducing the extinction coefficient. It is of interest to note that the reduction in the extinction coefficient was particularly noticeable in the mixing layer where higher relative humidities were recorded.

Other methods of obtaining extinction profiles gave consistent results. Those methods described in Section 5.5 proved to be reliable alternatives, particularly if the effects of aerosol and molecular extinction were considered separately.

Extinction profiles derived from cross-polarised returns were consistent with the profiles derived using other methods. In the present work poor signal-to-noise ratios were found in the cross-polarised returns from the relatively clear regions above the mixing layer and it was necessary to assume that the signal from these heights was purely molecular in order to separate the signal from the background noise. As the conventional analysis produced low extinction values in this region anyway, good agreement within the experimental uncertainties was still obtained throughout the profile. The good agreement also showed that although changes occur in the finer detail of the signals over short time scales, the long term behaviour tends to average these out and provide reliable results. For the present analysis, therefore, it was not necessary to observe both polarised components simultaneously as suggested by McNeil

and Carswell (1975), because reliable results could be obtained by averaging over a wide enough spatial area and by averaging parallel-polarised returns preceding and following the cross-polarised returns.

The presentation of lidar extinction values in two dimensions has provided an insight into the vertical and lateral extent of aerosol layers. The presentation was found to be much improved by employing an analysis which compared consecutive profiles and adjusted their relative normalisation or calibration to provide consistency in optical thicknesses between certain heights.

CHAPTER SEVEN

CONCLUDING REMARKS

A study has been made of the distribution of atmospheric aerosols in the stratosphere and troposphere using a ruby lidar. Modifications to the laser transmitter to reduce the incidence of breakdowns, and extensions to the system to permit tropospheric observations at various angles of elevation and azimuth have been described. Experiments performed on the EMI 9558B photomultiplier to be used in the lidar receiver showed that signal induced noise was insignificant in the present system. The development of a digital data logging system for the recording of lidar data and lidar system ("housekeeping") information on magnetic computer tape has been detailed.

Previous stratospheric observations have been extended to cover a total period of eight years to enable conclusions to be made regarding seasonal variations and long term trends in the aerosol scattering and its relationship with various meteorological variables. The vertical and horizontal distribution of tropospheric aerosols and the results of comparisons with airborne and radiosonde atmospheric measurements have been discussed.

7.1 Stratospheric Observations

Lidar observations of stratospheric aerosols at Adelaide during the period 1969 to 1971 have been supplemented by further observations during the years 1972 to 1976. During the former period dust from the Fernandina volcano caused an increase in stratospheric aerosol scattering which reached a peak in July 1969 followed by a general decline in the later years. The years 1972 and 1973 were characterised by low aerosol

scattering and it was very disappointing that the dramatic increase in scattering caused by the eruption of the Manam Island volcano (Gras, 1976) and Volcán de Fuego in late 1974 and 1975 was not observed at Adelaide because of equipment problems. Observations in March and April 1976 did, however, show slightly higher aerosol scattering than in 1973.

During the earlier observation period, when scattering from the stratospheric layer was strong, an annual variation in the aerosol scattering was detected at some heights. At 15 km the peak in scattering occurred in late winter-spring with a minimum in late summer-autumn. The seasonal behaviour compares favourably with that determined by Bigg (1976) with a balloon-borne impactor, and also with the global spread of dust from the eruption of Mt. Agung reported by Dyer and Hicks (1968). Any variation in later data was possibly masked by normalisation errors and the effect of day to day variations.

A comparison of the aerosol backscatter function measured by lidar with the monthly mean wind variations in the stratosphere was largely inconclusive. There is some evidence that strong eastward winds at 15 km and 20 km are associated with higher values of backscatter function and that winds at 20 km which blow polewards and to the west (SW) are associated with low or decreasing values of backscatter function. While this may reflect the transport of dust in the ridge-trough eddies as suggested by Gambling *et al*, (1971), actual daily observation of winds, rather than monthly mean observations, should be compared with simultaneous lidar observations before any stronger conclusions are drawn. Even then, the comparison of wind and dust observations by Hirono *et al*, (1974) and Russell *et al*, (1976), do not give much hope in this area as they found no

correlation, except during a stratwarm when a zonal wind reversal was accompanied by a drop in aerosol backscatter.

During the period following the eruption of the Fernandina volcano, significant correlations were measured between the integrated aerosol backscatter function and both the pressure of the tropopause and the minimum stratospheric temperature. Similar observations have also been reported by McCormick *et al*, (1978) in their observations of the post-Feugo volcanic aerosol decay. Low tropopauses and the consequent high tropopause pressures are associated with higher values of the integrated backscatter function. Hofmann *et al*, (1975) suggest that the lower tropopause provides a greater volume for the formation and transport of aerosols and that the variation is strongest in the lower stratosphere. Warmer minimum stratospheric temperatures are associated with higher values of integrated backscatter, but it is not known whether the aerosols lead to the heating of the stratosphere by absorption of sunlight, or whether the warm air masses containing higher amounts of aerosol are advected over the lidar site.

A significant correlation in the early data was found between the aerosol backscatter function integrated over the height range where the variability seems strongest (10 km to 15 km), and the geopotential height of the 250 mb (10 km) pressure surface. A much weaker correlation was found at greater heights. Higher aerosol amounts were found when the pressure surface was lower, possibly related to the trough and ridge synoptic system which Gambling *et al*, (1971) suggest is responsible for the poleward eddy transport of aerosols. If this is true, care should be taken when normalisation of the scattering profile in this height region

is necessary. The presence of an upper level trough in this region may indicate the presence of aerosols at the normalisation height and the possible underestimation of the aerosol scattering profile as discussed in Chapter 3.

Scattering by aerosols at altitudes above 30 km has been detected on several occasions either from extensions of the main stratospheric layer into the region 30 km to 40 km or from higher layers of possible extra-terrestrial origin. The frequency of occurrence of the upward extensions of the lower layer, especially since February 1970, make the region 30 km to 40 km unsuitable for the routine normalisation of scattering profiles, at least at the site of the present observations.

A comparison of the aerosol scattering profiles measured at Adelaide with almost contemporary observations from a similar northern hemisphere latitude revealed little difference either in the strength of scattering or in the distribution with height. The 1973 profile for Adelaide shows slightly greater values than the 1973 to 1974 profile of Russell *et al*, (1976), possibly because the general decline in aerosol values continued through 1974 and lower values were included in the northern hemisphere average. The general similarity of the stratospheric layers in both hemispheres agrees with the observations by Rosen *et al*, (1975) of the worldwide distribution of stratospheric dust with balloon-borne photoelectric particle counters.

The stratospheric aerosol optical thickness varied from a maximum value of about 0.016 to a minimum of 0.004 during 1969 to 1976. By using a representative stratospheric aerosol size distribution (Bigg, 1976) and calculations by Cadle and Grams (1975) of the globally averaged

percentage loss from a solar beam by absorption and scattering upwards from the stratospheric layer, the effect of the optical thickness variations on solar radiation were estimated. If the optical thickness changes measured at Adelaide were typical of global values then a change in the globally averaged percentage loss in solar radiation varied from 0.52 per cent to 0.13 per cent.

7.2 The Tropospheric Recording System

To enable the lidar to probe the troposphere more accurately and more quickly a data logging system was designed and built to record lidar scattering data and system information on seven-track magnetic computer tape. Each record contained the lidar scattering profile, the profile number, the laser output energy and the lidar beam elevation and azimuth angles. These and an "END OF RECORD" marker are written to tape in just over one second.

Ancillary electronic circuits built for use with the data logging unit included a laser output energy monitor with a digital output and a front panel LED display, and a fast logarithmic amplifier with an automatic correction for drift in the background signal.

During operation test lidar scattering profiles were viewed on an oscilloscope output monitor with the unit in the "MANUAL" mode while the recording settings were optimised. The unit was then switched to the "AUTOMATIC" mode where the lidar data were transferred to the tape recorder immediately after they had been collected by the transient recorder. The system proved to be both flexible and reliable and performed excellently during the atmospheric observation programme.

7.3 Tropospheric Observations

Areas considered in the observation of tropospheric aerosols were the determination of a representative backscatter-to-extinction ratio, the testing of the reliability and applicability of various analytical techniques, and the determination of boundary values for extinction profiles. Modifications and extensions to some existing methods of analysis permitted their wider use.

In order to determine the most accurate profiles of extinction coefficient from lidar backscatter signals, a value of the aerosol backscatter-to-extinction ratio that was representative of the aerosols being studied was sought. In deriving this ratio it was assumed that the aerosol extinction coefficient could be obtained from aerosol number density profiles if the effects of the relative humidity on the size of the aerosols were taken into account. It was also assumed that the ratio remained constant over the region of interest. As mentioned in Chapter 6 both of these assumptions seem justified by the observations of other workers.

The backscatter function was determined from the average of several lidar scans of the atmosphere at various elevation angles. The resultant value of the backscatter-to-extinction ratio, $P_A(\pi)/4\pi = (0.025 \pm 0.002)$, is compatible with various other theoretical and experimental values. Quenzel *et al* (1975), for example, using Mie scattering theory with 21 different haze size distributions, found the backscatter-to-extinction ratio for hazes probed with monostatic ruby lidars to be in the range 0.013 to 0.036 with a mean of 0.022. Experimentally determined values include $P_A(\pi)/4\pi = (0.012 \pm 0.002)$, (Waggoner *et al*, 1972), 0.026 to 0.040, (Hamilton, 1969) and 0.025 to 0.034, (Reagan *et al*, 1977).

Various methods for the analysis of tropospheric lidar backscatter signals were studied to determine which give reliable and consistent results. Some methods, such as the elevation scan method, are only valid under special atmospheric conditions whereas others are applicable generally.

The molecular normalisation method (Section 5.2) in its standard form, is not applicable in most cases because there is rarely a region of aerosol-free air in the range covered by the recorded lidar signal. Although the normalisation of a profile in the clearer air above the mixing layer often causes tolerably small errors for extinction values within the layer, the errors for the region above, which still contains some aerosols, are often unacceptably large.

When the molecular normalisation method is modified, as in the present work, to accept a non-zero boundary value of aerosol extinction, it is useful for the analysis of all backscatter profiles. In this case the limitation to the accuracy of the method is imposed mainly by the accuracy of the boundary value and, to a lesser extent, the uncertainty in the backscatter-to-extinction ratio. The basic assumption with the method is that the aerosol backscatter-to-extinction ratio remains constant with height.

The methods analysed in Section 5.5 involve the solution of differential equations which relate the rate of change with range of the lidar signal to the rate of change of the backscatter function and the extinction coefficient. The method in its simplest form, with a solution typified by Equation 5.18, does not always give accurate results because the total extinction coefficient is not proportional to the total backscatter function in those regions where the turbidity (β_A/β_M) changes. When the method is extended to consider both aerosol and molecular components separately, it is applicable generally and gives identical results to the

molecular normalisation method when the same boundary values are used. The advantage of this method over the molecular normalisation method is mainly computational; it does not require iterations at each step of the analysis to produce an extinction profile.

The computations required by both the methods just discussed can be simplified by the introduction of an analytic approximation for the molecular scattering component. The savings are in computing time and programme memory. The ground level molecular extinction coefficient $\beta_M(0)$, and the molecular scale height H, can be obtained from radiosonde profiles if they are available, or estimated from ground level meteorological data and standard scale height values. A study of radiosonde data used with lidar observations during the period 1969 to 1976 showed that excellent fits to the data up to a height of 6 km could be achieved by an exponential analytic approximation.

The depolarisation ratio method, as extended in the present work (Sections 5.4 and 6.4) produces extinction profiles which agree with those produced by the two methods just discussed and with profiles of aerosol extinction derived from profiles of particle number density measured by Pollak counter. The method is applicable in most circumstances, the main limitation being the weak scattering from clearer regions which is often lost in background sky noise. A further complication arises if the equipment includes a device which increases the gain of the receiver, and hence the sky noise, with the square of the range. The effect of the noise could be reduced by rotating the lidar so that the plane of polarisation of the receiver is perpendicular to that of the sun light scattered from the sky and by using a receiver with a linear response in the region of

difficulty. Under these circumstances it should be possible to measure the perpendicular component of the backscatter up to much greater heights. This would allow the absolute determination of the depolarisation ratio and increase the likelihood of the detection of an aerosol free region with a ratio of 0.015.

For those cases where the aerosol extinction coefficient predominates at all heights, the molecular extinction profile can be neglected completely as in the original analysis which produced only number density ratios. Then aerosol extinction profiles can be derived solely from measurements of the two polarised components of the backscatter and a boundary value of extinction.

The agreement of extinction profiles derived by the depolarisation method with those derived by other methods justifies the technique used in this thesis of producing average extinction profiles from temporal and spatial averages of depolarised signals. The simultaneous measurement of both components does not seem to be necessary for the cases studied here.

A decrease in the values of the depolarisation ratio within the mixing layer and a simultaneous decrease in extinction values, observed when the mixing layer was increasing in depth, was found to be the result of a decrease in particle number density. It seems that roughly the same number of particles was distributed through a greater volume of atmosphere, thus producing a lower density.

The fundamental limitation to the use of the elevation scan method is the requirement of horizontal homogeneity of scattering. Although some observational periods appeared at first to be suitable (e.g. the early morning and late afternoon on 760916), there always seemed to be sufficient variability to produce poor results except over small height ranges.

However, when the conditions do exist it is an excellent method as it can produce profiles of both backscatter and extinction, and therefore, a value of the aerosol backscatter-to-extinction ratio. Usually though, its best use appears to be in the derivation of boundary values.

Most of the methods of analysis described in this thesis require boundary values of the extinction coefficient. Those methods for the determination of boundary values found to be successful were the elevation scan method or the two beam method when the homogeneity of the atmosphere is limited to a small region, and the use of atmospheric visibility measurements. For the reasons discussed earlier, nephelometer measurements gave values which were too low and the method was not used. The use of visibility measurements was only used as a last resort but they seemed to give compatible results when compared with other measurements.

The presentation of the spatial distribution of aerosols on the vertical plane was improved by the comparison of consecutive lidar profiles and the minor adjustment in the normalisation of each profile to produce consistent results. These diagrams showed that, on those days studied, horizontal homogeneity of scattering did not exist except over small height ranges. The broader features of the scattering profiles were common to profiles measured at all elevation angles and azimuth directions; only the smaller details destroyed the homogeneity. The accumulation of scattering material within the mixing layer stood out clearly as did the enhanced scattering from layers higher in the atmosphere. The height of these elevated layers, whose horizontal extent was at least 10 km on some occasions, often corresponded to regions of increased relative humidity or particle number density.

A study of consecutive diagrams in Section 6.2 showed the change in the spatial distribution of aerosols with time. On one afternoon a secondary layer was detected just above the original position of the mixing layer boundary, rather than a simple increase in the depth of the mixing layer. This unexplained phenomenon was followed the next afternoon by the development of a similar, broader layer.

7.4 Suggestions for Future Work

7.4.1 Statospheric Observations

The present stratospheric recording system could be improved vastly at very little cost and with only a small amount of effort and time. The technique of recording signals from four overlapping height ranges, one at a time, is very wasteful in terms of time, power and the general attrition of lidar components.

On many occasions observations have been restricted to only the first one or two height ranges when clouds or breakdowns have stopped work. The proposed system, set out briefly below, would eliminate this problem by accepting signals from all heights in a 38 km band each laser firing. It also has the added advantage of recording each pulse and the corresponding lidar parameters directly onto magnetic tape, and thus eliminates the laborious copying of photon counts from the 10-channel counter display and the punching of data onto computer cards.

In a feasibility test performed by the author, photoelectron pulses from the discriminator-scaler driver unit were used as input pulses for a 6-bit binary counter which was followed by a 6-bit ladder-type digital to analogue converter. The resulting output, a signal which increased rapidly to the maximum level and reset to zero every 64 pulses, was sampled every 1 μsec by the 256 word tropospheric data logging system. Thus the cumulative photoelectron (signal plus noise) count rate at any range was determined. The receiver chopper was set so it was opening during the arrival of photons from the lower regions of the atmosphere. In this way it had the effect of a neutral density filter whose transmission increased with range, thereby limiting the count rate from the lower heights

to acceptable levels but passing the full signal from the greater heights. Improvements here would be to modify the shape of the chopper blade, or to slow the motor, so this variable attenuation occurs over a greater range, and to trigger the laser firing with a signal from an optical sensor of the position of the chopper blade to reduce the effect of motor jitter.

By recording signals from the whole height region from, say, 7 km to 45 km at one time, the required number of laser firings would be considerably reduced, or alternatively, the precision in the measurement of scattering profiles would be greatly increased, especially at low altitudes where errors would be reduced to a fraction of one per cent. The basic height increment in this case would be 150m but counts from several increments could be added to increase the accuracy at the expense of height resolution.

Because each profile is stored with its system information, variations in the structure of the stratospheric aerosol layer during the night could be studied with much greater precision than the present system allows.

The greatest difficulty in the interpretation of lidar data is the normalisation problem. This could be reduced by making the lowest height of observation 7 km or even 5 km, and thereby reducing the likelihood of a scattering minimum occurring below the minimum observable height. Other possibilities exist. According to Cohen and Graber (1975) the depolarisation ratio of the backscattered signal will take the value for pure air (0.015) when an aerosol-free region is detected, and a suitable normalisation height can, therefore, be identified.

Alternatively, by comparing the Raman shifted radiation from atmospheric nitrogen molecules with the unshifted radiation from gas and particles, the contribution from gas molecules alone can be deduced (Cooney, 1975), at least up to 5 km to 6 km height, and this allows the possibility of matching a normalised tropospheric pulse with the lower end of the stratospheric profiles. As the department has acquired a tunable dye laser, greater photomultiplier sensitivity in the region of the Raman shifted radiation, and therefore a greater maximum height would be obtained by transmitting at a shorter wavelength. While there is still some uncertainty in calculating aerosol extinction at one wavelength from values at another, aerosol-free regions would be common to both.

With the possibility of stratospheric observations being made from the CSIRO at Aspendale in the future, the interesting possibility of the study of longitudinal variations in the structure of the stratospheric aerosol layer arises. With the facilities available at the CSIRO Division of Atmospheric Physics, the variability in aerosol scattering, ozone amount, winds and the synoptic patterns at various heights could be studied with the aim of furthering the knowledge of aerosol transport processes in the stratosphere.

The interpretation of variations in the lidar derived values of aerosol backscatter function is not straightforward as changes can be brought about by variations in the aerosol number density, refractive index, size distribution or shape of the aerosol particles. It is desirable, therefore, that periodic comparison experiments be made between the lidar and balloon-borne photoelectric particle counters and impactors, preferably

simultaneously and at the same site, to determine the cause of major or long term changes in the stratospheric aerosol layer.

7.4.2 Tropospheric Observations

The development of a climatology of values of backscatter-to-extinction ratio for different types of day would be most useful in the analysis of tropospheric backscatter data. The elevation scan method should be used where possible as it provides profiles of backscatter function and extinction coefficient which are measured simultaneously, in the same place, and with the same device.

Alternatively, the values may be calculated, as done here, by comparing averaged lidar backscatter signals with extinction profiles derived from aerosol number density profiles and corrected for relative humidity variations. Ideally a relative humidity sensor should be mounted on the aeroplane used for sampling, and used in preference to radiosonde values.

For the analysis of lidar backscatter signals in terms of extinction coefficient, either the modified molecular normalisation method or Equation 5.25 should be used. The depolarisation method is acceptable over shorter ranges and has the ability to detect aerosol-free regions which are useful as boundary values for the other methods.

For the derivation of boundary values, either the elevation scan method or the two beam method should be used where possible. Visibility measurements, although they provided reliable values when taken simultaneously and on site in the present study, should still be treated with caution because the wavelength dependence of aerosol scattering is not known with

great certainty, and it may change with time and place.

The comparison of consecutive diagrams of the spatial distribution of aerosols will be useful in determining the movement of aerosols and air masses, and for the study of complex atmospheric structures and other features of general meteorological interest. For example, the progress of the sea breeze front could be studied and the height and velocity of the return flow determined by observing the movement of aerosols in the flow. By taking consecutive elevation scans at different azimuths the spread and dispersal of smoke plumes from industrial chimneys can be studied, and the results used to test various models which describe this phenomenon.

BIBLIOGRAPHY

Ahlquist, N.C. and Charlson, R.J.	1969	Atmospheric Environment, 3, 551
Allen, R.J. and Evans, W.E.	1972	Rev. Sci. Instrum. 43, 1422
Allen, R.J. and Platt, C.M.R.	1977	Appl. Opt. 16, 3193
Aruga, T., Kamiyama, H., Jyumonji, M., Kobayashi, T. and Inaba, H.	1974	Rep. Ionos. Space Res. Jap. 28, 65
Australian Bureau of Meteorology	Pre-1970	(a) Monthly Climate Data, Upper Air
	1970 onwards	(b) Australian Climatological Survey, Upper Air Data
Ayers, G.P., Bigg, E.K. and Turvey, D.E.	1979	J. Appl. Meteorol. 18, 449
Bain, W.C. and Sandford, M.C.W.	1966	J. Atmos. Terr. Phys. 28, 543
Barrett, E.W. and Ben-Dov, O.	1967	J. Appl. Meteorol. 6, 500
Barteneva, O.D.	1960	Izv. Bull. Acad. Sci. USSR Geophys. Ser. p.1237
Bartusek, K.	1970	Ph.D Thesis, Department of Physics, University of Adelaide
Bartusek, K., Gambling, D.J. and Elford, W.G.	1970	J. Atmos. Terr. Phys. 32, 1535
Barnhardt, E.A. and Streete, J.L.	1970	Appl. Opt. 9, 1337
Bevington, P.R.	1969	"Data Reduction and Error Analysis for Physicists" McGraw-Hill, N.Y.
Bigg, E.K.	1956	J. Meteorol. 13, 262
Bigg, E.K.	1975	J. Atmos. Sci. 32, 910

Bigg, E.K.	1976	J. Atmos. Sci. 33, 1080
Blifford, I.H. and Ringer, L.D.	1969	J. Atmos. Sci., 26, 716
Bowman, M.R., Gibson, A.J. and Sandford, M.C.W.	1969	Nature, 221, 456
Bridgman, H.A.	1979	J. Appl. Meteorol. 18, 105
Brownlee, D.E., Ferry, G.V. and Tomandl, D.	1976	Science, 191, 1270
Bullrich, K.	1964	Advances in Geophysics, (Academic Press, N.Y.) Vol. 10
Cadle, R.D.	1972	EOS Trans AGU. 53, 812
Cadle, R.D., Kiang, C.S. and Louis, J.F.	1976	J. Geophys. Res. 81, 3125
Castleman, A.W. Jr., Munkelwitz, H.R. and Manowitz, B.	1974	Tellus, 26, 222
Chýlek, P., Grams, G.W. and Pinnick, R.G.	1976	Science, 193, 480
Clemesha, B.R., Kent, G.S. and Wright, R.W.H.	1966	Nature, 209, 184
Clemesha, B.R. and Nakamura, Y.	1972	Nature, 237, 329
Clemesha, B.R. and Rodrigues, S.N.	1971	J. Atmos. Terr. Phys. 33, 1119
Clemesha, B.R. and Simonich, D.M.	1978	J. Geophys. Res. 83, 2403
Cohen, A., Cooney, J. and Geller, K.	1976	Appl. Opt. 15, 2896
Cohen, A. and Graber, M.	1975	J. Appl. Meteorol. 14, 400
Cohen, A. and Kleiman, M.	1978	J. Appl. Meteorol. 17, 234
Cohen, A., Neumann, J. and Low, W.	1969	J. Appl. Meteorol. 8, 952

Collis, R.T.H.	1965	Science, 149, 978
Collis, R.T.H. and Ligda, M.G.H.	1966	J. Atmos. Sci. 23, 255
Collis, R.T.H. and Russell, P.B.	1976	in "Laser Monitoring of the Atmosphere" Ed. E.D. Hinkley. Springer-Verlag, Berlin, Heidelberg, N.Y.
Collis, R.T.H. and Uthe, E.E.	1972	Opto Electronics. 4, 87
Cooney, J.	1975	Appl. Opt. 14, 270
Cooney, J. and Pina, M.	1976	Appl. Opt. 15, 602
Covert, D.S., Charlson, R.J. and Ahlquist, N.C.	1972	J. Appl. Meteorol. 11, 968
Cunnold, D.M., Gray, C.R. and Merritt, D.C.	1973	J. Geophys. Res. 78, 920
Curcio, J.A. and Knestrick, G.L.	1958	J. Opt. Soc. Amer. 48, 686
Deirmendjian, D.	1963	Rand Corporation Report, R-407-PR
Deirmendjian, D.	1964	Appl. Opt. 3, 187
Deirmendjian, D.	1965	J. Geophys. Res. 70, 743
Deirmendjian, D.	1969	"Electromagnetic Scattering on Polydispersions" American Elsevier
Deirmendjian, D.	1973	Adv. Geophys. 16, 267
Delany, A.C., Pollock, W.H. and Shedlovsky, J.P.	1973	J. Geophys. Res. 78, 6249
De Luisi, J.J., Furukawa, P.M., Gillette, D.A., Schuster, B.G., Charlson, R.J., Porch, W.M., Fegley, R.W., Herman, B.M., Twitty, J.T. and Weinman, J.A.	1976(a)	J. Appl. Meteorol. 15, 441
	1976(b)	J. Appl. Meteorol. 15, 455
Dyer, A.J. and Hicks, B.B.	1968	Quart, J. Roy. Meteorol. Soc. 94, 545
Elterman, L.	1966	Appl. Opt. 5, 1769

Elterman, L.	1968	A.F.C.R.L.-68-0153 Environmental Res. Paper No. 285
Elterman, L.	1976	Appl. Opt., 15, 1113
Elterman, L., Toolin, R.B. and Essex, J.D.	1973	Appl. Opt. 12, 330
Elterman, L., Wexler, R. and Chang, P.T.	1969	Appl. Opt. 8, 893
Eloranta, E.W., King, J.M. and Weinman, J.A.	1975	J. Appl. Meteorol. 14, 1485
E.M.I. Electronics Ltd. Valve Division	1967	EMI Brochure 30m/16-67 (PMT) Issue 1
Farlow, N.H., Ferry, G.V., Lem, H.Y. and Hayes, D.M.	1979	J. Geophys. Res. 84, 733
Fegley, R.W. and Ellis, H.	1975	Appl. Opt. 14, 1751
Fernald, F.G., Herman, B.M. and Reagan, J.A.	1972	J. Appl. Meteorol. 11, 482
Fernald, F.G. and Schuster, B.G.	1977	J. Geophys. Res. 82, 433
Fernald, F.G., Schuster, B.G., Danielsen, E.F. and Deaven, D.G.	1975	Opt. Quantum Electr. 7, 141
Ferry, G.V. and Lem, H.Y.	1974	Paper presented at Environmental Impact of Aerospace Operations in the High Altitude, 2nd Int. Conf. July 8-10, San Diego, Calif. Amer. Meteorol. Soc. Boston. pp27-32
Fiocco, G. and Grams, G.W.	1964	J. Atmos. Sci. 21, 323
Fitzgerald, J.W.	1975	J. Appl. Meteorol. 14, 1045
Fox, R.J., Grams, G.W., Schuster, B.G. and Weinman, J.A.	1973	J. Geophys. Res. 78, 7789
Friedland, S.S., Katzenstein, J. and Zatzick, M.	1956	J. Geophys. Res. 61, 415

Friend, J.P.	1966	Tellus, 18, 465
Gambling, D.J., Bartusek, K. and Elford, W.G.	1971	J. Atmos. Terr. Phys. 33, 1403
Gambling, D.J. and Bartusek, K.	1972	Atmospheric Environment, 6, 181
Gibson, A.J.	1972	J. Phys. E.,Sci. Instrum. 5, 971
Gibson, A.J. and Thomas, L.	1975	Nature, 256, 561
Gibson, F.W.	1976	Appl. Opt. 15, 2521
Gill, R., Geller, K., Farina, J., Cooney, J. and Cohen, A.	1979	J. Appl. Meteorol. 18, 275
Giovane, F. and Schuerman, D.W.	1976	J. Geophys. Res. 81, 5383
Grams, G.W. and Fiocco, G.	1967	J. Geophys. Res. 72, 3523
Gras, J.L.	1976	Geophys. Res. Lett. 3, 533
Gras, J.L.	1978	Nature, 271, 231
Gras, J.L. and Laby, J.E.	1978	J. Geophys. Res. 83, 1869
Gras, J.L. and Michael, C.G.	1979	J. Appl. Meteorol. 18, 855
Gruner, P.	1942	Hand.d. Geophys. (Borntraeger, Berlin) 8, 432
Gruner, P. and Kleinert, H.	1927	Die Dämerungerscheinen in Problemen der Kosmichen Physik. 10, 1-113, Henre Grand, Hamburg
Hall, F.F. and Ageno, H.Y.	1970	Appl. Opt. 9, 1820
Hamilton, P.M.	1969	Atmospheric Environment, 3, 221
Hänel, G.	1970	Beitr. Phys. Atm. 43, 119
Hanel, G.	1971	Beitr. Phys. Atm. 44, 137
Hanel, G.	1976	J. Atmos. Sci. 33, 1120
Harris, F.S. and Rosen, J.M.	1976	in "Atmos. Aerosols, Their Optical Properties and Effects" NASA, CP-2004, MA2-1

Harrison, H., Herbert, J. and Waggoner, A.P.	1972	Appl. Opt. 11, 2880
Herrman, H., Pantani, L., Stefanutti, L. and Werner, C.		Alta Frequenza, 43, 732-468E
Hirono, M., Fujiwara, M., Uchio, O. and Itabe, T.	1974	Can. J. Chem. 52, 1560
Hofmann, D.J. and Rosen, J.M.	1976	Report, Department of Physics and Astron.,Univ. of Wyoming, Laramie, Wyoming, See also, EOS Trans, AGU 1975
Hofmann, D.J., Rosen, J.M. and Pepin, T.J.	1974	Proc. 3rd Conf. on CIAP, A.J. Broderick, T.M. Hard, Eds. NTIS Report No. DOT-TSC-OST-74-15
Hofmann,D.J., Rosen, J.M., Pepin, T.J. and Kroening, J.L.	1972-1974	Progress Reports dated June 1972, April 1973, June 1973 and Feb. 1974 Dept. of Physics and Astron., University of Wyoming
Hofmann, D.J., Rosen, J.M., Pepin, T.J. and Kroening J.L.	1973	Proc. 2nd Conf CIAP, A.J. Broderick Ed. NTIS Report DOT-TSC-OST-73-4
Hofmann,D.J., Rosen, J.M., Pepin, T.J. and Pinnick R.G.	1975	J. Atmos. Sci. 32, 1446
Hogan, A.W.	1976	J. Appl. Meteorol. 15, 611
Horvath, H. and Charlson, R.J.	1969	Amer. Ind. Hygiene Assoc. J. 30, 500
Inaba, H.	1976	in "Laser Monitoring of the Atmosphere" Ed. E.D. Hinkley, Springer-Verlag, Berlin, Heidelberg N.Y.
Johnson, W.B. and Uthe, E.E.	1971	Atmospheric Environment, 5, 703
Junge, C.E.	1953	Tellus, 5, 1
Junge, C.E.	1954	J. Meteorol. 11, 323

Junge, C.E.	1961	J. Meteorol. 18, 501
Junge, C.E.	1963	"Air Chemistry and Radioactivity" Academic Press, N.Y.
Junge, C.E., Chagnon, C.W. and Manson, J.E.	1961	J. Meteorol. 18, 81
Junge, C.E., and Manson, J.E.	1961	J. Geophys. Res. 66, 2163
Kasten, F.	1968	Beitr. Phys. Atm. 41, 33
Kent, G.S., Clemesha, B.R. and Wright, R.W.H.	1967	J. Atmos. Terr. Phys. 29 169
Kent, G.S. and Keenlislide,W.	1974	J. Atmos. Sci. 31, 1409
Kent, G.S., Keenlislide, W., Sandford, M.C.W. and Wright, R.W.H.	1972	J. Atmos. Terr. Phys. 34, 373
King, M.D., Byrne, D.M., Herman, B.M. and Reagan, J.A.	1978	J. Atmos. Sci. 35, 2153
Kruse, P.W., McGlaughlin, L.D. and McQuistan, R.B.	1962	"Elements of Infra-red Technology" (Wiley, N.Y.)
Kunkel, K.E., Eloranta, E.W. and Shipley, S.T.	1977	J. Appl. Meteorol. 16, 1306
Laby, J.E. and Unthank, E.L.	1974	Proc. Int. Conf. on Structure and Composition and General Circulation of Upper and Lower Atmospheres and Possible Anthropogenic Perturbations, IAMAP/IAPSO 1st Special Assemblies Melb. Aust. Jan. 1974. N.J. Derco and E.J. Truhaler, Eds.
Landsberg, H.	1938	Ergeb. Kosmichen Phys. 3, 155
Lazrus, A. and Gandrud, B.	1974(a)	J. Atmos. Sci. 31, 1102
Lazrus, A. and Gandrud, B.	1974(b)	J. Geophys. Res. 79, 3424
Lenhard, R.W.	1973	Bull. Amer. Meteorol. Soc. 54, 691

Mason, J.B.	1975	Appl. Opt. 14, 76
McCormick, M.P., and Fuller W.H. (Jr)	1975	Appl. Opt. 14, 4
McCormick, M.P., Lawrence, J.D. (Jr), and Crownfield, F.R. (Jr)	1968	Appl. Opt. 7, 2424
McCormick, M.P., Swissler, T.J., Chu, W.P., and Fuller, W.H. (Jr)	1978	J. Atmos. Sci. 35, 1296
McNeil, W.R. and Carswell, A.I.	1975	Appl. Opt. 14, 2158
Middleton, W.E.K.	1963	"Vision through the Atmosphere" Univ. of Toronto Press, Toronto.
Mie, G.	1908	Ann. Phys. 25, 377
Miranda, H.A. (Jr), Dulchinos, J. and Miranda, H.P.	1973	Report AFCRL-TR-73-0700
Morton, G.A.	1968	Appl. Opt. 7, 1
Mossop, S.C.	1963	Nature, 199, 325
Mossop, S.C.	1964	Nature, 203, 824
Mossop, S.C.	1965	Geochim et Cosmochim Acta, 29, 201
Nilsson, B.	1979	Appl. Opt. 18, 3457
Northam, G.B., Rosen, J.M., Melti, S.H., Pepin, T.J., McCormick, M.P., Hofmann, D.J. and Fuller, W.H. (Jr)	1974	Appl. Opt. 13, 2416
Ottway, M.T.	1972	Paper presented at the 4th Conf. on Laser Radar Studies of the Atmosphere, Group on Laser Atmos. Probing, Tucson, Arizona.
Ottway, M.T., Kent, G.S. and Wright, R.W.H.	1971	J. Atmos. Terr. Phys. 33, 1337

Pal, S.R. and Carswell, A.I.	1977	J. Appl. Meteorol. 16, 70
Paltridge, G.W. and Platt, C.M.R.	1973	J. Atmos. Sci. 30, 734
Pearson, P.H.O.	1973(a)	W.R.E. (now Defence Research Centre, Salisbury, S.A.) Technical Note 799, (WR&D) Dept. Supply, Australian Defence Scientific Service
Pearson, P.H.O.	1973(b)	W.R.E. Technical Note 1002 (WR&D) Australian Defence Scientific Service
Pettifer, R.E.W.	1975	J. Atmos. Terr. Phys. 37, 669
Pettifer, R.E.W. and Healey, P.G.	1974	J. Phys. E., Sci. Instrum. 7, 617
Pettifer, R.E.W., Jenkins, G.J., Healey, P.G. and Convery, J.H.	1976	Opt. Quantum Electr. 8, 409
Pinnick, R.G., Rosen, J.M. and Hofmann, D.J.	1976	J. Atmos. Sci. 33, 304
Platt, C.M.R.	1977	J. Appl. Meteorol. 16, 339
Platt, C.M.R.	1978	J. Appl. Meteorol. 17, 482
Pourney, J.C., Renault, D. and Orzay, A.	1979	Appl. Opt. 18, 1141
Quenzel , H., Ruppersberg, G.H. and Schellhase, R.	1975	Atmospheric Environment, 9, 587
Reagan, J.A., Spinhirne, J.D. and Byrne, D.M.	1977	J. Appl. Meteorol. 16, 911
Rosen, J.M.	1964	J. Geophys. Res. 69, 4673
Rosen, J.M.	1968	J. Geophys. Res. 73, 479
Rosen J.M.	1969	Space Sci. Rev. 9, 58
Rosen, J.M.	1971	J. Appl. Meteorol. 10, 1044

Rosen, J.M. and Hofmann, D.J.	1977	J. Appl. Meteorol. 16, 56
Rosen, J.M., Hofmann, D.J. and Laby, J.	1975	J. Atmos. Sci. 32, 1457
Rosenberg, G.V.	1960	Soviet Phys. Usp. 3, 346
Rosinski, J.	1972	J. Atmos. Terr. Phys. 34, 487
Rosinski, J., Nagamoto, C.T. and Bayard, M.	1975	J. Atmos. Terr. Phys. 37, 1231
Rössler, F.	1968	Space Res. 8, 633
Rossler, F.	1972	Space Res. 12, 423
Russell, P.B. and Hake, R.D. (Jr)	1977	J. Atmos. Sci. 34, 163
Russell, P.B., Livingstone, J.M. and Uthe, E.E.	1979	J. Atmos. Sci. 36, 1587
Russell, P.B., Viezee, W. and Hake, R.D. (Jr)	1973	1st Semi-Annual Report 2217, Contract NAS2-7261, Stanford Research Institute, Menlo Park, California
Russell, P.B., Viezee, W. and Hake, R.D. (Jr)	1974(a)	Final Report 2217, Contract NAS2-7261 Stanford Research Institute, Menlo Park, California.
Russell, P.B., Viezee, W., Hake, R.D. (Jr) and Collis, R.T.H.	1974(b)	"Credibility and Significance of Lidar observations of the Stratospheric Aerosol" paper presented at the 6th Int. Laser Radar Conf. Sendai, Japan, 3-6 September
Russell, P.B., Viezee, W., Hake, R.D. (Jr) and Collis, R.T.H.	1975	"Lidar Observations of the Stratospheric Aerosol: Summary of Results and a Calibration.Error Assessment" paper presented at 4th Conf. on CIAP, 4-7 Feb DOT, Cambridge, Mass.

Russell, P.B., Viezee, W., Hake, R.D. (Jr) and Collis, R.T.H.	1976	Quart. J. Roy. Meteorol. Soc. 102, 675
Sandford, M.C.W. and Gibson, A.J.	1970	J. Atmos. Terr. Phys. 32, 1423
Sassen, K.	1976	J. Appl. Meteorol. 15, 292
Sassen, K.	1977	J. Atmos. Sci. 34, 1444
Shaw, G.E., Reagan, J.A. and Herman, B.M.	1973	J. Appl. Meteorol. 12, 374
Shettle, E.P. and Fenn, R.W.	1975	AGARD Optical Propagation in the Atmosphere 27-31 Oct, Lynby, Denmark, Conf. Proc. CP-183 pp 2-1 to 2-16
Schuster, B.G.	1970	J. Geophys. Res. 75, 3123
Steinvall, V. and Agren, C.H.	1975	J. Appl. Meteorol. 14, 603
Swissler, T.J. and Harris, F.S.	1976	in "Atmospheric Aerosols, Their Optical Properties and Effects" NASA-CP-2004 p MC11-1
Toon, O.B. and Pollak, J.B.	1973	J. Geophys. Res. 78, 7031
Toon, O.B. and Pollak, J.B.	1976	J. Appl. Meteorol. 15, 225
Twitty, J.T., Parent, R.J., Weinman, J.A. and Eloranta, E.W.	1976	Appl. Opt. 15, 980
Twomey, S.	1976	J. Atmos. Sci. 33, 1073
Twomey, S.	1977	"Atmospheric Aerosols", Amsterdam: Elsevier Scientific, Developments in Atmospheric Science No. 7
Van der Hulst, H.C.	1957	"Light Scattering by Small Particles" Wiley and Sons, N.Y.
Viezee, W., Uthe, E.E. and Collis, R.T.H.	1969	J. Appl. Meteorol. 8, 274

Volz, F.E. and Goody, R.M.	1962	J. Atmos. Sci. 19, 382
Waggoner, A.P., Ahlquist, N.C. and Charlson, R.J.	1972	Appl. Opt. 11, 2886
Werner, C.	1972	Opto-Electronics, 4, 125
Woodcock, A.H.	1953	J. Meteorol. 10, 362
Woodman, D.P.	1974	Appl. Opt. 13, 2193
Yamamoto, G. and Tanaka, M.	1969	Appl. Opt. 8, 447
Young, S.A.	1976	J. Atmos. Terr. Phys. 38, 667
Young, S.A. and Elford, W.G.	1979	Nature, 278, 540

ADDENDUM

Throughout this thesis it has been assumed that in the troposphere at the ruby laser wavelength, the volume absorption coefficient β_a is negligible when compared with the volume scattering coefficient β_s, and that the volume extinction coefficient β_e is therefore equal to the scattering coefficient. However, under those conditions where this is not true, a more complete analysis is required. Using the quantities defined in Section 1.5.2,

$$\beta_e = \beta_a + \beta_s = Q_A \pi r^2 n + Q_s \pi r^2 n .$$

Now if the backscatter efficiency is Q_B then

$$Q_B = \frac{P(\pi)}{4\pi} Q_s ,$$

and

$$B(\pi) = \frac{P(\pi)}{4\pi} Q_s \pi r^2 n .$$

Therefore

$$\frac{B(\pi)}{\beta_e} = \frac{P(\pi)}{4\pi} \cdot \frac{Q_s}{Q_A + Q_s} = \frac{P(\pi)}{4\pi} \cdot \bar{\omega}_0 .$$

Then

$$\frac{P(\pi)}{4\pi} = \frac{B(\pi)}{\beta_e}$$ when $\bar{\omega}_0$ is unity. Fig. 1.12(f) shows calculated values of $\bar{\omega}_0$ for different values of absorption, or imaginary part of the particle's refractive index. Values of the imaginary refractive index measured by Reagan and Hermann (1980) [J. Appl. Meteorol, 19, 426] have an average of .003 with a maximum upper limit of .015. In very polluted, sooty atmospheres higher values may be obtained and in these cases the figure shows that $\bar{\omega}_0$ is significantly less than unity.

APPENDIX I

DERIVATION OF THE LIDAR EQUATION

According to van de Hulst (1957), when polarised light of intensity I_0 ($W.sr^{-1}$) and wave number $k = 2\pi/\lambda$ is incident on a volume v (Figure A.1) containing n particles per unit volume, the scattered intensity at a distance r and an angle θ to the incident beam is

$$I = \frac{I_0 v}{r^2} \left[\frac{n. F(\theta, \phi)}{k^2} \right] . \qquad \text{A1.1}$$

The angle ϕ is the angle between the direction of the electric polarisation and the plane containing the incident and scattered waves, and $F(\theta, \phi)$ is a function which describes the angular distribution of the scattering. The quantity in the brackets can be re-written as

$$n F(\theta, \phi)/k^2 = n \sigma P(\theta, \phi)/4\pi = \beta P(\theta, \phi)/4\pi ,$$

where σ is the scattering cross section, β is the volume scattering coefficient and $P(\theta, \phi)$ is the scattering phase function. (Deirmendjian 1964). If we write $B(\theta, \phi) = \beta P(\theta, \phi)/4\pi$, where $B(\theta, \phi)$ is the volume scattering function, then Equation A1.1 becomes

$$I = I_0 v B(\theta, \phi)/r^2 . \qquad \text{A1.2}$$

For air molecules and plane polarised light the phase function is $P_M(\theta, \phi)/4\pi = (3/8\pi)(\cos^2\theta \cos^2\phi + \sin^2 \phi)$ and for unpolarised light

$$P_M(\theta) = (3/16\pi) (\cos^2\theta + 1) .$$

Here the subscript M refers to scattering by air molecules. For a monostatic lidar the separation of the transmitter and receiver is small and the scattering angle θ is very close to 180°, especially at the ranges usually considered, and both phase functions reduce to $P_M(\pi) = 1.5$.

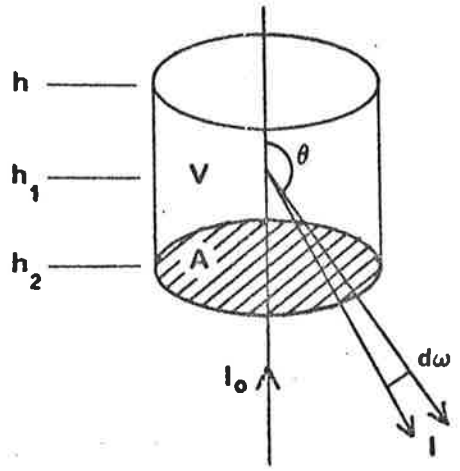

FIG A.1 Scattering geometry

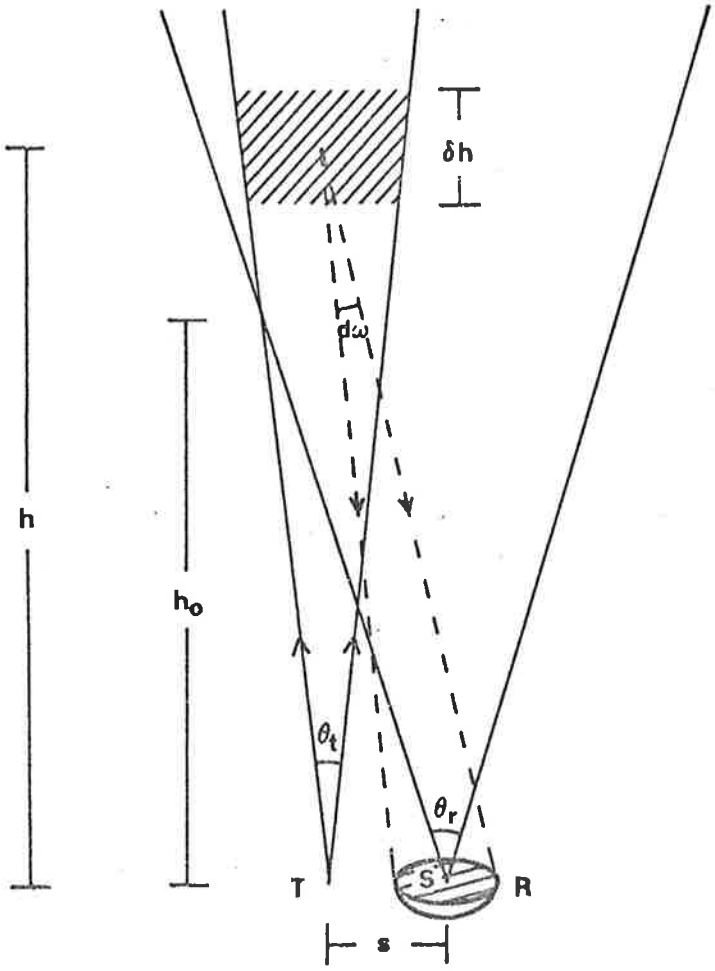

FIG A.2 Lidar geometry.

At a height h in the atmosphere the volume backscatter function for air molecules can be written as

$$B_M(\pi, h) = (P_M(\pi)/4\pi) . \beta_M(h) = (3/8\pi) \beta_M(h) . \qquad A1.3$$

Similarly the volume backscatter function for aerosols is given by

$$B_A(\pi, h) = (P_A(\pi)/4\pi) . \beta_A(h) . \qquad A1.4$$

As the aerosols are likely to have a range of optical properties, the quantities in this equation should be considered as average values for the particular aerosol sample being studied.

Consider now the scattering of light from a pulse transmitted by a vertically pointing lidar (Figure A.2) with a transmitter T of divergence θ_t and receiver R of divergence θ_r separated by a distance s. As θ_r is greater than θ_t the whole transmitted pulse will be in the field of view of the receiver above a height h_o. Because the divergence of the transmitted laser pulse θ_t is small the volume v illuminated by the pulse is approximately cylindrical with a cross sectional area A (Figure A.1). The length of the pulse is $L = c\tau$ where c is the velocity of light and τ is the duration of the pulse.

At some time $t = h/c$, when the top of the pulse is at height h and the base at h_2, a photon in the leading edge is scattered back towards the receiver. A short time $(\tau/2)$ seconds later it has reached height h_1, which is midway between h and h_2, and is now level with the trailing edge of the pulse which has moved up to height h_1. Any photons now backscattered from the trailing edge of the pulse will be indistinguishable from those photons just scattered from the leading edge. Further, any photons arriving at the detector with those just

described could have come from anywhere in the illuminated volume between heights h and h_1, and this determines the limit of the range resolution of the lidar. Thus the effective volume which contributes to the scattering received by the lidar at time (h_1/c) seconds later is

$$v/2 = AL/2 = Ac\tau/2 . \qquad \text{A1.5}$$

If the original transmitted power of the lidar pulse is p_o and the transmittance of the atmosphere from ground level to height h is $T(o, h)$, then the intensity I_0 $(W. sr^{-1})$ at height h is

$$I_0 = p_o . T(o, h)/d\omega_t = p_o h^2 T(o, h)/A . \qquad \text{A1.6}$$

where the solid angle subtended by the volume v with base area A at height h is $d\omega_t = A/h^2$.

By combining equations A1.2 to A1.6 we have the total power p backscattered from the volume into a small solid angle $d\omega$.

$$P = p_o T(o, h) . \frac{c\tau}{2} (B_M(\pi, h) + B_A(\pi, h)) d\omega .$$

If the collecting surface of the receiver has area S then $d\omega = S/h^2$. On its path back to the lidar the scattered radiation experiences further attenuation by the atmospheric transmittance and the power received by the lidar from height h is

$$p(h) = [p_o \frac{c\tau S}{2}] (B_M(\pi, h) + B_A(\pi, h)) . T^2(o, h)/h^2 . \qquad \text{A1.7}$$

For a lidar measuring scattering from the troposphere this power is incident on a photomultiplier tube. The instantaneous signal voltage $V(h)$ at the anode is proportional to the product of the power $p(h)$, the conversion efficiency of the photomultiplier Q in amps per

watt, the optical efficiency of the lidar receiver η_0 , and the anode load resistor R_L . So

$$V(h) = [\, R_L \eta_0 \, Q \,]\, p(h), \qquad \text{A1.8}$$

or

$$V(h) = K\,(B_M(\pi, h) + B_A(\pi, h)).\ T^2(o, h)/h^2 . \qquad \text{A1.9}$$

The efficiency and conversion factors and the lidar equipment parameters have been grouped together to form a system constant K in the form of the lidar equation for the troposphere.

For a stratospheric lidar the return signal is much weaker and photon counting techniques must be used. In this mode of operation those individual photons that arrive in a small time interval Δt and are detected, are counted, and the total stored in one of the registers of a multi-channel counter. If the number of transmitted photons is $N = p_o \tau \lambda/kc = E\lambda/kc$, where E and λ are the laser energy and wavelength and k is Planck's constant, and if η_E is the combined electrical efficiency of the amplifiers, discriminator and counter, and Q is the photomultiplier quantum efficiency, then the received photoelectron count rate is

$$N(h) = (E\lambda S\, \eta_0\, \eta_E\, Q\ /\ 2k)\ (B_M(\pi, h) + B_A(\pi, h)).T^2(0,h)/h^2. \qquad \text{A1.10}$$

Provided the counting time interval Δt is short the number of photoelectrons counted in the register is $C(h) = N(h).\ \Delta t = 2N(h).\ \Delta h/c$. Using equation A1.10 gives

$$C(h) = (E\lambda S\, \eta_0\, \eta_E\, Q\, \Delta h/c)\ (B_M(\pi, h) + B_A(\pi, h)).T^2(0,h)/h^2.$$

or if the system parameters are combined again into a system constant K ,

$$C(h) = K\,(B_M(\pi, h) + B_A(\pi, h)).T^2(0,h)/h^2. \qquad \text{A1.11}$$

APPENDIX II

"A Digital Tape Recording System for Transient Data"

By

S.A. Young.

A DIGITAL TAPE RECORDING SYSTEM FOR TRANSIENT DATA

S. A. YOUNG.

Department of Physics
University of Adelaide
ADELAIDE, SOUTH AUSTRALIA 5000

THE UNIVERSITY OF ADELAIDE

DEPARTMENT OF PHYSICS

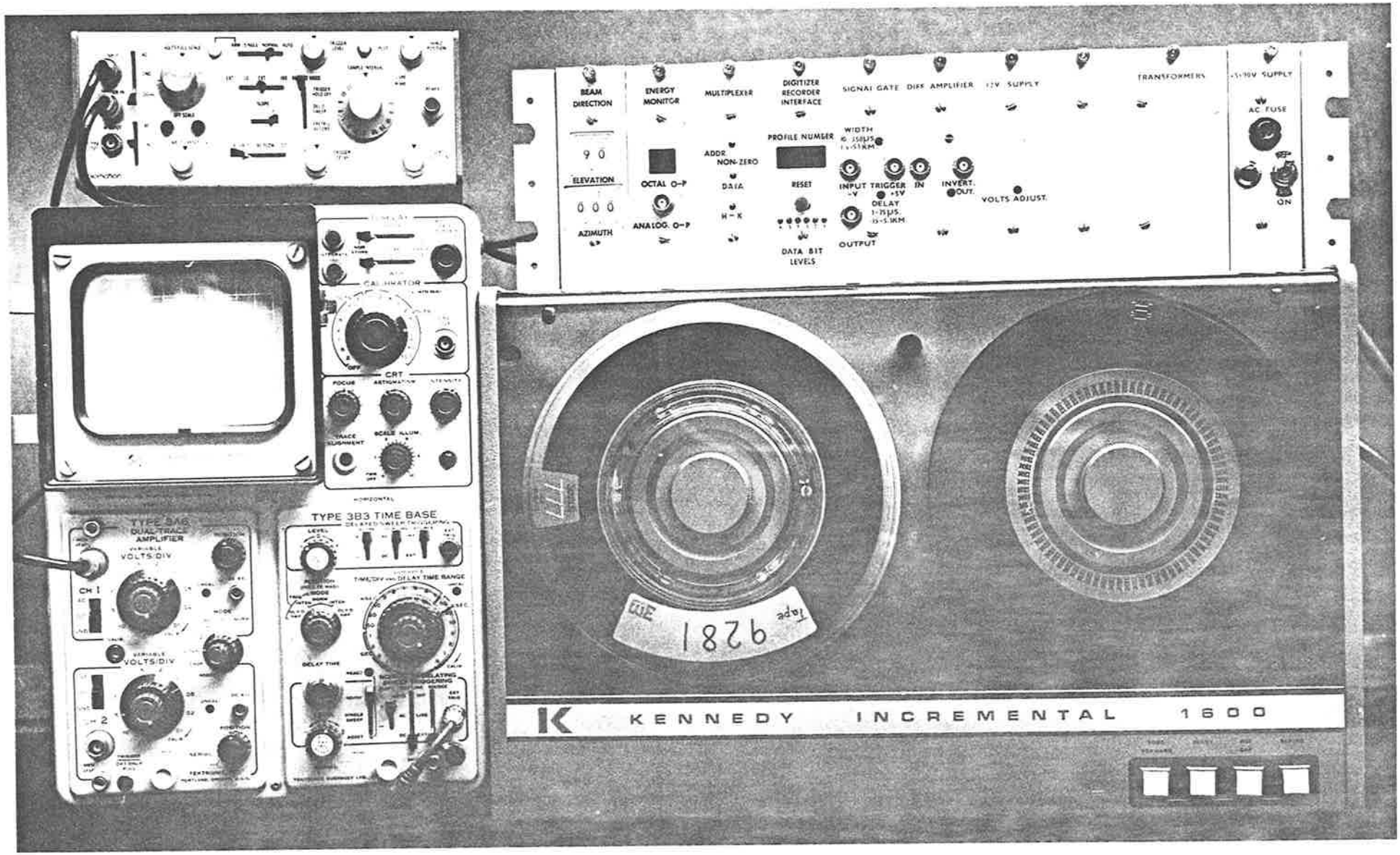

PLATE 1. The Recording System and Oscilloscope Monitor.

C O N T E N T S

A DIGITAL TAPE RECORDING SYSTEM FOR TRANSIENT DATA

S. A. Young.
Department of Physics
University of Adelaide.
ADELAIDE, SOUTH AUSTRALIA 5000

1. INTRODUCTION

Transient data is recorded in six-bit binary form on half-inch magnetic computer tape using a Biomation 610B Transient Recorder, a Kennedy 1600 Incremental Tape Recorder and interface and control equipment. The system is shown in Plate 1. The flexibility of the transient recorder is such that signals arriving at various times, either before or after the arrival of a trigger pulse, can be sampled digitally at intervals of between 0.1 micro-seconds and 50 milliseconds. A multiplexing system also allows fifteen "housekeeping" words of information to be written on to tape after the data.

The unit can be operated in either a manual or an automatic mode. When switched to the manual mode the stored data in the transient recorder can be displayed on an oscilloscope and inspected for suitability before it is transferred to the tape recorder by pressing the "PLOT" button. In the automatic mode the unit senses when the storage of the data in the transient recorder memory is complete and automatically initiates the transfer to the tape recorder.

The front panel display includes a three digit shot or record number which may be reset to zero with a switch, and six LED's (light emitting diodes) which indicate the level ("0" or "1") of each bit of each word of data during readout. Two other LED's indicate when either housekeeping or transient recorder data are being written and a third is a multiplexer address indicator.

Although the system was specifically designed for the collection and storage of tropospheric lidar data, it could be used with any data suitable for

digitization and storage in the 256 six-bit words of the Biomation Transient Recorder.

2. CONSTRUCTION

The complete unit fits on two boards measuring 16.5 cm by 9 cm. These boards were each made from one and a half "LEKTROKIT" circuit boards joined together and attached to a printed circuit strip which slides into a 44 pin end connector. Each board has an aluminium front panel and fits into a rack holding other electronic circuits associated with the lidar system.

Apart from the six data level inverters which supply current to the LED indicators and the inverters for the Write-Step and End of Record commands all the electronic circuiting is constructed of TTL integrated circuits. The multiplexers are Fairchild 74150 sixteen input multiplexers and the monostables are 74121s and 9602s. The other integrated circuits are mostly from the Fairchild 7400 series.

A single, regulated five volt power supply required for the TTL integrated circuits and the transistor circuits used in the unit also provides power to other housekeeping circuits in the electronics rack.

3. CIRCUIT LOGIC AND OPERATION

A simplified block diagram of the system is shown in Figure 1 and a detailed description of the circuits is given below.

3.1 The Auto Plot Circuit

During manual operation the line from the "PLOT" button in the transient recorder is normally grounded. Once the button is depressed this line "floats" high enough to trigger the circuit which initiates the transfer of data to tape.

The automatic plot mode circuit is shown in Figure 4 and operates as follows. After the last word of data has been stored in the memory of the transient recorder the "RECORD" output drops back to the low state. As can be seen in the timing diagram, Figure 2 lines c to h , the combination of monostables MS1A and MS2A causes the R-S flip-flop FF1A to change state 550 µsec later. This delay is made necessary by the fact that the memory of the transient recorder memory is cycled during this time. Monostable MS5A is triggered by the next 300Hz clock pulse which in turn triggers FF1A which reverts to its original state thus triggering MS6A which produces the "AUTOPLOT" pulse.

Monostables MS2A and MS5A provide narrow, one microsecond pulses for triggering FF1A. Wider pulses could cause the flip-flop to toggle if both inputs were to be in the low state at the same time.

3.2 The Write-Step Circuit

The memory of the transient recorder is cycled continuously with each word in the memory being available every 512 µsec. As a result, when the words are being copied from memory in the asynchronous mode used here, a delay of up to 512 µsec occurs between the arrival of the PLOT pulse and the availability of the first memory word. A similar delay is experienced when subsequent words are requested by the arrival of the clock pulses at the EXTERNAL PLOT RATE input of the transient recorder.

The Write-Step circuit is shown in Figure 5 and the relevant timing is shown in lines i to m in Figure 2. As the words become available at the data output of the transient recorder the FLAG output switches to the high state where it stays until the arrival of the next clock pulse. Once the complementary output of MS1A ($\bar{Q}$) is in the low state, the gate G1 will

pass all the flag levels to MS7A which produces pulses of 50 µsec duration as required by the WRITE-STEP input of the tape recorder. The first 255 words are read from memory in this fashion. The last word and the corresponding flag are only available for 100 µsec. As this time is too short for the system to respond reliably, the word is discarded by placing a simple filter on the FLAG line.

3.3 The Housekeeping and Combined Work-Step Circuits

Six multiplexers, one for each bit, are used to write both data and housekeeping information on to magnetic tape. The circuit which performs this operation is shown in Figure 6, and the timing is shown in Figure 3 lines a to k .

The contents of the transient recorder's memory are transferred while the multiplexers are at address zero and the fifteen housekeeping words at the remaining addresses of the sixteen input multiplexers. A four-bit binary counter which shifts the addresses of the multiplexers is held at address zero during transfer of the transient recorder data. The WRITE COMMAND output of the transient recorder stays in the high state for the first 224 words of output only. The remaining 128 msec are supplied by MS3A and MS4A which then trigger FF2B, MS2B and FF1B. The outputs of FF1B are labelled RESET and $\overline{\text{RESET}}$. Until the arrival of the trigger pulse from MS2B the RESET line is held high inhibiting the counter, and the inverted data write-step pulses pass through the AND-OR-INVERT gate to the inverter driver and the tape recorder.

Once the RESET line goes low the counter and multiplexer addresses change from zero. During this time monostables MS6B and MS5B produce 50 µsec housekeeping Write-Step pulses which are delayed by 2 µsec with respect to the clock pulses to avoid coincidences.

After the fifteenth pulse the return of the counter address to zero is detected by a four input NAND gate which triggers MS1B and in turn FF1B. This sends the RESET line high again inhibiting the counter until the next record is to be transferred to the tape recorder.

3.4 The End of Record and Counter Display Circuits

When the counter address returns to zero, MS1B produces a 50 μsec End of Record pulse (EOR) via MS3B and MS4B. The timing relationship of these pulses is shown in Figure 3 lines ℓ to n .

As can be seen in Figure 7, the EOR pulse is used to increment the record counter and front panel display. The counter consists of three 7490 decade counters connected to three LED displays. The outputs are also joined to three of the inputs of the multiplexers so the record number can be recorded.

3.5 The Inverter-Driver Circuits

The data level inverter-drivers, shown in Figure 8, supply enough current through the 2N3646 transistors to drive the LED level indicator lamps. They, and the inverter-drivers used for the EOR and Work-Step command pulses were designed to ensure that the correct logic levels required by the tape recorder were satisfied. The tape recorder's DTL, "positive true" logic requires a "one" level of between 4V and 6V, and a "zero" level of between 0V and 0.5V.

4. PERFORMANCE

In the automatic mode one record can be written on to tape in about one second. The additional time required for the writing of an EOR marker allows a maximum cycling time of about one and a half seconds. This time could be shortened if a tape recorder with a writing rate faster than the present 300 word

per second were used. A simple change to the timing resistors of the XR-320 clock and of MS3A, a delay monostable, would allow a higher writing rate. The existing rate, though, has been quite adequate for present purposes.

The multiplexers used permit fifteen words of housekeeping data to be written on to tape after the transient recorder output. At present only the first nine words are used. These words contain, in order, the six-bit output from the laser energy monitor, one four-bit binary-coded-decimal (BCD) word for each of the three record counter digits, two for the lidar elevation angle, and three for its azimuth. Two extra words are set to zero as a marker to aid in the decoding of the information on the computer.

The unit has been used successfully to record tropospheric lidar signals and related operational information. The system should also be adaptable to other kinds of data which can be stored satisfactorily in 256 six-bit words.

APPENDIX I

TABLES OF PIN CONNECTIONS ON BOARDS A AND B

Board A has only one edge connector with 22 electrically insulated connectors on each side, numbered 1 to 22 and A to Z respectively.

Board B has two edge connectors, each similar to that on Board A. The pins on the main board connector are numbered 1-1 to 22-1 and A-1 to Z-1 and those on the secondary connector are numbered A-2 to Z-2, and 1-2 to 22-2.

The abbreviations used in these tables are listed at the end of this Appendix.

BOARD A

PIN	DESIGNATION	PIN	DESIGNATION
1	OV Earth	A	OV Earth
2	BM data 2^0 I/P from MUX 1	B	
3	2^1 MUX 2	C	Delayed Write Command O/P Pin 3.2 Board B
4	2^2 MUX 3	D	
5	2^3 MUX 4	E	Data Write-Step to Pin 5-2 Board B
6	2^4 MUX 5	F	Total Write-Step I/P to Inverter Driver
7	2^5 MUX 6	H	
8	+ 5V	J	
9	BM data 2^0 O/P to TR	K	
10	2^1	L	
11	2^2	M	Shot Number, Hundreds Digit A3 O/P to Board B
12	2^3	N	" " B3 O/P " " "
13	2^4	P	" " C3 O/P " " "
14	2^5	R	" " D3 O/P " " "
15	Clock O/P to BM and 4-2	S	" " Tens Digit A2
16	Record I/P from BM	T	" " " " B2
17	Auto-plot O/P to BM	U	" " " " C2
18	Flat I/P from BM	V	" " " " D2
19	Write Command I/P from BM	W	" " Units Digit A1
20	Total Write-Step O/P to TR	X	" " " " B1
21	$\overline{\text{EOR}}$ Command O/P to TR	Y	" " " " C1
22	$\overline{\text{EOR}}$ I/P to inverter driver	Z	" " " " D1

APPENDIX I (Continued)

BOARD B

PIN	DESIGNATION	PIN	DESIGNATION	PIN	DESIGNATION
1-1	0V	A-1	0V	1-2	x
2-1	BM data 2^5 O/P from MUX 6	B-1	Elevation Tens Digit A2	2-2	BM Record O/P from BM
3-1	2^4 5	C-1	" " " B2	3-2	Delayed Write Comm.
4-1	2^3 4	D-1	" " " C2	4-2	Clock I/P from Board A
5-1	2^2 3	E-1	" " " D2	5-2	Data Write Step I/P Board A
6-1	2^1 2	F-1	Elevation Units Digit A1	6-2	$\overline{\text{Write-Step}}$ O/P to Pin 22 Board A
7-1	2^0 1	H-1	" " " B1	7-2	$\overline{\text{EOR}}$ O/P to Pin F " "
8-1	+5V	J-1	" " " C1	8-2	x
9-1	BM data 2^5 I/P from BM	K-1	" " " D1	9-2	x
10-1	2^4	L-1	Azimuth Hund. Digit A3	10-2	x
11-1	2^3	M-1	" " " B3	11-2	Shot Number Hund. Digit A3
12-1	2^2	N-1	" " " C3	12-2	" " " " B3
13-1	2^1	P-1	" " " D3	13-2	" " " " C3
14-1	2^0	R-1	" Tens " A2	14-2	" " " " D3
15-1	Energy Monitor I/P 2^0 bit	S-1	" " " B2	15-2	" " Tens " A2
16-1	" " 2^1	T-1	" " " C2	16-2	" " " " B2
17-1	" " 2^2	U-1	" " " D2	17-2	" " " " C2
18-1	" " 2^3	V-1	" Units " A1	18-2	" " " " D2
19-1	" " 2^4	W-1	" " " B1	19-2	" " Units " A1
20-1	" " 2^5	X-1	" " " C1	20-2	" " " " B1
21-1	x	Y-1	" " " D1	21-2	" " " " C1
22-1	x	Z-1	x	22-2	" " " " D1

NOTES: (1) Data bits 1(2^0) to 6 (2^5) are linked to Multiplexers 1 to 6
(2) BCD bits eg. A3 represents Bit 1 (2^0), Hundreds Digit
A2 " " , Tens "
D1 " 4 (2^3), Units "

ABBREVIATIONS BM Biomation 610B Transient Recorder. TR Kennedy 1600 Incremental Tape Recorder
EOR, $\overline{\text{EOR}}$ End of Record and its Complement MUX Multiplexer
I/P Input to Board O/P Output from Board x No Connection

APPENDIX II DATA AND HOUSEKEEPING FORMAT ON TAPE

WORD	BIT 1	2	3	4	5	6	DESIGNATION
1	2^0	2^1	2^2	2^3	2^4	2^5	BM Word 1 } "D A T A"
2	2^0	2^1	2^2	2^3	2^4	2^5	BM Word 2 }
255	2^0	2^1	2^2	2^3	2^4	2^5	BM Word 255 }
256	2^0	2^1	2^2	2^3	2^4	2^5	Energy Monitor O/P
257	A3	B3	C3	D3	o	o	Lidar Shot Number, Hund. Digit (BCD)
258	A2	B2	C2	D2	o	o	Tens. " "
259	A1	B1	C1	D1	o	o	Units " "
260	A2	B2	C2	D2	1	1	Beam Elevation, Degrees, Tens Digit (BCD)
261	A1	B1	C1	D1	1	1	Units " "
262	A3	B3	C3	D3	1	1	Beam Azimuth, " Hund. " "
263	A2	B2	C2	D2	1	1	Tens " "
264	A1	B1	C1	D1	1	1	Units " "
265	o	o	o	o	o	o	Markers for checking during decoding
266	o	o	o	o	o	o	of tape data.
267	x	x	x	x	x	x	
268	x	x	x	x	x	x	
269	x	x	x	x	x	x	
270	x	x	x	x	x	x	
	END OF RECORD MARKER						

ABBREVIATIONS

x signifies undefined levels
BM Biomation Transient Recorder
BCD Binary Coded Decimal.

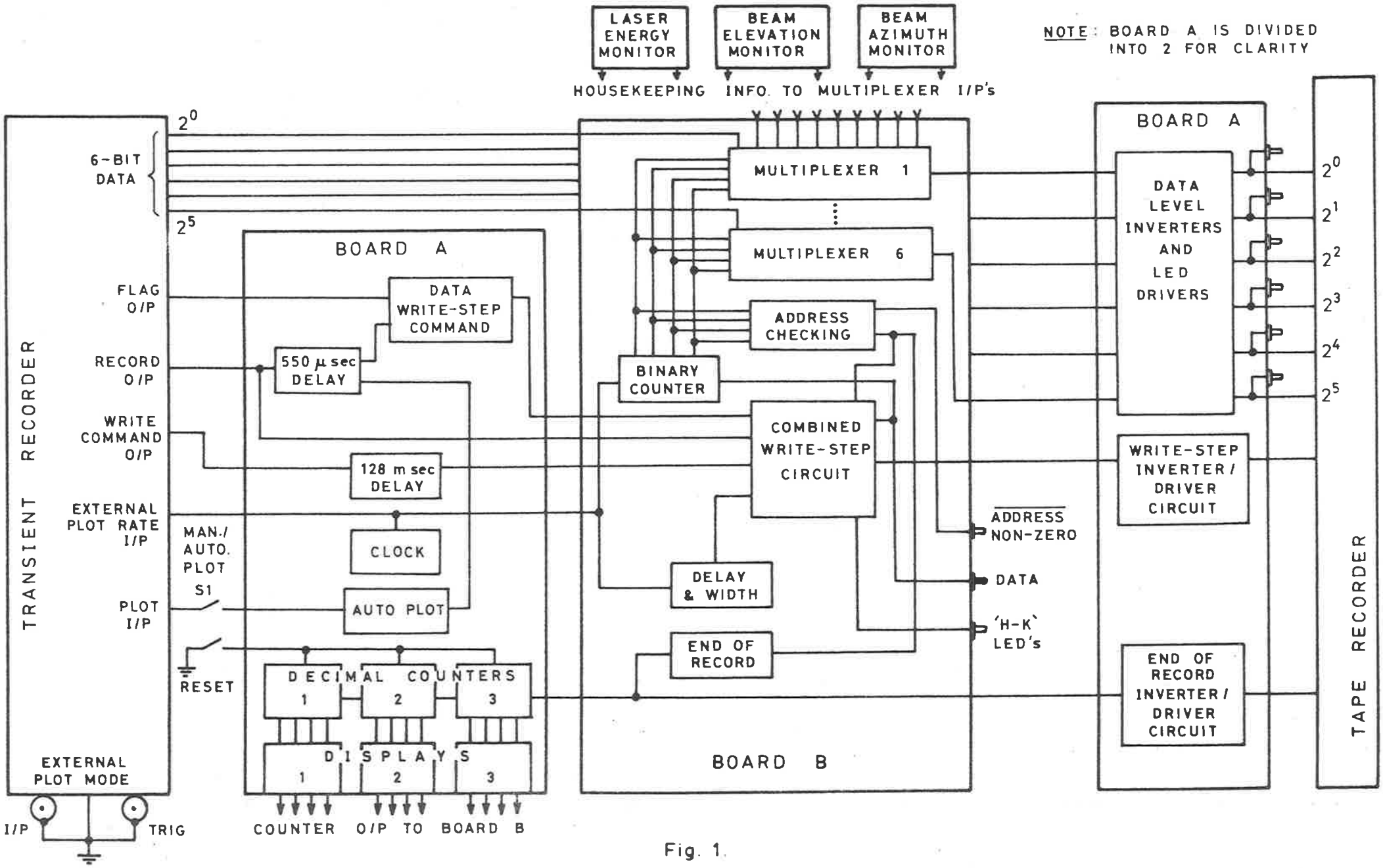
LASER ENERGY MONITOR
BEAM ELEVATION MONITOR
BEAM AZIMUTH MONITOR
HOUSEKEEPING INFO. TO MULTIPLEXER I/P's
NOTE: BOARD A IS DIVIDED INTO 2 FOR CLARITY
TRANSIENT RECORDER
6-BIT DATA
2^0
2^5
FLAG O/P
RECORD O/P
WRITE COMMAND O/P
EXTERNAL PLOT RATE I/P
MAN./ AUTO. PLOT S1
PLOT I/P
RESET
EXTERNAL PLOT MODE
I/P
TRIG
BOARD A
DATA WRITE-STEP COMMAND
550 μ sec DELAY
128 m sec DELAY
CLOCK
AUTO PLOT
DECIMAL COUNTERS 1 2 3
DISPLAYS 1 2 3
COUNTER O/P TO BOARD B
MULTIPLEXER 1
MULTIPLEXER 6
ADDRESS CHECKING
BINARY COUNTER
COMBINED WRITE-STEP CIRCUIT
DELAY & WIDTH
END OF RECORD
BOARD B
ADDRESS NON-ZERO
DATA
'H-K' LED's
BOARD A
DATA LEVEL INVERTERS AND LED DRIVERS
WRITE-STEP INVERTER / DRIVER CIRCUIT
END OF RECORD INVERTER / DRIVER CIRCUIT
2^0
2^1
2^2
2^3
2^4
2^5
TAPE RECORDER

Fig. 1.

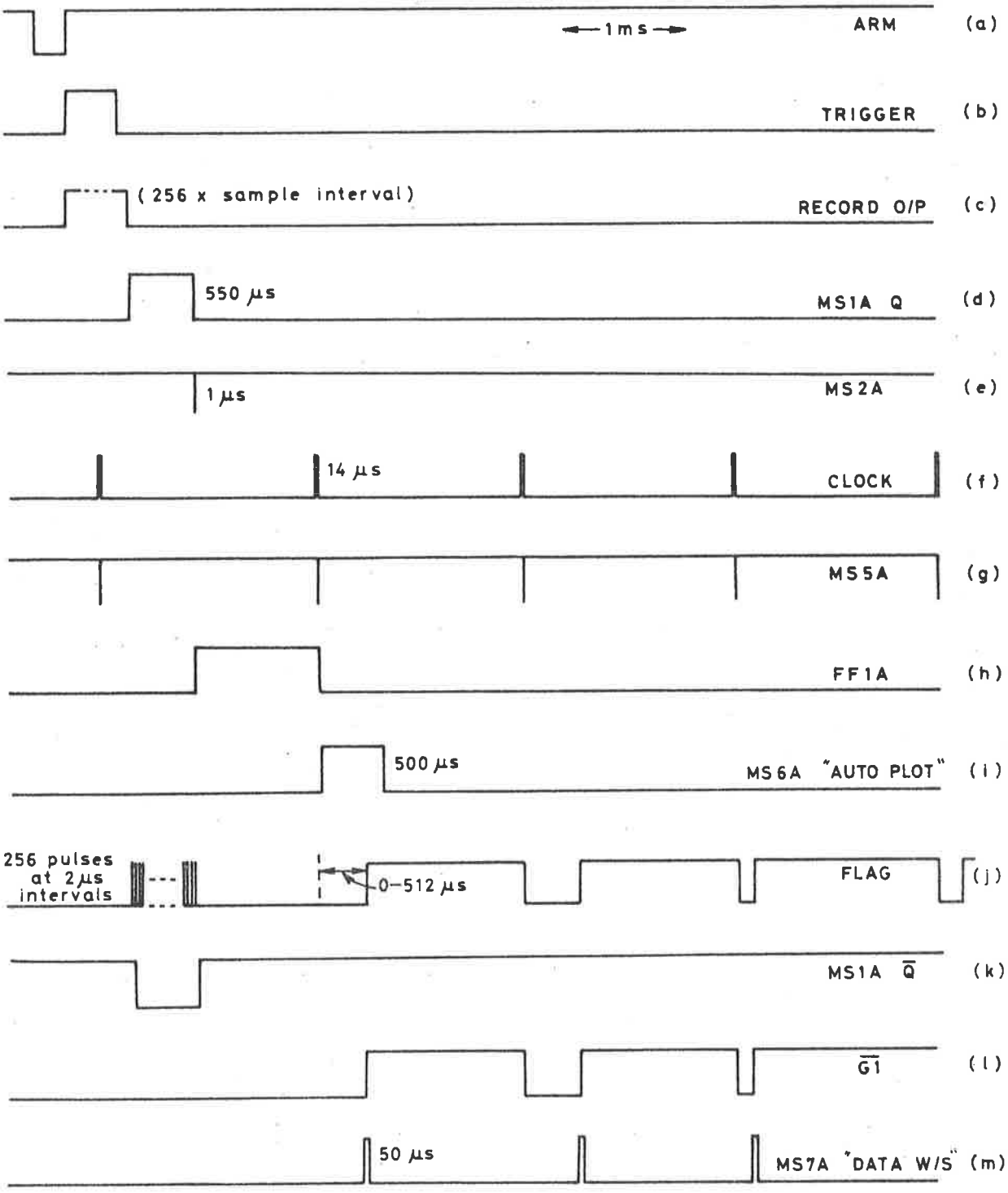

Fig. 2 PLOT PULSE & DATA WRITE-STEP TIMING

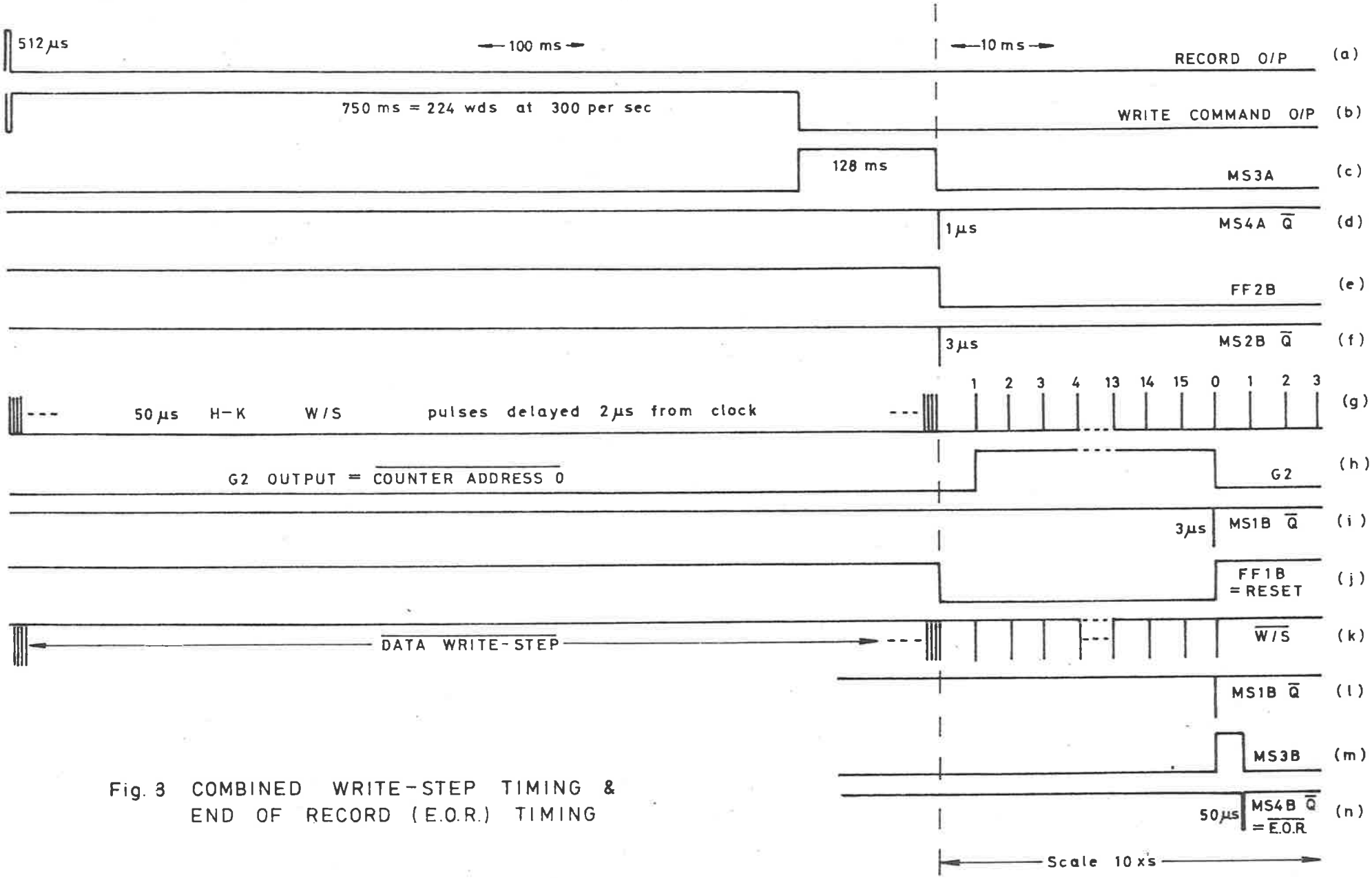

Fig. 3 COMBINED WRITE-STEP TIMING & END OF RECORD (E.O.R.) TIMING

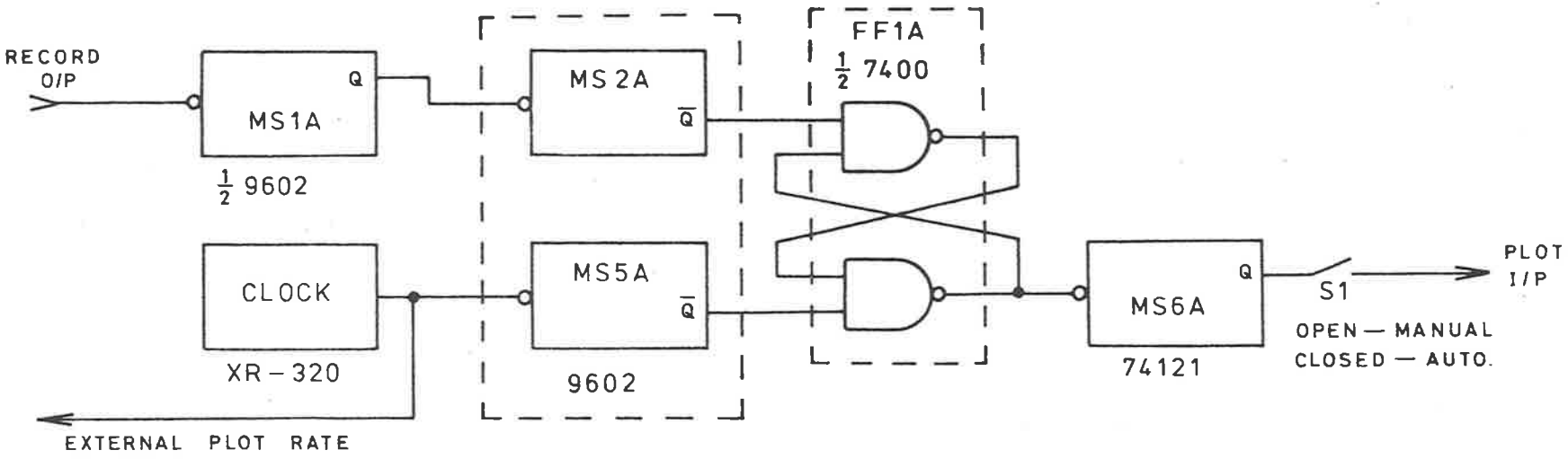

Fig. 4 AUTO PLOT CIRCUIT

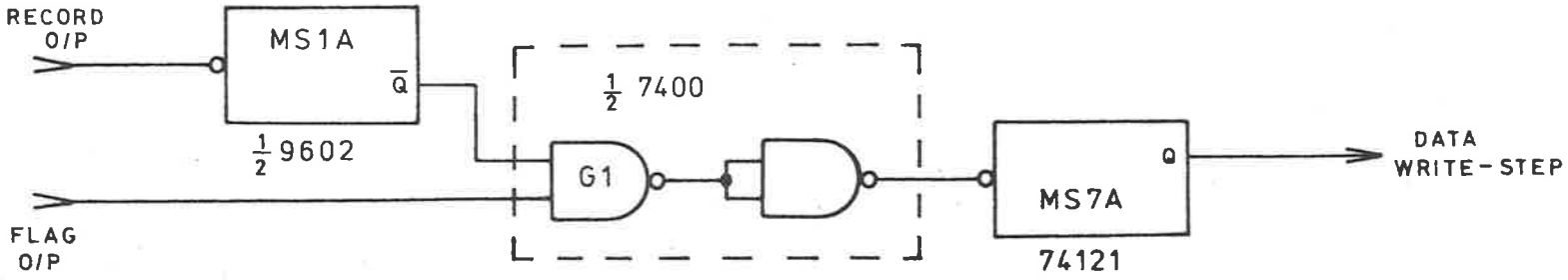

Fig. 5 DATA WRITE-STEP CIRCUIT

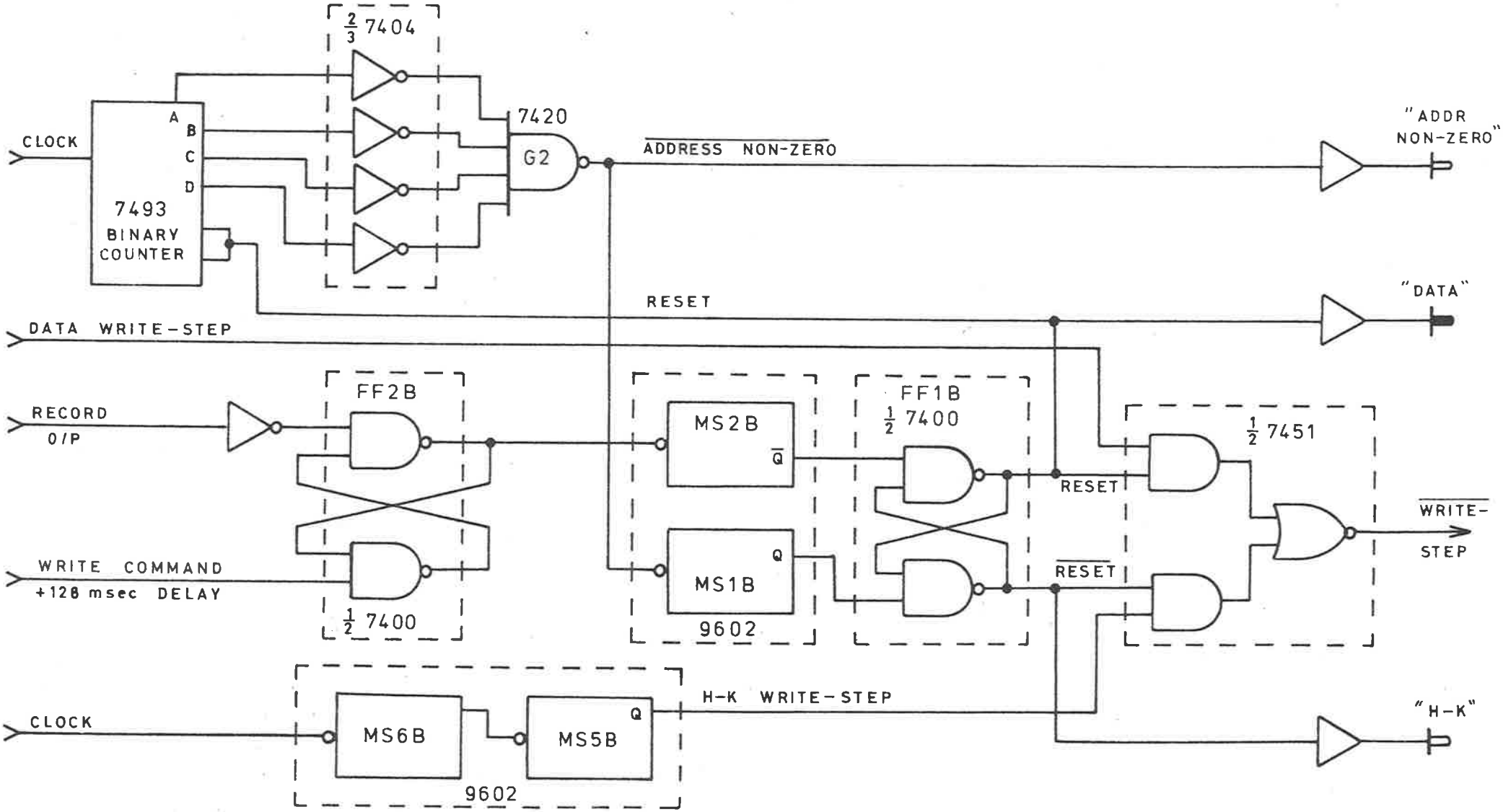

Fig. 6 COMBINED WRITE-STEP CIRCUIT

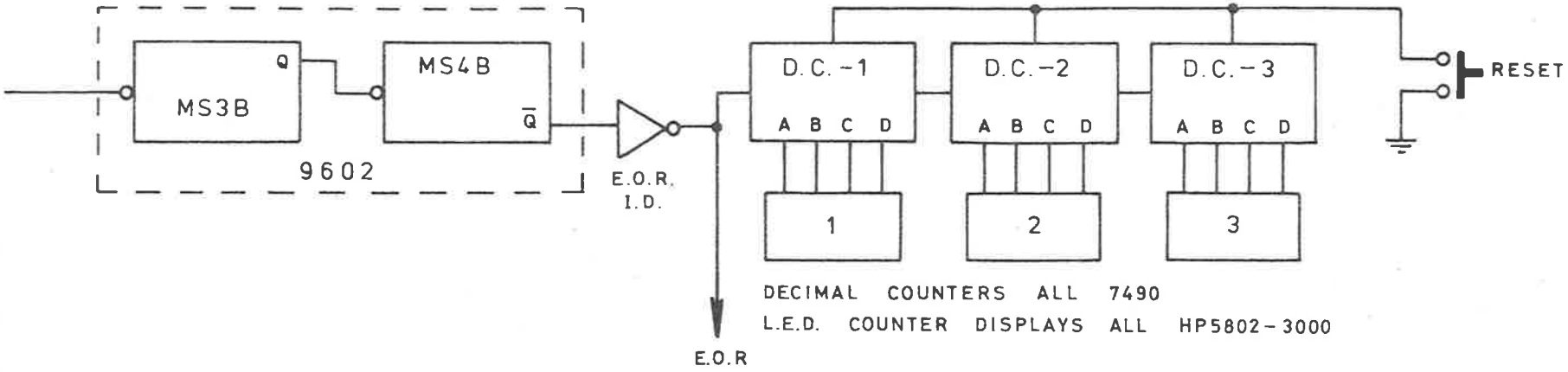

Fig. 7 END OF RECORD (E.O.R.) & COUNTER DISPLAY CIRCUITS

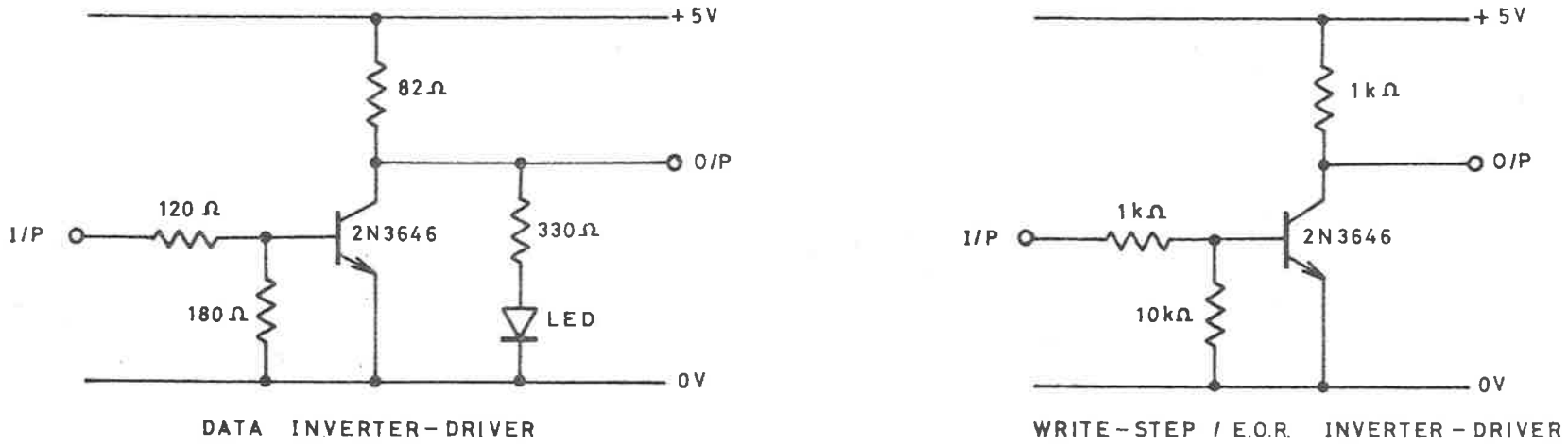

Fig. 8 INVERTER-DRIVER CIRCUITS (I.D.)

APPENDIX III

Reprint of Paper :

"Signal Induced Noise in Photomultipliers used in Lidar Receivers"

by

S.A. Young

(J. Atmos. Terr. Phys. 38, 667, 1976)

Young, S.A., (1976) Signal induced noise in photomultipliers used in lidar receivers.
Journal of Atmospheric and Terrestrial Physics, v. 38 (6), pp. 667-670, June 1976

APPENDIX IV

Reprint of Paper :

"Stratospheric Aerosol Optical Thickness Measurements at 35° S"

By

S.A. Young and W.G. Elford

(Nature, 278, 540, 1979)

Young, S.A., and Elford, W.G., (1979) Stratospheric aerosol optical thickness measurements at 35°S.
Nature, v. 278 (5704), pp. 540-541.